Gold-based Nanomaterials: Spectroscopy, Microscopy and Applications in Catalysis and Sensing

A thesis submitted in partial fulfillment of the requirement

for the Degree of Doctor of Philosophy

Rohul Hayat Adnan

BSc. in Chemistry (The University of Melbourne)

University of Canterbury

September 2014

Dedicated to Shahida Adam, for her love and untiring supports.

Thank you for always being there for me.

Hofstadter's Law: It always takes longer than you expect, even when you take into account Hofstadter's Law.

Douglas Hofstadter, *Gödel, Escher, Bach: An Eternal Golden Braid*

I certify that except where due acknowledgement has been made, the work is that of the author alone; the work has not been submitted previously, in whole or in part, to qualify for any other academic award; the content of the thesis is the result of work, which has been carried out since the official commencement date of the approved research program; any editorial work, paid or unpaid, carried out by a third party is acknowledged.

_____

Rohul Hayat Adnan

September, 2014

Abstract

The birth of nanotechnology era has revolutionized materials science, catalysis and field of optoelectronics. Novel and unique phenomena emerge when material dimensions are reduced to ultra-small size regime and enter nanometre (2-100 nm) realm. Such novel materials are expected to replace bulk materials, offering lower cost of manufacturing and enabling progress in many areas such as solar cell, drug delivery, quantum communication and computing, catalysis and sensing applications. With the progress in nanomaterial synthesis and fabrication, the need for the state-of-art characterization techniques became obvious; such techniques help to establish a complete understanding of the nature and interactions of nanosized materials.

In this thesis, the first part focuses on the synthesis of gold and ruthenium clusters, namely Au_8, Au_9, Au_{101}, Ru_3, Ru_4 and $AuRu_3$, using the well-established synthetic protocols in the literature. Apart from the standard lab-based characterization techniques such as nuclear magnetic resonance (NMR), UV-visible spectroscopy (UV-vis) and Fourier Transform Infra-red (FTIR), a less explored but useful technique far infra-red (far IR) spectroscopy, available at the Australian Synchrotron (AS), was employed to investigate the vibrational modes in these clusters. Peaks in the experimental far IR spectra were assigned unambiguously to specific vibrations by comparing with the ones generated *via* DFT calculations with the help of collaborators, group of Professor Gregory Metha, University of Adelaide. For the Au_9 cluster, three significant gold core vibrations are observed at 157, 177 and 197 cm^{-1} in the experimental spectrum. In the case of the Ru_3 cluster, only a single ruthenium core vibration is identified within the spectrum, at 150 cm^{-1} with the calculated force constant, k = 0.33 mdyne/Å. The Ru_4 cluster exhibits two metal core vibrations at 153 and 170 cm^{-1} with force constants of 0.35 and 0.53 mdyne/Å, respectively. Substitution with a gold atom yielding a mixed metal $AuRu_3$ cluster shifts the core transitions toward higher wavenumbers at 177 and 299 cm^{-1} with an increase in force constants to 0.37 and 1.65 mdyne/Å, respectively. This is attributed to the change in chemical composition and geometry of the metal cluster core. A combination of the DFT calculations and high quality synchrotron-based experimental measurements allowed the full assignment of the key transitions in these clusters.

Next, these clusters were fabricated into heterogeneous catalysts by depositing on different metal oxide nanopowders. Synchrotron X-ray photoelectron spectroscopy (XPS) and X-ray absorption spectroscopy (XAS) studies were performed at the Australian Synchrotron and the Photon Factory synchrotron in Japan to investigate the electronic structure of Au_8, Au_9 and Au_{101} on TiO_2 catalysts. The XPS analysis reveals that "as-deposited" Au_8 and Au_9 retain some un-aggregated clusters while Au_{101} show bulk-like gold. These findings are in line with TEM observations, where the aggregates (large particles, > 2 nm) of Au_8, Au_9 and Au_{101} are hardly seen under HRTEM. UV-visible diffuse

reflectance spectroscopy (UV-vis DRS) studies show the absence of localised surface plasmon resonance (LSPR) peaks in these "as-deposited" clusters, suggesting they are below 2 nm in size. Importantly, the XAS spectrum of "as-deposited" Au_9 clusters estimates that 60% of pure, un-aggregated Au_9 clusters and 40% of bulk gold in the sample. Upon calcination under O_2 and combined O_2 and H_2 (O_2-H_2), Au_8, Au_9 and Au_{101} clusters form larger nanoparticles (> 2 nm) with the appearance of LSPE peak in UV-vis DR spectra. In addition, majority of the phosphine ligands (that stabilise the gold core) dislodge and form phosphine oxide-like species by interacting with oxygen on the TiO_2 surface.

The third part focused on testing the catalytic performance of the supported Au_8, Au_9, Au_{101}, Ru_3, Ru_4 and $AuRu_3$ clusters on different TiO_2, SiO_2, ZnO and ZrO_2 in benzyl alcohol oxidation. Au_{101}-based catalysts display the highest catalytic activity with a turn-over frequency (TOF) up to 0.69 s^{-1}. The high catalytic activity is attributed to the formation of large Au nanoparticles (> 2 nm) that coincides with the partial removal of capping ligands. Au_8 and Au_9 clusters which contain NO_3^- counter anions are found to be inactive in benzyl alcohol oxidation. Further work shows that the presence of NO_3^- species diminishes the catalytic activity. Monometallic ruthenium clusters, Ru_3 and Ru_4, are found to be inactive yet the bimetallic $AuRu_3$ clusters are active in benzyl alcohol oxidation, suggesting the synergistic effect between ruthenium and gold metal. Investigation of catalytic testing parameters reveals that tuning selectivity of the product is possible through manipulating the reaction temperature.

Finally, a joint experiment with Prof. Wojtek Wlodarski's group at RMIT, Melbourne was undertaken to test the sensing ability of Au_9 clusters for hydrogen detection. Au_9 clusters were deposited onto radio-frequency (RF) sputtered WO_3 films at two different concentrations; 0.01(S1) and 0.1(S2) mg/mL. It was found that the optimal temperatures for sensor S1 and S2 were 300 °C and 350 °C, respectively. The sensor with lower Au_9 concentration (S1) displays a faster response and recovery time, and a higher sensitivity toward H_2. HRTEM studies reveal that the sensor S1 contain a significant population of sub-5 nm Au nanoparticles which might be responsible for a faster rate of H_2 adsorption and dissociation. The key finding in this study suggest that the addition of catalytic layer such as ultra-small Au_9 clusters results in improved sensitivity and dynamic performance (response and recovery time) of H_2 sensors.

In summary, this thesis demonstrated that cluster-based nanomaterials have wide range of applications spanning from catalysis to sensing. Further improvements in material synthesis and use of multiple complimentary characterization techniques allowed better understanding of the nature of the key active species (metal nanoparticles) assisting design of catalysts and sensors with enhanced performance.

Acknowledgements

A PhD thesis is never taken under vacuum. It always involves efforts of so many people contributing to the works done from the start of my PhD. Without them, I would not be able to walk through till the end. Firstly, I would like to thank my supervisor, Dr. Vladimir Golovko for allowing me to play with precious, noble metals such as Au, Pd and less expensive Ru, and for being patient in guiding me throughout this PhD. When I graduated from Melbourne as a physics student, I did not know so much about synthetic chemistry. But Vlad taught me a lot about experimental chemistry and some simple small tricks that tremendously improved the results and my synthetic skills; including how to do column chromatography, crystallization, and catalysis. I am also indebted to Professor Milo Kral, my co-supervisor who gave me access to use electron microscopy (TEM and SEM) at the Mechanical Engineering Department. I thank Mike Flaws, Technical Officer in Electron Microscope Laboratory, UC, for training me to use electron microscopes and maintaining these. I am truly grateful to have Dr. Matt Polson as another co-supervisor, who assisted me a lot with operation of instruments (TGA, GC and PXRD) and helped with synthetic chemistry. I thank Professor Bryce Williamson for valuable discussions focused on the data analysis *etc*.

I wish to extend my thanks to members of the Golovko group! In particular, I am indebted to Dave Anderson; who taught me how to synthesise gold clusters, Jan-Yves Ruzicka; who helped me with data processing for TEM and XPS, Faridah Abu Bakar; who helped me with PXRD and UV-vis DRS characterization methods, and Baira Donoeva and Daniil Ovoshchnikov; who helped me with catalysis. Importantly, million thanks go to the departmental support staff - without them I could not conducted any experiments. Special thanks to Danny and Nick; who built mini reactors for catalysis, Rob; who made numerous items of specialized glassware like Schlenk flasks and lines, Wayne; who always helped to repair electrical equipment like vacuum pumps *etc.*, Laurie and Gill; who helped me to find the best deal and order chemicals, Marie and Meike; who helped to establish HLPC methodology and record NMR spectra.

I also wish to express my gratitude to Associate Professor Gregory Metha (Department of Chemistry, University of Adelaide) and his students, Trystan Bennett and Jason Alvino, who performed DFT calculations and simulated far IR spectra as well as analysed XAS spectra. Many thanks go to Professor Gunther Andersson (School of Chemical and Physical Sciences, Flinders

University); who analysed the XP spectra and performed MIES experiments back at Flinders (we have a joint publication on MIES spectra of Au_9 even though it is not reported in this thesis).

I acknowledge contributions made by Professor Wojtek Wlodarski and his PhD student. Mohammad Zamharir, who performed H_2 sensing experiments using Au9-modified materials at the School of Electrical & Computer Engineering, RMIT University, Melbourne.

I am truly indebted to Bright Sparks Unit (BSU) at University of Malaya for financial support and scholarship, their kind understanding of delays with publishing papers and perseverance in supporting me.

PhD is indeed a very stressful journey, yet the presence of supportive and cheerful friends around me is a blessing. For this, I would like to thank Davey, Govind, Vivek, Pragya and Evan from the next door. We have wonderful moments all along the journey. We shared foods and drinks, and more importantly, we share our problems, joys and sorrows among us. We have been through thick and thin. I hope our friendships last longer.

Finally, I must express million thanks to my family, Mom and Dad, without whom I would not be who and where I am today. Thank you to my fiancée, Shahida Adam, for her love and continuous supports to keep me going.

List of abbreviations used in this thesis

AAS	Atomic absorption spectroscopy
Au	Gold
Au_8	$Au_8(PPh_3)_8(NO_3)_2$ (atomically precise cluster)
Au_9	$Au_9(PPh_3)_8(NO_3)_3$ (atomically precise cluster)
Au_{101}	$Au_{101}(PPh_3)_{21}Cl_5$ (narrow particle size distribution cluster)
BzAc	Benzoic acid
CP	Co-precipitation
CTAB	Cetyl trimethyl ammonium bromide
DP	Deposition-precipitation
EtOH	Ethanol
EXAFS	Extended X-ray absorption fine structure
Far-IR	Far infrared
FESEM	Field emission scanning electron microscopy
FWHM	Full width at half maximum
GC-FID	Gas chromatography using flame ionization detector
GC-MS	Gas chromatography using mass spectrometer as a detector
HBP	High binding energy peak
HPLC-MS	High performance liquid chromatography using mass spectrometer as a detector
HLPC-UV	High performance liquid chromatography using UV detector
HRTEM	High resolution transmission electron microscopy
IEP	Isoelectronic point
IR	Infrared
LBP	Low binding energy peak
MB	Methyl benzoate
MeOH	Methanol
MOX	Metal oxides
NEXAS	Near edge X-ray absorption structure
NMR	Nuclear magnetic resonance
NP(s)	Nanoparticle(s)

P	Phosphorous
PAMAM	Polyamido amine
PEI	Polyethylene imine
Pd	Palladium
Ph	Phenyl
Pt	Platinum
PVA	Polyvinyl alcohol
PVP	Polyvinylpyrrolidone
PXRD	Powder X-ray diffraction
Ru	Ruthenium
SEM	Scanning electron microscopy
SR	Alkane thiol
SG	Glutathione
TEM	Transmission electron microscopy
TGA	Thermogravimetric analysis
TOABr	Tetraoctylammonium bromide
TPP	Triphenyl phosphine
UV-vis DRS	UV-visible diffuse reflectance spectroscopy
XAS	X-ray absorption spectroscopy
XPS	X-ray photoelectron spectroscopy

Contents

Chapter 3: Experimental details and characterization methods

Chapter 1

Introduction to the thesis

The first chapter in this thesis provides brief outline of foundations pertinent to the work carried out in this PhD research project. This includes motivations and objectives for my research, the organization and structure of this thesis and contributions made by the author and external collaborators.

1 General research background

Catalysis plays a critical and essential role in the industrial processes and environmental remediation technology; from production of fine chemicals, synthetic polymers, lubricants and drugs to controlling the emission of toxic gases from vehicles and industrial factories.[1] Catalysts are not only used to transform raw materials into high added value products, but also in energy applications, such as fuel cells and energy storage devices. As the demand for commodity chemicals blossoms, utilization of catalysis grows rapidly with over 90% of the chemical processes in industry employing catalysts.[2] Nanoscience has made a significant impact on catalysis by improving the activity, selectivity and stability of catalysts.[3] As emphasized by Somorjai, catalysis is the central field of nanoscience and nanotechnology.[4] Today, a wide range of chemical reactions is catalysed by nanomaterials such as metal and metal oxide nanoparticles, carbon nanotubes and porous materials.

Heterogeneous catalytic reactions occur on the surface of the catalyst material. Irving Langmuir (Nobel Chemistry Prize 1932) once stated, "Most finely divided catalysts must have structures of great complexity. In order to simplify our theoretical consideration of reactions at surfaces, let us confine our attention to reactions on plane surfaces. If the principles in this case are well understood, it should then be possible to extend the theory to the case of porous bodies."[5] To increase the rate of a reaction, it is necessary to increase the surface area of the active sites. Two major ways to increase the surface area of catalysts are to decrease the particle size or to fabricate porous catalysts. Reducing the catalyst size is an advantage because it lowers the cost of production and manufacturing catalytic materials. Moreover, the shape and surface composition of metal particles are known to influence the catalytic performance (activity and selectivity) of a catalyst. Atoms at the surface of the bulk material are different from the atoms inside the bulk material of the same element. Atoms at the surface have fewer direct neighbouring atoms than atoms in the bulk and consequently possess a lower coordination number. Figure 1.1 shows that the smaller the particle size, the larger the number of surface, edge and corner atoms in icosahedron

clusters. As a result, small metal nanoparticles are favoured in catalysis due to the large surface area to volume ratio and low coordination numbers of atoms at their surface.

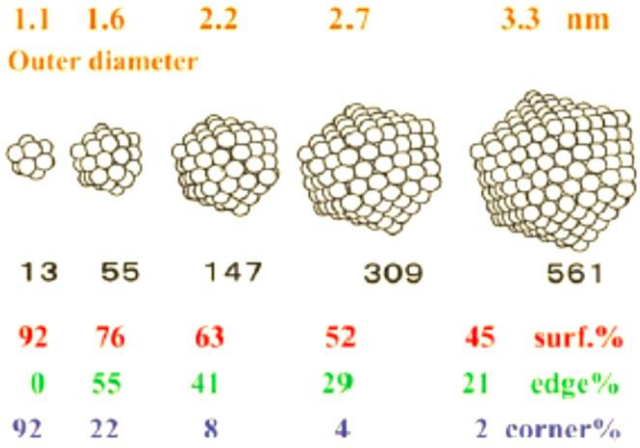

Figure 1.1 The outer diameters, the percentages of surface-exposed atoms, edge atoms and corner atoms in icosahedron clusters. Adapted from *Angew. Chem. Int. Ed., 2014, 53, 52*. Copyright Wiley-VCH publishing.

Apart from the unique physio-chemical properties of nanoparticles, the synthesis of nanoparticles using solution-chemistry methods offers benefits of the reduced cost of the material fabrication (*cf*. UHV techniques) and opportunity of a large-scale production.

1.1 Heterogeneous catalysis using nanomaterials

In general, a catalyst is defined as a material that accelerates (increases the rate of) a chemical reaction by providing an alternative, lower-energy reaction pathway without itself being consumed in the reaction (Figure 1.2).[6]

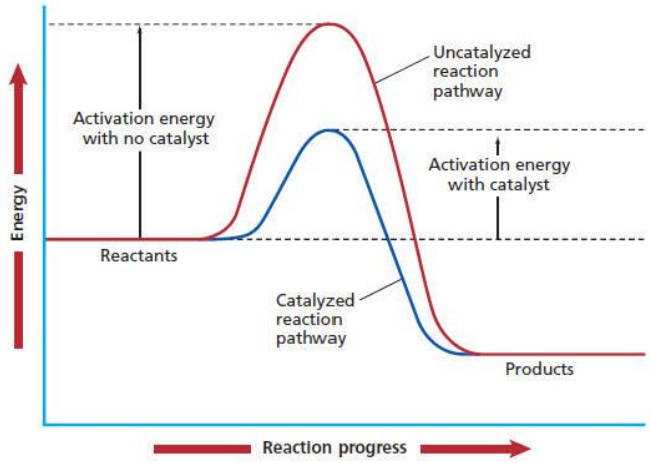

Figure 1.2 The reaction pathways in the absence and presence of a catalyst in a chemical reaction

For a chemical reaction that yields different possible products, preferred formation of one of the possible product is referred to as selectivity. The history of catalysis could be traced back to 1746 when John Roebuck began production of sulfuric acid in a lead chamber during the Industrial Revolution.[7] However, the scientific definition of catalysis was given almost 100 years later by Jakob Berzelius in 1835.[8] Since then, a range of industrially relevant and important processes adopted catalysts to facilitate or even enable the processes. Remarkable examples of implementation of catalysts in chemical processes include Sabatier process[9] and Fischer-Tropsch reaction.[10] A brief summary of historical milestone developments in catalysis is provided in Table 1.1.[11]

Catalysts can be generally divided into two major categories - homogeneous and heterogeneous catalysts. In homogeneous catalysis, the catalyst and the reactants exist in the same phase while in heterogeneous catalysis, the catalyst exists in a different phase *cf*. the reactants. Homogeneous catalysts have high activity and selectivity, but they are difficult to separate from the final products. With regard to this issue, heterogeneous catalysts are preferred in the industry because they can be easily recovered and recycled, allowing continuous mode of plant operation. However, heterogeneous catalysts suffer from low activity and selectivity because only a small fraction of the catalyst located on the surface of the material provides a platform for a reaction to occur. To overcome this issue, small-sized particles (nanoparticles) are homogeneously deposited onto solid supports such as activated carbon and metal oxides.[12]

Table 1.1 The historical development of catalysis

Catalytic reaction	Catalyst	Main author	Year
Sulfuric acid	Lead chamber	Roebuck	1746
Dehydration of alcohols	Acid	Priestley	1778
Esterification of organic acids	Acid	Scheele	1782
Dehydration of ethanol	Metal	Van Marum	1796
Oxidation of alcohols	Pt black	Priestley & Döbereiner	1810
Decomposition of H_2O_2 and NH_3	Metal	Thénard	1813
Hydrolysis of starch to glucose	Acid	Kirchoff	1814
Combustion	Pt	Davy	1817
Decomposition of NH_3	Fe>Cu>Ag>Au>Pt	Dulong	1823
Oxidation	Pt	Fusinieri	1824
Oxidation of SO_2 to SO_3	Pt	Philips	1831
Definition of catalysis		Berzelius	1835
Oxidation of NH_3 to HNO_3	Pt	Kuhlmann	1838
$HCl + O_2 \rightarrow Cl_2$	Cu	Deacon	1875
Esterification of acid	Acid	Bertholet	1879
Hydrolysis of esters	Acid	Bertholet	1879
Sulfuric acid	V_2O_5		1875
Friedel-Craft reactions	Lewis acid ($AlCl_3$)	Friedel & Crafts	1877
HNO_3 synthesis	Pt gauzes		1904
NH_3 synthesis from N_2 and H_2	Fe	Haber	1909
Hydrogenation	Ni	Sabatier	1912
$CO + H_2 \rightarrow CH_3OH$	ZnO-chromia	BASF	1923
$CO + H_2 \rightarrow$ hydrocarbons	Fe, Co	Fischer & Tropsch	1923
Hydrogenation of vegetable oils	Ni	Raney	1926
Petroleum cracking	Acid	Houdry	1930
Alkylation reaction for gasoline fuel	Acid	Ipatieff & Pines	1940
Synthesis of zeolites		Berrer & Breck	1946
Olefin hydrogenation	Au/MOX*	Bond & Sermon	1973
CO oxidation below 200 °C	Au/MOX*	Haruta	1987

*MOX stands for metal oxides

One of the significant applications of heterogeneous catalysis is automotive catalytic converters. Pt metals are widely used in catalytic converters to remove toxic substances from car exhausts.[13] A detailed molecular mechanism of the catalytic oxidation of CO over Pt surfaces was given by Gerhard Ertl (Nobel Prize in Chemistry in 2007), depicted in Figure 1.3 below.[14] However, there is an increasing concern about the environmental pollution resulting from the emission of Pt, Pd and Rh from catalytic converters; Pd and Rh are known to be carcinogenic.[15] A remarkable breakthrough was reported by Haruta *et al.* in 1987 when the authors discovered that small Au particles (~ 4.5 nm) were active in CO oxidation at low temperature.[16] This significant finding offers the possibility of replacing with gold the expensive and toxic Pt group metals in catalytic car converters (which also require high temperature for their operation).

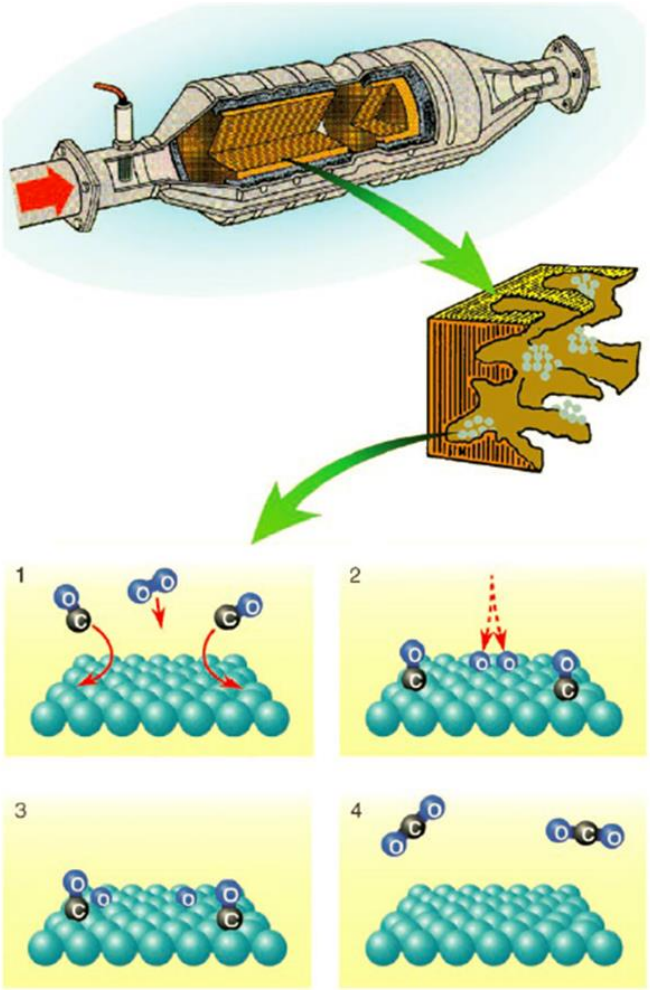

Figure 1.3 The scheme of mechanism of the CO oxidation over Pt catalytic converters. Adapted from *Angew. Chem. Int. Ed., 2008, 47, 3524*. Copyright Wiley-VCH publishing.

Besides Haruta's work, Hutchings independently discovered the high catalytic activity of auric chloride in acetylene hydrochlorination in 1985.[17] Since then, numerous publications appeared in the literature, extending the use of gold catalysts to oxidation of alcohols, alkenes and amines, coupling reactions and hydrogenation.[18-23] Figure 1.4 displays the number of publications focused on Au-based catalysts illustrating exponential increase in their numbers from 1985 until 2012.[24] A collection of review articles focused on selective oxidation and hydrogenation can be found in references 25-30.[25-30]

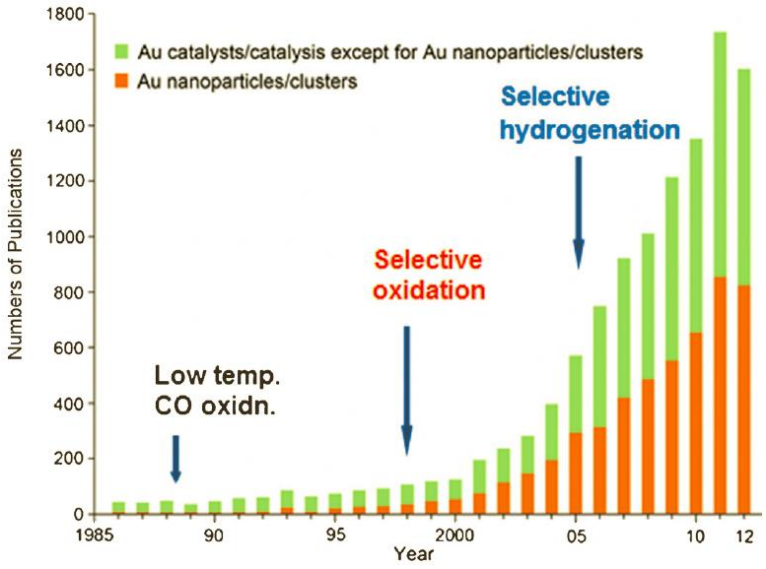

Figure 1.4 The number of publications dealing with Au catalysts and catalysis from 1985 until 2012. Adapted from *Angew. Chem. Int. Ed., 2008, 47, 3524*. Copyright Wiley-VCH publishing.

It is worth mentioning that despite the high catalytic activity of gold supported catalysts, for example in CO oxidation, the molecular mechanism is still often under debate with factors such as the oxidation state of Au species, the Au particle size, the geometry of active sites (edge or perimeter sites *etc.*), the nature of the support and the metal-support interaction playing key roles in explanation of observed activity. The lack of well-defined Au catalysts complicates the elucidation of the nature of the active sites. Consequently, it is very important to prepare uniformly sized and shaped Au nanoparticles on the support for model catalytic studies. One of the possible ways to address this issue is to use atomically precise Au clusters as key components in fabrication of catalysts. A number of atomically precise Au clusters stabilized by organic ligands (phosphines and thiols) has been synthesized since mid-last century. Their molecular formulae and structures have been elucidated by mass spectrometry and single crystal X-

ray diffraction studies. However, use of such clusters as precursors in fabrication of functional materials thus far has been very limited.

1.2 Aims of the thesis

The aim of this work is to synthesize Au clusters and mixed-metal clusters *via* wet-chemistry and to deposit and activate them on metal oxides supports to make heterogeneous catalysts. Different metal oxides are used to investigate the effect of inert and interacting metal oxides on the performance of resulting materials (activity and selectivity) in catalysis. In this work, the catalytic oxidation is tested using liquid phase aerobic alcohol oxidation of benzyl alcohol. Further application of metal clusters inspired by their performance in catalytic reactions is hydrogen sensing. The use of very low metal cluster loadings in catalysis and sensing offers low cost material fabrication route needed for bulk production. Not only metal clusters have high ratio of surface area to volume; they are also affected by a unique phenomenon called quantum size effect that display non-monotonous behaviour of scaling laws.

Another aim of this will be to characterize the physicochemical properties of the heterogeneous catalysts using multiple, complementary techniques using both lab-based and synchrotron-based techniques. Since every technique has its own advantages and limitations, it is necessary to use multiple characterization techniques, gather its separate information and build up a big picture of the heterogeneous catalysts. This crucial information helps to explain the nature of active site of supported Au clusters as heterogeneous catalysts.

1.3 Thesis organization

Chapter 1 provides general background for reported here research, aims of the thesis, thesis organization, contributions made by the author and external collaborators as well as mentions peer-reviewed publications based on reported here results. Additionally, the literature review about the synthesis of metal nanoparticles and clusters, and catalyst preparation is presented in this chapter.

Chapter 2 present a literature review about the history of nanomaterial and the basic underlying physics that constitutes the unique optical and electronic properties of metal nanoparticles, in particular gold nanoparticles. The synthesis of gold nanoparticles using wet-chemistry method and catalyst fabrication using different methods are also provided.

Chapter 3 focuses on the experimental details carried out in this research project including material synthesis, catalyst preparation and material characterisation. Basic principles of selected relevant characterization techniques, including their advantages and limitations, are described at the end of this chapter. This effort was made to lay down foundation for following results and discussion chapters and to fully emphasize why these complimentary techniques are crucial for adequate characterization of the functional materials (catalysts and sensors) reported here.

Chapter 4 presents results of the synchrotron far-IR investigation the metal-metal and metal-ligand bonding in metal and mixed-metal clusters informed by computational modelling studies. While the use of far-IR is still very rare, this chapter discusses the importance of it as a tool that might have significant impact in probing the vibrational modes of metal-metal and metal-ligands in metal clusters.

Chapter 5 presents spectroscopic and microscopic studies of the supported and activated metal clusters. Among of the spectroscopy used are XPS, XAS and UV-vis DRS. Microscopic imaging is performed using TEM.

Chapter 6 provides details of the study of the catalytic performance of the supported metal clusters such as Au_8, Au_9, Au_{101}, Ru_3, Ru_4 and Au-Ru_3 in liquid phase oxidation of benzyl alcohol. Different metal oxides, such as SiO_2, TiO_2, ZrO_2 and ZnO, were used as supports to study the effects of metal-support interactions in catalysis (with majority of studies carried out using SiO_2 and TiO_2).

Chapter 7 describes the application of Au_9 clusters deposited on WO_3 thin films for hydrogen gas sensing at industrially relevant H_2 concentrations. Effects of the Au cluster surface concentration (loading) and particle size on the sensing performance of resulting materials is described in detail in the light of data obtained using several complimentary characterization techniques (XPS, TEM, SEM *etc*.).

Chapter 8 provides and overarching summary of each of the main results and discussion chapters of this thesis and suggests several plausible directions for the future work.

1.4 Publications based on the results reported in this thesis

The PhD research reported here has led to several significant findings contributed to the body of knowledge in the area spectroscopic studies of metal clusters and heterogeneous catalysts:

1. R. H. Adnan, G. G. Andersson, M. J. Polson, G. F. Metha, V. B. Golovko. "Factors influencing catalytic oxidation of benzyl alcohol in liquid phase using supported phosphine-stabilized Au clusters." (accepted for publication in *Catalysis Science & Technology*).

2. M. Z. Ahmad, V. B. Golovko, R. H. Adnan, F. Abu Bakar, J.-Y. Ruzicka, D. P. Anderson, G. G. Andersson and W. Wlodarski. "Hydrogen sensing using gold nanoclusters supported on tungsten trioxide thin films." ***International Journal of Hydrogen Energy***, 2013, 38: 12865-12877.

3. D. P. Anderson, R. H. Adnan, J. F. Alvino, O. Shipper, B. Donoeva, J.-Y. Ruzicka, H. Al Qahtani, H. H. Harris, B. Cowie, J. B. Aitken, V. B. Golovko, G. F. Metha and G. G. Andersson. "Chemically synthesised atomically precise gold clusters deposited and activated on titania. Part II." ***Physical Chemistry Chemical Physics***, 2013, 15: 14806-14813.

4. J. F. Alvino, T. Bennett, D. P. Anderson, B. Donoeva, D. Ovoshchnikov, R. H. Adnan, D. R. Appadoo, V. Golovko, G. G. Andersson and G. F. Metha. "Far-infrared absorption spectra of synthetically-prepared, ligated metal clusters with Au6, Au8, Au9 and Au6Pd metal cores." ***RSC Advances***, 2013, 3: 22140-22149.

5. T. Bennett, R. H. Adnan, J. F. Alvino, V. Golovko, G. G. Andersson and G. F. Metha. "Identification of the Vibrational Modes in the Far-Infrared Spectra of Ruthenium Carbonyl Clusters and the Effect of Gold Substitution." ***Inorganic Chemistry***, 2014, 53: 4340-4349.

6. Andersson, G. G., V. B. Golovko, J. F. Avino, T. Bennett, O. Wrede, S. M. Mejia, H. S. Qahtani, R. H. Adnan, N. Gunby, D. P. Anderson and G.F. Metha (2014). "Phosphine-stabilised Au9 clusters interacting with titania and silica surfaces: The first evidence for the density of states signature of the support-immobilised cluster." ***The Journal of Chemical Physics*** 141(1), 014702.

Some of these results were presented in poster and oral presentation in seminars and conferences:

1. "Catalytic oxidation of benzyl alcohol using different metal clusters", MacDiarmid Student Symposium 2012 (Christchurch, NZ, November 2012).

2. "Liquid phase benzyl alcohol oxidation using supported Au_{101} on TiO_2 and SiO_2", NZIC Chemistry Conference (Wellington, NZ, December 2013).

3. Thesis in Three, "The novel physical and chemical properties of gold nanoparticles." Malaysian Post-graduate Association of Canterbury (MPAC) (Christchurch, NZ, August 2013)

Chapter 2

Literature review: synthesis of gold nanoparticles, catalyst preparation and characterization

Abstract

Nanomaterials have gathered much attention from synthetic chemists, theoretical physicists, engineers, biologists and material scientists. The nanomaterials as building blocks for architectures with enhanced performance in various applications due to their unique physical and chemical properties attracted attention ever since emergence of nanotechnology. Nanomaterials play a key role in a wide variety of research fields spanning from material science to medicine. The core of the field is in controlled fabrication of nanomaterials, followed by a complete characterization of produced materials using multiple complimentary techniques. This chapter discusses current developments in the area of nanomaterials with particular focus on fabrication of pure and supported gold nanoparticles and characterization techniques used to investigate the nature of such nanomaterials. Additionally, this chapter also highlights the challenges and difficulties in the field of nanomaterials as a missing knowledge gap and a motivational factor driving research in this area. This chapter starts with introduction of the general concepts and ideas, historical development of knowledge on gold nanoparticles up to the most recent discoveries in this field.

2.1 Introduction

In the late December 1959, Richard Feynman, Nobel Prize Winner in Physics in 1965, mentioned the ability to manipulate atoms and molecules as building blocks for new materials in his famous talk entitled "There's plenty of rooms at the bottom."[31] It is this talk that many authors commonly refer to as the birth of nanotechnology. Later, in 1974, Noria Taniguchi coined the term "nanotechnology" to describe the semiconductor technology processes, such as a thin film deposition, that has control over feature sizes in order of nanometers.[32] Gabor Somorjai then emphasized that catalysis is the central field of nanotechnology.[4] Nanotechnology is defined as the process of separation, consolidation and deformation of materials by one atom or molecule, while nanoscience is regarded as the study of physics and chemistry of materials in nanoscale size domain. Materials that are produced, processed, and fabricated with their dimensions within nanometre range are what we call nanomaterials today. The broad

applications of nanomaterials are found in far reaching fields including chemical sensors,[33-36] biosensors,[37-39] photovoltaic devices,[40-42] drug delivery,[43, 44] fuel cells,[45, 46] and catalysis[25, 47-49] (Figure 2.1). While there are different types of nanomaterials reported in the literature, such as metal nanoparticles, semiconductor nanocrystals, organic polymers, graphene and carbon nanotubes, this chapter focuses specifically on the noble metal nanoparticles and pays particular attention to gold nanoparticles.

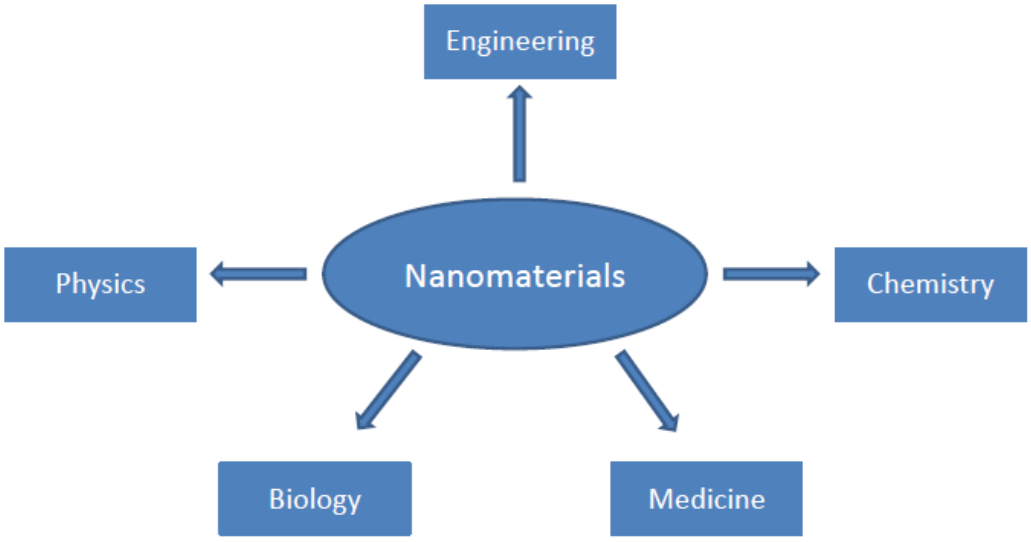

Figure 2.1 Nanomaterials play a key central for different scientific research fields

Coinage metal (copper, silver and gold) nanoparticles are of great interest because of their unique optical, electronic and catalytic properties.[50] Perhaps, the most famous example is the Lycurgus cup (see Figure 2.2) in the 5th century and cathedral windows that use colloidal gold nanoparticles to give brilliant, beautiful colours. This cup appears ruby red in the transmitted light and green in the reflected light. Coinage metal nanoparticles have surface plasmon resonance – their oscillating conduction band electrons can interact with the incident light, enabling potential applications in bio-imaging and bio–labelling, optoelectronic devices and surface enhanced Raman spectroscopy (SERS). When surface plasmon resonance is confined to the dimensions smaller than the wavelength of the incident light, such as that in metal nanoparticles (< 100 nm), it forms the localized surface plasmon resonance (LSPR). Interestingly, the LSPR peak maximum of these coinage metal nanoparticles is highly sensitive to their size, morphology and the dielectric constant of the surrounding medium, allowing tuning optical and electronic properties of these materials.

Figure 2.2 Lycurgus cup displayed in the British Museum/Art Source, NY. Left: reflection mode image; right: transmission mode image.

While the use of colloidal gold nanoparticles could be dated back to the 5th century AD, its systematic study started with the work of Michael Faraday in the 1850s, when he reduced tetrachloroaurate solution with phosphorous in carbon disulfide in a biphasic system.[51] Following the experimental work by Faraday, the theoretical aspect of the optical properties, including absorption and scattering, of metal colloids was successfully developed by Gustov Mie who solved Maxwell's equation for the interaction of light with a single metal nanoparticle.[52] However, the electronic properties of small metal particles were not fully understood until the establishment of quantum mechanics that offered an explanation of properties of various materials through the band theory model in the late 1950s.[53] Since then, a growing number of papers focused on the development of both experimental and theoretical aspects of nanoscience appeared in the literature.

2.2 Basic underlying physics

Chemists prefer to define metal clusters as atomically precise molecules having exact number of metal atoms and well-defined molecular structure that can be established using single crystal X-ray diffraction whereas term metal nanoparticles is reserved for the larger analogues of clusters which lack atomic precision. However, since nanotechnology research field involves people from various scientific backgrounds (physicists, engineers, biologists, material scientists), there is currently no general consensus over the rigorous definition of metal clusters and nanoparticles.[54-56] Experimental measurements on the optical absorptivity of thiolate-protected Au clusters show that the transition from metal to semiconductor, due to the quantum confinement, occurs at the critical size of ~ 2.2 nm.[57] Below this size

threshold, Au particles show molecular-like properties with discrete energy levels. Hence, for convenience, gold particle size below ~ 2 nm will be commonly referred to as clusters, whereas their larger counterparts (> 2 nm) will be referred to as nanoparticles throughout *this thesis*.[58] Here, the basic underlying physics of these materials are presented with an aim to explain selected differences between metal clusters and nanoparticles.

2.2.1 Quantum size effect

Nanoparticles (typically 2-100 nm, or containing more than 100s of atoms) occupy a niche between the bulk materials and discrete molecular clusters (typically from 2 to 100s of atoms). The free electron model with Fermi-Dirac statistics, also known as the Drude-Sommerfeld model, is commonly used to describe the band theory of metals; it is the simplest model developed by Arnold Sommerfeld who combined the classical Drude model with the quantum mechanical Fermi-Dirac statistics.[59] Although it neglects the important contributions from the electron-electron repulsion and electron-ion lattice interaction, this model is sufficiently accurate to the first order approximation.[60]

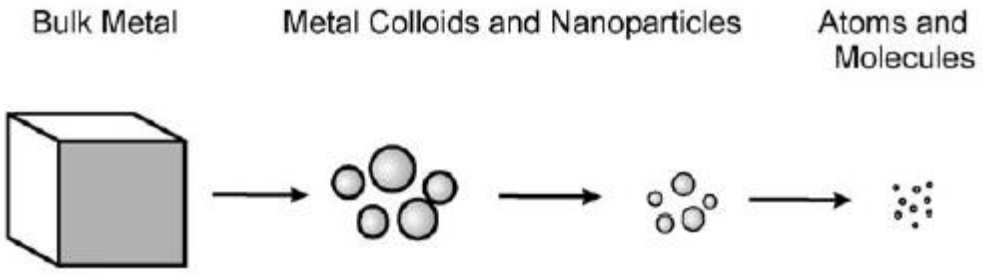

Figure 2.3 The transition from bulk metal to nanoparticles, clusters and atoms.

Gold metal has the electronic configuration of [Xe] $4f^{14}$ $5d^{10}$ $6s^{1}$ and melting point at 1,064 °C, adopts fcc crystal structure in its bulk form with the unit cell edge length of 0.408 nm and has the electron density of $6x10^{22}$ electrons per cm^3 for its 6s valence electrons. The free electron model assumes that electrons are in the cube shaped potential. Now let us suppose there are N electrons in a cube of volume a^3. From any undergraduate physics textbook, the Schrodinger's equation is written as:

$$\mathcal{H}\Psi = \left(-\frac{\hbar^2}{2m}\nabla^2 + V\right)\Psi = E\Psi \qquad 2.1$$

One can solve the Schrodinger equation by using the separation of variable method and then separate the variable x, y, and z in the Cartesian coordinate system. Hence, the eigenstates (energy levels) in Cartesian coordinates can be expressed as:

$$En = \frac{\pi^2\hbar^2}{2ma^2}n^2 \qquad 2.2$$

where, a is the length of the cube edge and n is the principal quantum number which takes positive integers 1, 2, 3, *etc.* and where $n^2 = n_x^2 + n_y^2 + n_z^2$. This equation gives the relation $E_n \sim n^2$ which forms a sphere with radius n (similar to the surface area of a sphere $SA=4\pi r^2$). The identical energy states are distributed on the spherical surface. Therefore, the volume of the sphere represents the number of energy states, s. The energy sates, s, are represented by the positive octants of the n-space since n_x, n_y and n_z takes only positive integer values, and we obtain the following equation

$$s = \frac{1}{8}\left(\frac{4}{3}\pi n^3\right) \qquad 2.3$$

Substituting n with the equation 2.2 gives us,

$$s = \frac{\pi}{6}\left(\frac{2ma^2}{\pi^2\hbar^2}\right)^{\frac{3}{2}}E^{\frac{3}{2}} \qquad 2.4$$

Differentiating the above equation with respect to energy, E, gives the density of state (DOS) and the reciprocal of the density of state is the spacing of the electronic energy level (δ).

$$\frac{ds}{dE} = \frac{a^3}{4\pi^2}\left(\frac{2m}{\hbar^2}\right)^{\frac{3}{2}}E^{\frac{1}{2}} \qquad 2.5$$

$$\delta = \frac{4\pi^2}{a^3}\left(\frac{\hbar^2}{2m}\right)^{\frac{3}{2}}E^{-\frac{1}{2}} \qquad 2.6$$

For a finite particle with exact number of atoms, the spacing of energy level (δ) increases substantially as the size, a, decreases. For a small metal particle at room temperature (~25° C or 298 K), the spacing of energy level is comparable to that of thermal energy; $E = k_bT = \delta$. Substituting all the constant and Fermi energy level for gold ($8.8\text{x}10^{-27}$ J), one can easily obtain the particle volume, a^3, to be ~ $5\text{x}10^{-27}$ m^3, giving the size dimension of ~ 1.7 nm.[60] However, it should be emphasized that this model

neglects a few things: 1) the electron-electron interaction, 2) the electron-ion interaction, and 3) the effect of ligands that stabilize the gold cluster and 4) quantum confinement effects which take into account the fact that the distribution function of the density of states changes as each dimension diminishes and the electronic structure ceases to behave in the same way as in the bulk material. Nevertheless, it gives a very good estimation for the critical size where the quantum size effect should appear for gold particles.

2.2.2 Absorption and scattering of light by metal nanoparticles

When Gustav Mie presented the qualitative description of the size dependent optical properties of a metal sphere in 1908, there was very little interest into studying the small metal particles at that time because physical and chemical methods to prepare such small metal nanoparticles were not fully developed yet except for the seminal work by Faraday. Furthermore, the characterization techniques such as electron microscopy (SEM, TEM), x-ray spectroscopy (XAS, XPS), and atomic force microscopy (AFM) were not fully established. The realization of the importance of the theoretical framework was later noticed to explain the behaviour of surface plasmon and its interaction with incident light.

The origin of the colour induced by the interaction with the incident light on metal is the coherent, collective oscillation of conduction electrons known as the surface plasmon resonance, SPR. These electrons move away from their equilibrium position when perturbed by external electromagnetic (light) field, producing a net charge which behaves like a restoring force that acts on these electrons in a spring-like way. When the surface plasmon resonates coherently at the frequency of the electromagnetic wave, a strong absorption occurs which is responsible for the observed colour produced by that metal. Surface plasmon can propagate freely along the metal-dielectric interface as surface-bound electromagnetic waves called surface plasmon polaritons, SPP. However, in metallic nanoparticles, these surface plasmons, confined due to nanosized dimensions and particular geometry of the nanoparticles, are unable to propagate freely and thus referred to as localized surface plasmon resonance (LSPR) as shown in Figure 2.4 below.

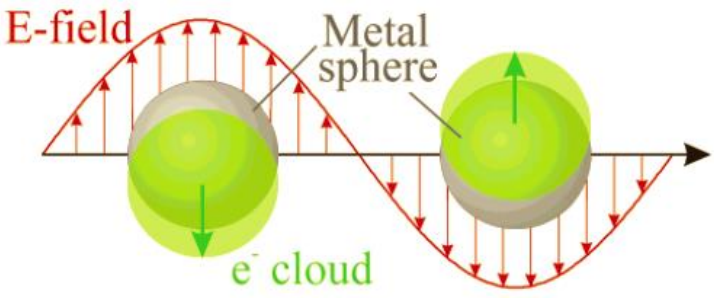

Figure 2.4 The illustration of the plasmon oscillation of a small metal nanoparticle particle. The conduction electrons are displaced relative to the nucleus upon excitation by electromagnetic wave. Adapted from *Journal of Physical Chemistry B 2003, 107, 668-677*. Copyright American Chemical Society.

For a spherical metal particle, Mie theory provides a rigorous solution to the Maxwell's equation of electromagnetic waves interacting with the frequency-dependent dielectric constant of the material.[52] His calculations suggest that the extinction cross section (the sum of absorption and scattering cross section) is dependent on the metal nanoparticle radius. Whether scattering or absorption will dominate depends on the size of metal nanoparticles. For a small particle (below *ca.* 20 nm), absorption takes place over scattering. When the metal nanoparticles have size smaller than the wavelength of the light, the dipole approximation may be applied, which provides simpler formulae. The polarizability of a small spherical metal nanoparticle is given by:

$$\alpha(\lambda) = 4\pi\varepsilon_0 R^3 \left|\frac{\varepsilon(\lambda) - \varepsilon_m(\lambda)}{\varepsilon(\lambda) + 2\varepsilon_m(\lambda)}\right| \qquad 2.7$$

where ε_0 is the vacuum permittivity, R is the particle radius, ε_m is the relative permittivity of the medium and $\varepsilon = \varepsilon' + i\varepsilon''$ is the complex relative permittivity of the particle. The scattering (σ_{sca}) and absorption (σ_{abs}) cross-sections are given by:

$$\sigma_{sca} = \frac{k^4}{6\pi\varepsilon_0^2}|\alpha(\lambda)|^2 \qquad 2.8$$

$$\sigma_{abs} = \frac{k}{\varepsilon_0}\mathrm{Im}[\alpha(\lambda)] \qquad 2.9$$

The resonance condition is fulfilled when $\varepsilon' = -2\varepsilon_m$ provided ε'' is small enough. Several numerical methods such as discrete dipole approximation (DDA), finite different time-domain (FDTD),

green dyadic method (GDM) are available to solve the Maxwell's equations in order to model the LSPR band.[61]

2.3 Preparation of nanoparticles

Two general routes can be employed to produce nanoparticles: the a) top-down and b) bottom-up approaches. The former route normally involves physical methods that mill the bulk material into nanoparticles such as ball milling,[62] laser irradiation,[63, 64] electron-beam lithography, photolithography, magnetron sputtering[65] or molecular beam epitaxy.[66, 67] However, these techniques require sophisticated and expensive equipment. In contrast, the bottom-up approach utilizing synthetic chemistry is a versatile and facile method to produce uniform nanoparticles on large scale.[68-72] In general, the preparation of metal nanoparticles consists of two parts: a) a reduction of metal cation precursor by reducing agents, b) a stabilization of the metal nanoparticles by organic molecules (ligands). Some of the reducing agents can act as stabilizers as well, hence simplifying the synthesis. Typical reducing agents are sodium borohydride, ascorbic acid, sodium citrate, formaldehyde, oxalic acid, ethylene glycols, carbon monoxide and hydrogen. Stabilizers are required to minimize the surface energy of metal nanoparticles in order to prevent the agglomeration of nanoparticles. In recent years, a wide variety of stabilizers have been explored including surfactants (CTAB, Tween 20), polymers (PVP, PVA), dendrimers (PAMAM, PEI), phosphine ligands, thiol ligands and sodium citrate.

In the following sub-section, a mini review of methods commonly employed for preparation of Au nanoparticles will be presented.

2.3.1 Citrate-capped Au nanoparticles (or Turkevich method)

With the invention of the electron microscope in the late 1930s, the truly scientific study on colloidal gold nanoparticles began with work by Turkevich *et al.* in 1951.[73] The authors introduced a simple, convenient and fast method used to prepare large gold nanoparticles by utilizing trisodium citrate as both reducing and stabilizing agent.[73] In this method, the aqueous solution of $HAuCl_4$ is boiled prior to the addition of the aqueous sodium citrate. After several minutes, a gradual colour change from yellow to colourless and eventually to red-wine is observed. This method produces gold nanoparticles larger than 5 nm, typically *ca.* 10-20 nm, due to the weak reducing ability of the citrate. Later, Fren *et al.* performed a thorough study on the effect of gold nanoparticle size and its size distribution by varying the concentration ratio of citrate to the gold precursor, allowing to tune average particle sizes within a wide range - from 16 to 150 nm.[74]

In addition to the improvement in the syntheses of gold nanoparticles, the mechanistic and kinetic studies of the gold nanoparticle formation were reported by several groups.[75-78] A breakthrough by Kumar *et al*. shows that the actual stabilizing agent in the citrate reducing method is the oxidation product of citrate, dicarboxy acetone (Figure 2.5).[79] He proposed that Au^{3+} is reduced to Au^{+} by the oxidation of citrate to form dicarboxy acetone. Then Au^{+} undergoes disproportion reaction to form the Au^{0} nuclei, leading to the growth of gold nanoparticles. Significant studies of the effect of pH,[80] temperature,[81] external stimuli (UV light irradiation, ultrasound)[82, 83] and water isotope (heavy water) have contributed a deep understanding on this simplest method to prepare gold nanoparticles.

Citrate-capped Au nanoparticles cannot be isolated and purified in the form of dry powder because citrate ligands weakly bind to the surface of Au nanoparticles and they aggregate upon centrifugation. Nevertheless, citrate ligands can be replaced by other strongly binding ligands such as thiols for surface functionalization in a ligand exchange process. Because of the simple preparation and strong tuneable absorption of light, citrate-capped Au nanoparticles have been used extensively as a wide variety of colorimetric sensors (chemical, gas, pH sensing).[33, 38, 84-86]

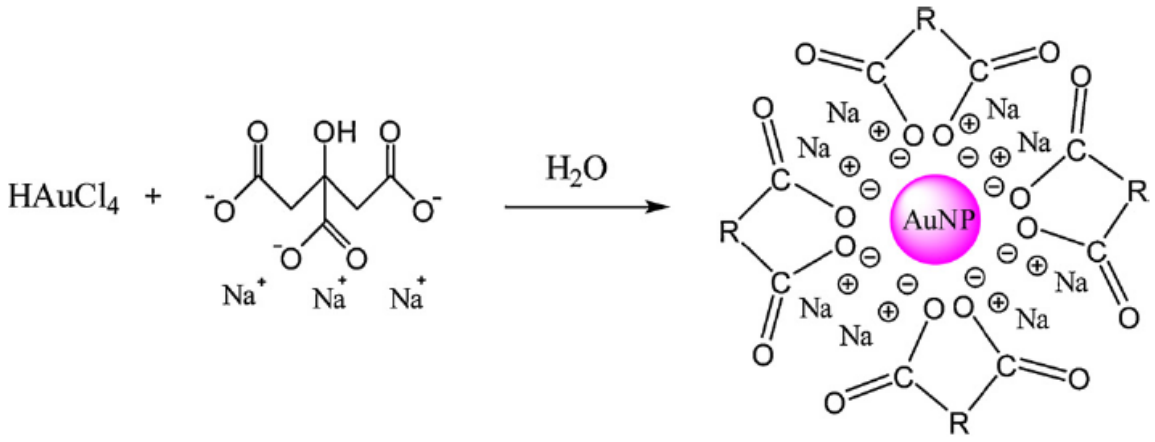

Figure 2.5 Scheme of synthesis of citrate-capped Au nanoparticles by Turkevich method. Adapted from *Coordination Chemistry Reviews, 2013, 257, 638*. Copyright Elsevier.

2.3.2 Thiolate-protected Au nanoparticles (or the Brust-Schiffrin method)

The synthesis thiolate-protected Au nanoparticles were motivated by the idea of 2-dimensional self-assembled monolayer by Mulvaney, Giersig, Dubois and Nuzzo in 1993.[87, 88] A year later, Brust *et al.* published a two-phase liquid (water and toluene) method to prepare thiolate-protected Au nanoparticles with a size range of 1-3 nm.[89] This method uses sodium borohydride as the reducing agent and tetraoctyl

ammonium bromide, TOABr, as the phase transfer agent. Unlike citrate-capped Au nanoparticles, the strong Au-S bond enhances the stability of thiolate-protected Au nanoparticles so that it could be isolated and dried as powder and redispersed in the solvent without aggregation or decomposition.[90] The advantages of thiolate-protected Au nanoparticles over citrate-capped ones are: a) large production up to gram scale, b) high thermal and air stability, c) easy surface modification and functionalization, and d) relatively small size and highly narrow size distribution.

While the Brust-Schiffrin method is widely employed to produce small and highly monodisperse Au nanoparticles, the detailed mechanism of the synthesis remains debatable. It was previously assumed that the thiol ligand reduced Au^{3+} to Au^{+} and form a $(AuSR)_n$ polymer-like structure as an intermediate.[58, 91] However, a remarkable work by Gouet and Lennon shows that rather $[TOA][AuBr_4]$ and $[TOA][AuBr_2]$ complexes are formed as intermediates.[92, 93] The addition of thiol ligands reduces $[TOA][AuBr_4]$ to $[TOA][AuBr_2]$ complexes. Finally, the addition of $NaBH_4$ further reduces $[TOA][AuBr_2]$ to form Au nanoparticles stabilized by thiol ligands. The general scheme is shown in Figure 2.6 below.

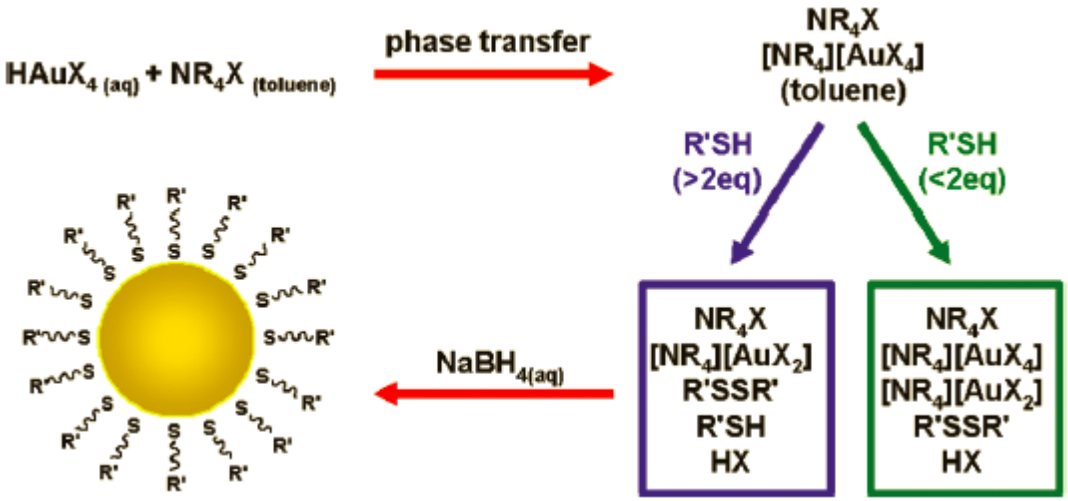

Figure 2.6 The general scheme of the Au nanoparticle synthesis in Brust-Schiffrin method. Adapted from *Journal of American Chemical Society, 2010, 132, 9582*. Copyright American Chemical Society.

In the last ten years, massive efforts have been focused on expanding and improving the synthesis of thiolate-protected Au nanoparticles to produce sub-2 nm gold particles; the so-called gold clusters. A very early work to prepare small Au clusters is credited to Alvarez *et al*. who prepared clusters with a size range of 1.4 - 1.7 nm and characterized them using mass spectroscopy and X-ray diffraction.[94] Several clusters were observed near 15, 23 and 29 kDa. However, it is worth noting that despite the very

small size of these clusters (< 2 nm), they are not truly monodisperse. The existence of larger gold nanoparticles complicates the theoretical calculations, optical spectroscopic measurements and data interpretations. Hence, clusters with a precise number of atoms and exact molecular structure are generally preferred as opposed to gold nanoparticles (> 2 nm) because the exact crystal structure can be established using single X-ray crystallography and its molecular formula can be confirmed using mass spectrometry.

Using a size focusing methodology that implies the principle of "survival of the robustest", several atomically precise thiolate-protected Au clusters have been synthesized and their structure has been established using X-ray crystallography; for example $Au_{25}(SR)_{18}$,[95] $Au_{36}(SR)_{23}$,[96] $Au_{38}(SR)_{24}$,[97] and $Au_{144}(SR)_{60}$.[98] In contrast to the Brust-Schiffrin protocol that uses a two-phase method, this size focusing method only uses one solvent system that avoids the use of the phase transfer agent (TOABr) and thus minimizing the impurity. This method avoids the tedious purification process that normally involves chromatographic separation, gel electrophoresis or fractionation.[99-101] In this method, a mixture of gold clusters are formed in the initial stage.[102] However, during the aging process or thiol etching, only gold clusters with the highest stability survive and the rest decompose.[103]

2.3.3 Phosphine-stabilized Au nanoparticles

Unlike thiolate-capped Au clusters and nanoparticles, phosphine-stabilised Au clusters have existed long before the former gained world-wide popularity. The history of phosphine-stabilised Au cluster starts with the preparation and characterization by single X-ray crystallography of the undecagold, $Au_{11}(PPh_3)_7(SCN)_3$ cluster by Malatesta and co-workers in 1969.[104] Since then, several phosphine-stabilized Au clusters have been synthesized and published in the literature including $Au_8(PPh_3)_8(NO_3)_2$, $Au_9(PPh_3)_8(NO_3)_3$, and $Au_4(PPh_3)_4I_4$. In general, phosphine-stabilized Au clusters are prepared by the reduction of the Au(I) complexes or salt by $NaBH_4$ at room temperature. For example, Teo *et al.* reported that the reduction of $HAuCl_4$ by $NaBH_4$ in ethanol produced $[Au_{39}(PPh_3)_{14}Cl_6]Cl_2$.[105] On the other hand, the reduction of the $AuPPh_3Cl$ complex in ethanol yields the undecagold cluster, $Au_{11}(PPh_3)_8Cl_3$.[106] Apart from $HAuCl_4$ and $AuPPh_3Cl$ as precursors, Velden *et al.* synthesized the $Au_9(PPh_3)_8(NO_3)_3$ (abbreviated as Au_9) cluster from the reduction of the light- and temperature-sensitive $AuPPh_3NO_3$ precursor by $NaBH_4$ in ethanol.[107] Au_9 plays a pivotal role as the precursor for other gold clusters such as $Au_8(PPh_3)_8(NO_3)_2$ and $Au_4(PPh_3)_4I_4$.[107]

While the triphenylphosphine ligand has been shown to be effective in preparing atomically precise Au clusters, a few attempts have been made to prepare the larger counterpart (gold nanoparticles). In 1981, Schmid *et al.* prepared the $Au_{55}(PPh_3)_{12}Cl_6$ cluster with an average core size of 1.4 ± 0.4 nm. However, their method involved using a toxic diborane gas as a reducing agent under an anaerobic condition. Such a method is not considered as a mild and green synthetic protocol. To overcome this issue, Hutchinson and co-workers developed a safer and more convenient method that involves a two-phase method and a phase transfer agent (TOABr).[108] In this method, they use $NaBH_4$ as the reducing agent and thus eliminate the use of a toxic diborane gas. Hutchinson and co-workers estimated that the clusters formed have an average formula of $Au_{101}(PPh_3)_{21}Cl_5$ (abbreviated as Au_{101}) which is based on the average size of 1.5 ± 0.4 nm according to TEM study. The scheme of the reaction pathway proposed by Hutchinson and co-workers is shown below;[108] Scheme 2.1 is not a balanced chemical equation because the product (Au_{101}) is not an atomically precise cluster, but a set of nanoparticles with particle size distribution which can be determined using TEM. Additionally, other by-products are not completely characterized and quantified due to difficulty in separating each component.

$$HAuCl_4 + 3PPh_3 \rightarrow AuPPh_3Cl + O{=}PPh_3 + PPh_3 + 3HCl + Au_{101}(PPh_3)_{21}Cl_5$$

Scheme 2.1 The reaction pathway for the formation of Au_{101} cluster

Later, Sardar *et al*. introduced a simple and fast synthetic protocol that avoids the tedious washing procedure that is necessary in Hutchinson's method.[109] In this method, $AuPEt_3Cl$ used as the gold precursor is dissolved in a biphasic mixture of toluene and acetonitrile together with triphenylphosphine. Then 9-BBN (9-borabicyclo-[3.3.1]nonane) is added as a mild reducing agent. Finally, the mixture is isolated by centrifugation and washed with hexane to remove impurities. Using this method, it is possible to vary the size of phosphine-stabilised Au nanoparticles from 1.2 to 2.8 nm with narrow size distributions. The advantage of phosphine-stabilized gold Au clusters or nanoparticles is that they can be precipitated, isolated and dried in the form of powder, similar to that of thiolate-stabilized gold clusters. Another advantage is the simple ligand exchange of phosphine with thiol resulting from the labile bonding between the phosphorous atom and gold.[110]

2.3.4 Polymer and dendrimer stabilized Au nanoparticles

Polymeric materials and dendrimers are commonly used to stabilize gold nanoparticles due to the steric repulsion resulting from the bulky and long-chain group of the polymers. Poly (N-vinyl-2-pyrrolidone (PVP) is the common polymer used to stabilize Au nanoparticles.[111] Tsukuda and co-workers synthesized small Au clusters with an average size of *ca.* 1.5 nm by reducing $HAuCl_4$ with $NaBH_4$ in the presence of PVP in water.[20] Interestingly, PVP-stabilized Au clusters are shown to be catalytically active in aerobic oxidation of alcohol in water.[112] Using multiple spectroscopic techniques, it is revealed that the catalytic activity arises from the increased electron density of the Au core due to the charge transfer from PVP. Hence, polymers have an influence on the electronic structure of Au nanoparticles and their catalytic activity. Other polymers including polyvinyl alcohol (PVA), and polyethyleneglycol (PEG) have been reported to produce highly stable gold nanoparticles.[113-115]

Dendrimers are highly-branched macromolecules, having a cauliflower shape and well defined composition and structures (Figure 2.7).[116] Having a shape that resembles a molecular cage, dendrimers can entrap and stabilize gold nanoparticles in the interior side that has functional groups such as amine, imide or carboxylic acid.[12] Two most commonly used dendrimers in the synthesis of the composite dendrimer-Au nanoparticles are polyamido amine (PAMAM) and polyethyleneimine (PEI), as displayed in Figure 8 below. The use of dendrimers as stabilizing agents has several advantages: a) dendrimer-encapsulated Au nanoparticles are highly stable against agglomeration, b) they provide control of solubility for homogeneous catalysis and immobilization for heterogeneous catalysis, c) due to mainly steric repulsion stabilization, not all Au surface is encapsulated, thus allowing a catalytic reaction with a substrate, and d) the dendrimer branches offer opportunity for tuning the selectivity of products in a catalytic reaction.[117, 118] The typical preparation of dendrimer-encapsulated Au nanoparticles involves the reduction of $HAuCl_4$ with $NaBH_4$ in water in the presence of dendrimers (Figure 2.8).[119] The size and size distribution of Au nanoparticles formed depend on the initial concentration ratio of dendrimer to Au and the rate of dendrimer generation.[120, 121]

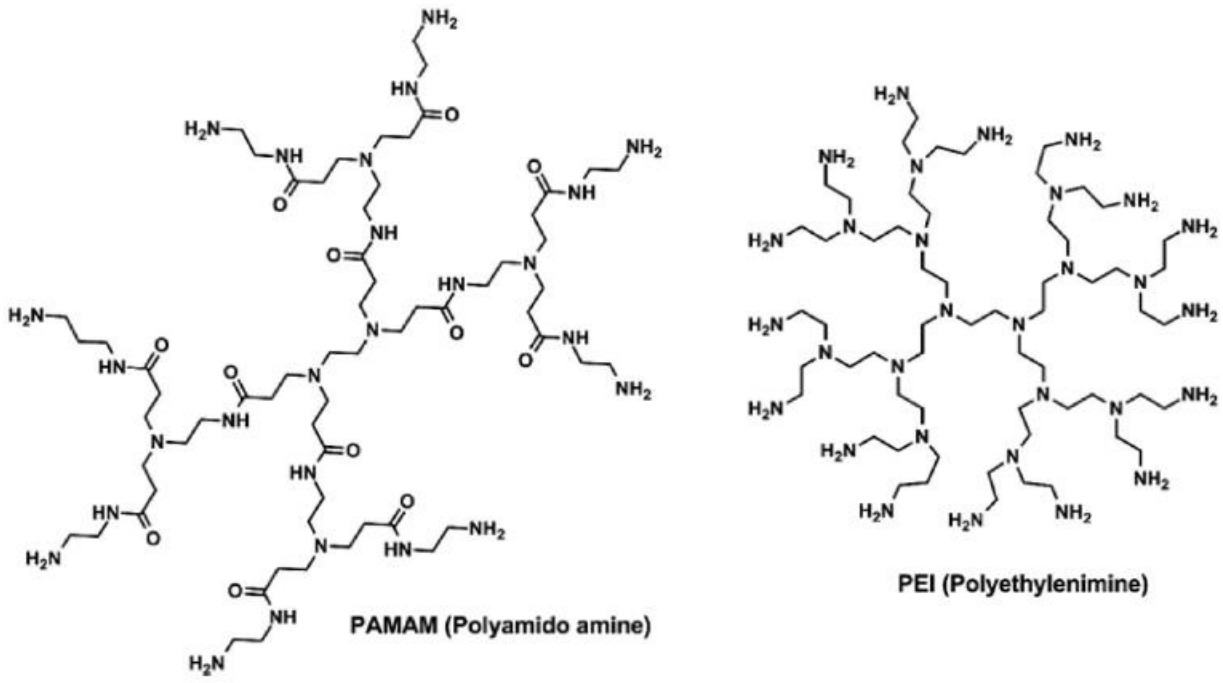

Figure 2.7 The structures of commonly used dendrimers to encapsulate Au nanoparticles. Adapted from *Chemistry of Materials 26(1), 72-83*. Copyright American Chemical Society.

Figure 2.8 A scheme of formation metal nanoparticles inside a dendrimer. Adapted from *Chemistry of Materials 26(1), 72-83*. Copyright American Chemical Society.

2.4 Gold in catalysis

By definition, a catalyst is a material that can speed up a chemical reaction without being consumed in the process.[6] Catalysis can be classified into two general classes: homogeneous and heterogeneous catalysis. In homogeneous catalysis, the catalyst exists in the same phase as the substrate,

while in the latter the catalyst has a different phase from the substrate. Heterogeneous catalysts are preferred in the industry and academic research due to their recovery and recyclability. However, heterogeneous catalysts suffer from a low activity and selectivity since only the surface area exposed to the substrate provides a platform for a catalytic reaction to occur. Typically, the fabrication of heterogeneous catalysts involve immobilizing active sites on a solid support such as metal oxides, charcoal, mesoporous materials or metal organic frameworks.

While gold has prevalent applications as plasmonic materials due to its surface plasmon resonance, little is known about its catalytic activity prior to the late 1980s.[122] Gold was not considered as an attractive choice in catalysis because it was known to be catalytically inactive and expensive. However, this view was no longer true when Haruta and co-workers observed that small gold nanoparticles of a mean size *ca.* 4.5 nm was catalytically active in CO oxidation at low temperature.[16] This finding reformed our understanding about the nature of small metal nanoparticles, in particular gold. Not only did it offer a new insight in scientific progress, but it also offered the possibility to replace the more expensive Pt-group metal catalysts that only work above 200 °C in catalytic converters that oxidize CO.[12] Since Haruta's discovery, many oxidation and hydrogenation reactions have been tested using gold nanoparticles as catalysts including oxidation of propene, glucose, glycerol and benzyl alcohol and hydrogenation of cinnamaldehyde, nitrophenol and methyl vinyl ketone.[30, 123-125]

2.5. Preparation of heterogeneous gold catalysts

2.5.1 Impregnation

The impregnation is the simplest method to prepare metal supported catalysts. In this method, the metal precursor, usually metal salts such as $HAuCl_4 \cdot 3H_2O$ or $AuCl_3$, is dissolved in water and brought into contact with the support.[126] The mixture is then aged for some time, dried and calcined. The most commonly used supports are Al_2O_3, MgO, SiO_2 and strongly interacting supports like TiO_2 and Fe_2O_3. Two impregnation methods can be classified depending on the volume of solution relative to the support: a) incipient wetness when the solution is less than the support volume and b) wet impregnation if the solution volume is used in excess.[127] The performance of catalysts prepared via this method depends primarily of the post-treatment conditions; calcination temperature, duration and atmosphere as well as the type of support used. The calcination under air at mild temperature (200 – 400 °C) is preferred to form Au nanoparticles on the metal oxide support.[128, 129] It is worth noting that, the gold oxide, Au_2O_3, decomposes to metallic Au and molecular oxygen at temperature above 200 °C due to high, positive

standard reduction potential of gold oxide (+1.5 V).[130, 131] If necessary, a reduction step under a H_2 atmosphere can be carried out to obtain metallic Au nanoparticles.

Despite its simplicity to prepare supported Au catalysts in a large-scale production for an industrial purpose, the catalytic activity is lower than the deposition-precipitation (DP) and co-precipitation (CP) method. A few modifications have been done to improve this method, including washing off the chloride residue (from $HAuCl_4$ precursor) in a step method developed by Delannoy *et al*.[128] and the two-step procedure by Xu *et al*.[129] The former method introduces a washing with ammonia solution (1 M, pH 11.5) step and then dried *in vacuo* at room temperature after the aging process of $HAuCl_4$ and the metal oxide support.[128] Using this improved method, catalysts consisting of small Au nanoparticles of around 3-4 nm are formed on the metal oxide support and exhibit comparable activity of those prepared by the deposition-precipitation method. The two-step procedure involves acidifying the $HAuCl_4$ precursor to induce its adsorption of onto the Al_2O_3 support and washing with ammnonia solution to convert Au chloride species into Au hydroxide. Finally, drying and calcining the catalyst at 400 °C for 4 hours in air produce highly disperse gold nanoparticles around 2.2 nm on the Al_2O_3 support.

The impregnation method utilizes the adsorption of anion $AuCl_4^-$ species on the support that is highly dependent on the isoelectric point (IEP) of the support material.[132] Isoelectric point (IEP) is defined as the pH at which the charge on the surface is neutral, while at pH below the IEP, the surface is positively charged due to the adsorption of H^+ ions, and at pH above the IEP, the surface is negatively charged.[133] The interaction of gold precursor ($HAuCl_4.3H_2O$) with the support proceeds by anionic adsorption allowing formation of gold nanoparticles from these precursor species during later stages of material processing, such as calcination.[127] Therefore, metal oxides with IEP ~ 7 (TiO_2, CeO_2, Fe_2O_3, ZrO_2) used as supports in this method usually give rise to catalytically active materials, whereas acidic support (SiO_2, WO_3, activated carbon) with much lower values of IEP appear to be inefficient in adsorbing $AuCl_4^-$ species, which precludes catalyst fabrication.[132]

2.5.2 Co-precipitation

Haruta *et al.* were the first to prepare highly active supported-Au catalysts for CO oxidation using several transition metal oxides supports including MnO_2, Fe_2O_3, Co_3O_4, NiO, CuO and Co-Mn composite in the co-precipitation method.[16] This method employs the aqueous solution of tetrachloroauric acid and transition metal nitrate as the precursors which can be precipitated as hydroxides or hydrated oxides with the addition of Na_2CO_3.[126, 127] Na_2CO_3 is preferably used to raise the pH of the solution as compared to NaOH because carbonates improve the pH stability.[127] In the solution of Na_2CO_3, gold chloride anions

gradually transform into gold hydroxides and release chloride anions. The precipitate is then washed, vacuum dried and finally calcined in air at a typical temperature of 400 °C.[134, 135] A reduction step in a reductive atmosphere is usually not required since gold precipitates decompose into metallic gold nanoparticles and deposit onto the surface of the support.

Using this method, Haruta *et al.* showed that supported Au catalysts were far more active than the impregnated catalysts under the same catalytic conditions.[135] As opposed to the conventional impregnation method which forms large Au nanoparticles (> 10 nm), the co-precipitation method produces small Au nanoparticles (< 5 nm).[134] However, there is a small possibility that some of Au nanoparticles being incorporated in the bulk material of the support during the co-precipitation process instead of on the surface, rendering low content of Au nanoparticles as the active site in catalysis.

2.5.3 Deposition-precipitation (DP) method

The deposition-precipitation (DP) is the first and most widely method used to produce highly active gold catalysts with a small Au nanoparticle size and narrow size distribution.[136] The key recipe to produce a highly active catalyst via this method is to prepare homogeneous distribution of similarly sized Au nanoparticles attached to the surface of the support.[126] This technique involves using a base to precipitate the metal precursor in the solution in the presence of the support powder. The role of a base here is to raise the pH of the solution, forming gold hydroxy species.[137] Figure 2.9 below shows Eh/pH diagram for the Au-Cl-H_2O system illustrating gradual substitution of Cl^- with OH^- within coordination sphere of Au(III) with increase of pH.[138]

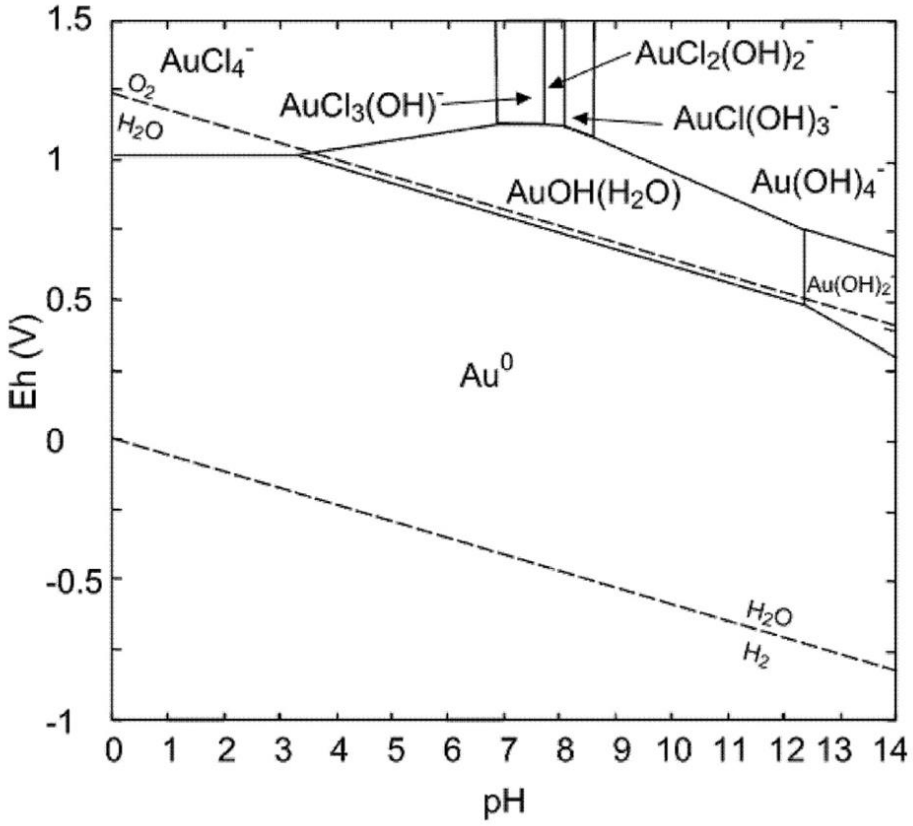

Figure 2.9 Eh/pH diagram for gold species in water. Adapted from American Mineralogist May-June vol. 88, 725-739 http://ammin.geoscienceworld.org/content/88/5-6/725/F1.expansion.html.

pH adjustment process is achieved remarkably using urea as the base, yielding a high loading of the Au precursor attached to the support with a small size and a narrow size distribution of Au nanoparticles. Urea, $CO(NH_2)_2$ is usually added at room temperature and the temperature is raised gradually to 90 °C to produce ammonium hydroxide homogeneously in the solution in a hydrolysis process (Scheme 2.2).[139] Because the formation of hydroxyl ions is slow and they are consumed immediately after they are formed, the hydroxyl ion concentration is low and the pH remains practically constant. During a precipitation process, the support acts as a nucleation site for the formation of the precipitates.

$$CO(NH_2)_2 + 3H_2O \rightarrow 2NH_4^+ + 2OH^- + CO_2$$

Scheme 2.2 The formation of ammonium hydroxide from urea decomposition

After the precipitation process, the catalyst is filtered, washed, and dried. A reduction step is generally required after drying by calcining the catalyst in air or under hydrogen atmosphere.[127] The size of Au nanoparticles depends primarily on the pH of the preparation solution and the calcination temperature. Haruta *et al.* introduced NaOH as the base to precipitate the Au precursor on TiO_2, Fe_2O_3 and Co_3O_4 and observed a high catalytic activity in the CO oxidation.[135] Despite the comparable catalytic activity of gold catalysts prepared by NaOH-assisted DP method to that of urea-assisted, the Au loading remains lower than that of urea-assisted because of high concentration of hydroxide.[137] The advantage of this DP method over the co-precipitation method is that all the active Au nanoparticles are deposited on the surface of the support, and none are doped within the bulk of the support material.[126] Nevertheless, this method is not applicable to acidic supports such as activated carbon and SiO_2 because the Au nanoparticle distribution is not highly dispersed on those supports.[127, 140]

Chapter 3

Experimental Details and Characterization Methods

Abstract

This chapter reports the experimental details including cluster synthesis, catalyst preparation, catalytic reactions and characterization using various different techniques. While the syntheses are well-established in the literature, some of the protocols are modified to give higher yields and better purity. It is well known in the area of nanomaterials that the reproducibility and large-scale synthesis of metal nanoparticles/clusters are the common issue. Here, the synthetic protocols are reported explicitly for every single step and some additional materials characterization experiments are performed to further confirm the purity of the products. The catalytic conditions are taken from the literature and further optimized to give the best result at ambient conditions. The fabrication of sensor thin films and experimental set up for hydrogen sensing are presented. Finally, the basic principles of characterization techniques such as transmission electron microscopy, and X-ray photoelectron, UV-visible spectroscopy and infrared spectroscopy are discussed briefly.

3 Introduction

The synthesis of numerous metal clusters is well described in the scientific literature since the 1960s. For example, clusters containing ruthenium clusters such as $Ru_3(CO)_{12}$ and $Os_3(CO)_{12}$ were synthesized in the late 1960s.[141, 142] At that time, $Ru_3(CO)_{12}$ was synthesized under high pressure of CO (~20 atm). Later Lavigne and co-workers introduced the synthesis of $Ru_3(CO)_{12}$ under mild conditions (at 1 atm CO, 70 °C and 3 hours) with improved yield.[143] In recent years, massive efforts have been allocated to improve the synthesis of metal clusters and/or nanoparticles.[144, 145] Here the synthetic methods of preparing metal clusters are reported according to the established protocols in the literature.

3.1 Synthesis of metal clusters or nanoparticles

3.1.1 Materials

All reactants were analytical reagent grade and used without further purification. Chloroauric acid was prepared using 99.99 % pure gold following the procedure detailed by Brauer.[146] Tetrachloroauric acid ($HAuCl_4.xH_2O$) was prepared by dissolving gold bar in *aqua regia* ($HCl:HNO_3$ = 3:1 v/v) solution

and evaporated to dryness. $RuCl_3.xH_2O$ was purchased from Precious Metal Online. Benzyl alcohol (> 99 %), benzaldehyde (> 99 %), methyl benzoate (99 %), benzoic acid (99.7 %), and anisole (> 99.5 % anhydrous) were purchased from Sigma Aldrich. HPLC grade methanol (99.9 %, Fisher Scientific) was degassed (N_2) and dried over pre-calcined alumina prior to use. Dichloromethane (99.9%), sodium borohydride (99%), sodium citrate (99%), toluene (99.9%), chloroform (99.9%), ethanol (99.9%) were purchased from Fisher Scientific. Acetone (99%), diethyl ether (99%), acetonitrile (99%) were purchased from Merck. NMR solvents such as CD_3OD and $CDCl_3$ were supplied by Cambridge Isotope Laboratories. Triflouroacetic acid (97%) and methyl lithium were purchased from Across Organic. Anatase (99.5 %, *ca*. 70 m^2/g, 10-30 nm particles) was purchased from SkySpring Nanomaterials. ZrO_2 (99.5%) and ZnO (99.5%) were purchased from US Nano. Instrument grade H_2 (99.98 % with < 20 ppm H_2O, BOC) and O_2 (99.2 % with < 10 ppm H_2O, Southern Gas Services Ltd.) were used for the calcination procedures.

3.1.2. $Au(PPh_3)Cl$

$Au(PPh_3)Cl$ is routinely prepared in our group according to method reported by Bruce *et al*.[147] Typically, a solution of triphenylphosphine (1.332 g, 5.078 mmol in 50 mL EtOH) was added to the solution of $HAuCl_4 \cdot 3H_2O$ (1.00 gram, 2.539 mmol in 10 mL EtOH) in a 100 mL volumetric flask. Triphenylphosphine solution was heated to 50 °C to complete dissolution *if necessary*. After stirring for 15 min, the white precipitate that formed was filtered on a fritted funnel #3 and washed with EtOH (2 x 5 mL). Finally, the white solid was dried *in vacuo* to obtain $Au(PPh_3)Cl$. The yield was 1.25 g (85 %). Characterization using ^1H NMR ($CDCl_3$): δ 7.52 (m) ppm with TMS as external reference, ^{31}P ($CDCl_3$): δ 33.2 (s) ppm with H_3PO_4 acid as external reference confirmed the purity of the product.

3.1.3. $Au(PPh_3)NO_3$

$Au(PPh_3)NO_3$ was prepared according to the synthetic procedure described by Malesta *et al*.[148] $AgNO_3$ (0.6867 g, 4.04 mmol) was dissolved in EtOH (125 mL) at 50 °C and then added to a solution of $Au(PPh_3)Cl$ (1.00 g, 2.02 mmol) in dichloromethane (40 mL) in 250 mL flask. After stirring for 30 min, the solution was filtered on a fritted funnel #4 and the filtrate was evaporated to dryness using rotary evaporator. The solid was washed with EtOH (3 x 50 mL) and then dissolved in chloroform (60 mL). The solution was filtered again to remove any impurities ($AgNO_3$) and the filtrate was evaporated to dryness using rotatory evaporator to obtain $Au(PPh_3)NO_3$. The yield was 0.8660 g (82.2 %). This compound is light- and temperature-sensitive. It was stored in a vial wrapped in Aluminium foil, in the fridge (4 °C).

Characterization using ^{31}P NMR ($CDCl_3$): δ 27.2 ppm (s) with H_3PO_4 acid as external reference verified the purity of the product.

3.1.4 AuMe(PPh_3)

Caution : Methyl lithium is very dangerous and reactive. Any chemical reaction dealing with methyl lithium needs to be under DRY atmosphere. Here I carried out the reaction the Schlenk flask fitted with rubber septum (Suba seal) under N_2 atmosphere. The glassware, stirrer bar and syringe were dried in oven overnight. Starting material ($AuPPh_3Cl$) was dried in desiccator overnight. Schlenk flask (250 mL) with stopper was connected to Schlenk line, degassed and purge with nitrogen three times. Then it was left in vacuo and heated using heat gun for 5 min to remove the residual water. It was then filled with nitrogen.

$AuMePPh_3$ was prepared according to the synthesis by Tamaki and Kochi.[149] $Au(PPh_3)Cl$ (1.00 g) was charged into 250-mL Schlenk flask. Dry toluene (*ca.* ~ 50 mL) was added to the flask with stirring. Methyl lithium in diethyl ether (1.6 M, 1.6 mL) was added dropwise while the Schlenk flask was immersed in dry ice-acetone mixture (roughly around 15 min). After the addition of methyl lithium, the flask was warmed up to room temperature and was kept stirring for 3 hrs.

EtOH (3 mL) and excess mili-Q water (30 mL) were added to the solution to get rid of excess methyl lithium. The aqueous phase from the mixture was discarded using separating funnel. The organic layer was kept in a separate beaker. The extraction of organic layer was repeated three time using toluene (30 mL). Sodium sulphate, Na_2SO_4 was added to dry the organic solution. The solution was carefully transferred into 100-mLmL round bottom flask and evaporated using rotary evaporator (without heating). The solid residue was pale brown. It was dissolved in toluene (40 mL) and charcoal was added to the solution to decolourise the solution. The solution was kept stirring for 1 hr at room temperature. It was then filtered through celite pad on fritted funnel. The volume of toluene was reduced to *ca*. 15 mL. n-pentane (45 mL) was added slowly and mixture was cooled to -18 C overnight to crystallize the product.

The yield of $AuMePPh_3$ obtained was 0.700 g (74%). ^1H NMR ($CDCl_3$/Ag foil) δ 0.55 (d, 3 H) with TMS as external reference, ^{31}P NMR ($CDCl_3$/Ag foil) δ 47.4 ppm with H_3PO_4 as external reference.

3.1.5 $(Au_9(PPh_3)_8)(NO_3)_3$ (referred to as Au_9)

The synthesis of Au_9 cluster followed the synthetic procedure from Ulrich Simon.[144] Typically, $Au(PPh_3)NO_3$ (1.005 g, 1.642 mmol) was suspended in EtOH (40 mL) while stirring. Then, $NaBH_4$ (0.0183 g, 0.042 mmol) dissolved in EtOH (23 mL) was added dropwise into $Au(PPh_3)NO_3$ solution. The mixture was stirred at room temperature for 2 h and then filtered. The filtrate (dark-red brown solution) was dried *in vacuo* using rotary evaporator. The solid residue was then dissolved in minimum amount of dichloromethane (5 mL). After filtering, the solvent was removed *in vacuo* using a rotary evaporator. The solid was then dissolved in tetrahydrofuran (40 mL) and was left undisturbed overnight (*ca.* 16 hours) to precipitate the solid. The precipitate was recovered by centrifugation at 5000 rpm (3 minutes) and then washed with tetrahydrofuran and hexane, alternately, for three times. Finally the precipitate was collected on fritted funnel #3 and rinse with hexane (15 mL x 3).

The yield obtained for Au_9 clusters was 530 mg (68%). The purity and identity of Au_9 clusters were verified using ^{31}P NMR ($CDCl_3$): δ 57.1 ppm (s) with H_3PO_4 acid as external reference. The UV/Vis spectrum displayed in Figure 3.1 was identical to the published data, confirming the pure product of Au_9 cluster.[144] The four peaks in the UV-vis spectrum correspond to the electronic transition in the cluster, not plasmonic excitation. Elemental analysis gave the result: %C: 42.6 (42.6), %H: 3.08 (2.99) and %N: 1.01 (1.04) with the values in parentheses are the calculated values.

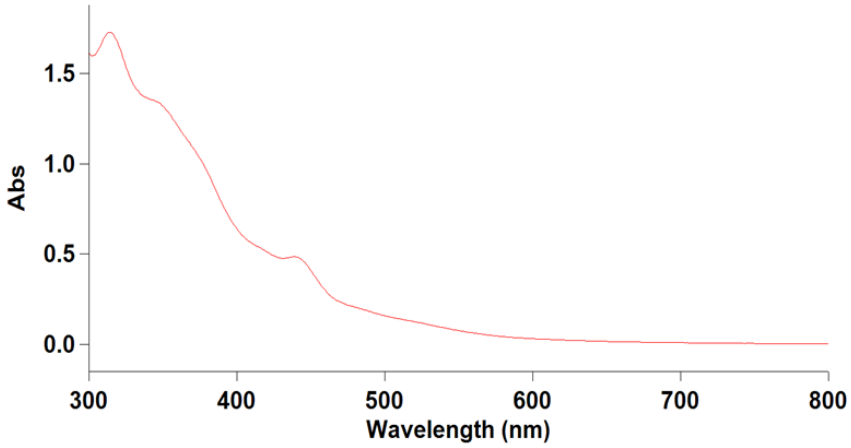

Figure 3.1 UV/Vis spectrum of Au_9 cluster in dichloromethane.

3.1.6 $Au_8(PPh_3)_8(NO_3)_2$ (referred to as Au_8)

Au_8 clusters were synthesized according to the protocol developed by Velden *et al.*[107] Au_9 clusters (0.220 mg) and 10-fold excess of PPh_3 were mixed in a dichloromethane (20 mL) and left stirred at room temperature for 30 minutes. After that the product was precipitate by adding toluene (200 mL) slowly through the wall of the flask. After 5 hours, the product was collected on fritted funnel #4 and washed with toluene (15 mL × 3) and hexane (15 mL × 3), alternately. The yield of Au_8 produced was 180 mg (85%). Au_8 clusters were verified using ^{31}P NMR ($CDCl_3$): δ 54 ppm (s) with H_3PO_4 acid as external reference. Elemental analysis gave the result: %C: 45.7 (45.5), %H: 3.27 (3.16) and %N: 0.81 (0.74) with the values in parentheses are the calculated values.

3.1.7 $Au_{101}(PPh_3)_{21}Cl_5$ (referred to as Au_{101} cluster)

The synthesis of Au_{101} cluster followed the preparation established by James Hutchison.[108] Chloroauric acid, $HAuCl_4.3H_2O$ (1.00 g, 2.539 mmol) in milli-Q water (60 mL) was stirred in 250 mL flask until it was completely dissolved to give bright yellow solution. Then toluene (60 mL) was added to the solution followed by addition of (TOAB) tetraoctylammonium bromide **(**1.40 g, 2.56 mmol) to the bi-phase mixture, resulting in a colourless aqueous phase and a red organic phase. The mixture was stirred vigorously for 5 min before the addition of triphenylphosphine (2.30 g, 8.76 mmol). The mixture was further stirred vigorously for 10 min. A solution of sodium borohydride, $NaBH_4$ **(2**.00 g, 52.9 mmol) in mili-Q water (10 mL) was added to the mixture *rapidly with stirring* and the mixture turned reddish-brown. The mixture was stirred for 3 h after the addition of sodium borohydride.

The aqueous and organic layers were separated using 250-mL separating funnel. The aqueous phase was discarded. The organic layer was washed 3 times with 100 mL mili-Q water. The organic layer was filtered using a fritted funnel #4 to remove any insoluble impurities (PPh_3, $AuPPh_3Cl$, $OPPh_3$). The filtrate was evaporated to dryness using a rotary evaporator. The crude product was dissolved in chloroform (35 mL). n-pentane (300 mL) was added *slowly* to the solution to precipitate the product. The suspension was filtered through a fritted funnel #4 to collect the crude product. The product was washed with the following solvents combination to remove TOAB:

- 2 x (100 mL hexane followed by 100 mL 2:3 MeOH:H_2O)
- 2 x (100 mL hexanes followed by 100 mL 1:1 MeOH:H_2O)
- 100 mL hexanes
- 2 x (150 mL 3:1 pentane:chloroform)

- 2 x (150 mL 2:1 pentane:chloroform)
- 2 x (150 mL 1:1 pentane:chloroform)

The purified product was rinsed with dichloromethane through the fritted funnel and then evaporated *in vacuo*. The yield was 180 mg. The ^{1}H NMR showed the composition of Au_{101} cluster as a broad band at δ 6-8 ppm. TEM image (Figure 3.2) shows the mean Au particle size around 1.6 ± 0.4 nm.

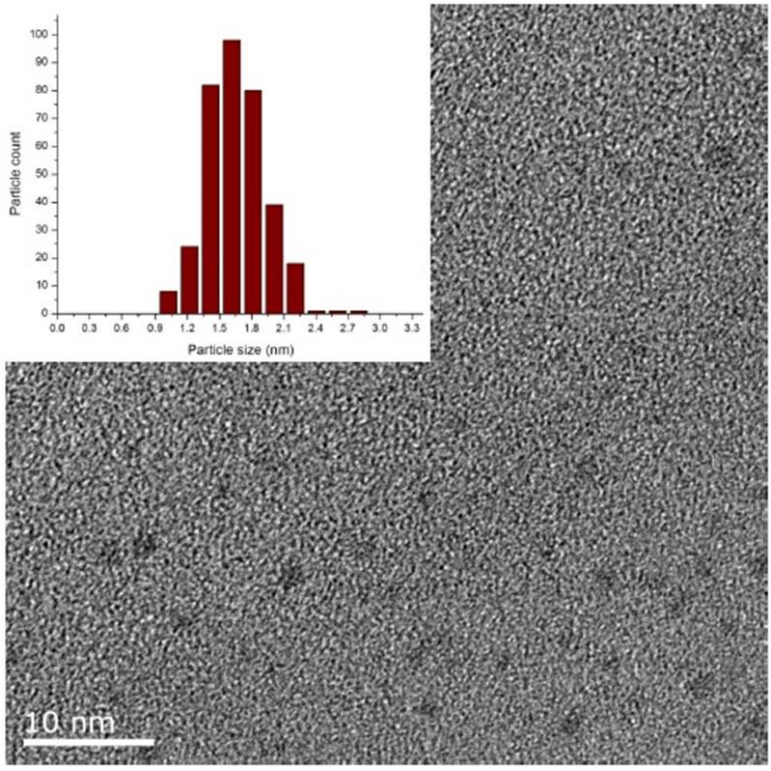

Figure 3.2 A representative TEM image of Au_{101} cluster on holey carbon film coated Cu 300 Mesh grid.

3.1.8 $Ru_3(CO)_{12}$ (referred to as Ru_3)

The preparation of $Ru_3(CO)_{12}$ was done according to the new method developed by Lavigne *et al.*[143] $RuCl_3.xH_2O$ (5.005 g) and 2-ethoxyethanol (250 mL) were introduced into in 3-neck round bottom 500-mL flask. The solution was first deaerated by bubbling nitrogen gas for 10 min. Then the flask was connected to reflux condenser. A lateral neck was connected with glass bubbler where CO gas inlet was introduced. A fast CO stream (2 bubbles per second) and vigorous stirring were maintain at this initial step. The solution was then heated to 80 ^{0}C for 45 min, in which the colour of the solution turned from black to red blood gradually. Then, the solution was heated up to reflux at 135 ^{0}C for 40 min, where transparent yellow solution was obtained. The solution was cooled down to 78 ^{0}C (the temperature needs to be strictly below 85 ^{0}C. KOH pellets (2.39 g) were added directly to the solution at 78 ^{0}C through

another lateral neck. The CO stream was stop temporarily at this moment for addition of KOH pellets). After the addition of KOH pellets, the solution gradually darkened over a total period of 40 min. At the end of the reaction, yellow solid was observed at the bottom of the flask. The heating was then stopped, but CO bubbling and stirring were maintained. Slow cooling from 78 ^{0}C to room temperature allowed crystallization of $Ru_3(CO)_{12}$ to occur effectively. The flask was vented under nitrogen for 10 min to remove CO gas.

The yellow solid was collected by centrifugation at 5000 rpm for 5 min and washed thoroughly with EtOH (3 × 20 mL) and milli-Q water (3 x 20 mL). The yield obtained was 1.40 g (35% yield) of $Ru_3(CO)_{12}$. Infrared in KBr liquid cell showed three bands (νCO cm^{-1}, cyclohexane): 2061 (vs), 2029 (s), 2010 (w).

3.1.9 $Ru_4(H)_4(CO)_{12}$ (referred Ru_4)

$Ru_4(H)_4(CO)_{12}$ was prepared according to the synthesis by Piacenti *et al.*[150] with a slight modification as to meet our Parr reactor specification. $Ru_3(CO)_{12}$ (1.01 g) and dry hexane (50 mL) were introduced into Teflon liner. The synthesis of $Ru_4(H)_4(CO)_{12}$ was done using Parr reactor. The solution was purged with H_2 gas three times to remove any residual oxygen. It was pressurized with H_2 at 125 bar. The temperature was raised gradually to 111 °C. The solution was maintained under 125 bar at 111 °C for 2 hours. Then it was cooled down slowly to room temperature while maintaining under H_2 atmosphere and with stirring overnight. Crystallization occurred during the slow cooling down. The yellow-orange solid obtained was washed with hexane (15 mL × 3). The yield obtained was 0.75 g (86 % yield). Infrared in KBr liquid cell (νCO cm^{-1}, cyclohexane): 2080 (s), 2066 (vs), 2030 (m), 2024 (s), 2008 (w) confirming that the product was pure.

3.1.10 $Ru_3(\mu\text{-}AuPPh_3)(\mu\text{-}Cl)(CO)_{10}$ (referred to as $AuRu_3$)

The synthesis of $Ru_3(\mu\text{-}AuPPh_3)(\mu\text{-}Cl)(CO)_{10}$ was done followed the preparation by Lavigne,[151] under inert nitrogen atmosphere (using Schlenk line). In a typical experiment, $Ru_3(CO)_{12}$ (310 mg, 0.48 mmol) and $AuPPh_3Cl$ (240 mg, 0.48 mmol) were degassed under vacuum for 30 min. Then they were dissolved in dry dichloromethane (50 mL) in 100 mL flask. The solution was refluxed for 18 h under the flow of nitrogen. The colour changed from orange to dark violet. After cooling and solvent removal under vacuum, the mixture was chromatographed on silica gel 60 (Mesh 200-430) with a combination of toluene:hexane (1:5 by volume). Two bands were afforded: yellow band corresponds to $Ru_3(CO)_{12}$ and purple band corresponds to $Ru_3(\mu\text{-}AuPPh_3)(\mu\text{-}Cl)(CO)_{10}$.

The yield of $Ru_3(\mu\text{-}AuPPh_3)(\mu\text{-}Cl)(CO)_{10}$ was 157 mg. Characterization using ^1H NMR ($CDCl_3$) δ: C_6H_5 7.47-7.51 (m), ^{31}P NMR ($CDCl_3$) δ: 70.5 ppm. IR (cyclohexane, cm^{-1}): 2092 (m), 2044 (vs), 2022 (s), 2008 (s), 1992 (m), 1983 (sh), 1965 (m) verified the purity of the product.[152]

3.1.11 $[Au(PPh_3)_3O][BF_4]$ (referred to as Au_3O)

The preparation of $[Au(PPh_3)_3O][BF_4]$ follows the equation according to the protocol establish by Bruce *et al.*[147] Ag_2O was prepared by adding the solution of NaOH (0.305 g in 10 mL water) to a solution of $AgNO_3$ (1.203 g in 10 mL water) under stirring and away from light. After 10 minutes, the produced brown precipitate was removed by filtration on a fritted funnel #3, washed with water (5 mL × 2), EtOH (5 mL × 2), acetone (5 mL × 2) and dried in air. The freshly prepared Ag2O was added to a solution of $Au(PPh_3)Cl$ (1.003 g, 2.0 mmol in 70 mL acetone) under stirring. $NaBF_4$ (1.253 g, 11.4 mmol) was added to the above solution. The solution was stirred rapidly for 1 hour. After this time, acetone was removed using rotary evaporator. The solid residue was extracted with chloroform (10 mL × 3). The combined filtrate was added to dry Et_2O to precipitate the product. The precipitate was removed by filtration on a fritted funnel #3. The yield recorded was 0.765 g, (77%). Melting point determination gave the value 204-206 °C. The identity and purity of Au_8 clusters were verified using ^{31}P NMR ($CDCl_3$): δ 23.8 ppm (s) with H_3PO_4 acid as external reference.

3.2 Catalyst preparation and activation

3.2.1 Deposition of clusters onto supports

Au clusters were deposited on the support using the slightly modified method reported by Anderson *et al.*[153, 154] The solvent was removed under reduced pressure instead of using nitrogen flow. Typically, the support, TiO_2 (3.00 g), was dried *in vacuo* at 200 °C for several hours (~ 5 h) prior deposition. After cooling to the room temperature, the support was suspended in dichloromethane (50 mL) with vigorous stirring (750 rpm). A calculated amount of gold clusters (to yield 0.17 wt% Au loading) was dissolved in dichloromethane and then was added to the suspension of TiO_2 and left stirring at room temperature. Finally, the solvent was removed in vacuo at room temperature and the catalysts were stored in a wrapped vial and kept inside the fridge. Similar protocol was also applied to deposit onto other supports such as SiO_2 (fumed), ZrO_2 and ZnO. The thickness of Au clusters on the support was not measured using atomic force microscopy (AFM) due to the material produced in the powder form.

3.2.2 Heat treatment on supported gold clusters

Two conditions for heat treatment were applied on TiO_2-supported gold clusters: a) calcination under pure O_2 atmosphere at 200 °C for 2 h, and b) calcination under pure O_2 at 200 °C for 2 h followed by calcination under H_2 at 200 °C for 2 h. Typically, 1.000 g of catalysts were added into a Schlenk flask with a magnetic stirring bar inside. The Schlenk flask was wrapped in aluminium foil to prevent exposure to light and connected to a Schlenk line which was connected to a gas cylinder (either O_2 or H_2). The Schlenk flask was degassed under vacuum and purged with gas. This degas-purge cycle was repeated for three times to remove air and ensure high purity of the gas atmosphere inside the Schlenk tube. The Schlenk tube was left connected to the manifold through which corresponding gas was passing; gas flow was set to *ca*. 1 bubble per second. The Schlenk flask was then put inside the pre-heated oil bath at 200 °C on a hotplate stirrer for 2 hours. Then the Schlenk flask was removed from the oil bath and allowed to cool to room temperature. For heat treatment of O_2 followed by H_2, a Schlenk flask containing O_2-treated catalysts was connected to a Schlenk line which was connected to H_2 cylinder. A similar procedure as described for previous calcination protocol was applied. Note that the catalysts were labelled in the following manner: loading Au_x/support-treatment (x = 8, 9, 101)

3.3 Sample preparation for far-IR measurement

$Au_9(PPh_3)_8(NO_3)_3$ (referred here as Au_9),[144] $Ru_3(CO)_{12}$ (referred here as Ru_3),[143] $Ru_4H_4(CO)_{12}$ (referred here as Ru_4)[150] and $Ru_3(AuPPh_3)(\mu\text{-}Cl)(CO)_{10}$ (referred here as $AuRu_3$)[151] were chemically synthesised using previously published protocols. The crystal structures were obtained from Cambridge Crystallographic Database; Au_9 (Figure 3.3, CSD refcode MIVPOX), Ru_3 (Figure 3.4, CSD refcode FOKNEY), Ru_4 (Figure 3.5, CSD refcode FOKPAW) and $AuRu_3$ (Figure 3.6, CSD refcode CEYTIJ). Samples were prepared by mixing by varying amounts of metal clusters with polyethylene (PE) if dilutions were required and pressing (using standard KBr press used for making IR samples) to form a pellets of *ca*. 7 mm in diameter. The spectra were recorded at several mass dilutions in PE due to the wide range of absorptivity the clusters exhibited across the measured spectral window. Specifically, the spectra were recorded at following mass dilutions: 1:1 and 1:5 for Ru_3:PE, 1:1 and 1:10 for Ru_4:PE and 2:1 and 1:5 for $AuRu_3$:PE. For the Au_9 cluster, the sample was prepared by pressing 50 mg of pure cluster to form the pellet.

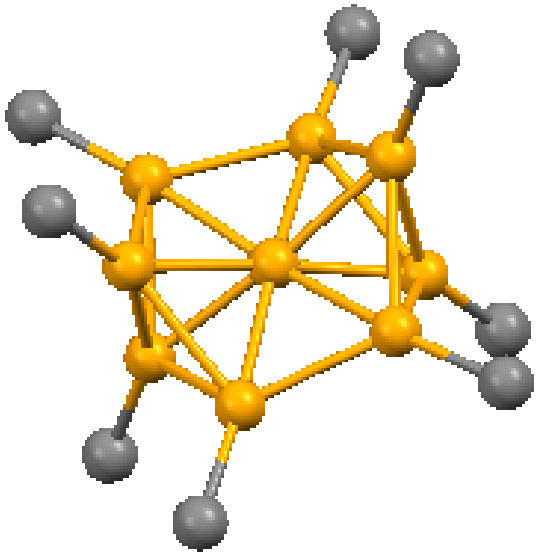

Figure 3.3 The crystal structure of $Au_9(PPh_3)_8^{3+}$ cation. Gold atoms are shown in orange and phosphorous atoms are shown grey. Phenyl groups of the PPh_3 ligands are omitted for clarity. Adapted from *European Journal of Inorganic Chemistry, 2008, 106.* Copyright Wiley publishing.

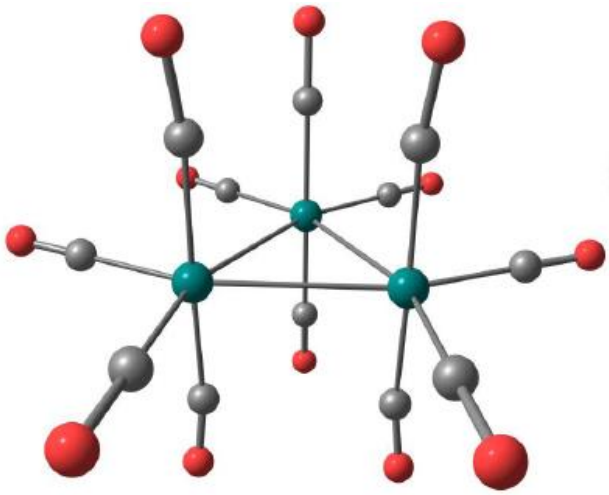

Figure 3.4 The crystal structure of $Ru_3(CO)_{12}$. Oxygen atoms are shown in red, carbon atoms in grey and ruthenium atoms in green. Adapted from *Inorganic Chemistry 53(9): 4340-4349*. Copyright ACS publishing.

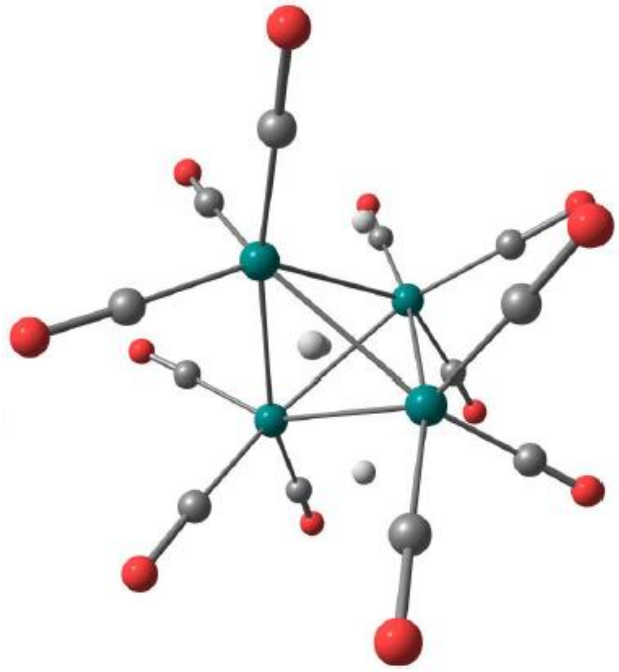

Figure 3.5 The crystal structure of $Ru_4H_4(CO)_{12}$. Oxygen atoms are shown in red, carbon atoms in grey, ruthenium atoms in green and hydrogen atoms in white. Adapted from *Inorganic Chemistry 53(9): 4340-4349*. Copyright ACS publishing.

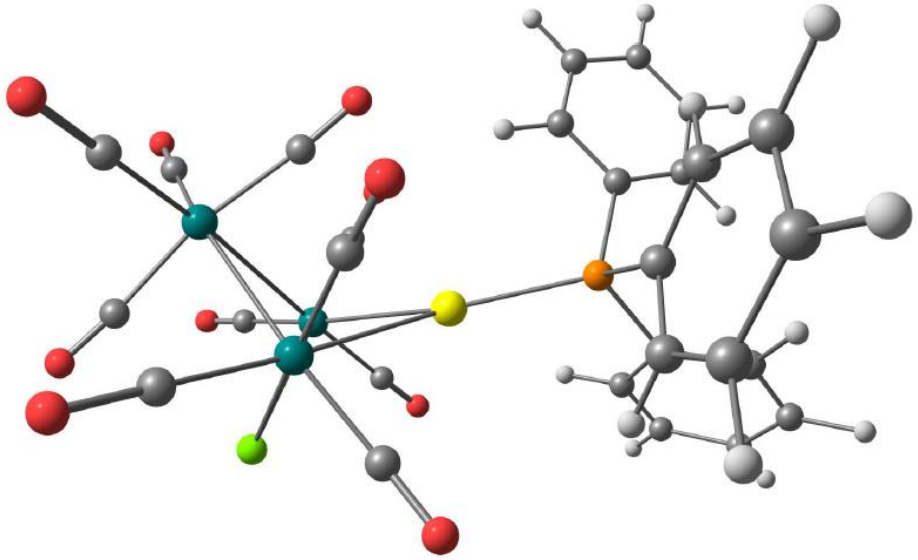

Figure 3.6 The crystal structure of $Ru_3(\mu\text{-}AuPPh_3)(Cl)(CO)_{10}$. Oxygen atom are shown in red, carbon atoms in grey and ruthenium atoms in green, hydrogen atoms in white, chlorine atom in green, gold atom in yellow and phosphorous in orange. Adapted from *Inorganic Chemistry 53(9): 4340-4349*. Copyright ACS publishing.

3.3.1 Recording of the far-IR spectra

High quality far-IR absorption spectra were recorded using IFS125 Bruker FT spectrometer located at the far-IR beamline, at the Australian Synchrotron. The transmission spectrum for each sample was recorded from 50 – 650 cm^{-1}, at 1 cm^{-1} resolution utilizing the synchrotron light source (200 mA in top-up mode), with a 6 μm thick multilayer Mylar beamsplitter in combination with a Si bolometer detector. This bolometer was equipped with an 800 cm^{-1} far-IR cut-on cold-filter consisting of a 13 μm PE film overlaid with a 6 μm diamond scatter layer. All spectra were recorded at room temperature and were baseline corrected.

3.3.2 DFT calculations

These calculations were performed by theoretical chemistry students Jason Alvino and Trystan Bennet at the University of Adelaide (group of Associate Professor Gregory Metha) as a part of this collaborative project. Geometric optimization and harmonic vibrational frequency calculations (including force constant, k) for cluster metal cores and ligands (but not anionic counter ions which were not directly bonded to the cluster core) were undertaken using M06 density functional, with all atoms treated using the LanL2DZ basis set and related Effective Core Potential (ECP) in the Gaussian 09 suite program. Starting geometries were taken from the Cambridge Crystallographic Database.

For Au_9, the counter ions (NO_3^-) were not included in calculations as these are located far away from the cluster core and surrounding, directly bonded PPh_3 ligands, within crystalline lattice; however, the overall charge of the cluster core (+3) was maintained. Optimizations were performed with symmetry constraints, *i.e.*, in the *C1* point group. The optimized geometry was followed by a harmonic frequency calculation to confirm that the geometry was a true minimum with no imaginary frequencies. Inspection of the imaginary modes revealed that they correspond to slight rotations of phenyl groups and cannot be eliminated despite the numerous attempts at re-optimization using finer grid sizes and alternative minimization algorithms. In light of the small magnitude and local nature of these vibrations, we concluded that they do not adversely affect our assessment of the core cluster vibrations, which are of primary interest for this study. Each computed stick spectrum was then convoluted with a Gaussian line shape function with 8 cm^{-1} full width at half maximum using the GaussView 5 program.

For Ru_3, Ru_4, $AuRu_3$, all calculations were performed as closed-shell species. The optimizations were performed in the D_{3h} and D_3, S_4, and C_1 point groups for Ru_3, Ru_4 and $AuRu_3$, respectively. The calculations were carried out using an unpruned (199 974) grid for numerical integral evaluation, and

tighter optimization cut-off threshold (Gaussian keyword opt=very tight), with all other cut-offs being left at the default. For D_{3h} Ru_3 structure, it was optimized to a stationary point with one low-magnitude imaginary frequency (*vide infra*). Population analysis calculations were undertaken on the three clusters using the Gaussian 09 suite programs. These were undertaken at the same level of theory as the optimization and frequency calculations: M06/LanL2DZ, with an unpruned (199 974) numerical integration grid. The calculations were performed using the Gaussian keywords relevant to each population analysis method: "Pop-NBO" for natural bond order calculation, "Pop=Hirshfeld" for Hirshfeld calculations,, "Pop=HLYGat" for the Hu-Lu-Yang model utilizing Gaussian's standard atomic densities, and "iop(6/80=1)" for the Löwdin population method, while Mulliken was taken as default.

3.4 Characterization of the supported Au clusters

3.4.1 Synchrotron XPS beamline and sample preparation

A suspension of TiO_2-supported gold clusters in dichloromethane was prepared with concentration of *ca*. 1 mg/mL. A 10 µL drop of each sample was deposited onto a clean Si wafer (6 x 6 mm) and dried in air. Each sample was then fixed by double-sided copper tape onto gold-plated sample holder plate with up to 6 samples affixed onto each plate for XPS analysis.

XPS spectra were recorded at Soft X-ray Beamline (SXR) at the Australian Synchrotron using a SPECS Phoibos 150 hemispherical electron analyser with photon energy set to 690 eV. The beam was adjusted to an irradiation spot size of ~ 600 x 600 µm, giving an X-ray photon flux of approximately 10^{12} photons $mm^{-2}\cdot s^{-1}$. High resolution XPS spectra of C, O, Si, P, Ti and Au were recorded at a pass energy of 10 eV, producing instrumental resolution of 295 meV. Scans were repeated several times to ensure that no photon-induced changes occurred in the sample. Stability of the energy of the X-ray was monitored using a bulk gold reference and binding energy for each element was corrected against minor charging if required using adventitious C XPS peak (285 eV) as an internal reference.

3.4.2 X-ray absorption spectroscopy (XAS)

Au L_{III}-edge X-ray absorption spectra were recorded at Australian National Beamline Facility (ANBF, beamline 20B) at the Photon Factory, Tsukuba, Japan. Harmonic rejection was achieved by detuning a channel-cut Si[111] monochromator by 50%. Unsupported clusters were recorded in transmission mode as pressed pellet with a 1:5 dilution in cellulose. Supported cluster samples were recorded neat in fluorescence mode with the sample suspended in a 1 x 5 aluminium sample holder secured between Kapton tape, measured using a 36-pixel Ge-monolith fluorescence detector (Canberra/Unisys) at 90 °C to the incident beam. All data were collected at ~ 18 K using a closed-cycle He cryostat. The following energy ranges were used for X-ray absorption near-edge structures (XANES) data collection: pre-edge region from 11700 to 11900 eV (10 eV steps), XANES region from 11900 to 11960 eV (0.5 eV steps), and post-edge region from 11960 to 13145 eV (0.05 $Å^{-1}$ steps in k-space). An Au foil standard was used to calibrate the energy scale to the first peak of the first peak of the first derivative of the Au L_{III} edge (assumed to be 11920 eV).

3.4.3 Transmission electron microscope (TEM)

TEM images were recorded using a Philips CM-200 high resolution transmission electron microscope (HRTEM) operating at 200 kV. A holey carbon film coated Cu 300 Mesh grid was used as the TEM grid. Typically, the TEM samples were prepared by suspending *ca*. ~ 1 mg of supported gold clusters in methanol (1.5 mL) in a small vial (capacity 3 mL). The suspension was sonicated for 2 minutes to give a homogeneous mixture. A drop of the mixture was deposited onto the TEM grid using a syringe. The sample was dried in air for 30 minutes. Complete drying was achieved by placing the TEM grid coated with the sample in a clean vial which was then put in a desiccator connected to vacuum pump for 2 hours. Sample preparation was done immediately prior to TEM studies to get a fresh sample. The images were analysed using Image J software. The particle size was determined by drawing a straight line from one edge to the opposite edge of each particle. Statistical evaluation was performed (including particle size distribution histograms) by measuring the size of at least 250 particles in different areas of the grid. From the author's experience, the number of bin per histogram is chosen to be 10-12 to give a normal distribution. The size of the bin then depends on the range of particle size and the number of bin.

3.4.4 UV-visible diffuse reflectance spectroscopy (UV-vis DRS)

UV-vis DR spectra were recorded using a Cintra 404 (GBC Scientific Equipment) spectrophotometer. The wavelength range used in scanning was from 350 nm to 750 nm. The slit width was 2.0 nm with step size of 0.32 nm. The background was calibrated using a Teflon pellet. A small amount (~ 30 mg) of supported gold clusters was deposited onto the sample holder and pressured with spatula to make a thin film. The sample holder was then affixed inside the spectrophotometer to record the spectra.

3.5 Catalytic testing

The catalytic oxidation of benzyl alcohol was performed in stainless steel autoclaves (total internal volume of 57 mL) equipped with Teflon liners and magnetic stirrers, with temperature control of the reaction achieved by using hotplate stirrer controlled by a thermocouple immersed into the reaction mixture. Typically, a mixture of 0.270 g, 2.50 mmol benzyl alcohol and 0.135 g, 1.25 mmol anisole (internal standard) in methanol (25 mL) were charged into a Teflon liner. Then, 0.345 g, 2.50 mmol K_2CO_3 and 50 mg of catalyst were added, giving benzyl alcohol to Au molar ratio of 5800. A purge-vent cycle was completed 3 times with pure oxygen to ensure high purity of the atmosphere before the autoclave was pressurised with 5 bar of oxygen and heated to a specific temperature for desired particular reaction time. At the end of a catalytic test, the reaction was stopped by cooling the autoclave to 3 °C in an ice-bath. The reaction mixture was centrifuged at 5000 rpm for 15 minutes to separate product mixture and the catalyst. The catalyst was washed with methanol (3 x 15 mL) and dried *in vacuo* prior to recycling. Each catalytic test was repeated at least in triplicate giving lower than 3 % differences in conversion and selectivity.

Product mixtures were analysed using high performance liquid chromatography (HPLC) Dionex Ultimate 300 system equipped with UV detector and fitted with a Luna 5µ C18(2) (250 x 4.60 mm) reversed phase column. The eluents were mixtures of 0.05 v/v% trifluoroacetic acid in water (70 %) and acetonitrile (30%). Gold content was measured using atomic absorption spectroscopy (AAS) Varian SpectraAA 220 FS with ASL hollow cathode lamp for the Au element.

3.6 Hydrogen sensing test

3.6.1 WO_3 film deposition

Conductometric transducers of 8 × 12 mm size were used in this experiment. A 50 nm thick layer of chromium (Cr) was deposited in order to provide sufficient adhesion between the quartz substrate and Au film of the electrodes, followed by deposition of 100 nm thick Au film using an industrial scale electron beam evaporator Balzer™. Photolithography and etching were employed to fabricate Au interdigitated electrode (IDT). After dicing, the thin films were cleaned with acetone, methanol, de-ionized and blow-dried with N_2 flow to remove the impurities and organic contaminants prior to radio-frequency (RF) sputtering of the WO_3 film. The parameters used for the RF sputtered WO_3 film of ~500 nm thickness (as measured using surface profilometer and later confirmed by FESEM)[155] are given in Table 3.1 below.

Table 3.1 Deposition parameters for the WO_3 film by RF sputtering.

Tungsten target purity	Sample to target distance (mm)	Base pressure (Torr)	Pressure during deposition (Torr)	Gas (v/v%)	Substrate temperature (°C)	RF power (W)	Film thickness (nm)
99.95%	70	10^{-5}	2×10^{-2}	Ar(10) O_2(90)	300	80	500

3.6.2 Au_9 cluster deposition onto thin films

Two different concentrations of Au_9 cluster solution in methanol, 0.01 and 0.1 mg/mL were prepared in 25 mL vials. The transducer thin films prepared above were dip-coated in the Au_9 cluster solutions for 30 minutes and then quickly blow-dried using moderate nitrogen gas flow to remove the solvent. The transducer thin films were labelled as S1 for a lower concentration (0.01 mg/mL) and S2 for a higher concentration (0.1 mg/mL) of Au_9 solution. The thin films were then annealed in static air at 200 °C for 2 hours with a temperature ramp up/down of 2 °C/min in order to remove the organic ligands, which may block the access of H_2 to the Au cores.[156] The annealed samples were then attached to Au contact ribbons using silver paste and resin (1:1 ratio). A subsequent heat treatment at 100 °C (by using a hot plate) for 15-20 minutes was performed to solidify the paste.

3.6.3 Experimental set up for H_2 sensing tests

The experimental set up for H_2 sensing test is shown in Figure 3.7. The sensors were mounted within a gas chamber connected to mass flow controllers. A constant gas flow of 200 sccm within the enclosed chamber was maintained throughout the test. In order to investigate the optimal operating temperature, the sensors were exposed to the H_2 at 0.06 v/v% in synthetic air during a series of on/off cycles with cycle step (either on or off) duration of 180 s. The initial H_2 exposure cycling tests were carried out at room temperature and once completed the temperature was increased stepwise with an interval of 50 °C: it was first increased to 50, then to 100 and so on up to 450 °C. An external heater was connected to a thermocouple for *in situ* measurements in order to control the temperature. After the optimal temperatures were identified, the sensors were exposed to different H_2 concentrations ranging from 0.06 to 1.0 v/v% (in synthetic air). A computerized gas calibration system was used to adjust the H_2 concentration to 0.06, 0.13, 0.25, 0.50, 0.75 and 1.0 v/v % (in synthetic air). A computer with data logger software was used to log the data in real time. The sensor response was calculated using the equation $S=R_a/R_g$, where R_a is the resistance of the sensor in pure air and R_g is the resistance of the sensor in H_2-air mixture, respectively.

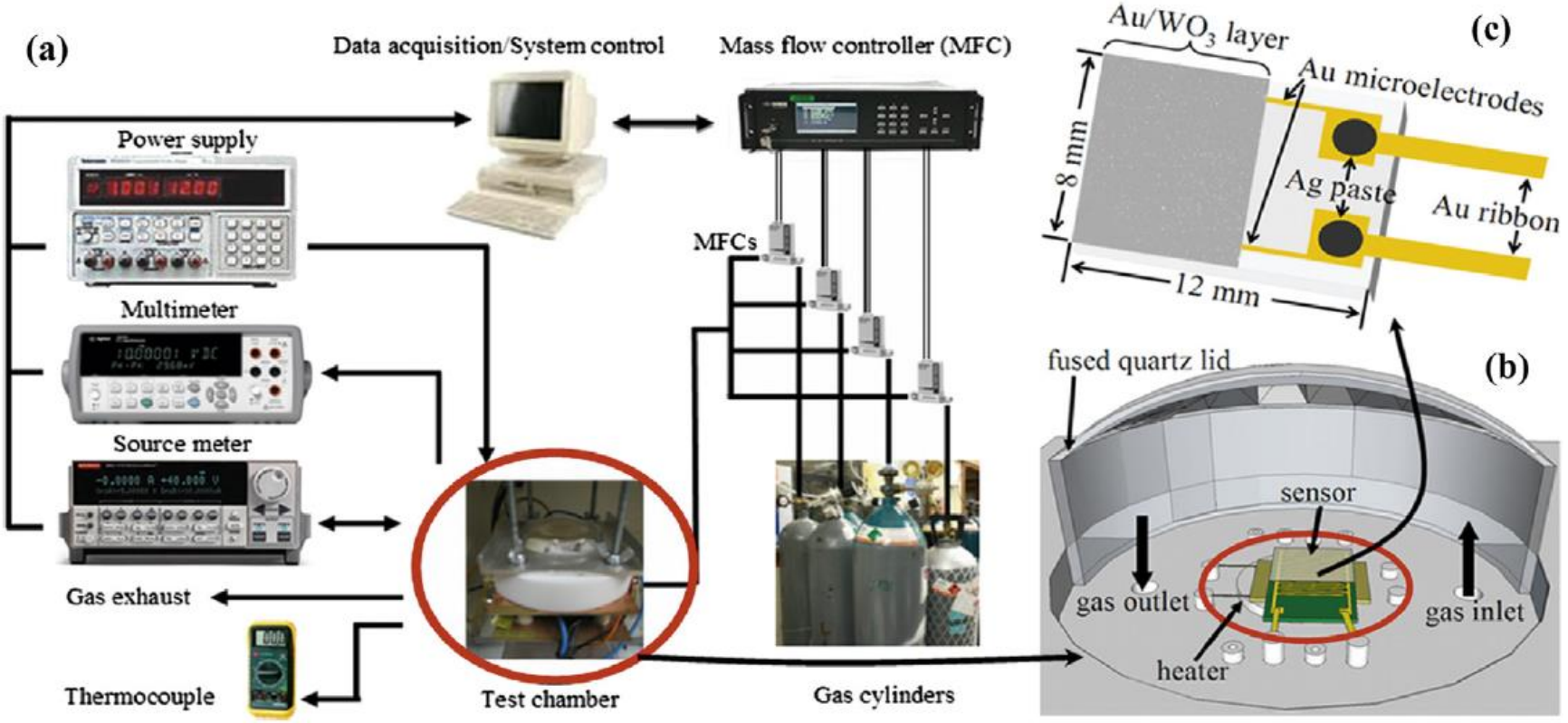

Figure 3.7 The illustration of a) H_2 sensing system, b) the sketch of test chamber, and c) Au/WO_3 based sensor. Adapted from the *International Journal of Hydrogen Energy, 2013, **38**, 12865*. Copyright Elsevier publishing.

3.6.4 Characterizations of the thin films

TEM images were obtained using the high resolution TEM Philips CM-200 operating at 200 kV and a holey carbon film coated Cu 300 mesh grid as the TEM specimen support/holder. The statistical evaluation and histogram were performed and constructed (respectively) using at least 400 particles per sample. TEM samples of Au/WO_3 were prepared by scrapping small portion of the thin film using a clean scalpel into a small vial. Ethanol was added and the mixture was shaken using vortex agitator. The solutions then were drop cast onto TEM grids and left undisturbed to evaporate the solvent for about an hour. Complete dryness was achieved by drying *in vacuo* for one hour prior to TEM session.

X-ray diffraction analysis was carried out using a Bruker D8 Discover micro-diffractometer fitted with a General Area Detector Diffraction System with a potential of 40 kV and a current of 40 mA and filtered with a graphite monochromator in the parallel mode (175 mm collimator with 0.5 mm pinholes). Data was collected at room temperature using Cu Kα radiation (λ = 1.54178 Å).

X-ray photoelectron spectroscopy (XPS) was performed in an ultra-high vacuum (UHV) apparatus with a base pressure of 10^{-10} mbar range built by SPECS (Berlin, Germany). The apparatus is equipped with a non-monochromatic X-ray source for Mg and Al Kα radiation. The spectra of photoelectrons emitted were collected with a hemispherical Phoibos 100 energy analyser from SPECS. High resolution spectra were collected using pass energy of 10 eV. The angle between the X-ray radiation and the analyser is 54°. The XP spectra were fitted in the same manner as explained in Experimental Details in Chapter 4.

3.7 Characterization techniques

3.7.1 UV-visible spectroscopy

The UV-visible spectroscopy is a very powerful tool to probe the optical property of both metal nanoparticles and clusters that are closely related to their electronic structure. In fact, it is well known that many metal clusters are coloured due to the existence of localized and discrete orbitals.[141, 152, 157] For example, Simon and co-workers measured the optical absorption of the $Au_{11}(PPh_3)_7Cl_3$ (abbreviated as Au_{11}) cluster as a dilute solution in toluene and observed distinct features in the absorbance spectrum which display the molecular-like property of Au_{11} cluster (Figure 3.8).[145] When this spectrum is plotted in terms of absorbance *vs.* energy by using the Planck's equation E(eV) = 1240/λ(nm), the tangent to the curve that intercepts with x-axis (energy) represent the band gap (HUMO-LUMO transition); it is called

Tauc plot (Figure 3.9).[145] Using this method, Simon and co-workers estimated the band gap of the first electronic transition to be *ca.* 2.0 eV (corresponding to 620 nm in effective wavenumbers), which matched closely with the theoretical calculation of the Au_{11} simplified structure.[158]

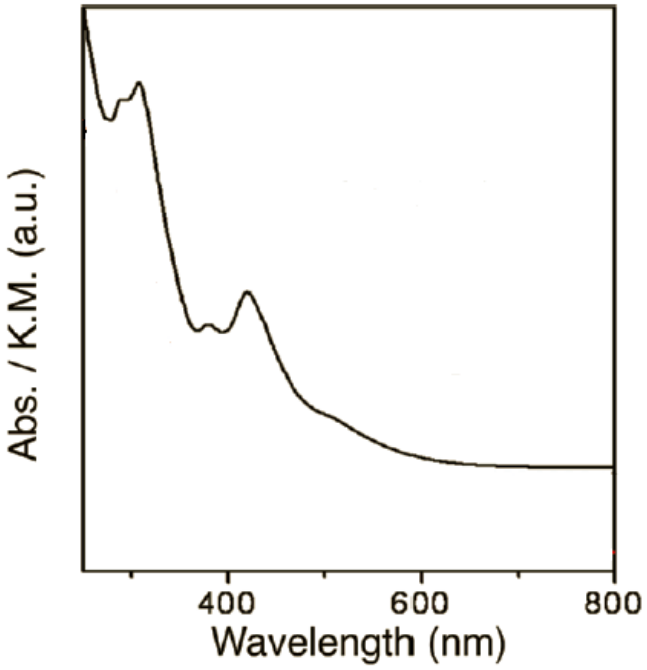

Figure 3.8 UV-visible spectrum of Au_{11} cluster in CH_2Cl_2 solution. Adapted from *The Journal of Physical Chemistry C 113(31): 13457*. Copyright ACS publishing.

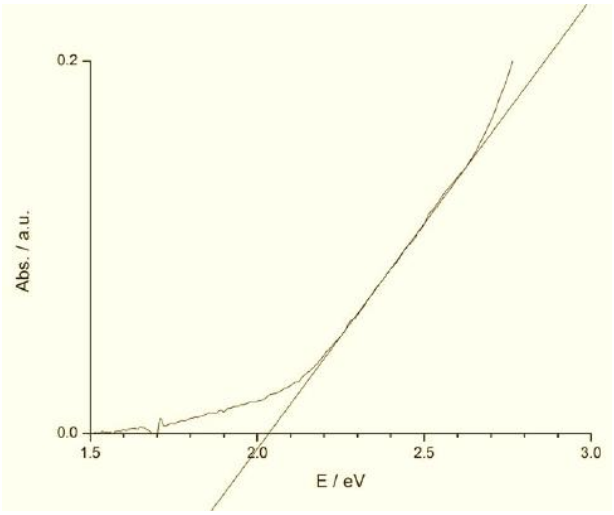

Figure 3.9 Absorbance spectrum of Au_{11} cluster in toluene with the estimation of the first electronic transition to be around *ca.* 2.0 eV. Adapted from the *European Journal of Inorganic Chemistry 2013(12): 2002-2006*. Copyright Wiley-VCH publishing.

The coinage metal colloidal nanoparticles (Cu, Ag, Au) exhibit unique optical properties due to the presence of LSPR band at 600, 420 and 520 nm for Cu, Ag and Au, respectively.[159] The position and intensity of the LPSR mode depends strongly on particle size and morphology, the composition of nanoparticles (alloy, core-shell), capping ligands, solvents and the dielectric constant on the surrounding medium. [160, 161] Zhao *et al*. synthesized citrate-capped Au nanoparticles with a varying average size from 19 to 47 nm and observed the red-shift (towards longer wavelength) of the LSPR band as the Au size increased.[162] Mulvaney and co-workers showed that when Pt is deposited on the Au core, the LSPR peak is blue-shifted and damped with the increasing concentration of Pt due to the high imaginary part and more negative dielectric function of Pt (Figure 3.10).[163] In summary, the position of the LSPR band and its shift (either red- or blue shift) can be monitored from the UV-visible spectrum and can provide useful information about the size, shape and composition of Au nanoparticles.

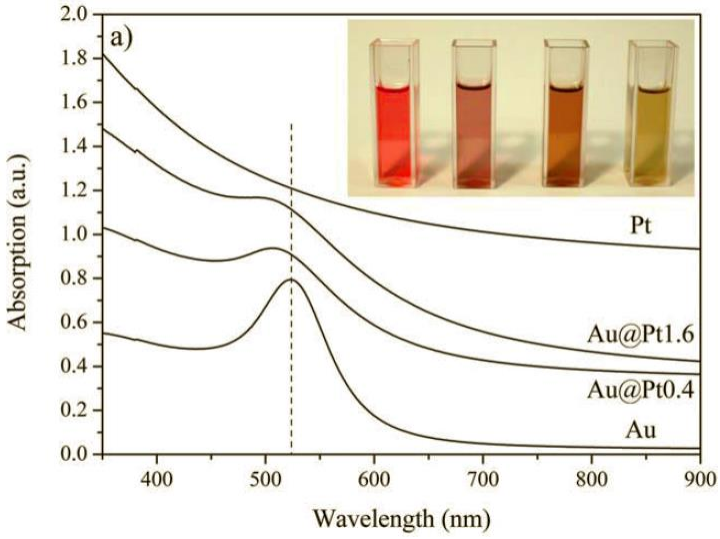

Figure 3.10 Absorbance spectrum of Au, Pt and Au@Pt colloidal nanoparticles in ethanol. The dotted line is the position of wavelength maximum for LSPR peak of Au nanoparticles. The LSPR peak maximum shows blue-shift (toward shorter wavelength) when coated with Pt nanoparticle shells. Adapted from *Nanoscale, 2012, 4, 5972*. Copyright RSC publishing.

For supported Au nanoparticles, the UV-visible spectrum is recorded using the UV-visible diffuse reflectance spectroscopy (UV-vis DRS). The powder is usually pressed into a thin film and affixed to the sample holder. Liu *et al*. measured the optical absorbance of triphenylphosphine-stabilized Au_{11} cluster ($Au_1$1:TPP) in solution (CH_2Cl_2) and in solid state (UV-vis DRS).[106] The characteristic peak of Au_{11} cluster at 415 nm (in solution) is red-shifted and broadened when the cluster is deposited onto the SBA-15 support (see Figure 3.11). They attribute this shift due to the change in the electronic structure of the Au_{11} cluster when it interacts with the support. In addition to the optical absorbance of Au clusters, the disappearance of sharp and distinct peaks and emergence of the LSPR band suggest the size evolution of the cluster (< 2 nm) towards nanoparticles (> 2 nm), as shown in Figure 3.12.[164]

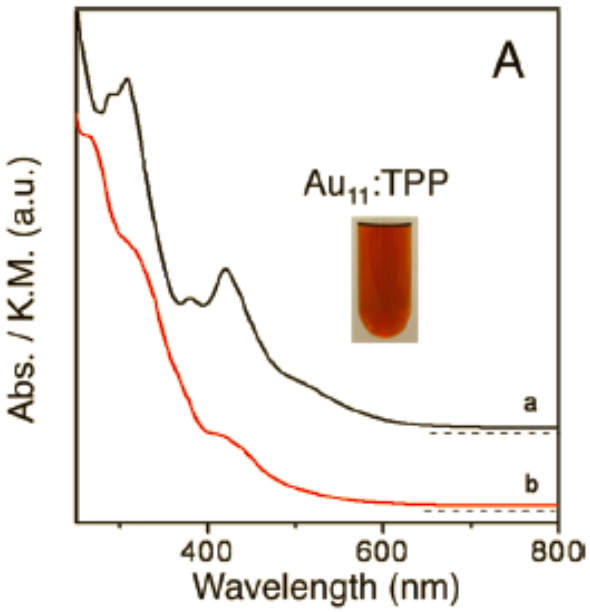

Figure 3.11 UV-visible spectrum of Au_{11}:TPP cluster a) in CH_2Cl_2 solution and b) deposited on the SBA-15 support using diffuse reflectance technique. Adapted from *The Journal of Physical Chemistry C 113(31): 13457*. Copyright ACS publishing.

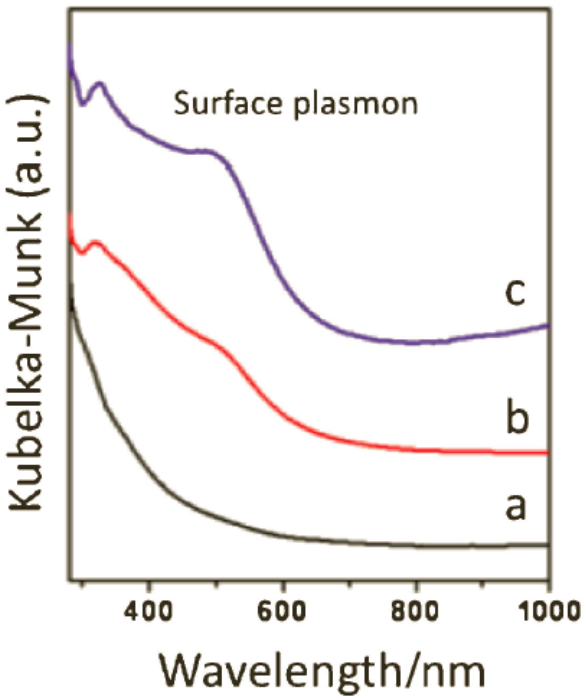

Figure 3.12 UV-vis DRS spectra of different size Au/SiO2 catalysts derived from Au11 clusters, a) 0.8 nm, b) 1.5 nm and c) 1.9 nm. Adapted from *Chemistry Letter, 2010, 39, 159*. Copyright The Chemical Society of Japan publishing.

3.7.2 Transmission electron microscopy (TEM)

The transmission electron microscope (TEM) is the most primarily tools to "see" nanoparticles directly. As opposed to the optical (light) microscope which uses visible light, an electron microscope uses coherent beam of electrons accelerated by voltage applied within the electron gun (100-1300 kV) to reach high energy (120-400 keV) and to have very small wavelength in order to observe the sample allowing the resolution down to atomic scale. For metal nanoparticles, among the information that can be extracted from TEM imaging include particle size, lattice spacing (and crystal phase) and morphology (shape). Unlike other techniques that measure the average value (bulk) of a particular property, the TEM measures the property of an individual particle. A collection of images taken from several different areas under the TEM is crucial for the statistical analysis. The possible ways of how electrons interact with the sample specimen are shown below (Figure 3.13).

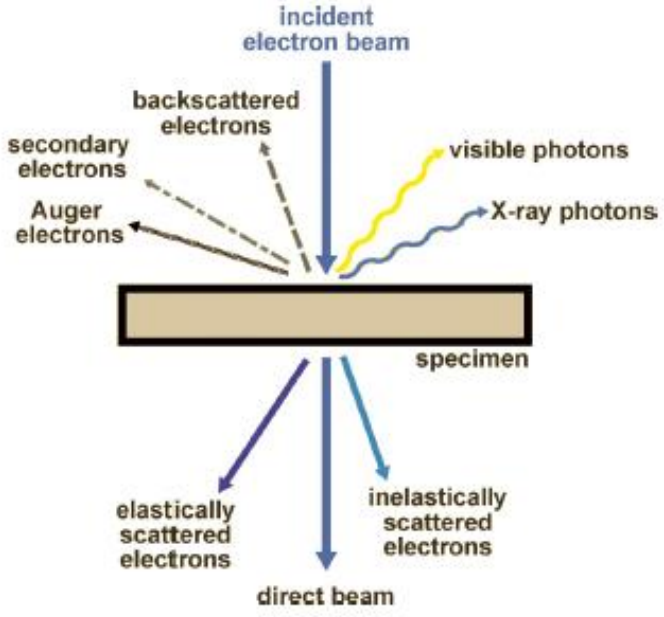

Figure 3.13 The possible outcomes of the signals obtained when the incident electron beams interact with the sample.

The TEM image is produced from direct/transmitted electron beams. There are three most significant scenarios that can happen when an electron beam hit a sample:

a) It is un-scattered (*i.e*. transmitted without interacting with any atom)
b) It is deflected but loses no energy (*i.e*. elastically scattered)
c) It loses an energy and is probably scattered (*i.e*. inelastically scattered, X-ray may be emitted)

If all these scenarios are allowed to happen inside a TEM, they all will contribute to the image formation and all regions of specimen look the same. Hence, no contrast between areas of different thickness or composition will be developed. A specialized device is affixed in TEM to separate the scenario a) from b) and c); an objective lens aperture (Figure 3.14e).

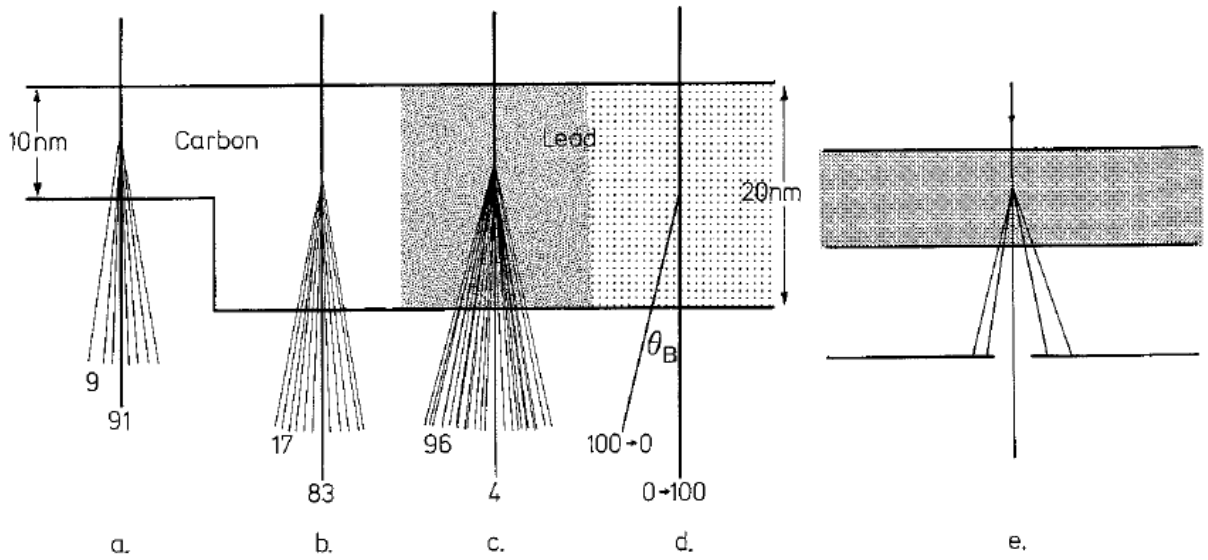

Figure 3.14 The trajectories of 100 electrons passing through four different regions a) 10 nm amorphous carbon, b) 20 nm amorphous carbon, c) 20 nm of amorphous lead and d) 20 nm of crystalline lead. The effect of inserting an objective aperture (e) to stops all scattered electrons at a certain angle.

Figure 3.14 shows the fate of 100 electrons passing through four different regions (it is a hypothesis case to illustrate the contrast development although it is rather unusual, but it helps explaining the basic concept). If all the 100 electrons pass through the sample without interacting (transmitted), then the images formed will show no difference between regions a) until d). Region a) consist of 10 nm of amorphous carbon, which is a light atom (a light atom, Z = 6). It scatters electron weakly and only 9 out of 100 electrons are scattered (91 electrons transmitted) at a certain angle (say 0.5° or more). Region b) consists of twice the thick of amorphous carbon (20 nm) in region a) and scatters more electrons (17 electrons). Region c) has the same thickness as the amorphous carbon (10 nm) but consist of amorphous lead (a heavy atom, Z = 82) instead of amorphous carbon. Here, majority of the electrons (96 electrons) are scattered because of the heavier atomic weight of lead (*cf.* carbon) but only at a small angle. Region d) consists of crystalline lead instead of amorphous lead, of the same thickness. In this case, the electrons will diffract and interfere with the scattered electrons to form a diffraction pattern. To make the images of different regions (a-d) distinguishable, all the scattered electrons at a certain angle (here we use 0.5° as mentioned earlier) must be excluded from contributing to the image formation. An objective lens

aperture, see region e), is inserted below the specimen to exclude the scattered electron, and thus allowing different brightness for each region. The more the scattered electrons are blocked, the darker the image formed. In this example, 10 nm amorphous carbon looks quite bright and 20 nm amorphous lead looks darker. Therefore, for imaging an ultra-small particle (< 1.5 nm), the difficulty arises from the diminishing contrast between the sample and the background.[165] This situation restricts the formation of a sharp image for an accurate analysis.

In the bright field (BF) mode, the aperture is placed in the back focal plane of the objective lens such that it allows only direct electron beams to pass (Figure 3.15a). In this mode, the image is formed from the reduced direct beams when interact with the sample. The contrasts that contribute to the image are mass-thickness and diffraction contrast where heavy atoms and larger particles appear dark. Alternatively, if the direct beam is blocked, allowing one or more diffracted beams to pass, it is termed as the dark field (DF) mode (Figure 3.15b). Because diffracted beams interact strongly with the sample, the DF mode is very useful to study about crystal defects, stacking faults and crystal orientations.

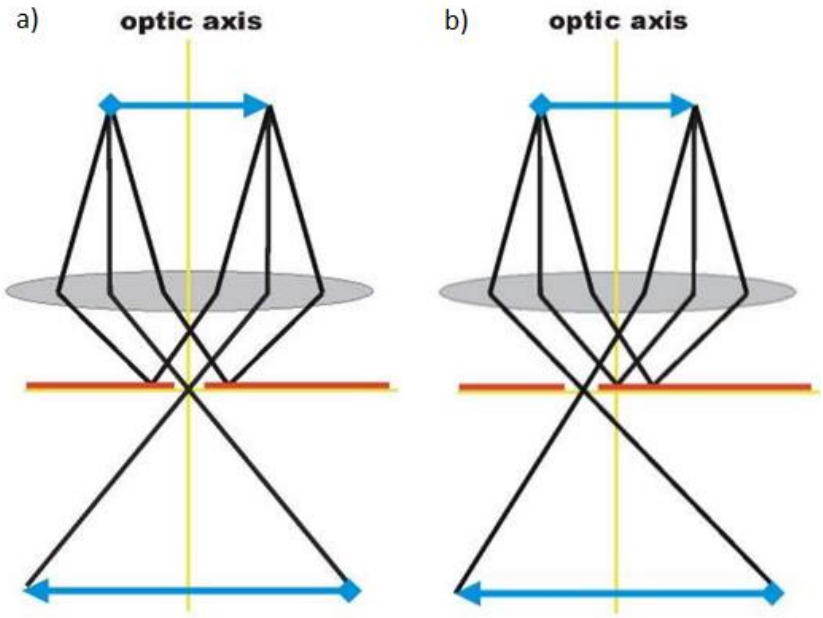

Figure 3.15 The imaging mode in a TEM: a) bright field (BF) mode and b) dark field (DF) mode.

A typical 200 kV TEM has a resolution uncertainty around 0.2 nm.[159] Resolution is defined as the shortest distance between two separate objects under a microscope that can be distinguished as distinct entities. Nevertheless, the resolution limit of the TEM is not limited by the electron wavelength since the electron wavelength is 0.0025 nm at 200 kV, but is limited by the spherical aberrations of the lenses, the stability of the microscope at a high voltage (chromatic aberration) and mechanical vibrations.[166]

Therefore, the smallest size of a particle that can be observed in a conventional 200 kV TEM is around 1.5 nm.[167] Imaging the accurate size and morphology of nanoparticles requires higher magnification and enhanced contrast. However, at higher magnification, only few particles are available on the screen for the evaluation. An enhanced contrast can be obtained with a higher accelerating voltage, but it may cause damage to the nanoparticles.

Even with perfectly monochromatic (singled-wavelength) electrons, standard lenses in TEM are far away from perfect because the electrons far from the optical axis must travel further. The electron beams at high angle are brought closer to the lens as compared to the beams a smaller angle.[168] This incorrectly focused beam at a high angle results a smearing in the image of a point formed at the focus plane. The smallest image of a point occurs just in front of the image plane and is called the spherical aberration disc of least confusion, depicted as a disk of least confusion in Figure 13 (bottom graphics). An aberration correction is performed to bring all electron beams into a single focus point, like those using a perfect lens (top graphics in Figure 3.16). A remarkable work highlighted by Scherzer in 1947 suggested the use of nonround lenses to get rid of the spherical aberration.[169] The multipole lenses are capable to produce a negative value of spherical aberration and thus cancelling the positive value of the spherical aberration to focus electron beams at a single focus point. The two basic designs of aberration corrector are based on the octupole/quadrupole assembly[170] and the hexapole assembly.[171]

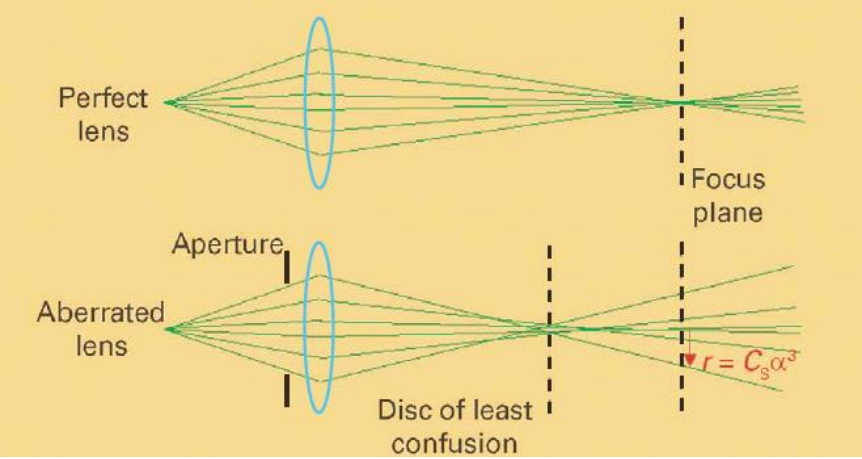

Figure 3.16 The electron beam passing through a a) perfect lens and b) spherical aberrated lens. Adapted from *Materials Today* ***7****(12): 42*. Copyright Elsevier.

The TEM image taken from an aberration corrector TEM shows a significant improvement in the image resolution (Figure 3.17). The black ring in at a radius 0.19 nm and smaller radius indicates undesirable contrast reversal due to the direct consequence of a spherical aberration. However, in an aberration corrected TEM, the dark rings disappear as a result of aberration correction and the contrast is continuous beyond 0.19 nm, allowing imaging a sharp image beyond the resolution limit with an enhanced contrast.

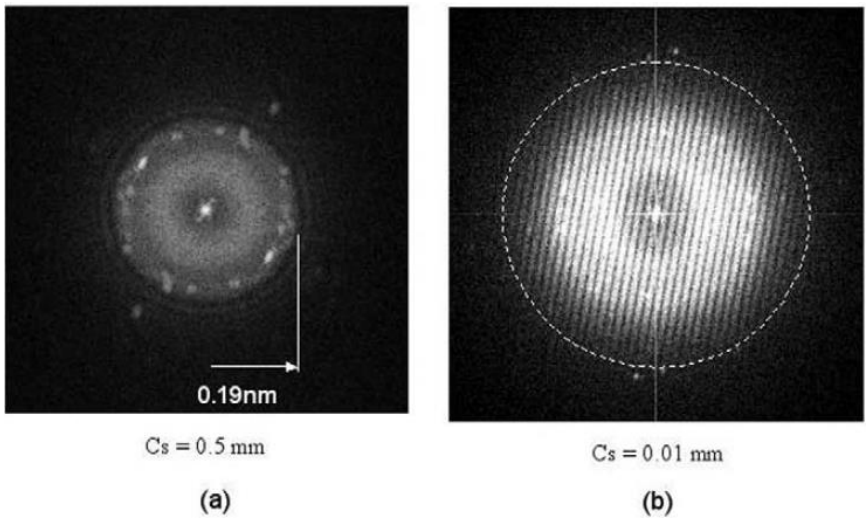

Figure 3.17 The TEM images from a) uncorrected TEM and b) spherical aberration corrected TEM. Adapted from *Materials Today 7(12): 50-55*. Copyright Elsevier.

The aberration correction design is typically found in the high angle annular dark field (HAADF) mode typically in a scanning TEM (STEM).[172] The HAADF mode operates at a pre-selected angular range and collects the incoherently scattered electrons at a high angle while exclude the direct electron beam.[173] The result is that the contrast strongly depends on the Z number of an element (the so-called Z-contrast) and thickness of the sample.[174] In this way, imaging supported-Au nanoparticles on metal oxide is advantageous because the contrast is improved by the high Z number of Au and low Z number of the metal oxide. For example, Li *et al.* probed the atomic composition and three dimensional (3D) structure of Au_{309} using an HAADF-STEM.[175] Despite the powerful ability to image down to atomic resolution, the TEM itself could not provide information about the ligands bonding (adsorbed *vs*. dislodged) and average (bulk) measurement. Complementary techniques such as X-ray absorption spectroscopy (XAS), X-ray photoelectron spectroscopy (XPS) and UV-visible spectroscopy are crucially required to reveal detailed local and averaged over bulk of the sample information about the nature of supported catalysts.[176]

3.7.3 X-ray photoelectron spectroscopy (XPS)

X-rays are known to be an ionizing radiation, which are able to eject electrons from an atom. Each element has a characteristic binding energy of the core electrons corresponding to the specific eigen-states (energy levels). When X-ray beams hits a sample, the core electrons are ejected (referred to as photoelectrons) if the X-ray beam has an energy higher than the binding energy of elements in the sample. Photoelectrons from deep below of the surface (few microns deep) undergo inelastic scattering with atoms in the sample and consequently are unable to escape from the surface of the sample to reach the detector. These photoelectrons have a mean free path that decays exponentially with the distance travelled; the the mean free path of photoelectron is defined as the average distance that a photoelectron with a given energy travels between successive inelastic collisions).[177, 178]Because of inelastic scattering of photoelectrons from deep inside the sample, only photoelectrons near the surface (1-10 nm) can escape from the surface and reach the detector giving rise to the surface-sensitivity of XPS technique. The X-ray photoelectron spectroscopy (XPS), also formerly known as Electron Spectroscopy for Chemical Analysis (ESCA), is a surface-sensitive technique that is primarily utilized to determine the electronic structure of metal nanoparticles/clusters.[179] The XPS uses Al (1486.6 eV), Mg (1253.6 eV) K_α line or synchrotron light source to produce soft energy X-ray radiations in the range of 100 – 2,000 eV. The XPS measurement is typically performed under ultra-high vacuum (UHV) to minimize the interaction between the emitted photoelectrons and gases or impurities. The XPS set-up is shown in Figure 3.18 below.

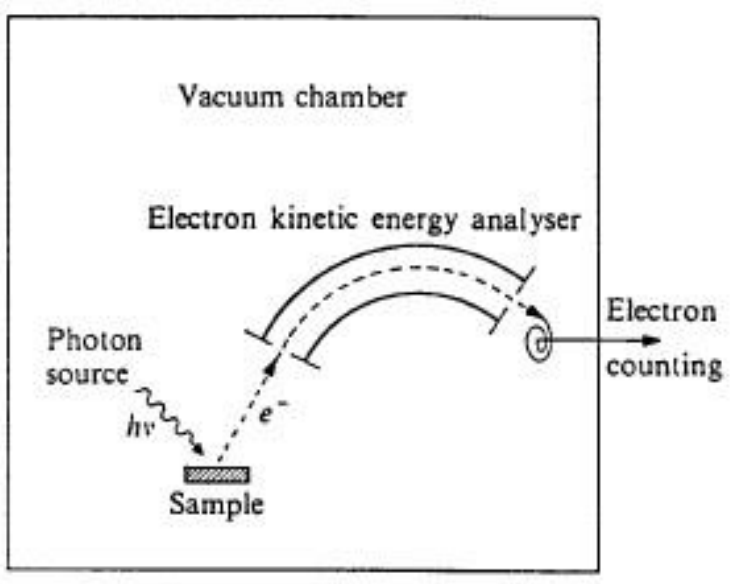

Figure 3.18 The XPS instrumental set-up.

By measuring the kinetic energy of the emitted photoelectron, the binding energy can be calculated from the equation. 3.1. Because the kinetic energy of the emitted electrons depends on the oxidation state of the metal, the chemical environment, and the type of element, several valuable bits of information can be obtained from the XPS spectrum including the chemical composition, the surface chemistry, oxidation states and the relative size of the metal nanoparticles/clusters.[159] Qualitative fingerprint of specific element is provided by the peak position of the binding energy and full-width half maximum (FWHM) of the peak position. The peak position and FWHM, however, are strongly influenced by the oxidation state of the element, initial and final state effect, particle size effect and interaction of the particle with the substrate.[154] Quantitative analysis is performed by measuring the ratio of the peak intensities to give the estimate elemental percentage. However, the quantitative analysis is limited by the mean free path of the photoelectron where the intensity is reduced for particles larger than the mean free path of the photoelectron. [153] The emission process of photoelectron when radiated with X-ray beams is shown in Figure 3.19.

$$KE = h\nu - BE - \phi \qquad 3.1$$

where KE is the kinetic energy of emitted photoelectrons, $h\nu$ is the X-ray energy, BE is the binding energy of the elements, and ϕ is the spectrometer work function.

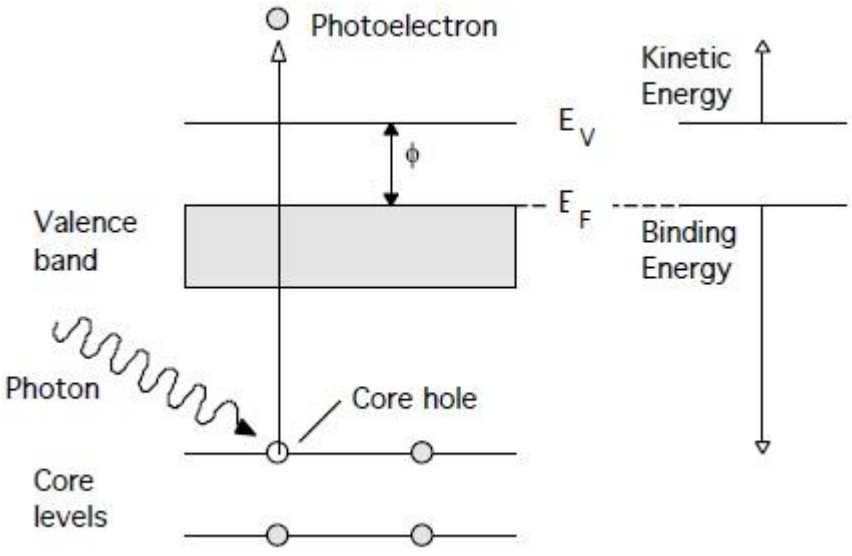

Figure 3.19 The emission of photoelectron when radiated with incident X-ray beams.

The standard value for Au $4f_{7/2}$ peak reported in the literature is 84.0 eV with a separation from the $4f_{5/2}$ peak by 3.67 eV.[180] The splitting of the Au 4f signal into doublet ($4f_{7/2}$ and $4f_{5/2}$) is fixed due the quantum mechanical nature of spit-orbit coupling of the Au 4f orbitals.[154] For convenience and simplicity, only the position and FWHM of the Au $4f_{7/2}$ peak is described when discussing about Au XP spectra. Shumaker-Parry *et al*. demonstrated the use of XPS to determine the oxidation state and the chemical composition of the phosphine-stabilized Au cluster having an average size of 1.7 nm.[109] The authors assigned the Au nanoparticle surface as a zero oxidation state as evident by the presence Au $4f_{7/2}$ peak at 84.1 eV (Au^0), with the absence of peaks at 84.9 eV (Au^+) and 87.3 eV (Au^{3+}). Using the ratio of intensity calculations, the estimate the chemical composition of the gold cluster to be $Au_{146}(PPh_3)_{15}Cl_7$.

While conventional TEM is a powerful technique to image the particle size, instrument limitations retard the imaging process in determining a particle size below ~ 1.5 nm. Importantly, several authors already reported XPS studies on size-selected gold clusters below 2 nm.[181-184] Based on these findings, it is found that the binding energy for Au $4f_{7/2}$ and $4f_{5/2}$ peaks and their full width half maximum (FWHM) increase with decreasing Au particle size.[159] For this reason, Anderson *et al.* investigated the electronic property and the relative size of chemically synthesized, atomically-precise phosphine-stabilized Au clusters (Au_8, Au_9, Au_{11} and Au_{101}) supported on commercial TiO_2 (P25 Degussa).[154] The authors found a general agreement of the shift of peak position towards higher binding energy and broadening of FHWM of the Au $4f_{7/2}$ due to the finite size effect and element constituting the Au clusters (Figure 3.20). Based on these findings, the authors interpreted the shift in Au $4f_{7/2}$ and the broadening of the FWHM as a function of gold cluster size, rather than the oxidation state of Au. The smaller Au clusters have few residual electrons that can screen the excited hole (after electrons are ejected from the core level) causing a delay in relaxation to the ground state.[185, 186] Hence, the larger effective positive charge (of the hole) slows down the photoelectron motion by Coulumbic attraction force, causing the shift in the peak position towards a higher binding energy (refer to the equation 3.1 above). The authors concluded that there is no significant agglomeration of Au clusters deposited of strongly interacting TiO_2 support.

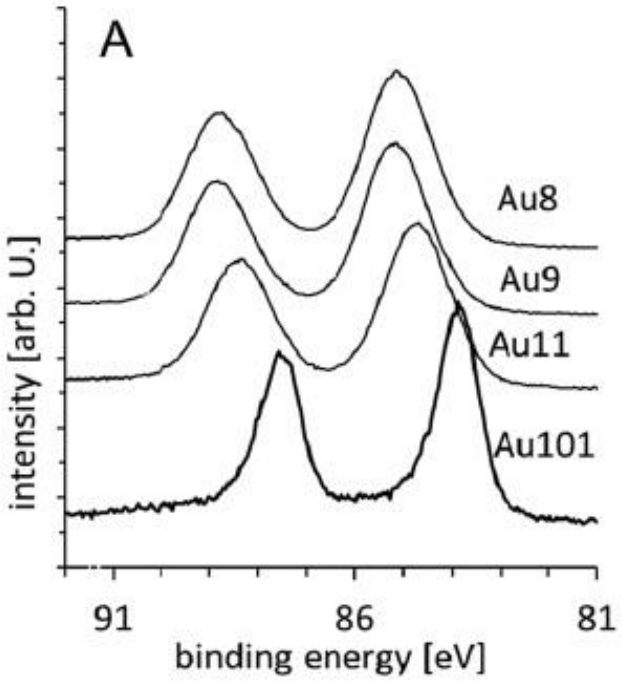

Figure 3.20 Au $4f_{7/2}$ and $4f_{5/2}$ spectra of untreated phosphine-stabilized Au cluster (Au_8, Au_9, Au_{11}, Au_{101}) supported on P25 TiO_2.

3.7.4 X-ray absorption spectroscopy (XAS)

The X-ray absorption spectroscopy (XAS) is a technique to measure the electronic structure and local geometry of materials. The XAS is divided into two main spectral regions depending on their energy; X-ray absorption near edge structure (XANES) or sometimes called Near edge X-ray absorption fine structure (NEXAFS) at a low energy absorption and Extended X-ray absorption fine structure (EXAFS) absorption at a higher energy, as seen in Figure 3.21 below. The XANES region is very sensitive to the oxidation state and symmetry of a molecule and results from multiple scattering contributions of the photoelectrons due to the low excitation energy. In contrast, the EXAFS region is very sensitive to the coordination number and bond length of a molecule and results from a single scattering contribution due to the high excitation energy. Unlike the XPS which is usually set to single excitation energy in order to measure the kinetic energy of photoelectrons, the XAS spectrum is obtained by scanning through a set of an energy range to measure the absorption of X-rays with specific energy. At a certain energy where there is a sharp increase in absorption, an absorption edge occurs corresponding to the binding energy of a particular shell (usually K, L_I, L_{II}, L_{III} or M). Unlike X-ray photoelectron spectroscopy (XPS), the XAS technique uses high energy X-ray radiations (so-called hard X-rays) in the energy range of 5-31 keV, and is thus generally performed at a synchrotron beamline facility.

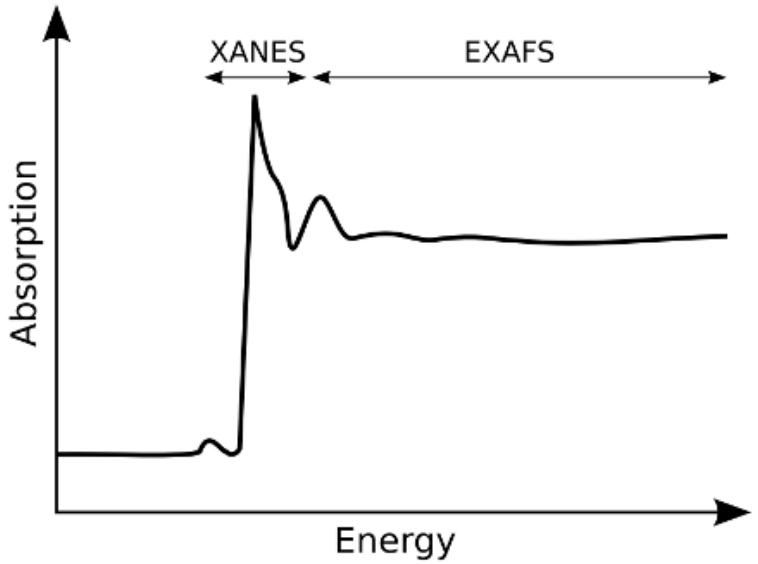

Figure 3.21 A typical XAS spectrum consisting of XANES and EXAFS spectral regions.

When X-rays interact with the core electron in an atom, the electron is ejected leaving an excited core-hole state. The excited state can then relax to the ground state by two most significant mechanisms; fluorescence process and emission of an Auger electron. The Auger electron dominates the lower excitation energy (the XANES region) and fluorescence is dominated by higher excitation energy (the EXAFS region). For this reason, two basic modes are run to measure the XAS spectrum; either in fluorescence or/and transmission mode. Measuring the XAS spectrum in transmission mode requires the sample to be moderately concentrated which is not accessible for supported metal catalysts. Hence, fluorescence mode is generally preferred to obtain the XAS spectrum in this case. However, the presence of other scattered X-rays or other fluorescent impurities may dominate the fluorescent spectrum. The detector also measures the isotropic emission from the sample over a small solid angle which limits the fluorescence measurement. The X-ray fluorescence from a molecule is strictly dependent on the emission line governed by the selection rules (allowed and forbidden transitions). Using this information and quantum mechanical calculations (which include the symmetry, geometry, and coordination number of a particular model), it is possible to identify the electronic and symmetry properties of a particular molecule. To provide transmission and fluorescence detections, the fluorescence detector is affixed at a right angle to the incident X-ray beam, as shown in Figure 3.22.

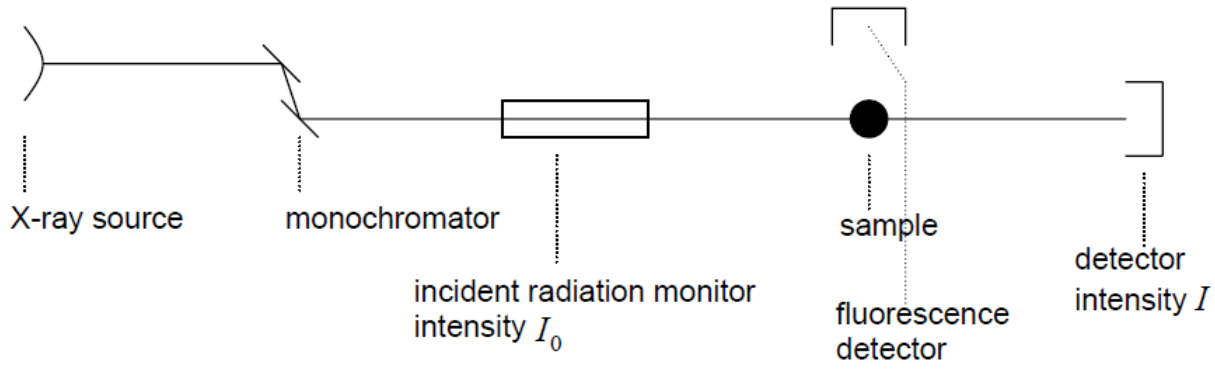

Figure 3.22 Experimental set up for the XAS experiment.

3.7.5 Thermogravimetric (TGA) and elemental analysis (EA)

The thermogravimetric analysis involves heating a sample under a flowing gas, usually N_2, at a constant rate to measure the weight loss of a sample. For organic ligand stabilized nanoparticles, TGA enables the determination of the percentage of the metal core relative to the overall nanoparticle composition. Additionally, the decomposition temperature of organic ligands reflects the stability of nanoparticles against temperature. This information is particularly useful when using the heat treatment to remove the capping ligands of supported metal nanoparticles for catalysis. Hutchinson and co-workers determined the percentage of the Au core in $Au_{101}(PPh_3)_{21}Cl_5$ and found a close agreement with the empirical formula calculated by the XPS technique.[108]

The elemental analysis is a standard technique to measure the elemental composition, primarily C, H, and N, in a combustion process. Together with the TGA result, the elemental analysis allows the verification of the sample purity. Elemental analysis is principally useful in characterizing ligands for the ligand exchange process provided the chemical composition of incoming and outgoing ligands are subtly different.

2.7.6 Infrared and Raman spectroscopy

The infrared (IR) and Raman spectroscopy are the key tools to study the vibrational modes of metal clusters or nanoparticles.[187, 188] Since vibrational modes of a particular functional group occur at specific, unique frequency, they represent the fingerprint of the molecule. The key requirement for a molecule to be IR active is that it must have a change in dipole moment as a result of vibrations when IR radiation is absorbed, though a permanent dipole moment is not necessary.[189] Using these techniques, it is possible to monitor the change in chemical bonding of ligands as the ligands interact with the metal

nanoparticles surface during the synthesis, surface functionalization or ligand exchange process. By comparing the IR spectrum of the free ligand with the ligand adsorbed on metal nanoparticles, Brust *et al.* were able to deduce that p-mercaptophenol forms a composite when interacting with the Au nanoparticle.[90] The study demonstrates that the absence of the S-H stretching mode suggests that thiolate ligands are attached to the Au nanoparticle surface *via* the thiol functional group. Similarly, Aslam *et al.* compared the IR spectrum of a free oleylamine with the oleylamine-stabilized Au nanoparticles and observed the disappearance of N-H stretching mode at 3325 cm^{-1} when the oleylamine adsorbed on the Au nanoparticle surface.[190] They proposed that the oleylamine anchors to the Au nanoparticle surface via the N atom in the amine group. Biji *et al.* utilized the Fourier transform Infrared reflection-absorption spectroscopy (FTIR-RAS) to confirm the Janus structure of amphiphilic Au nanoparticles by detecting the vibrational changes in the adsorbed ligands.[191]

While the IR spectroscopy has been a central tool to examine the vibrational modes of stabilizing ligands, the far IR (50 – 650 cm^{-1}) spectroscopy could probe the metal core transitions.[192] Despite an immense and successful effort to synthesize atomically precise metal clusters, only a few studies have been reported in the literature.[193, 194] This could be due to the complication of obtaining high quality far IR spectra across a wide range of frequencies. Another issue is that the metal-metal transition is predicted to occur below 200 cm^{-1} at a low intensity.[195] Alvino *et al.* reported high quality far IR spectra of phosphine-stabilized gold-based clusters (Au_6, Au_8, Au_9 and Au_6Pd) using the high intensity synchrotron far IR beamline.[193] By comparing the experimental spectra with the simulated spectra calculated using DFT, they were able to unambiguously assign the specific metal core vibrations and thus, provide a characteristic spectrum for each gold cluster.

Similar to IR spectroscopy, Raman spectroscopy is a complementary technique to probe the vibrational modes of metal clusters because they both have different selection rules.[188, 196] For example, some vibrational modes are calculated to be intense in the Raman but weak in the far IR spectrum.[157, 195] For a molecule to be Raman active, there must be a change in polarizability of the molecule during vibrations.[189] The use of Raman spectroscopy is exceptionally useful to probe low frequency vibrations down to *ca.* 50 cm^{-1} and across a wide range of frequencies.[192] For example, Raman spectra of iridium carbonyl clusters reveal the Ir-Ir stretching vibrations in the range of 120 – 210 cm-1.[197] Even though several Raman spectra for Au nanoparticles and clusters have been recorded, the data about Au-Au core vibrations are still missing in the literature. For example, Varnholt *et al.* measured the vibrational modes of Au-S bonds on different staple motifs of thiolate-protected Au clusters.[55] They showed that these vibrations depend on the size of Au clusters and the staple configurations. The measurement of the Raman spectrum of metal clusters is often complicated by the decomposition or aggregation of clusters as

a result of the strong local heating from the intense laser beam and the fluorescence from the clusters that mask the Raman active bands in the spectrum.[192]

Chapter 4

Far-infrared spectra of metal clusters

This chapter reports the results of a joint project with our collaborators, groups of Dr. Gregory Metha (University of Adelaide) and Dr. Gunther Andersson (Flinders University) in Australia. The author specific role in this project is to synthesize and purify the clusters and to record the far-IR spectra at the far-IR beamline at the Australian Synchrotron. The simulated spectra were computationally calculated using DFT by Greg's students, Trystan Bennet and Jason Alvino. The experimentally obtained far-IR spectra were then compared with predicted IR spectra for the assignment of the key vibrational modes. Two publications have results from this work and have been published in the journals *RSC Advances* ***3****(44): 22140-22149* and *Inorganic Chemistry* ***5****3(9): 4340-4349*.

Abstract

The synchrotron far-infrared (IR) beamline was used to obtain far-IR absorption spectra of a series of ligated metal clusters; $Ru_3(CO)_{12}$ (denoted by Ru_3), $H_4Ru_4(CO)_{12}$ (denoted by Ru_4), $Ru_3Au(PPh_3)Cl(CO)_{10}$ (denoted by $AuRu_3$) and $Au_9(PPh_3)_8(NO_3)_3$ (denoted by Au_9) in solid state. The significant peaks in the experimentally obtained far-IR spectra were assigned unambiguously with the help of the predicted IR spectra based on DFT geometry optimizations and frequencies calculations in gaseous phase. Distinct peaks of metal core vibrational bands at low-frequency, low intensity and metal-ligand vibrations at higher frequencies were observed for each cluster; 150 cm^{-1} for Ru_3, 153 and 170 cm^{-1} for Ru_4, 170 and 185 cm^{-1} for Au_9 and 177 and 299 cm^{-1} for Ru_3Au. High intensity absorption peaks near 420 cm^{-1} in the $Au_9(PPh_3)_8(NO_3)_3$ spectrum were assigned to metal-ligand vibrations; the P-Ph3 stretches. Strong absorption peaks due to metal-ligand vibrations at *ca*. 590 cm^{-1} for Ru_3, 580 cm^{-1} for Ru_4, and 560 cm^{-1} for $AuRu_3$ predicted by computationally simulated IR spectra are also observed in the experimental IR spectra, thus allowing for exclusive identification of the vibrational modes of these clusters.

4.1 Introduction

There is a growing interest in the use (in catalysis *etc*.) of atomically precise metal clusters with well-defined molecular structure and exact number of atoms as opposed to metal nanoparticles, which have a wide size distribution and ill-defined morphology. The advantage of using such atomically precise metal clusters as catalyst precursors is the potential to achieve high-precision control of the active site,

allowing studying size-reactivity relationships in catalysis.[48] Two routes are commonly used to prepare metal clusters: a) a physical approach that involves production of size-selected clusters in the gaseous phase followed by deposition onto surface and b) a chemical approach that utilizes the synthesis from metal precursor, reducing and protecting agents. The former approach has been utilized by Yoon *et al*. to test CO oxidation at low temperature using Au_8 clusters deposited on MgO surface.[198] The authors observed high conversion as low as 140 K while smaller clusters were found to be inactive. The latter approach offers the opportunity of the scaled-up production (*cf.* gas phase cluster synthesis) and avoids the use of expensive and/or complex set-ups. For example, $Au_{25}(SR)_{18}$,[199] $Au_{38}(SR)_{24}$,[97] $Au_{40}(SR)_{24}$,[200] and $Au_{144}(SR)_{60}$[201] have been synthesized chemically and employed in selective oxidations and hydrogenations.[48, 202-204] Other metal clusters such $Ru_3(CO)_{12}$ have been used in Water Gas Shift Reaction[205] and $PtRu_5(CO)_{15}(\mu\text{-}SnPh_2)(\mu_6\text{-}C)$ in hydrogenation of dimethyl terephthalate to cyclohexanedimethanol.[206]

While X-ray photoelectron spectroscopy (XPS) and X-ray absorption (XAS) are extensively employed to investigate the electronic structure and chemical environment of metal clusters, other spectroscopic techniques such as far-IR spectroscopy are practically unexplored. Far-IR spectra, as well as Raman spectra, constitute very characteristic "fingerprints" of each unique compound due to the specific vibrational frequencies of functional groups associated with each structure, reflecting on the chemical bonding.[207] Very early works to probe the vibrational modes of ligated metal clusters, for example $Ru_3(CO)_{12}$ and $Os_3(CO)_{12}$ clusters, involves using Raman spectroscopy by Quicksall in 1968[142] and far IR spectroscopy by Adams in 1982.[208] Following their reports, numerous publications appeared in the literature utilizing Raman and IR spectroscopy to study metal carbonyl clusters including those by Kettle and Stanghellini,[209] Battiston *et al.*,[187, 188] Butler *et al*.[210, 211] and Trevor.[196, 212] The authors focused on vibrational studies of metal carbonyl clusters, particularly the CO stretching region. However, no attention was given to the study of the metal core vibrations.

Unlike some progress with far-IR studies of metal carbonyl clusters, despite immense efforts on the chemical synthesis of atomically precise Au clusters containing phosphine or/and thiol ligands and their structural characterization, very few studies focused on the detailed far-IR studies of these clusters.[213] Janet *et al.* studied the Au-S stretching of gold nanoparticles of size ~2 nm protected by different alkane-thiols using far-IR spectroscopy and found that the Au-S stretching peaks appeared below 300 cm^{-1}.[214] The authors concluded that the *broad* peaks observed in the far-IR spectra can be attributed to existence of multiple binding sites of thiol ligands at the surface of Au nanoparticles as the result of polydispersity of these Au nanoparticles. Until recently, the only systematic study of atomically precise thiolate-protected Au clusters $Au_{144}(2\text{-PET})_{60}$, $Au_{40}(2\text{-PET})_{24}$, $Au_{38}(2\text{-PET})_{24}$, $[Au_{25}(2\text{-PET})_{18}]^-$

TOA^+ and $Au_{25}(2\text{-PET})_{18}$ using far-IR spectroscopy was performed by Dolamic *et al*.[195] The authors concluded that the far-IR spectra can be considered as a fingerprint for each cluster because different clusters produce different far-IR spectra albeit the differences in these spectra were very small.

In contrast to a strong Au-S bonding in thiolate-protected gold clusters, phosphine-stabilized Au clusters have a labile bond between Au-P. Bour *et al.* reported that metal-ligand vibration in $PtAu_8(PPh_3)_8(NO_3)_2$ cluster appears at 450 cm^{-1}.[215] However, lower frequency bands (< 400 cm^{-1}) which are expected to correspond to the vibrational motions of the metal core are not reported in any study because they are too weak in intensity. In recent years, attempts have been made to correlate the experimentally obtained spectra recorded using far-IR multiple photon dissociation (FIR-MPD) spectroscopy in combination with quantum mechanical calculations performed to identify IR-active vibrations.[207, 216, 217] Gruene *et al*. studied the structure (geometry) of neutral Au_7, Au_{19} and Au_{20} clusters in the gas phase using the FIR-MPD spectroscopy since the vibrational modes are very sensitive to the structure of Au clusters.[207] The advantage of this approach is that it allows the study of exact three-dimensional (3D) geometry of clusters with any interaction with the surrounding ligands and offers more precise quantum mechanical calculations. However, this approach requires a complex and specialized set up. Gold clusters are produced by means of laser vaporization from a gold rod in a continuous flow of Kr and He at 100 K.[207] Under these conditions, gold cluster-Kr complexes are produced. The cluster beam set up is coupled to a pulsed far-IR beam delivered by the Free Electron Laser for IR Experiment (FELIX). The complexes are then ionized by an F2-excimer laser and mass-analysed in a time-of-flight mass spectrometer. Resonance of the far-IR light with an IR-active vibration of a given cluster may lead to the absorption of several photons and evaporation of Kr ligand which is detected as a depletion of the corresponding mass-spectrometric signal. The absorption spectra are reconstructed from recording the mass-spectrometric signal while scanning the wavelength of FELIX.

Because the catalytic properties of metal clusters are determined by their electronic structure and geometric, it is very meaningful to investigate the metal-metal core and metal-ligand vibrations that are sensitive to their electronic structure and geometry. Motivated to identify the low frequency vibrational modes of atomically precise, ligand-stabilized metal clusters, we performed the far-IR measurement of low intensity, low frequency vibrational modes of the clusters using high intensity synchrotron Far-IR beamline at the Australian Synchrotron. The experimentally obtained far-IR spectra were then compared with the predicted based on DFT calculations spectra of the metal clusters including ligands. Here, we focused on the phosphine-stabilized gold cluster, $Au_9(PPh_3)_8(NO_3)_3$. We also investigated the vibrational frequencies of metal cores of ruthenium carbonyl clusters, $Ru_3(CO)_{12}$ and $Ru_4H_4(CO)_{12}$, and compared these with that of the gold-adduct cluster, $Ru_3(AuPPh_3)(\mu\text{-}Cl)(CO)_{10}$. As small a change as one atom

results in a shift of metal core vibration observed upon moving from Ru_4 to bimetallic $AuRu_3$. This study allows us to identify the key features within the far-IR spectra and to assign these to specific vibrational motions of the metal cores and metal-ligand (Au-P bonds) moieties.

4.2 Results and discussion

4.2.1 General

Figures 4.1-4.4 illustrate the crystal structures superimposed with the optimized structures, with only metal atom (Au and/or Ru) shown for convenience and simplicity (the other atoms are included in DFT calculations but not in the pictures). The superimposed structures exhibit a very close resemblance between gas phase and condensed phase geometry. The difference between DFT-optimized structure (atoms coloured with yellow balls in Figure 4.1 for example) and crystal structure (atoms coloured with green balls in Figure 4.1 for example) arises because DFT-optimized structure is constructed in gas-phase while crystal structure is obtained from solid state in which lattice packing and pi-interaction (from triphenylphosphine) may result in minor changes. Since all the molecules are optimized starting from the crystal structure to the final gas phase geometric minima, there is a general trend towards longer bond lengths in the gas phase structures (see specific discussions for each of the clusters later). The simulated spectra are shown as dotted lines (see Figure 4.5 for example). The calculated peaks only involve fundamental vibrations and do not include overtones or combination bands. While the number of vibrations is huge up to 650 cm^{-1}, only certain vibrations that met the following two criteria were considered. Firstly, only normal modes associated with the metal core vibrations that contribute to significant motion of Au, Ru, C,O, Cl and P atoms were identified in order to differentiate from other low frequency modes. Secondly, the calculated peaks only include any normal modes which have significant calculated IR intensity (> 1 km/mol).

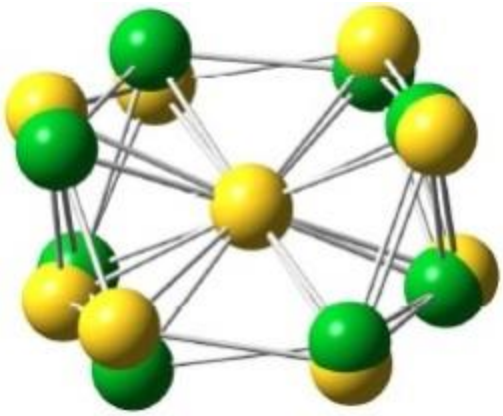

Figure 4.1 X-ray crystal structure (green) and DFT optimized structure (yellow) of Au_9 cluster metal core. Only Au atoms are shown for clarity. Adapted from *RSC Advances* ***3****(44): 22140-22149.* Copyright RSC publishing.

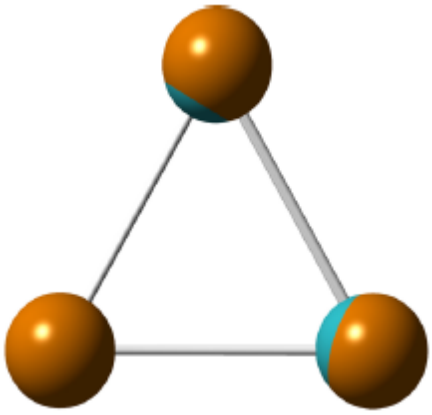

Figure 4.2 X-ray crystal structure (blue) and DFT optimized structure (brown) of Ru_3 cluster core. Only Ru atoms are shown for clarity. Adapted from *Inorganic Chemistry* ***5****3(9): 4340-4349*. Copyright ACS publishing.

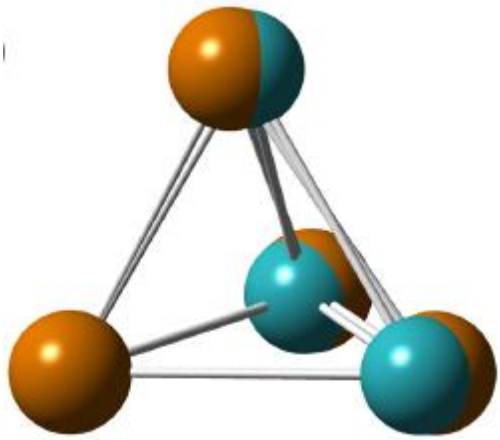

Figure 4.3 X-ray crystal structure (blue) and DFT optimized structure (brown) of Ru_4 cluster core. Only Ru atoms are shown for clarity. Adapted from *Inorganic Chemistry 53(9): 4340-4349*. Copyright ACS publishing.

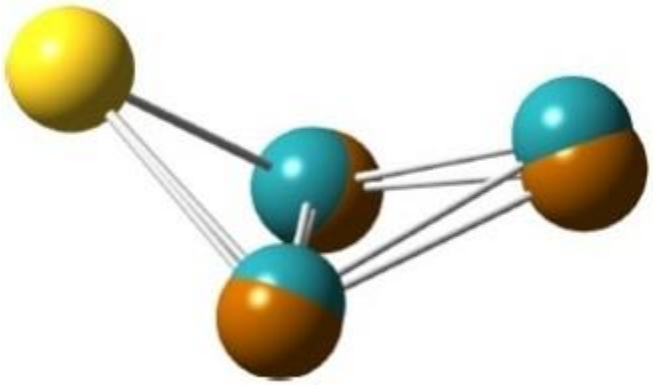

Figure 4.4 X-ray crystal structure (blue) and DFT optimized structure (brown) of $AuRu_3$ cluster core. Au atom is shown in yellow. Adapted from *Inorganic Chemistry 53(9): 4340-4349*. Copyright ACS publishing.

The normal modes are listed as either individual peaks or groups of peaks in the spectra. Table 4.1-4.4 shows the corresponding peak numbering starting from low energy as those in the spectra, their peak assignment with a brief description of each transition. Of particular interest, the metal core vibrations are illustrated in Figures 4.6, 4.9, 4.11 and 4.13 with the corresponding peaks marked with asterisk in Table 4.1-4.4.

For Ru_3, an elongation of Ru-Ru bond from 2.85 to 2.90 Å occurs. An elongation of Au-Ru bond from 2.75 to 2.82 Å with an opening of the butterfly structure from 117.2 to 123.4° occurs in bimetallic $AuRu_3$ cluster. However in Ru_4 cluster, a decrease in Ru-Ru bond length from 2.95 to 2.91 Å occurs, perhaps because of the presence of bridging H atoms moving further away from the centre of mass. For Ru_3, Ru_4 and $AuRu_3$ far-IR spectra, the region from 50 to 350 cm^{-1} has been scaled from the calculated numbers by the functional-independent correction factor (equation. 4.1) as reported by Fielicke *et al*. for low frequency vibrations estimated by DFT calculations, which yield better agreement for far-IR transitions than traditional vibrational frequency correction.[216]

$$\upsilon_{corr} = 22\ cm^{-1} + \upsilon_{call}*0.94 \qquad 4.1$$

4.2.2 Au_9 cluster

Figure 4.5 shows the experimentally obtained (solid line) and simulated (dotted line) far-IR absorbance spectra of the Au_9 cluster. A very strong absorption peak at 440 cm^{-1} appears in the far-IR spectrum of the Au_9 cluster. An associated simulated spectrum also evidently shows this feature. An assignment according to normal mode analysis demonstrates that these vibrations (entry #10 in Figure 4.5 and Table 4.1) are due to P-Ph_3 stretching modes with high intensity originate from the substantial number of triphenylphosphine ligands (8 PPh_3 ligands per Au_9 cluster), yielding up to three P-Ph vibrations. A set of four similar transitions arising from Ph-twisting matches the shoulder observed at 430 cm^{-1}. Calculations predicted weak intensity peaks around 397-411 cm^{-1} (#8, see Figure 4.5 and Table 4.1) in the simulated spectrum. However, the experimentally obtained far-IR spectrum showed very distinct peaks. A combination of the two normal modes in the cluster, involving phenyl group twisting vibrations, contributes to this enhanced intensity peak. An intense peak predicted to be at 426 cm^{-1} (#9, Table 4.1) due to the similar twisting mode matches the peak at 430 cm^{-1} in the experimentally recorded far-IR spectrum. A collection of PPh_3 distortion modes calculated to be around 253 cm^{-1} matches well with the intense peak at 251 cm^{-1} in the experimental spectrum. The broad features at 217 and 220 cm^{-1} in the experimental spectrum were assigned to peaks at 211 (#5) and 224 (#6) cm^{-1}, respectively, which originate due to PPh_3 rocking vibrations.

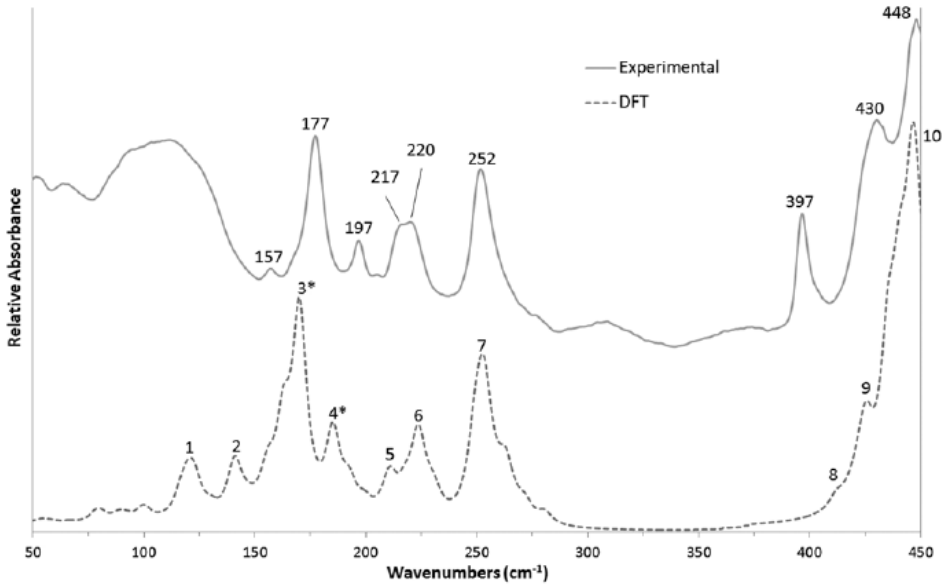

Figure 4.5 Experimentally obtained (solid line) and simulated (dotted line) spectra of the Au_9 cluster. Adapted from *RSC Advances* ***3****(44): 22140-22149.* Copyright RSC publishing.

Table 4.1. A summary of all calculated contributing transitions for the Au_9 cluster and their assignment to the predicted peak, as well as positions of the corresponding experimentally obtained peaks in the far-IR spectrum (assigned peaks), and a brief description of the assigned transition modes.

#	Peak (cm^{-1})	Contributing vibration (cm^{-1})	IR intensity (km/mol)	% Au motion	% P motion	Assigned peak (cm^{-1})	Mode description
1	121	116.0	2.1	1.9	1.7		
		119.3	2.7	6.0	2.4		
		120.0	2.4	5.6	2.3		
		122.9	4.6	3.6	1.7		
2	141	140.9	7.2	8.3	5.8	157.2	Au core distortion
3	170	162.8	11.2	8.1	4.6	177.4	Au core distortion
		170.1*	28.0	17.7	3.3		
4	185	185.2*	11.2	17.7	1.7	196.7	Au core distortion
5	211	210.7	2.0	0	1.1	216.5	Ph rock
		211	3.2	0	0.8		
6	224	217.6	2.7	0	1.2		Ph rock
		222.2	2.3	0	0.7		
		223.7	5.6	0	0.7		
		224.2	3.1	0	1.4		
7	253	248.9	6.6	0	1.0	251.7	PPh_3 distortion
		251.6	6.2	0	0.8		
		252.2	3.2	0	0.6		
		253.9	9.9	0	0.9		
8	411 (shoulder)	411.8	0.9	0	1.0	396.8	Ph twist
		412.2	0.7	0	1.0		
9	426	424.5	1.5	0	3.2	430.0	Ph twist
		424.6	1.9	0	3.0		
		425.4	3.6	0	4.7		
		425.5	1.9	0	2.5		
10	447	435.2 – 44.8.8	8.1	0	13	447.9	PPh_3 distortion

The distinct, sharp peaks observed at 177 and 197 cm^{-1} match perfectly with the predicted peaks at 170 and 185 cm^{-1}, respectively, in the simulated spectra, both having originated from metal core vibrations. These peaks are of particular interest for this study because the calculations predicted that they should have high intensity and predicted peaks matching the observed features in the experimental spectrum perfectly. These peaks are corresponding to the metal core vibrations and are illustrated in Figure 4.6. A small peak at 157 cm^{-1} is assigned to another metal core vibration which was predicted to occur at 141 cm^{-1}. This feature is attributed to the vibration mode of the central Au atom contributing to 8% Au motion relative to other eight surrounding Au atoms and was calculated to have lower intensity than other Au core vibrations.

Series of small peaks predicted to be below 140 cm^{-1} in the simulated spectrum did not resemble the observed broad features in the experimental spectrum. These peaks arise due to transitions of large-amplitude motions of P-Ph_3 ligand group. The experimentally observed broad features most likely arise from the dampening of low frequency vibrations due to the nature of the sample (pressed pellet, condensed phase) while the simulated spectrum was generated for the cluster in the gas-phase.

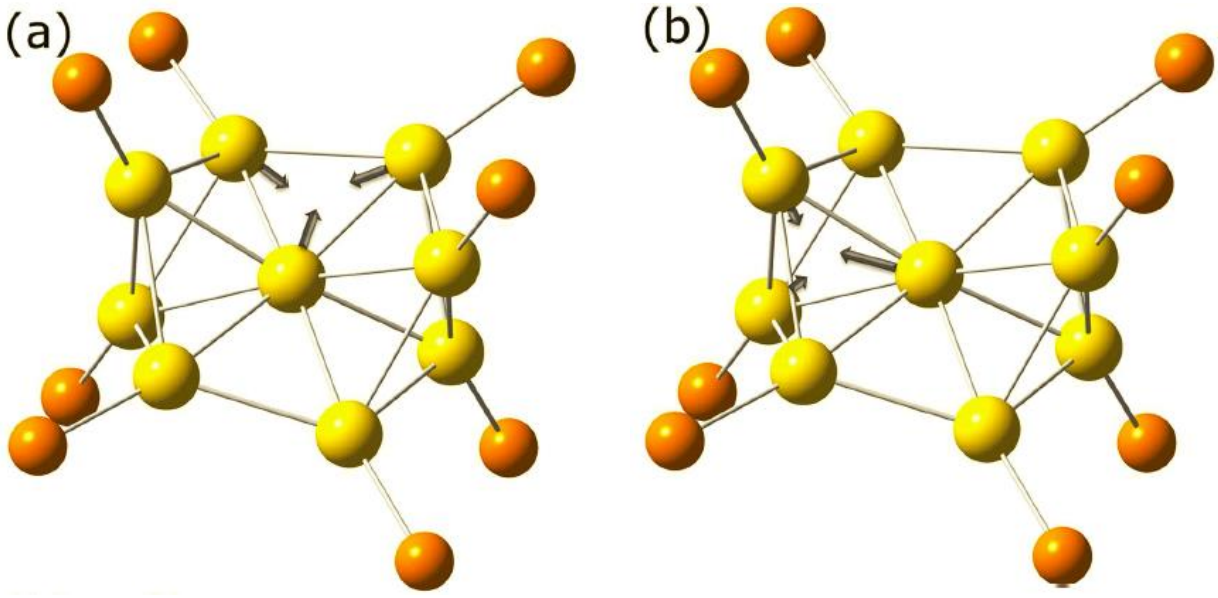

Figure 4.6 Calculated normal mode displacement associated with the Au_9 metal core vibrations at a) 170 cm^{-1} and b) 185 cm^{-1}. Phenyl groups are omitted for clarity. Colours: yellow – gold atoms; orange – phosphorus atoms. Adapted from *RSC Advances **3**(44): 22140-22149.* Copyright RSC publishing.

4.2.3 Ru_3 cluster

The crystal and molecular structure of the $Ru_3(CO)_{12}$ cluster have been known for a long time.[141, 218] Due to its high chemical reactivity, the $Ru_3(CO)_{12}$ cluster has been exploited as a precursor for the synthesis of other high nuclearity ruthenium or ruthenium-based clusters such as $Ru_6C(CO)_{17}$, $Ru_5C(CO)_{15}$,[219] $[N(PPh_3)_2][Ru_{10}H(C)(CO)_{24}]$,[220] $[N(PPh_3)_2]_3[Ru_{11}H(CO)_{27}]$,[221] and $Ru_6Au_2C(CO)_{16}(PPh_3)_2$.[222] Attempts have been made to study this cluster spectroscopically *via* Raman and IR techniques in order to correlate its reactivity with the chemical bonding and molecular geometry. The cluster has a nearly ideal D_{3h} configuration in solid phase as established previously by several groups, corresponding to the most sterically hindered structure. [211, 223-225] However, quantum mechanical (DFT) and molecular mechanics calculations show that its lower symmetry, the D_3 configuration, is the most stable structure in the gas phase.[226] Computational calculation by Peng *et al.* showed that the D_3 optimized configuration has a lower energy compared to that of D_{3h} configuration by 1.7 – 3.1 kcal/mol.[227] Bennett *et al.* showed that the gas phase calculation predicts the D_3 to be lower in energy by 2.7 kcal/mol, consistent with those found by Peng *et al.*[194] Gervasio *et al.* showed that the geometry optimization of the $Ru_3(CO)_{12}$ cluster always leads to the loss the D_{3h} symmetry, leading to the more stable D_3 configuration.[228] The authors also propose that the stability of D_{3h} symmetry in solid phase is perhaps due to the crystal packing effect. Following these arguments, we employed D_{3h} symmetry in the analysis of far IR spectrum of the Ru_3 cluster. The simulated far-IR spectra for D_3 and D_{3h} are shown in Figure 4.7 for comparison.

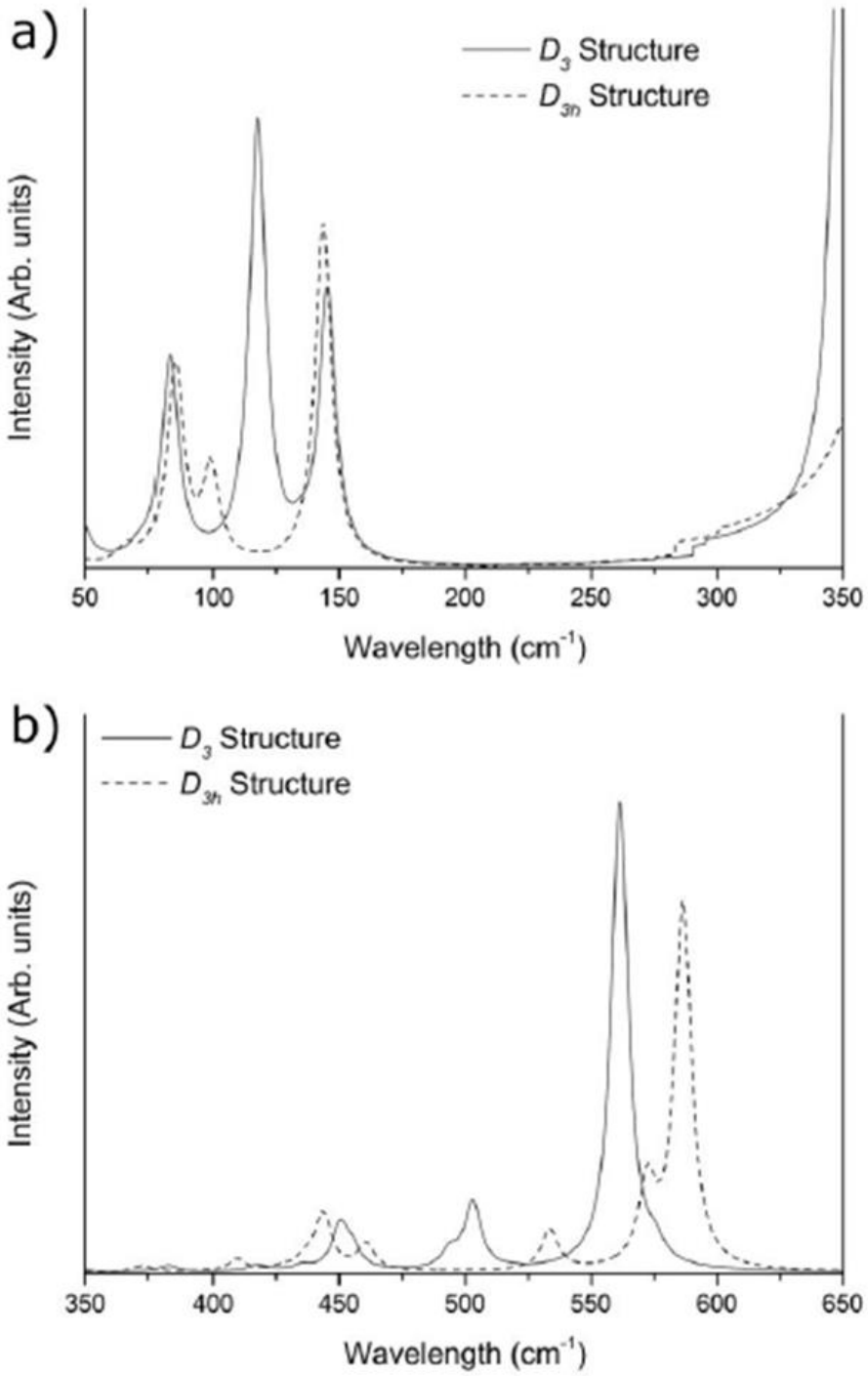

Figure 4.7 Simulated far IR spectrum of Ru_3 cluster with optimized both geometries; D_3 (solid line) and D_{3h} (dotted line) configurations in a) 50-350 cm^{-1} region and b) 350-650 cm^{-1} region. Adapted from *Inorganic Chemistry* ***5****3(9): 4340-4349*. Copyright ACS publishing.

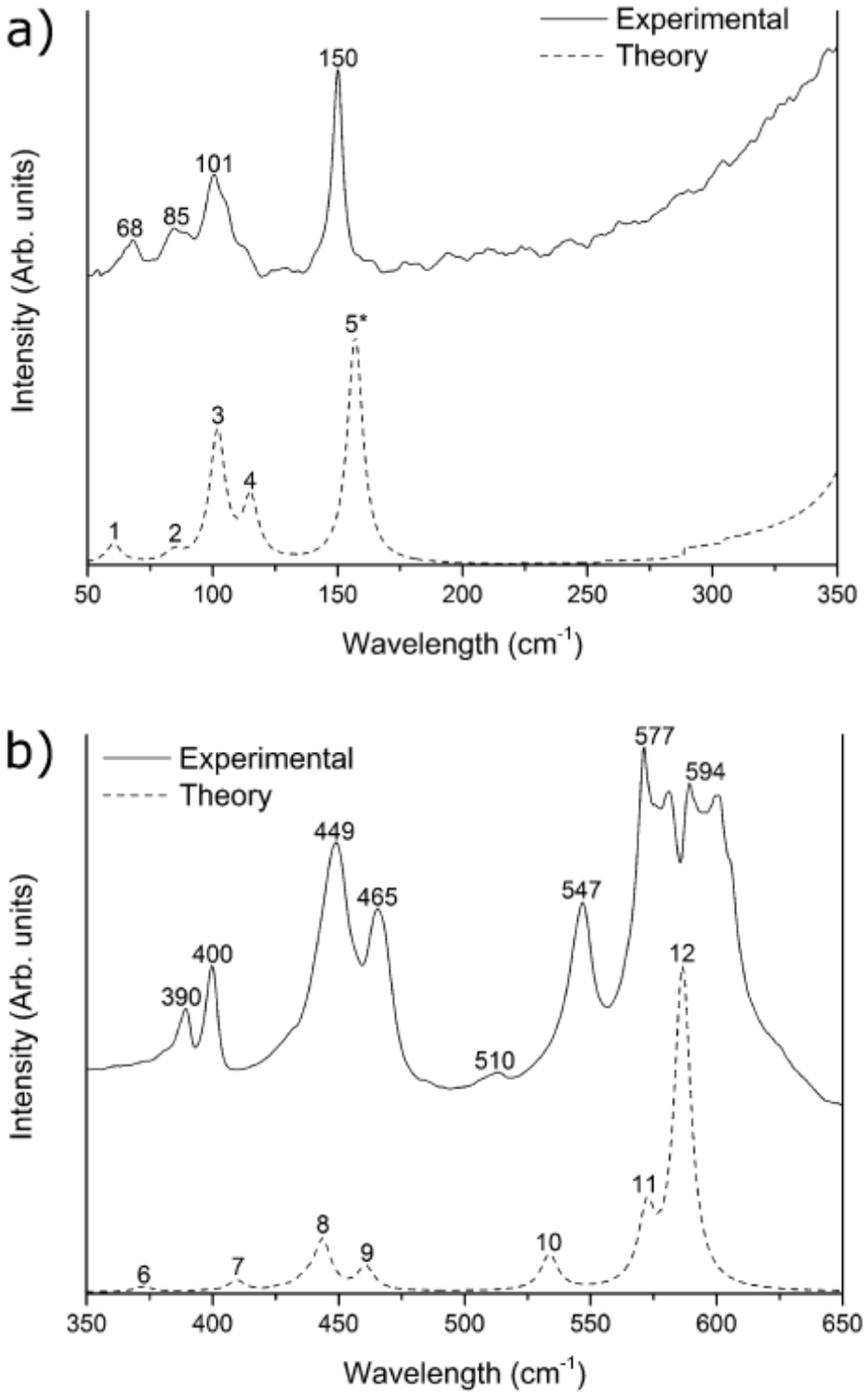

Figure 4.8 Experimental (solid line) and simulated (dotted line) of far-IR spectra of Ru_3 cluster in a) 50-350 cm^{-1} region and b) 350-650 cm^{-1} region. Adapted from *Inorganic Chemistry 53(9): 4340-4349.* Copyright ACS publishing.

The far-IR spectrum of the Ru_3 cluster is shown in Figure 4.8 above. A very intense absorption predicted to occur at 150 cm^{-1} was assigned to the peak #5 in the experimental spectra. This peak originates from degenerate asymmetric distortions (k = 0.33 mdyne/Å) with ~28% contribution from Ru_3 core (Figure 4.9). The moderately intense peak that appears at lower energy, 101 cm^{-1} in the experimental spectrum is assigned to predicted peak #3 and its high-energy shoulder to peak #4. The other two lower energy peaks that appear at 65 and 85 cm^{-1} are assigned to peaks #1 and #2 in the simulated spectrum, respectively. The assignment for these two peaks is under debate. While Adam and Taylor attribute these peaks to the lattice mode,[208] Kettle *et al*. suggested a contribution from intermolecular motions to describe these peaks,[209] which reinforces findings of our earlier study on far-IR spectra of Au-based clusters.[193]

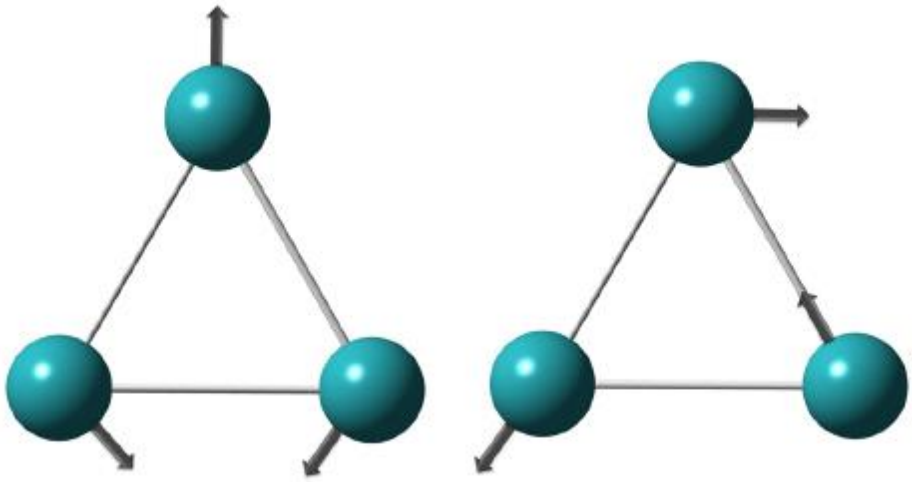

Figure 4.9 Calculated normal mode displacement of metal core vibrations for Ru_3 cluster corresponding to the peak at 143.6 cm^{-1}. Only Ru atoms are shown. Adapted from *Inorganic Chemistry 53(9): 4340-4349*. Copyright ACS publishing.

A large and broad doublet that appears at 577 and 594 cm^{-1} is assigned to the predicted peaks #11 and #12, arising from degenerate axial C-Ru-C bending and degenerate Ru-$(CO)_4$ bending modes, respectively. A slightly lower energy peak calculated to appear at 534 cm^{-1} (peak #10) arising due to a single axial C-Ru-C bending mode is assigned to the peak at 547 cm^{-1} in the experimentally obtained spectrum. However, a very tiny peak observed at 510 cm^{-1} in the experimental spectrum is not found in the simulated spectrum, and thus no transition is described to the peak. A doublet calculated to appear at 444 and 461 cm^{-1} matches closely in both position and intensity to the observed doublet at 449 and 465 cm^{-1} and is attributed to the axial Ru-(CO) stretches and degenerate equatorial C-Ru-C stretches. Finally, the remaining two weak peaks at 390 and 400 cm^{-1} originating from equatorial Ru-(CO) bending modes are assigned to the peaks #6 (373 cm^{-1}) and #7 (410 cm^{-1}), respectively. A summary of all the calculated

vibrational modes and their assignment to the experimental observed peaks with a brief description of the vibrational modes is shown in Table 4.2 below.

Table 4.2 A summary of all calculated contributing transitions for the Ru_3 cluster and their assignment to the predicted spectral peak, as well as the experimentally obtained far-IR spectrum, and a brief description of the assigned transition modes.

#	Peak (cm^{-1})	Contributing vibration (cm^{-1})	IR intensity (km/mol)	%Ru motion	Assigned (cm^{-1})	Mode description
1	41	40.8	0.08	3.9	68	Equatorial C-Ru-C bend
2	67	66.6	0.04	4.0	85	Equatorial C-Ru-C bend
3	85	85.0	1.0	14.4	101	Equatorial CO vertical wag
4	99	99.1	0.2	17.7		Axial CO horizontal wag
5	144	143.6*	0.9	28.3	150	Ru_3 asymmetric distortion
6	373	372.6	5.7	2.3	390	Equatorial C-Ru-C bend
7	410	396.7	1.6	7.8	400	Equatorial C-Ru-C bend
		409.5	11.4	4.5		Equatorial C-Ru-C bend
8	444	427.3	3.1	8.2	449	Equatorial Ru-(CO) streches
		436.4	9.0	12.3		Equatorial C-Ru-C asymmetric stretches
		443.6	104.7	19.6		Axial Ru-(CO) stretches
9	461	460.7	24.6	10.8	465	Equatorial C-Ru-C symmetric stretches
10	534	533.7	74.2	3.6	547	Axial C-Ru-C bend
11	573	572.3	73.7	13.5	577	Axial C-Ru-C bend
12	586	586.5	332.4	12.3	594	Ru-$(CO)_4$ bend

4.2.4 Ru_4 cluster

The experimental and simulated far-IR spectra in the range of 50-650 cm^{-1} for Ru_4 cluster are shown in Figure 4.10. To our knowledge, several studies focused on the IR spectrum of Ru_4 cluster in the range of 1800-2200 cm^{-1} have been reported but none at lower wavenumber (< 650 cm^{-1}).[150, 229, 230] The experimentally obtained spectrum exhibits a unique "multiplet" centred around 110 cm^{-1}. This multiplet, arising from Ru_4 core distortion and Ru-(CO) bending modes, was assigned to the peak #4 in the calculated spectrum. The predicted peaks (#1-3) do not resemble any corresponding feature in the experimental spectrum, and thus were not assigned.

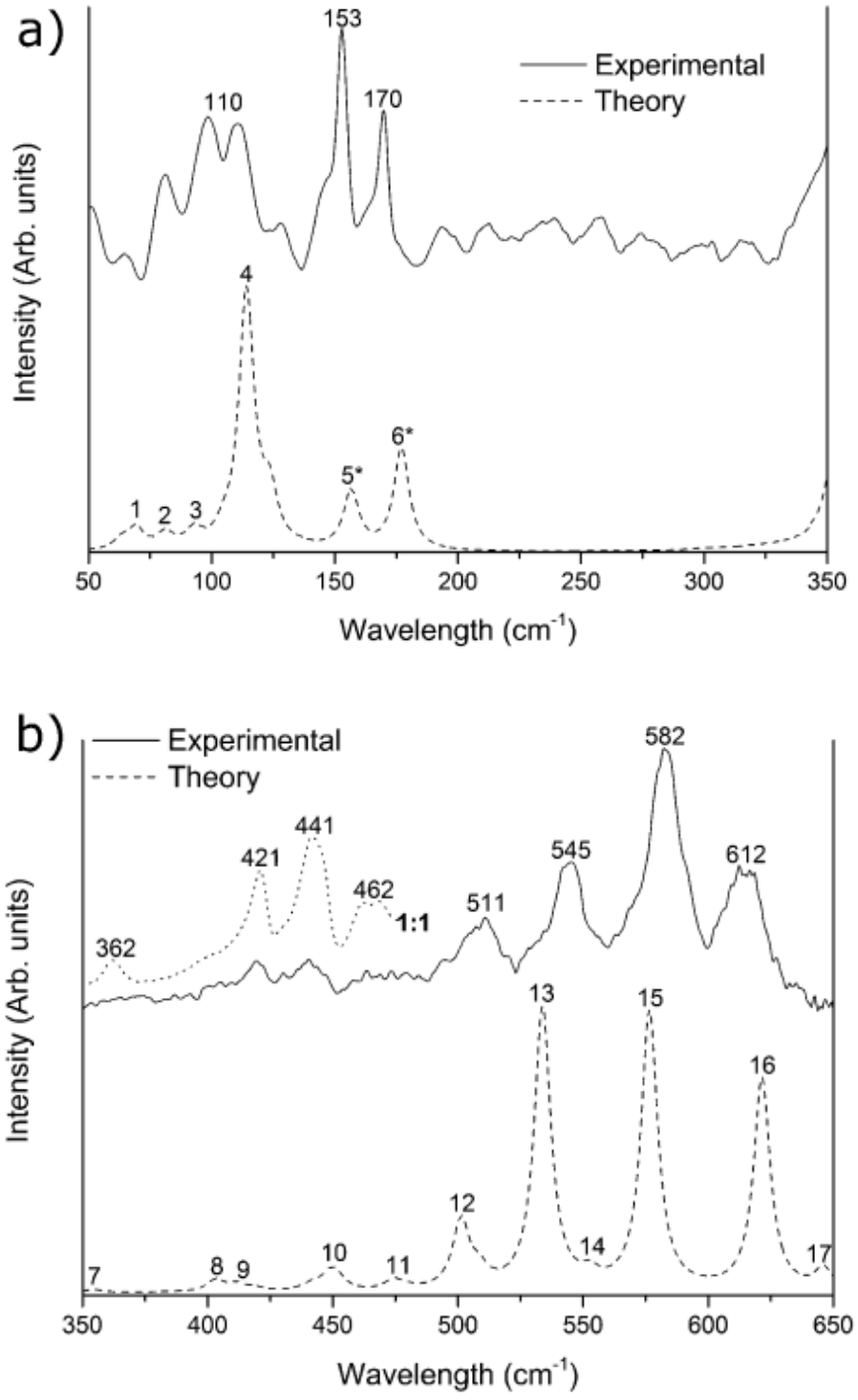

Figure 4.10 Experimental (solid line) and simulated (dotted line) of far-IR spectrum of Ru_4 cluster in a) 50-350 cm^{-1} region and b) 350-650 cm^{-1} region with the top dashed line is the experimental spectrum obtained at higher concentration of Ru_4 in PET. Adapted from *Inorganic Chemistry 53(9): 4340-4349*. Copyright ACS publishing.

Two sharp, intense, and higher energy features observed at 153 and 170 cm^{-1} are attributed to the asymmetric distortion of the Ru_4 cluster core and were assigned to the peaks #5 and #6, respectively. The calculated force constants for these peaks are 0.35 mdyne/Å (peak #5) and 0.53 mdyne/Å (peak #6), which include 34% and 38 % contribution from Ru core vibrational modes, respectively. The predicted force constants, particularly for the lower energy peak at 153 cm^{-1}, are consistent with the calculation for the Ru_3 cluster mentioned above, being similar in value (*cf.* 0.33 mdyne/Å for Ru_3 core vibration). Despite having similar reduced mass, the higher energy vibration appears at 170 cm^{-1} due to the higher k value. Figure 4.11 illustrates the asymmetric vibrational modes of the Ru_4 core.

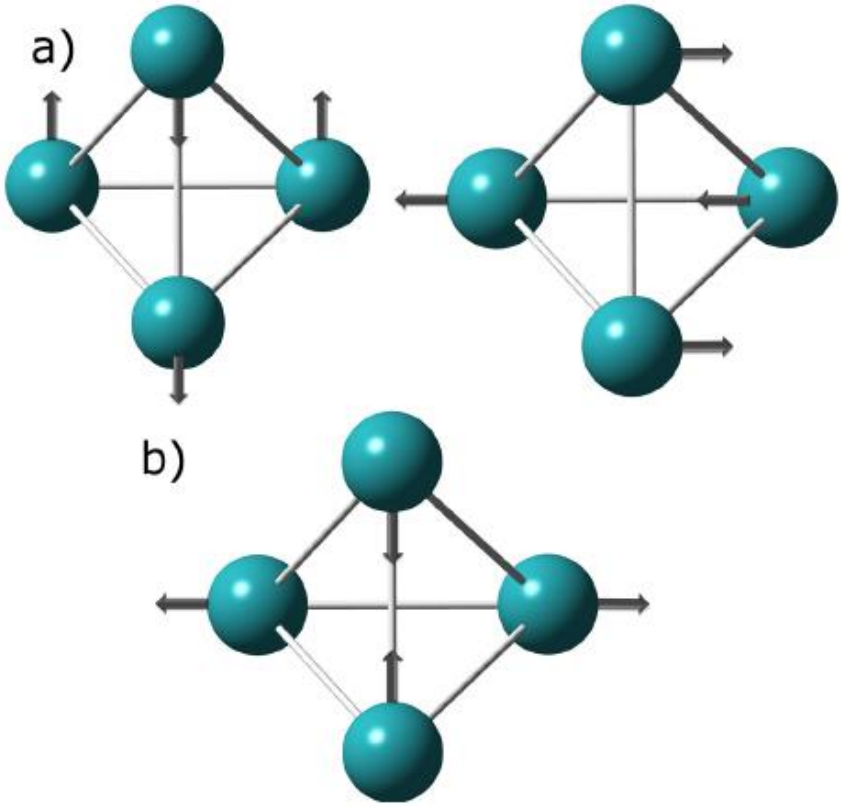

Figure 4.11 Calculated normal mode displacement of metal core vibrations for Ru_4 cluster at a) degenerate modes at 143 cm^{-1} and b) 165 cm^{-1}. Only Ru atoms are shown. Adapted from *Inorganic Chemistry* ***5****3(9): 4340-4349*. Copyright ACS publishing.

The features within the 350-650 cm^{-1} region in the experimental spectrum resemble closely the predicted features within the simulated spectrum. Four peaks (peak #7, 8, 10 and 11) calculated to appear within 350-480 cm^{-1} were also observed in the experimental spectrum. The weak, broad, and lowest energy peak at 362 cm^{-1} was assigned to peak #7 and arises due to the degenerate hydrogen ligands

transition. The next higher energy peak that appears at 421 cm^{-1} which is due to the Ru-C stretch modes was assigned to the both peaks #8 and #9. The predicted peak #10 was calculated to contain a series of vibrational modes, which originate from degenerate Ru-C stretching and Ru-C-O bending modes, and was assigned to the peak at 441 cm^{-1} in the experimental spectrum. The experimental spectrum also displayed a broad doublet at 462 cm^{-1} that was assigned to the predicted peak #11. This peak was calculated to have transitions due to the Ru-C_3 bending and degenerate Ru-C stretching modes. A moderately intense peak observed at 511 cm^{-1} was assigned to the predicted peak #12 and calculated to arise from C-Ru-C stretching modes. Two high intensity features that were calculated to contain a combination of Ru-C bending modes also appeared at 545 and 582 cm^{-1} in the experimental spectrum and matched closely to the predicted peaks #13 and #15. Finally, the experimental spectrum also exhibited an intense peak at 612 cm^{-1} which is due to another hydrogen ligand motion and was assigned to peak #16.

Table 4.3 A summary of all calculated contributing transitions for the Ru_4 cluster and their assignment to the predicted spectral peaks, as well as the experimentally obtain far IR spectrum, and a brief description of the assigned transition modes.

#	Peak (cm^{-1})	Contributing vibration (cm^{-1})	IR intensity (km/mol)	%Ru motion	Assigned peak (cm^{-1})	Mode description
1	50	50.3	0.3	7.6		Ru-$(CO)_3$ distortion
2	63	62.6	0.1	13.0		Ru-$(CO)_3$ distortion
3	75	75.1	0.1	9.9		Ru-$(CO)_3$ distortion
4	98	98.0	2.0	20.8	110	Ru_4 distortion
		108.1	0.4	15.7		(OC)-Ru-(OC) bend
5	143	143.3*	0.5	33.7	153	Ru_4 asymmetric distortion
6	165	165.0*	1.6	38.3	170	Ru_4 asymmetric distortion
7	354	354.4	1.5	3.8	362	H_2 motion
8	403	403.1	6.3	10.0	421	C-Ru-C asymmetric stretch
9	411	411.6	3.9	10.0		Ru-C stretch
		419.0	3.6	15.6		Ru-C stretch
10	449	438.4	0.8	9.0	441	Ru-C_3 distortion
		442.3	6.0	6.3		Ru-C-O bend
		451.6	6.1	12.9		Ru-C stretch
11	473	474.3	5.0	12.2	462	Ru-C stretch
		479.5	2.6	11.8		Ru-C_3 distortion
12	500	501.2	35.7	12.5	511	C-Ru-C asymmetric stretch
		508.7	15.8	16.7		C-Ru-C asymmetric stretch
13	533	533.8	147.6	11.7	545	Ru-C_3 bend
14	553	552.8	12.0	6.3		H_4 asymmetric in plane motion
15	576	576.5	199.0	14.5	582	C-Ru-C bend
		576.6	46.2	12.6		C-Ru-C bend
16	621	621.5	111.0	10.5	612	H_2 motion
17	646	646.0	22.0	8.7		H_4 motion

4.2.5 $AuRu_3$ cluster

The experimentally obtained far-IR spectrum of the $AuRu_3$ cluster exhibits four main peaks in the 50-350 cm^{-1} region at 177, 218, 299 and a doublet at 254 and 261 cm^{-1} including a multiplet below 150 cm^{-1} (Figure 4.12a). The spectrum reveals an intense feature that appears at 177 cm^{-1} with few higher energy shoulders that originate from a combination of Cl-Ru_3-Au distortion having 9 % Au and 15 % core contributions, and Ru_3 distortion. This feature was assigned to the peak #7 (165 cm^{-1}) in the simulated spectrum, which was calculated to have a force constant of 0.37 mdyne/Å. Another metal core transition due to the Ru_2Cl stretching mode, containing 21 % Ru core contribution, was predicted to happen at 285 cm^{-1} (peak #11). The calculated force constant for this transition is 1.65 mdyne/Å in which resembles closely force constant estimated for the intense, sharp peak at 299 cm^{-1} in the experimental spectrum.

More significantly, the effect of an Au adduct in the $AuRu_3$ cluster on metal core transitions is highlighted by the appearance of the peak at 177 cm^{-1}, higher than that of the Ru_3 (150 cm^{-1}) and Ru_4 (153 cm^{-1}) clusters. This unequivocal consequence is a result of the smaller reduced effective mass (23.2 amu, *cf*. 26.8 amu for Ru_3 and 28.7 amu for Ru_4) and larger force constant (0.37 mdyne/Å, *cf*. 0.33 for Ru_3 and 0.35 for Ru_4) of the $AuRu_3$ cluster compared to the Ru_3 and Ru_4 clusters. Another core transition at 299 cm^{-1} was predicted to have a comparable force constant, 1.65 mdyne/Å to that of ligand-free Ru_3 cluster (1.86 mdyne/Å) as reported previously by Li Fang *et al*.[231] Finally, the predicted peak #10 at 245 cm^{-1} was calculated to have a combination of a metal core vibration and P-Ph_3 bending modes and was assigned to the broad doublet feature at 254 and 261 cm^{-1} in the experimental spectrum. This metal core vibration was attributed to a significant Ru_2-Cl motion consisting of 23 % Ru contribution. Ambiguity arises for the sharp and intense peak at 218 cm^{-1} which could be ascribed to either peak #8 or #9, having less than 5% contribution from the metal core. Figure 4.13 illustrates the metal core vibrations for $AuRu_3$ cluster core at 165 cm-1 arising from the Cl-Ru_3-Au distortion and 284.8 cm-1 arising from the Ru_2-Cl stretching.

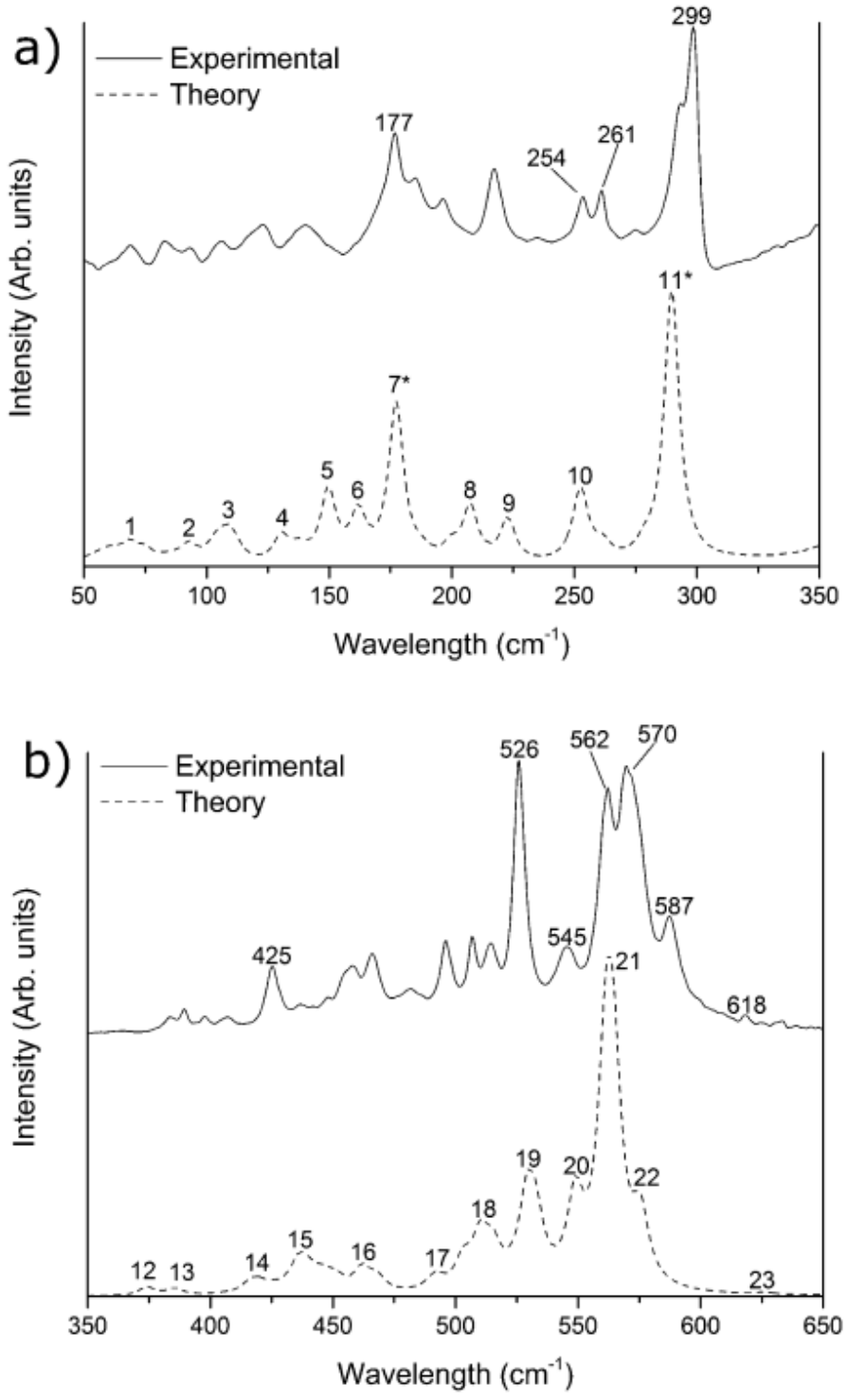

Figure 4.12 Experimental (solid line) and simulated (dotted line) of far-IR spectra of $AuRu_3$ cluster in a) 50-350 cm^{-1} region and b) 350-650 cm^{-1} region. Adapted from *Inorganic Chemistry 53(9): 4340-4349*. Copyright ACS publishing.

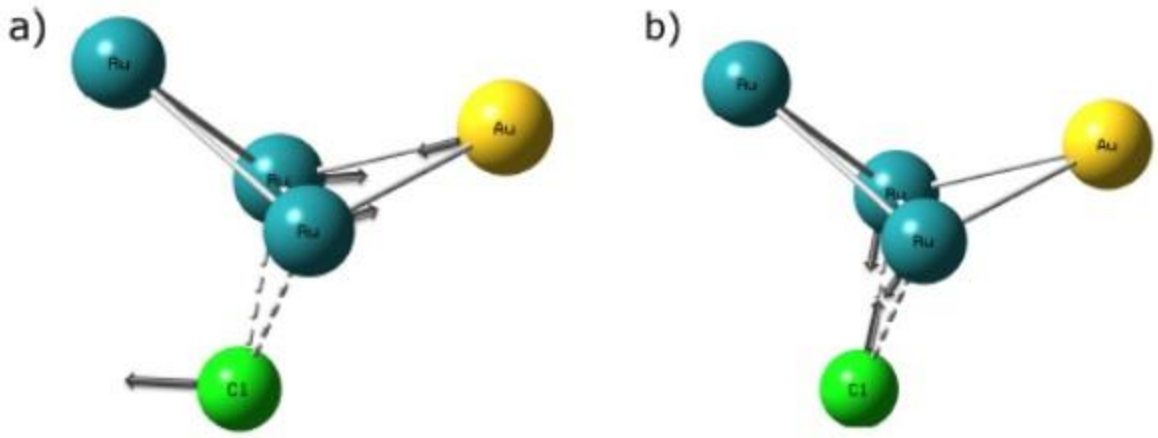

Figure 4.13 Calculated normal mode displacement of metal core vibrations for $AuRu_3$ cluster core at a) 165 cm^{-1} and b) 284.8 cm^{-1}. Adapted from *Inorganic Chemistry* ***5****3(9): 4340-4349*. Copyright ACS publishing.

In the region of experimental far-IR spectrum of $AuRu_3$ cluster between 350 and 650 cm^{-1}, there are many large and small peaks, consistent with the predicted transitions in the simulated spectrum (Figure 4.12b). Due to the complexity of the spectrum, only main features were ascribed to the specific transitions. Calculations predicted that a series of metal ligand vibrations including Ru-C-O, C-Ru-C and Ru-C_3 bending, phenyl group distortion, and Ru-(CO) stretching should to occur at around 425 cm^{-1} (peak #15) and could be assigned to the intense and broad feature at 437 cm^{-1}. Two sharp, strong absorption peaks observed at 526 and 545 cm^{-1} matched closely the predicted peaks at 530 (#19) and 549 cm^{-1} (#20) respectively. The transitions associated with these peaks arise from a combination of Ru-C_3, C-Ru-C and C-Ru-C_2 bending and phenyl group distortion. The experimental spectrum also displays a doublet at 562 and 570 cm^{-1} which arises due to two C-Ru-C bending modes which were assigned to the peak #21. A small, higher energy shoulder at 587 cm^{-1} was predicted to originate from Ru-C_3 bending and ascribed unambiguously to the peak #22. Finally, a very weak feature that appears at 618 cm^{-1} which was assigned to the peak #23 contains a distortion from the phenyl group. A summary of all the calculated vibrational modes and their assignment to the experimental observed peaks with a brief description of the vibrational modes is shown in Table 4.4 below.

Table 4.4 Summary of all calculated contributing transitions for the $AuRu_3$ cluster and their assignment to the predicted spectral peak, as well as the experimentally obtained far IR spectrum, and a brief description of the assigned transition modes

#	Peak (cm^{-1})	Contributing vibrations (cm^{-1})	IR intensity (km/mol)	%Au motion	%Ru motion	Assigned (cm^{-1})	Mode description
1	50	51.8	0.1	1.8	3.7		P-Ph motion
		56.4	0.3	0.6	5.8		(OC)-Ru-(CO) bending
		63.3	0.1	2.1	3.8		P-Ph motion
2	75	75.0	0.4	4.3	8.9		Ru_3-Au distortion
		76.5	0.1	2.1	7.7		(OC)-Ru-(CO) bending
3	92	86.4	0.3	8.4	7.2		Ru_2-Au distortion
		87.7	0.1	2.8	5.0		C-Ru-C bending
		89.1	0.2	4.8	6.8		C-Ru-C bending
		92.2	0.7	1.2	14.9		Ru-Cl-Ru streching
		95.1	0.3	2.1	15.0		Ru_3 distortion
4	116	115.3	0.8	3.2	17.5		Ru3-Cl distortion
		120.5	0.1	2.4	7.0		(OC)-Ru-(CO) bending
		123.6	0.3	6.7	24.8		Ru_3-Au distortion
5	136	135.8	2.2	3.2	13.2		Ru_3-Au distortion
6	149	148.5	1.1	4.9	14.4		Cl motion
		149.5	0.4	3.3	22.1		Ru_3-Au distortion
7	165	165.2*	5.0	8.6	15.3	177	Cl-Ru_3-Au distortion
		176.4	0.2	3.1	26.7		Ru_3-symmetrical distortion
8	197	189.2	0.5	2.1	1.4		P-C-C bending
		197.4	1.7	1.1	0		Ph group rocking
9	214	213.7	1.4	1.1	0		Ph group rocking
10	245	243.4	0.2	0.8	23.3	254 and 261	Ru_2-Cl asymmetric motion
		245.4	2.1	0	0		P-Ph_3 bending
		254.8	0.5	0	0		P-Ph_3 bending
11	285	273.0	0.4	0	0	299	P-Ph3 bending
		284.8*	8.6	0	21.4		Ru2-Cl stretching

12	374	371.6	0.2	0	0.8		Ru-C-O bending
		373.9	6.3	0	3.8		C-Ru-C bending
		374.8	2.7	0	4.2		Ru-C-O bending
13	385	385.4	6.0	0	4.8		Ru-C-O bending
		386.0	1.3	0	3.2		Ru-C-O bending
		399.8	0.2	0	11.5		Ru-C-O stretching
14	419	404.8	0.7	0	2.1		Ph group out-of-plane distortion
		408.4	0.1	0	0		Ph group out-of-plane distortion
		415.2	5.6	0	10.4		C-Ru-C asymmetric stretching
		417.4	6.2	0	9.2		C-Ru-C asymmetric stretching
		420.2	8.2	0	10.8		Ru-C-O bending
15	437	425.0	3.5	0	5.4	425	C-Ru-C bending
		428.5	1.8	0	7.5		Ru-C-O bending
		432.0	2.8	0.8	2.0		Ph group out-of-plane distortion
		435.4	3.3	0.7	2.9		Ph group out-of-plane distortion
		436.1	25.7	0	11.9		Ru-(CO) stretching
		439.0	4.2	0.7	5.0		Ru-C_3 bending
		439.8	11.8	0.7	5.9		Ru-C_3 bending
		443.4	6.3	0	10.1		Ru-(CO) stretching
		446.4	12.0	0	8.5		C-Ru-C bending
		450.5	8.3	0	9.1		Ru-(CO) stretching
		452.5	5.4	0	0.9		P-Ph_3 distortion
16	462	461.8	24.3	0	10.8		Ru-C_3 bending
		468.0	15.0	0	12.1		Ru-C_3 bending
17	492	489.3	1.5	0	4.7		Ru-C_4 bending
		491.9	14.5	0	6.4		Ru-C_2 bending
18	511	503.2	29.4	0	0.8		Ph group out-of-plane

							distortion
		510.1	50.6	0	11.5		C-Ru-C bending
		515.3	34.8	0	3.5		P-Ph_3 distortion
		517.7	1.8	0	10.8		Ru-C_4 bending
19	530	523.3	3.7	0	15.2	526	Ru-C_3 bending
		529.2	84.5	1.0	0.8		Ph group out-of-plane distortion
		532.8	57.7	0	13.0		C-Ru-C bending
20	549	548.9	87.5	0	11.0	545	C-Ru-C_2 bending
21	563	561.3	207.9	0	13.7	562 and 570	C-Ru-C bending
		564.4	193.0	0	13.8		C-Ru-C bending
22	574	575.0	37.5	0	12.4		Ru-C_3 bending
		576.0	32.2	0	11.9		Ru-C_3 bending
23	626	625.0	0.3	0	0		Ph group in-plane distortion
		626.4	1.7	0	0		Ph group in-plane distortion

4.3 Conclusion

High quality far-IR spectra of gold, ruthenium and gold-ruthenium clusters were obtained using the far-IR beamline at the Australian Synchrotron. Within the experimental spectra, the metal core vibrations are observed to appear at low frequency with low intensity matching well calculated peaks in the simulated spectra. For the Au_9 cluster, three significant gold core vibrations are observed at 157, 177 and 197 cm^{-1} in the experimental spectrum. In case of Ru_3 cluster, only a single metal core vibration is identified within the spectrum, at 150 cm^{-1}. The calculated force constant for this transition is k = 0.33 mdyne/Å. The Ru_4 cluster exhibits two metal core vibrations at 153 and 170 cm^{-1} with force constants of 0.35 and 0.53 mdyne/Å, respectively. Substitution with a gold atom yielding a mixed metal $AuRu_3$ cluster shifts the core transitions toward higher wavenumbers at 177 and 299 cm^{-1} with an increase in force constants to 0.37 and 1.65 mdyne/Å, respectively. This shift was attributed to the change in chemical composition and geometry of the metal cluster core. In summary, combining the DFT calculations and high quality synchrotron-based experimental measurements allow the assignment of the key transitions in these clusters *for the first time*.

Chapter 5

Spectroscopy and Microscopy Studies of Supported Phosphine-capped Au Clusters

This chapter discusses about the microscopic and spectroscopic characterization of Au-based catalysts derived from Au clusters on metal oxides. The author specific role in this project is to synthesize the gold clusters (Au_8, Au_9 and Au_{101}) and deposited them onto metal oxide supports (TiO_2, SiO_2, ZnO and ZrO_2). Then different calcination treatments were performed on the gold catalysts. Finally, the author also performed TEM imaging of the gold catalysts together with statistical analysis and recorded the UV-vis DR spectra. The XP spectra and XAS were recorded by David Anderson, Baira Donoeva, Daniil Ovoshchnikov (Golovko group) and Hasan Al Qahtani (group of Prof. Gunther Andersson from Flinders University). The XP spectra were fitted by Dr. Gunther Andersson (Flinders University) and XAS spectra were fitted by Jason Alvino and Trystan Bennet with the help of Hugh H. Harris from the University of Adelaide. Part of this work has been published in the journal *Physical Chemistry Chemical Physics, 2013, 15(35): 14806-14813*.

Abstract

Series of heterogeneous catalysts were fabricated using sol-immobilisation method by depositing phosphine-stabilised gold clusters Au_8, Au_9 and Au_{101} synthesized *via* wet-chemistry onto TiO_2 (anatase) and SiO_2 (fumed)support. Only the TiO_2-supported heterogeneous catalysts were studied using synchrotron X-ray photoelectron spectroscopy (XPS) due to charging, while all materials were characterised using transmission electron microscopy (TEM), UV-Vis diffuse reflectance spectroscopy (UV-Vis DRS) and atomic absorption spectroscopy (AAS). It was found that the gold clusters did not retain their original size and agglomerated to form larger gold nanoparticles after calcination at 200 °C for 2 hours under different atmospheres: under O_2 (referred to as calcined-O_2) and under O_2 followed by H_2 (referred to as calcined-O_2-H_2). The increase in the gold nanoparticle size for TiO_2-based samples is consistent with the increase in wavelength of the peak maximum position of localized surface plasmon resonance (LSPR) band in the UV-vis DR spectra. TEM images further confirm the aggregation of the gold nanoparticles after calcination. In addition, XAS spectra for supported Au_9 cluster on TiO_2 also revealed that agglomerated Au clusters resemble bulk gold metal.

5.1 Introduction

Heterogeneous catalysis plays a crucial role in chemical industry including agricultural chemistry, pharmaceuticals and the polymer industry. Numerous chemical reactions, such as the Haber-Bosch process for the synthesis of ammonia,[232] oxidation of carbon monoxide in automobile exhaust converters,[233, 234] polymerization of olefins[235, 236] and the Ostwald process for the synthesis of nitric acid,[237] are assisted by heterogeneous catalysts. Industrial catalysts are typically made using cheap large-scale methods, such as co-precipitation and impregnation, which often lack control over the key active sites. Typical approaches towards highly controlled fabrication of model heterogeneous catalysts mainly involve two distinct routes. The first route involves deposition of size-selected metal clusters, obtained by the evaporation of the metal source into the gaseous phase under ultra-high vacuum (UHV) conditions, on the flat substrate. The second one involves the chemical synthesis of metal clusters or nanoparticles followed by their deposition onto support. The latter route offers the advantages of scaling-up production, simplicity of the technique and wider range of support materials (including powders and porous materials). A major challenge in the fabrication of heterogeneous catalysts is the difficulty to achieve good control over the metal nanoparticle size, composition and uniform distribution of nanoparticles on the support without significant aggregation.

Established methods have been used to deposit the metal nanoparticles with a good control of metal nanoparticle size and composition, and homogeneous distribution of metal nanoparticles on the support.[238-240] The simplest method is the impregnation of metal salt precursor or organometallic compound on the support followed by reduction of the metal salt leading to formation of metal nanoparticles on the support.[127, 241] However, this method only works to give a good control of metal nanoparticle size and composition on some metal oxide supports.[129] The size of metal nanoparticles formed and their distribution on the support are highly dependent on the conditions: a) pH and concentration of the metal precursor; b) isoelectronic point of the metal oxide; and c) calcination temperature and other conditions (temperature programme and atmosphere).[127, 242] Other methods which rely on using templates such as emulsions,[71] polymers,[243] dendrimers,[117, 244] polyoxometalates,[245, 246] or metal-organic frameworks (MOFs)[247, 248] containing metal nanoparticles have improved the control over metal nanoparticle size and distribution on the support.

With the improvement in chemical synthesis of highly monodisperse metal nanoparticles in the last ten years, a simple and facile method of depositing pre-synthesized metal clusters or nanoparticles on various metal oxides that is applicable to both acidic and basic oxides has been developed by Zheng and Stucky.[242] In this method, the relatively weak interactions (due to the van der Waals forces) between

metal nanoparticles and the support in aprotic solvent are utilised to establish homogeneous deposition of metal nanoparticles on the metal oxide support. The support-immobilized metal nanoparticles are then easily recovered by centrifugation. This method also allows fabrication of catalysts with high metal loading which is technically difficult to achieve using conventional deposition-precipitation and co-precipitation methods. Furthermore, this method is not limited to depositing Au nanoparticles only, but is also applicable to other pre-synthesised nanoparticles including Pd, Ag and Pt nanoparticles. A similar method is also established later, except the recovery of supported-metal catalysts is achieved by evaporating the solvent either under reduced pressure or nitrogen flow.[48]

Another problem that typically occurs in catalyst fabrication is the aggregation of metal nanoparticles during calcination which is often performed to remove the organic ligands that protect the metal core. Aggregation of metal nanoparticles results in formation of larger particles – process driven by minimization of the surface energy. This phenomenon has been observed even at room temperature while the capping ligands are still present on the surface of metal nanoparticles.[249] There are two possible mechanisms of aggregation, which differ by details of the specific processes under different conditions. Surface diffusion is believed to dominate the sintering mechanism below the melting point of metal nanoparticles.[249] When the heating is involved, the capping ligands dislodge from the metal surface exposing the metal core and simultaneously allowing the nanoparticles to form aggregates in order to stabilise the surface of nanoparticles. Hence, a careful heat treatment is needed to remove the organic ligands and not to cause huge aggregation. Au forms bonds with organic ligands with their strength decreasing in the following order: S > N > P > O. Thiol ligands (sulphur containing molecules) have been widely exploited in preparing atomically precise gold clusters (Au_{25}, Au_{38}, Au_{102}) and highly monodisperse gold colloids.[68] However, due to the strong bonding between thiol and gold, difficulty in removing the thiol ligands under mild conditions (temperature *etc*.) could be a problem. In addition, it has been known previously that sulphur could poison catalysts inhibiting their activity.[250] Hence, the use Au nanoparticles stabilized by weaker bonding capping ligands containing benign, non-poisoning donor atoms could be plausible solution to this problem, as miler conditions feasible in this case could help to minimize aggregation.

Phosphine-capped Au nanoparticles offer the advantage of facile removal of the phosphine ligands using mild heat treatment.[154] These are atomically-precise gold clusters with a specific number of gold atoms, phosphine ligands and anionic counter ions. The exact structures of many of the gold-phosphine clusters have been established using the single X-ray crystallography technique.

Au nanoparticles show remarkable catalytic activity once their size is reduced to less than 5 nm.[135, 251] The catalytic activity of such small gold nanoparticles has been observed in various chemical reactions such as CO oxidation at low temperature (< 0 °C),[16] benzyl alcohol oxidation, glycerol oxidation,[252] hydrogenation of citral,[253] and hydrogenation of nitrobenzene.[254] Interestingly, the catalytic activity of such small gold nanoparticles increases dramatically once the gold size is reduced below 2 nm. The turn-over frequency increases as the gold particle size decreases as measured in benzyl alcohol oxidation[164] and cyclohexane oxidation.[203] The use of phosphine-capped Au clusters or nanoparticles in heterogeneous catalysis will allow the study of structure-property or composition-property relationships in heterogeneous catalysis. Since catalytic activity of Au catalysts is associated with their electronic structure, the study of electronic properties of supported phosphine-capped gold clusters using X-ray photoelectron spectroscopy is significant.

XPS is a very fundamental tool used for studying electronic properties of gold clusters. The information provided by XPS spectra includes binding energy of the core electrons, oxidation state of gold and the chemical environment between Au nanoparticles and the support. The useful signal for analysing the electronic structure of gold comes from the Au $4f_{7/2}$ and $4f_{5/2}$ orbitals, which provides sensitive measurement for the electronic structure of Au. The position of the Au $4f_{7/2}$, peak and its full-width half maximum (FWHM) are influenced by a few contributing factors. Firstly, the oxidation state plays a primary role in the peak position. The standard value for binding energy of the Au $4f_{7/2}$ electrons in the case of the bulk gold (Au^0) particles supported on TiO_2 appears at 83.8 eV according to the literature; while the separation between the Au $4f_{7/2}$ and $4f_{5/2}$ peaks is constant at 3.67 eV due to the quantum mechanical nature of spin-orbit coupling.[154, 255] A complete oxidation of bulk gold to form Au_2O_3 shifts the Au $4f_{7/2}$ peak to 85.8-86.2 eV, depending upon the substrate and the thickness of gold oxide layer.[256, 257] Secondly, initial and final states also affect the peak position and the FWHM, which depend on the cluster size and its interaction with the substrate.[185, 258] Initial states are influenced by the change in the electronic structure resulting from the reduction in the size of clusters and the interaction between clusters and the substrate.[259] After excitation of electrons in a cluster by X-ray photons, the cluster can remain in a charged state for a certain period of time, which depends on the cluster size and the type of substrate; this is referred as the final state effect.[260] In many cases, interpreting the change in peak positions in terms of initial and final state effects from experimental data is difficult for Au because the Auger lines are weak.[261] Nonetheless, many authors relate the influence of cluster size on the peak positions and FWHM through the final state effect.[186, 262-264] In addition, the XPS technique also reveals the chemical state of the phosphine ligands that stabilise the Au clusters and their environment, which

might affect the catalytic activity of the Au clusters. Further detailed discussion with specific examples using phosphine-stabilized Au clusters on TiO_2 are presented in the Results and Discussion section.

While XPS is very valuable in studying the electronic structure of Au clusters, an additional tool such as UV-vis DRS also provides the relevant information about the electronic state of Au clusters that corresponds to their size. It is known that colloidal Au nanoparticles exhibit a brilliant red colour due to the interaction of incident light with collective oscillation of free electrons on the gold surface known as localised surface plasmon resonance (LSPR). Au nanoparticles around 10 nm in size absorb green light and thus appear red.[61, 265] Indeed, Au nanoparticles were used in stained glass windows in cathedrals during the middle ages.[266] Interestingly, the LSPR peak maximum of Au nanoparticles is very sensitive to their size, morphology, and the dielectric constant of the surrounding medium.[122] This characteristic allows the use of UV-visible spectroscopy to probe the changes of Au nanoparticle size. In general, it is found that the LPSR peak maximum shifts towards longer wavelengths as the Au nanoparticles' size increases, although in some cases this general trend breaks down due to dielectric constant of the surrounding medium.[267, 268]

Imaging the Au nanoparticle size would be another pivotal tool to study the actual size of the gold clusters and establish a link with XPS analysis and UV-vis DRS spectra about aggregation of the supported gold clusters. Transmission electron microscopy (TEM) is a common tool used to study the size, polydispersity and dispersion of Au nanoparticles on the support. As opposed to light microscope, TEM uses accelerated electrons to produce smaller electron wavelength and thus allowing imaging as small clusters as 0.7-1 nm (under ideal conditions). However, the typical lower limit of producing a sharp image can be attributed to another factor - need for good contrast between the cluster and the support. Ultra-small Au clusters weakly scatter and diffract the electron beam due to small number of atoms (albeit with high Z) while material of support, even in the case of oxide (silica, titania etc.) nanoparticles could deflect comparable proportion of the incident beam (due to thickness of support being 10s of nm).[165] When this happens, good contrast needed to produce sharp images of small clusters immobilized on support cannot be achieved. Therefore, multiple, complementary techniques are needed to link together all these separate parts of information and build a big and comprehensive picture about the nature of the supported Au clusters.

It is found that a systematic study of different size of phosphine-capped Au clusters is missing in the literature. Only a very few earlier related reports on the XPS analysis of clusters can be found in the literature. For example, Attekum *et al*. reported an XPS study of Au_8, Au_9 and Au_{11} stabilized by triarylphosphine ligands on graphite substrate with different anionic counter ions.[269] However, the binding

energy (BE) of the Au $4f_{7/2}$ electron was not correlated to the size effect, instead they attributed the variations in BE to be due the different nature of the Au atoms (periphery *vs*. central) within the clusters. Battistoni *et al*. performed an XPS study on Au_1, Au_8, Au_9 and Au_{11} clusters stabilized by triphenylphosphine ligands and correlated the BE of Au $4f_{7/2}$ electrons with different geometries and coordination environments in Au clusters.[270] Chusuei *et al*. deposited $Au_6(PPh_3)_6[BF_4]_2$ (referred to as Au_6) onto a planar $TiO_2(110)$ support and removed triphenylphosphine ligands *via* electron-stimulated desorption.[264] They observed a shift by +0.4 eV for the Au $4f_{7/2}$ in which the authors have attributed to the reduction in size of the Au_6 cluster after ligand removal.

Motivated to carry out a systematic study on a series of supported Au clusters and the effect of different heat treatments on the size of the clusters, a series of triphenylphosphine-capped Au clusters, $Au_8(PPh_3)_8(NO_3)_2$, $Au_9(PPh_3)_8(NO_3)_3$ and $Au_{101}(PPh_3)_{21}Cl_5$, were deposited and activated these on the surface of TiO_2 (anatase) powder to make materials which later will be tested as prospective heterogeneous catalysts (Chapter 5). Here, we aim to study the electronic properties of these TiO_2-supported gold clusters using synchrotron X-ray photoelectron spectroscopy (S-XPS) and UV-visible diffuse reflectance spectroscopy (UV-vis DRS). Transmission electron microscopy (TEM) was used to image the Au particle sizes and assess dispersion on the support.

Initially, the commercially supplied fumed SiO_2 and TiO_2 nanopowders, both anatase and rutile phase were chosen as supports. Nanopowder is chosen because it has high surface are-to-volume ratio suitable for catalytic applications. The choice of TiO_2 as support was due the fact that TiO_2 is a reducible metal oxide and forms strong metal-support interaction with Au nanoparticles.[271] TiO_2 exists in three phases; namely anatase, rutile and less commonly known brookite.[272] Anatase has a band gap of 3.20 eV whereas rutile has a band gap of 3.03 eV. Reducible metal oxide is defined such that it can easily lower its oxidation state of metal species within lattice (for example Ti^{4+} to Ti^{3+}) accepting electronic charge transfer from the donor species and stabilizing the excess charge at localised d or f orbitals of the metal cations.[273] Fumed SiO_2 is a non-reducible (inert) mesoporous oxide with larger surface area (~ 200 m^2/g cf. only 50 m^2/g for TiO_2). However, during XPS studies at the Australian Synchrotron, it was found that as supplied rutile support was already contaminated with zinc rendering rutile-based series useless. The SiO_2-supported catalysts were strongly charging during the XPS measurement resulting in the distortion and unacceptably large shifts of the obtained signals even after calibration with C 1s peak which were not useful in providing accurate data for XPS analysis. The author attempted to record the XP spectra using both the Synchrotron XPS and lab-based XPS systems with the help from other collaborators. Here, the details of the XPS and UV-vis DRS spectroscopy and TEM studies of phosphine-capped Au clusters on TiO_2 (anatase) and TEM images and UV-vis DR spectra of Au_{101} clusters supported onto SiO_2, ZrO_2 and

ZnO supports are provided. The gold loading was determined using atomic absorption spectroscopy (AAS). Toward the end of this chapter, I provide the XAS spectrum of Au_9 cluster only and its analysis. Here, for convenience, a particle whose size below 2 nm and nanoparticles whose size is above 2 nm are referred to as cluster and nanoparticles, respectively; following Haruta's definition albeit this convention is not generally agreed by some authors.[47]

5.2 Results and Discussion

5.2.1 General

The Au_8 and Au_9 clusters are atomically-precise, monodisperse clusters protected by triphenylphosphine ligands.[107] The Au_{101} cluster is not molecular in structure but is highly monodisperse with a mean particle size of 1.6 nm.[108] The 0.17 weight % Au was chosen as to minimise the aggregation of gold clusters, yet still able to produce signals for in XPS spectra using synchrotron XPS. Au 4f, P 2p, Si 2p, Ti 2p, C 1s and O 1s regions were used to record XPS spectra for all supported gold clusters and gold reference sample. The dominant carbon signals arise from either triphenylphosphine ligands or adventitious hydrocarbons. Calibration of the peak positions of other elements was performed done by fixing C 1s peak to be at 285 eV because the adventitious hydrocarbons displayed a very constant C 1s peak position that is present in all samples exposed to air. The titanium signal was measured to be at 459.1 ± 0.1 eV and arise solely from the TiO_2 support in the sample. The silicon wafer used as a substrate produced two weak silicon signals: one corresponded to Si measured at 98.9 ± 0.2 eV and the other corresponded to SiO_2 measured at 102.6 ± 0.3 eV. Care was taken to minimize these during data acquisition by selecting the best spot with minimal charging and minimal Si signals. The oxygen signals were detected mostly due to TiO_2 (530 ± 0.4 eV) and SiO_2 (531.9 ± 0.3 eV). The gold and phosphorous signals from the gold clusters were measured to be in the region 83.6 – 85.6 eV and 131.9 – 133.4 eV, respectively. The standard $4f_{7/2}$ Au peak of bulk gold (reference gold bar permanently located in the XPS system) was detected to be 84.0 eV validating the energy calibration described above. The shift in $4f_{7/2}$ peak from supported gold clusters was determined using the standard Au $4f_{7/2}$ peak of bulk gold as reference. The intensity of a peak is calculated by measuring the peak area of the simulated spectrum. Due to the ultra-small size (less than 2 nm) of Au_8, Au_9, and Au_{101} clusters they did not exhibit LPSR peak in UV-vis DR spectra because of the absence of the conduction electrons which are responsible for coupling with incident light needed to produce collective plasmon modes.[60] Hence, these clusters behaved more as non-metallic species (depending on the band gap, these could be classified either as semiconductors or insulators) as opposed to metallic nanoparticles with sizes greater than 2 nm.[274]

5.2.2 Untreated catalysts

Au 4f spectra of untreated catalysts for Au_8, Au_9 and Au_{101} clusters show two doublets consisting of $4f_{7/2}$ and $4f_{5/2}$ peaks (Figure 5.1-5.3). The spectra for Au_8 and Au_9 clusters require fitting with two peaks for each of the Au $4f_{7/2}$ and Au $4f_{5/2}$ components. With regard to the $4f_{7/2}$ peak, the position at lower binding energy (referred here as Au-LBP) at is at 83.7 ± 0.1 eV and the position at higher binding energy (referred here as Au-HBP) is at 85.3 ± 0.2 eV (Table 5.1). The FWHM for Au-LBP is 1.0 to 1.1 ± 0.1 eV and FWHM for Au-HBP is 1.5 to 1.9 ± 0.2 eV. Based on the previous XPS study by Anderson *et al*. on different size of Au clusters, they assigned the Au-LBP peak to the agglomerated clusters and the Au-HBP peak was assigned to non-agglomerated clusters.[154] The shift of Au peak position toward higher energy and the increase in FWHM peak width corresponding to the decrease in the cluster size were previously reported for reduced size of Au clusters.[186, 257, 258] The position and FWHM peak are influenced by the initial and final state effect as reported explicitly by Borman *et al*.[185] Briefly, the initial state refers to the oxidation state or charge of the atom from which the electron is emitted while the final state effect reflects the relaxation or de-excitation process of the charged atom when excited by X-ray photon. An atom in a cluster cannot relax the same way as the atom in bulk material due to reduced screening effect of the hole by electrons. Hence, the relaxation energy and life-time are different in both cases. As a result a finite number of atoms and structure in a cluster, the final state effect generally most prevalent for small clusters. When a core electron is emitted by an atom due to excitation by an X-ray photon, a hole is generated and creates a net positive charge on the cluster.[275] The Coulomb interaction between the hole and emitted electron (photoelectron) reduces the kinetic energy of the photoelectron and thus results in the peak positions appearing at a higher binding energy.[262] This effect is enhanced with the decreasing Au cluster size because of a smaller amount of residual electrons to cancel the electric field of the hole.[186] As a result, the smaller the size of Au clusters, the higher the shift in the binding energy. In the cases of Au_8 and Au_9, both Au-LBP and Au-HBP are present in the Au 4f spectra while the Au-HBP is negligible in Au_{101} spectra. Using this information, it can be deduced that untreated supported Au_8 and Au_9 clusters still retain some fraction of clusters with their pristine cluster size and the remainder of clusters agglomerate.[153] The peak position of Au $4f_{7/2}$ of the Au_{101} cluster is found to be close to the value of binding energy (83.7-84 eV) corresponding to the bulk Au suggesting that the Au_{101} cluster already resembles bulk gold.[134]

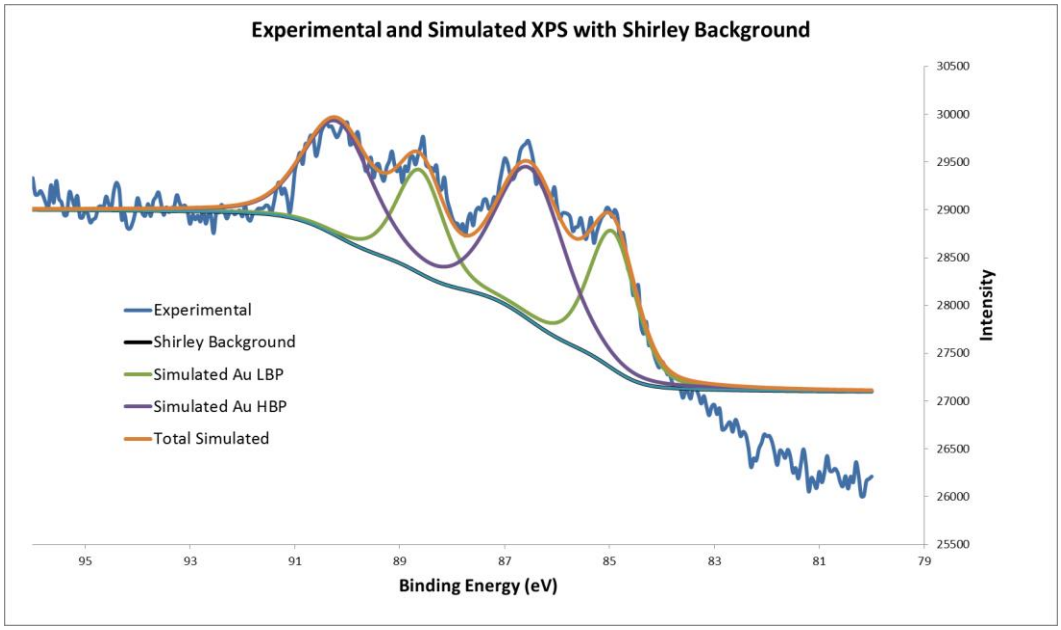

Figure 5.1 Au 4f XP spectrum of 0.17 wt% Au_8/TiO_2 untreated. Courtesy of Professor Gunther Andersson.

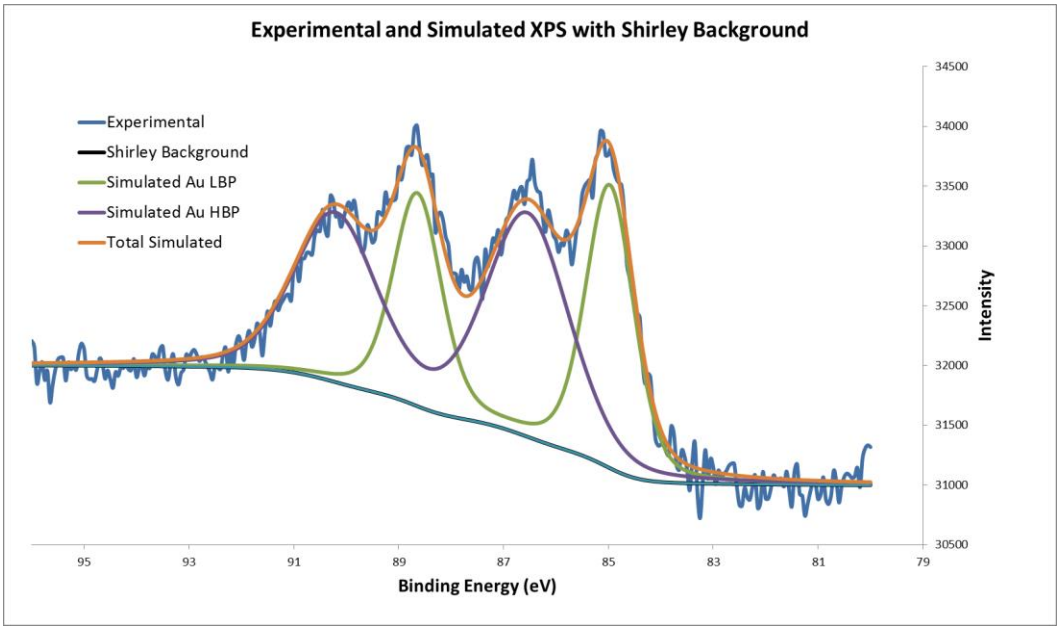

Figure 5.2 Au 4f XP spectrum of 0.17 wt% Au_9/TiO_2 untreated. Courtesy of Professor Gunther Andersson.

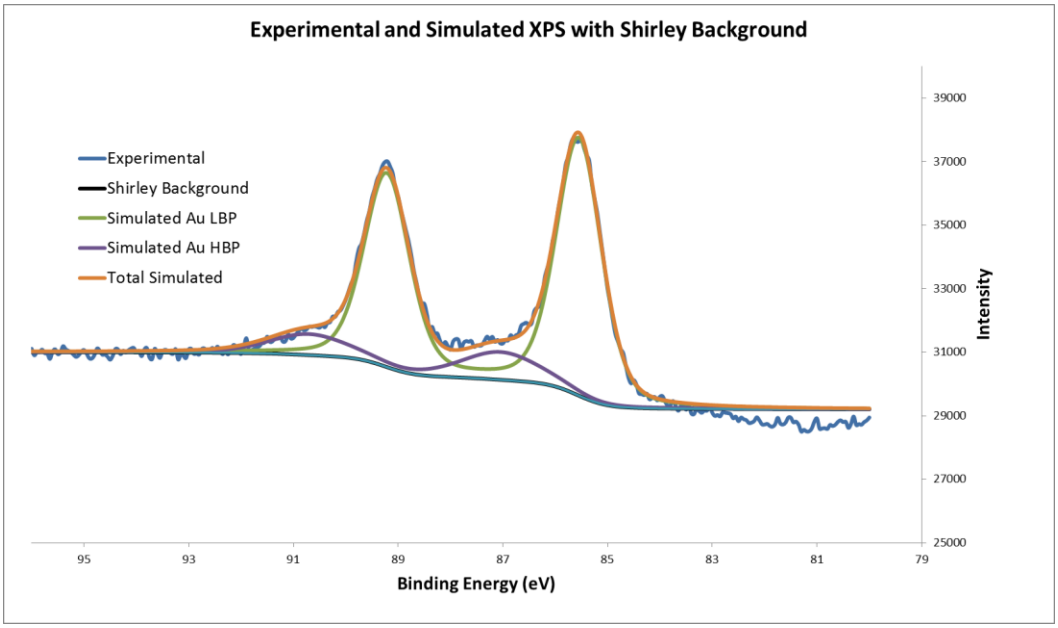

Figure 5.3 Au 4f XP spectrum of 0.17 wt% Au_{101}/TiO_2 untreated. Courtesy of Professor Gunther Andersson.

It is also worth mentioning that the peak area of Au-HBP and Au-LBP are almost the same for Au_8 and Au_9 clusters, suggesting that almost equal proportions of unaggregated clusters and aggregated ones (Table 5.1). The intensity ratio of Au-HBP/Au-LBP for the Au_8 and Au_9 cluster are 1.3 and 1.6 respectively. This finding is in contrast with the earlier study by Anderson *et al*. for Au clusters supported on pre-treated acid washed P25 TiO_2.[154] The authors showed that majority of signal for untreated Au_8 and Au_9 cluster was found as Au-HBP, suggesting that acid washed TiO_2 minimized the aggregation.

Table 5.1 Position and FWHM of the Au $4f_{7/2}$ peaks for untreated catalysts.

Catalyst	Peak	Energy (eV)	FWHM (eV)	Intensity ratio HBP/LBP
0.17% Au_8/TiO_2	Au-LBP	83.7 ± 0.1	1.1 ± 0.2	1.6 ± 0.3
	Au-HBP	85.3 ± 0.2	1.5 ± 0.2	
0.17% Au_9/TiO_2	Au-LBP	83.7 ± 0.1	1.1 ± 0.2	1.3 ± 0.3
	Au-HBP	85.3 ± 0.2	1.9 ± 0.2	
0.17% Au_{101}/TiO_2	Au-LBP	83.7 ± 0.1	1.1 ± 0.2	0
	Au-HBP	-	-	

The P 2p XP spectra of untreated catalysts for Au_8, Au_9 and Au_{101} clusters showed two peaks (see bottom of the spectra in Figure 5.4-5.6. The lower binding energy peaks (referred here as P-LBP) at 131.9 ± 0.2 eV are assigned to phosphorous ligands bonded to the gold cluster cores and the higher binding energy peaks (referred here P-HBP) at 133.1 ± 0.2 eV are assigned to phosphorous oxide-like species from phosphorous ligands detached from the gold clusters and oxidised by interaction with TiO_2.[154] It is clear from Figure 5.4-5.6 that P-HBP is the dominant peak, suggesting that phosphine ligands detached from gold clusters and established interaction with TiO_2 even after cluster deposition to form phosphorous-oxide like species. Analysis on intensity ratios between Au and P binding energy peak shows that the intensity ratio of total Au/P-LBP and Au-HBP/P-LBP is much higher than that on pristine gold clusters (Table 5.2) for all untreated supported Au clusters, suggesting that most phosphorous ligands detach from the Au core - and form strong bonds with oxygen on the TiO_2 surface to form phosphorous-oxide like species. The smaller intensity ratio of total Au/total P than intensity ratio Au/P of gold clusters can be explained by the aggregation of Au clusters on TiO_2 (Table 5.2). The total signal intensity for larger Au nanoparticles is much smaller than that of the Au clusters because of the limited electron mean free path of the ejected photoelectrons. Hence, the intensity ratio total Au/total P is much smaller than that in the case of pristine gold clusters.

Table 5.2 Intensity ratios of the Au and P peaks for each of the untreated samples.

Sample	Au-HBP/P-LBP	Total Au/P-LBP	Total Au/total P	Au/P in pristine cluster
Au_8/TiO_2-untreated	2.2 ± 0.5	3.6 ± 0.5	0.4 ± 0.1	1:1
Au_9/TiO_2-untreated	5.7 ± 1	8.6 ± 1	0.5 ± 0.1	1.1:1
Au_{101}/TiO_2-untreated	5.2 ± 1	27.3 ± 3	2.5 ± 0.5	5:1

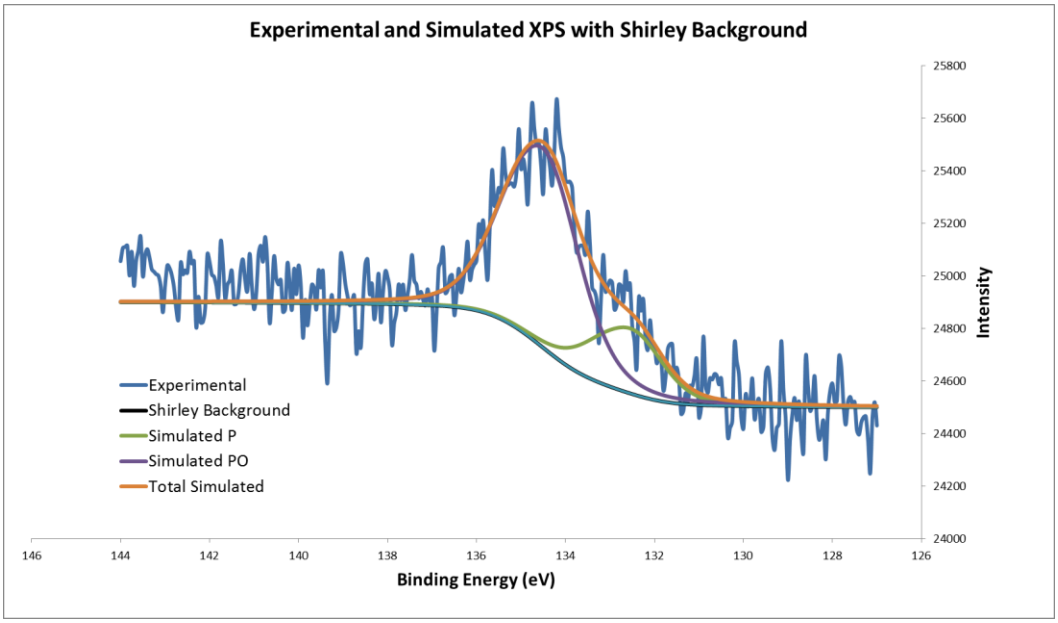

Figure 5.4 P 2p XP spectrum of 0.17 wt% Au_8/TiO_2 untreated. Courtesy of Professor Gunther Andersson.

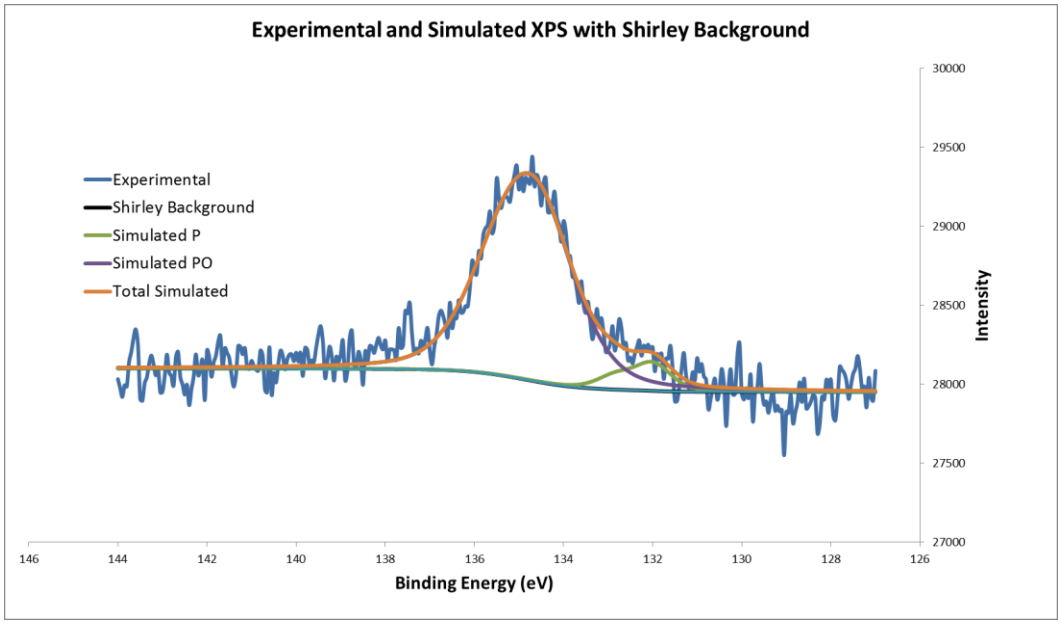

Figure 5.5 P 2p XP spectrum of 0.17 wt% Au_9/TiO_2 untreated. Courtesy of Professor Gunther Andersson.

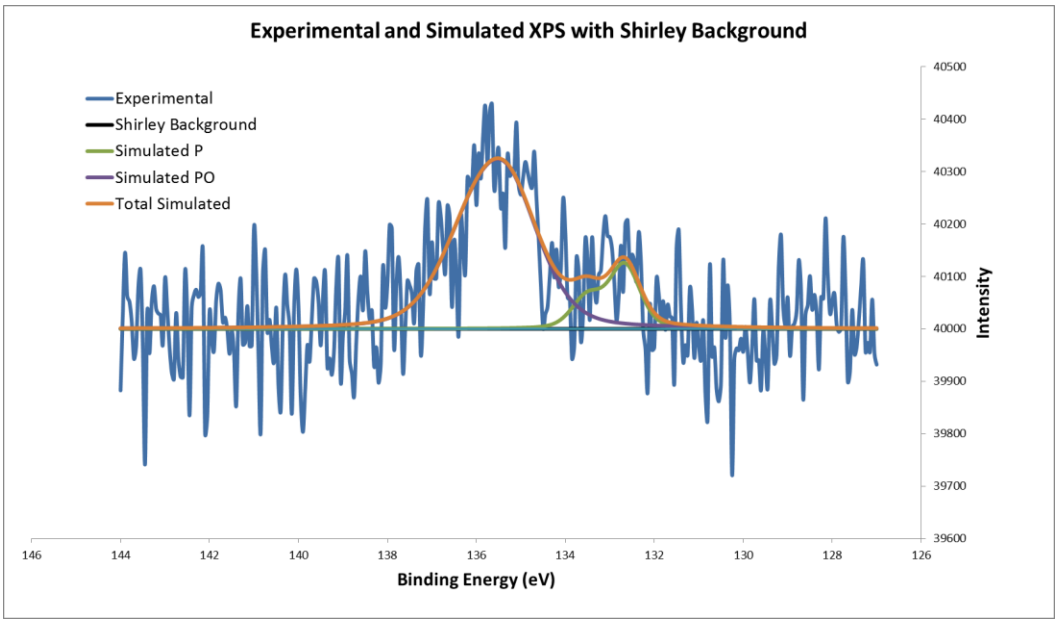

Figure 5.6 P 2p XP spectrum of 0.17 wt% Au_{101}/TiO_2 untreated. Courtesy of Professor Gunther Andersson.

Representative TEM images of untreated Au_8 and Au_9 clusters on TiO_2 are shown in Figures 5.7 and 5.8 below; the arrow indicates the ultra-small gold cluster. Due to the resolution limit of the TEM and poor contrast of these clusters over support material, imaging such small clusters is very challenging. The difficulty arises because the much thicker TiO_2 support scatters electron beams more strongly than the cluster, and thus to develop a good contrast between the support and the cluster in order to obtain a sharp image is very difficult. Despite difficulties in imaging ultra-small particles due to the poor contrast in the case of supported Au_8 and Au_9 clusters on TiO_2, the absence of larger gold particle which are easily visible in TEM is evident. Together with the XPS analysis of untreated Au_8/TiO_2 and Au_9/TiO_2, these TEM imaging attempts permit us to conclude that Au_8 and Au_9 clusters exist as intact clusters and ultra-small (TEM "invisible") nanoparticles after deposition on TiO_2. Due to the very small Au loading (0.17 wt% Au) on TiO_2 and very small number of particles per unit area found in many images, the statistical histograms are not provided for Au_8 and Au_9 clusters. This situation is akin to finding a needle in a haystack. Au_{101} clusters show a minimal aggregation on TiO_2 after deposition (Figure 5.9). The mean Au_{101} size on TiO_2 is 2.0 ± 0.4 nm; only a slight increase from the pristine size of Au_{101} clusters, 1.6 ± 0.4 nm.[108] This size correlates well with the XPS analysis of Au_{101}/TiO_2 showing that Au_{101} is similar to bulk gold.

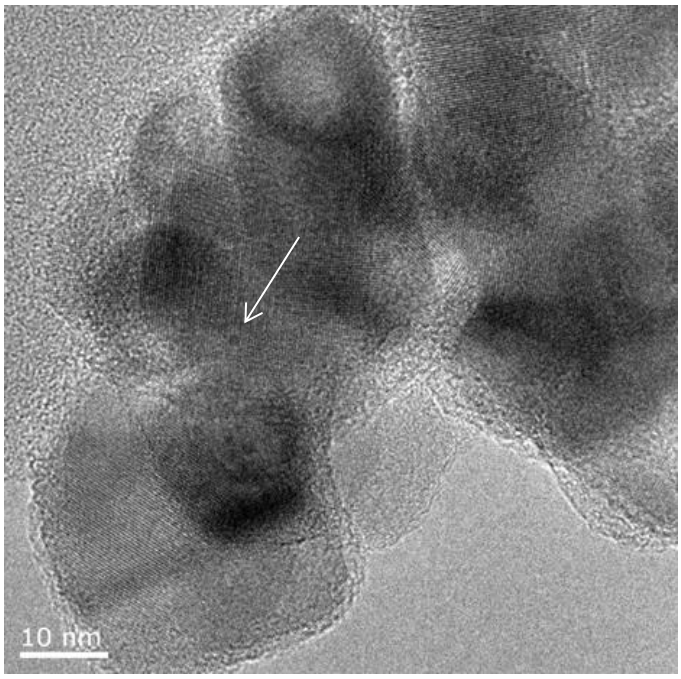

Figure 5.7 A representative TEM image of untreated 0.17 wt% Au_8/TiO_2 catalyst. The arrow shows the gold cluster.

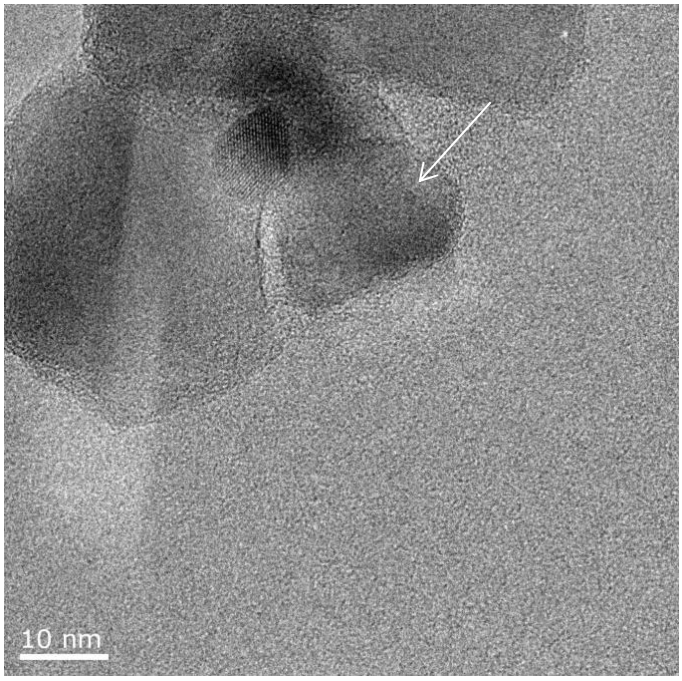

Figure 5.8 A representative TEM image of the untreated 0.17 wt% Au_9/TiO_2 catalyst. The arrow shows the gold cluster.

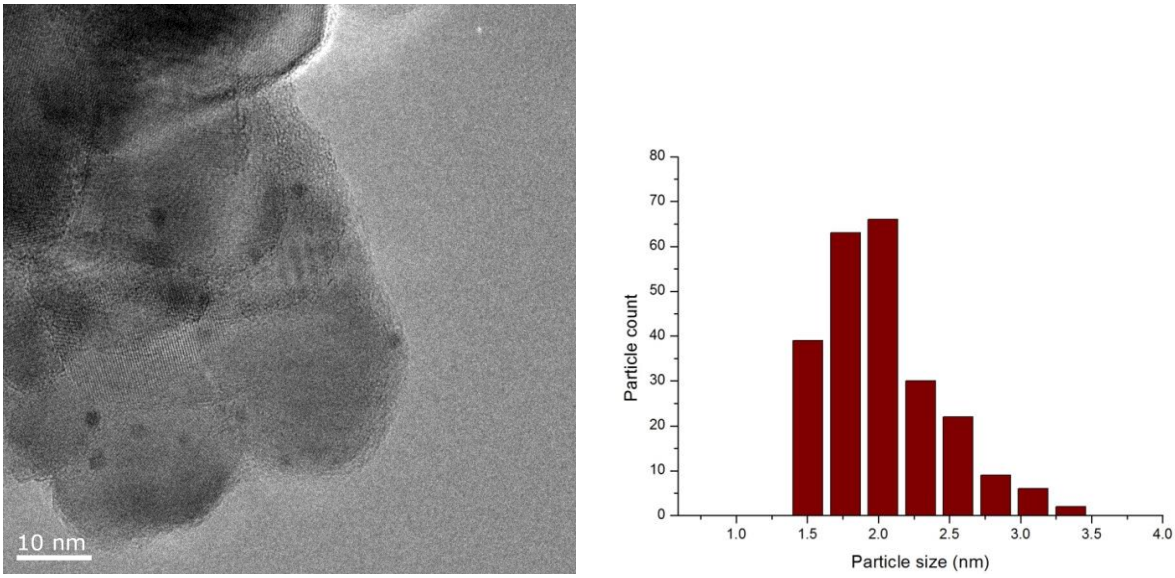

Figure 5.9 A representative TEM image of the untreated 0.17 wt% Au_{101}/TiO_2 catalystd (left) and the corresponding statistical Au particle size distribution histogram (right).

To further verify that the majority of gold clusters in Au_8, Au_9 and Au_{101} untreated samples is below 2 nm as the statistical histogram suggests, UV-vis DR spectra showed the absence of LSPR peak maxima (Figures 5.10-5.126-8, bottom, black patterns). As mentioned in Chapter 2, the absence of LSPR peak suggests that the size of Au clusters is below *ca.* 2 nm. While TEM measures individual particle sizes of gold clusters and aggregates providing statistical distributions and particle size ranges, UV-vis DRS measures spectra which arise due contributions by all of the particles within the irradiated spot, giving a good idea of the bulk average composition as the spot size is huge compared to the amount of material usually studied in TEM. Hence, in this case, the statistical histogram provided by TEM by measurement of individual particle sizes matches well with the UV-vis DR spectra. However, it should be noted that for particles with sizes below 2 nm UV-vis DR spectra cannot be used to assess the actual size of the aggregates of the supported Au clusters (as these will be still below lower LSPR particle size threshold); some aggregation might occur but the majority of aggregates would be still smaller than 2 nm.

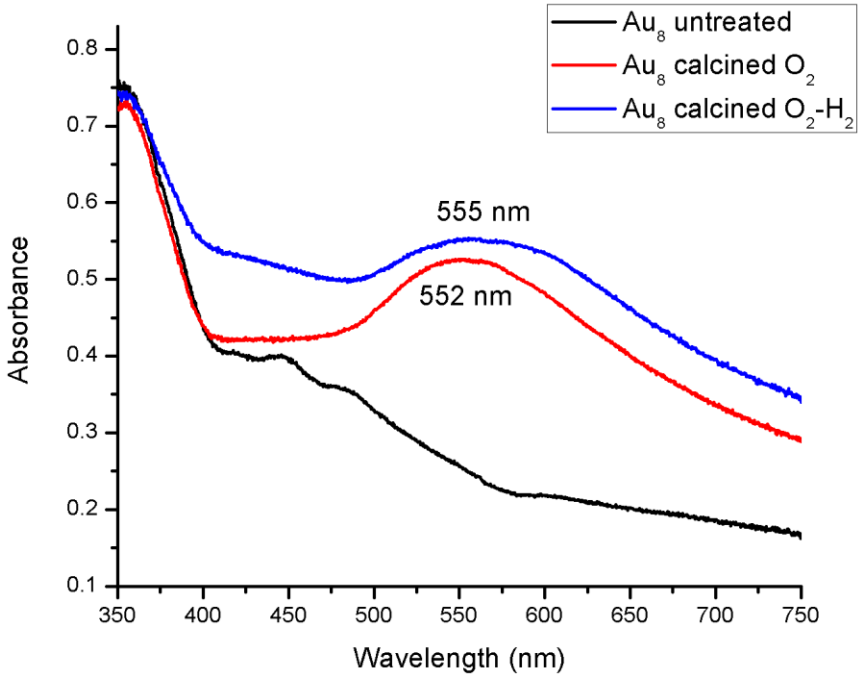

Figure 5.10 UV-vis DR spectra of 0.17 wt% Au_8/TiO_2 catalyst.

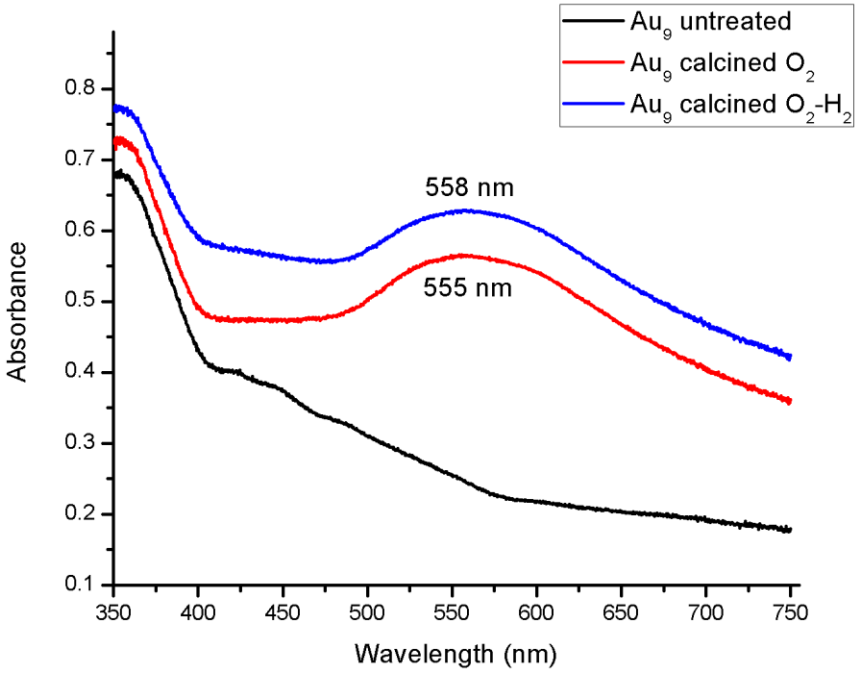

Figure 5.11 UV-vis DR spectra of 0.17 wt% Au_9/TiO_2 catalysts.

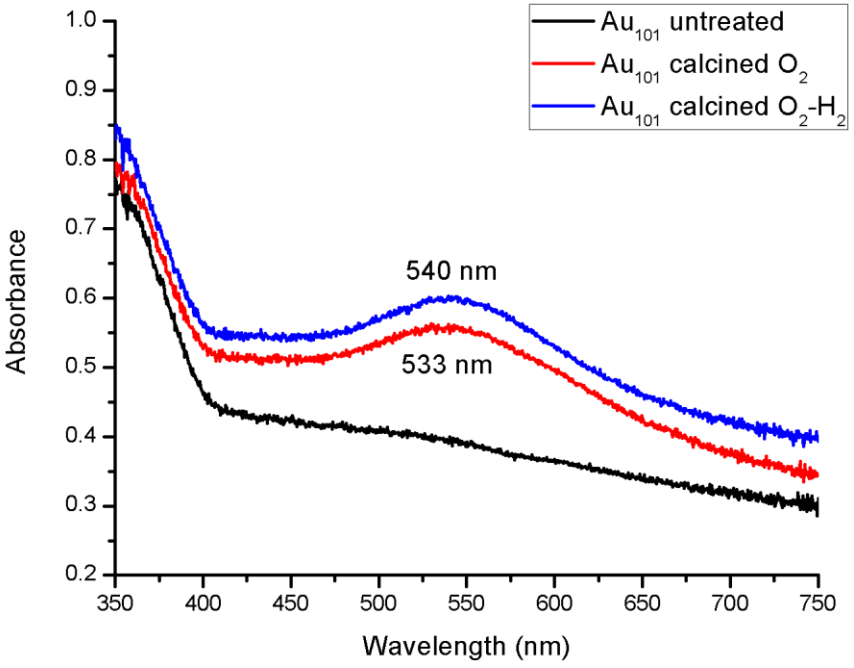

Figure 5.12 UV-vis DR spectra of 0.17 wt% Au_{101}/TiO_2 catalysts.

5.2.3 Catalysts calcined under O_2 atmosphere

Au nanoparticles stabilized by organic ligands must be first treated to remove the organic ligands in order to expose the Au core for easier access of the reagent/substrate in the case of applications in catalysis.[276] The most popular method to remove organic ligands is *via* calcination at mild temperature (200-400 °C) under air flow.[277, 278] The effect of heat treatment might contribute to the change in electronic structure, particle size and geometry of Au catalysts, as well as the catalytic activity.[279] For example, Zanella and Louis investigated the effect of calcining Au catalysts under different gases (air, H_2 and Ar) on the particle size.[280] The authors found that calcination under H_2 minimized the sintering of Au nanoparticles as compared to air and Ar. *Qian et al.* performed calcinations on Au/SiO_2 catalysts under O_2 and He.[279] Despite using different calcination conditions (He *vs.* O_2), they observed a similar catalytic activity for the Au/SiO_2 catalyst. Heat treatment under oxygen rich environment is known to assist the removal of ligands due to their partial or complete oxidation.[281] Moreover, even harsher conditions have been employed to remove organic ligands such as using O_2 plasma or strong oxidizing agents.[184, 282] In the study presented here, mild conditions (at 200 °C for 2 hours) were employed under pure O_2 (99.2%) to remove triphenylphosphine ligands from the Au core clusters. Figure 5.13-5.15 shows the XP Au 4f spectra for Au_8, Au_9 and Au_{101} calcined under O_2. The XP Au 4f spectra for Au_8 show two peaks for the Au $4f_{7/2}$ component corresponding to the Au-HBP and Au-LBP whereas XP spectra for Au_9 and Au_{101} show only one peak at the Au-LBP position. The position the Au-LBP is found at 83.7 eV and that of the Au-HBP is at 85.4 eV for the Au_8 cluster (Table 5.3). The peak areas of Au-LBP and Au-HBP are almost the same for Au_8 whereas the signal intensity for Au_9 and Au_{101} is almost solely at the Au-LBP position.

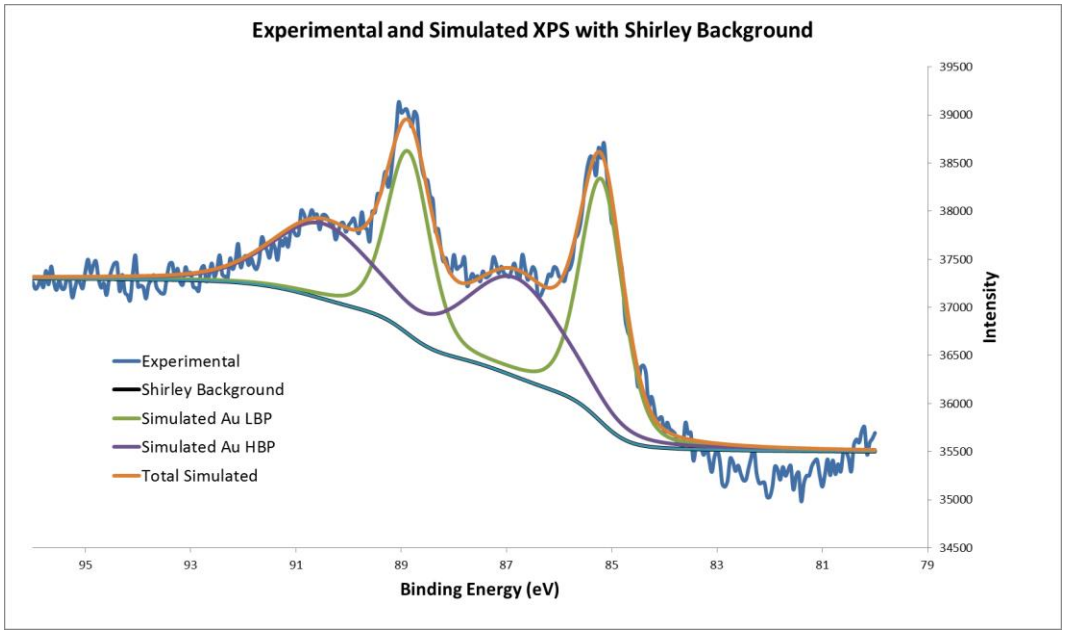

Figure 5.13 Au 4f XP spectrum of 0.17 wt% Au_8/TiO_2 calcined under O_2. Courtesy of Professor Gunther Andersson.

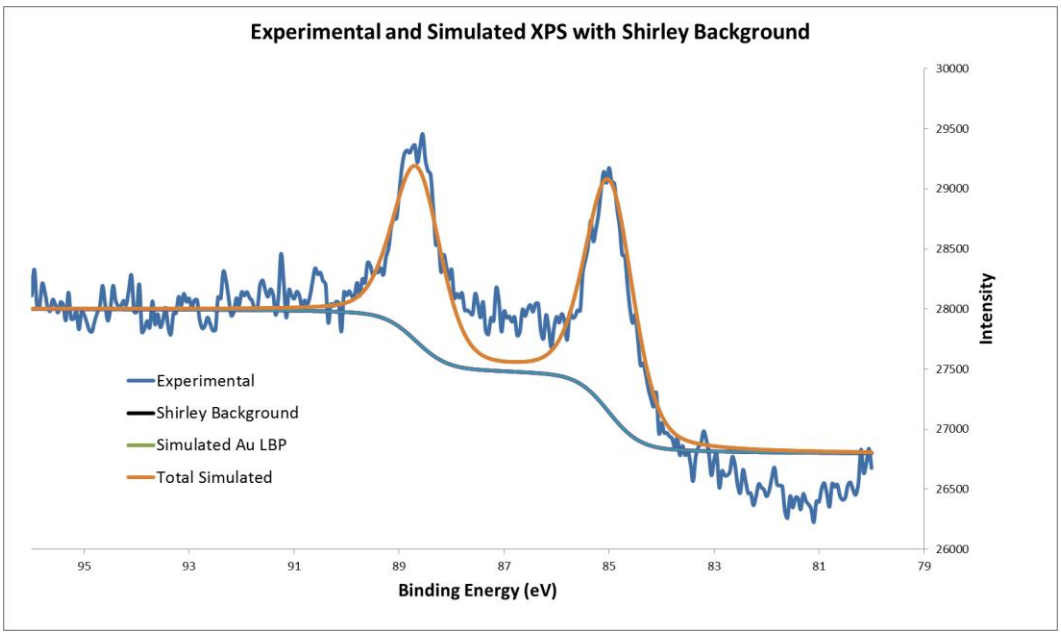

Figure 5.14 Au 4f XP spectrum of 0.17 wt% Au_9/TiO_2 calcined under O_2. Courtesy of Professor Gunther Andersson.

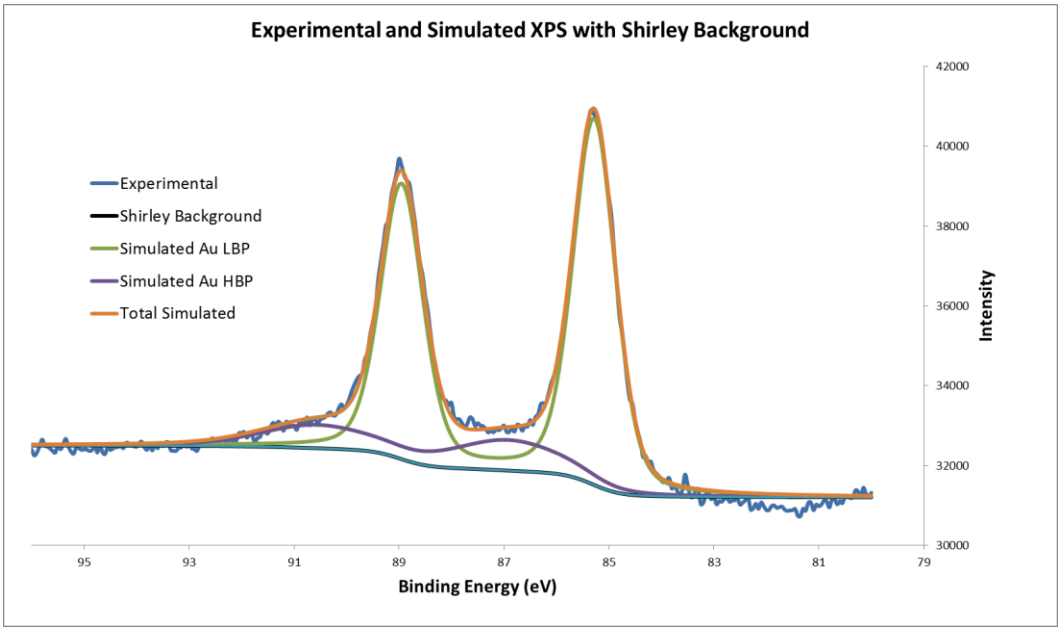

Figure 5.15 Au 4f XP spectrum of 0.17 wt% Au_{101}/TiO_2 calcined under O_2. Courtesy of Professor Gunther Andersson.

The XP P 2p spectra for Au_8 and Au_{101} showed small intensity in the P-LBP whereas it reduces to zero for Au_9 (Figure 5.16-5.18). These findings indicate that for the Au_9 cluster, the phosphine ligands are mostly removed from the gold-core and form phosphine-oxide like species by interaction with the oxygen on TiO_2 surface. For Au_8 and Au_{101}, phosphine ligands exist both as minority population of phosphine ligands still bound to gold core and majority population corresponding to the phosphine-oxide like species. The almost similar value of intensity ratios of Au-HBP/P-LBP and total Au/P-LBP for Au_8 indicate that a considerable faction of Au_8 clusters still retain their original size (*ca.* 1 nm) with some phosphine ligands remain intact and bonded to the Au core of the cluster). However, Au_9 and Au_{101} clusters undergo significantly more pronounced aggregation to form large, bulk gold-like nanoparticles.

Table 5.3 Position and FWHM of the Au $4f_{7/2}$ XP peaks for catalysts calcined under O_2.

Catalyst	Peak	Energy (eV)	FWHM (eV)	Intensity HBP/LBP
0.17 wt% Au_8/TiO_2-O_2	Au-LBP	83.7 ± 0.1	1.0 ± 0.2	
	Au-HBP	85.3 ± 0.2	2.2 ± 0.1	
				0.9 ± 0.2
0.17 wt% Au_9/TiO_2-O_2	Au-LBP	83.7 ± 0.1	1.1 ± 0.2	
	Au-HBP	-	-	
				0
0.17 wt% Au_{101}/TiO_2-O_2	Au-LBP	83.8 ± 0.1	1.1 ± 0.2	
	Au-HBP	-	-	
				0

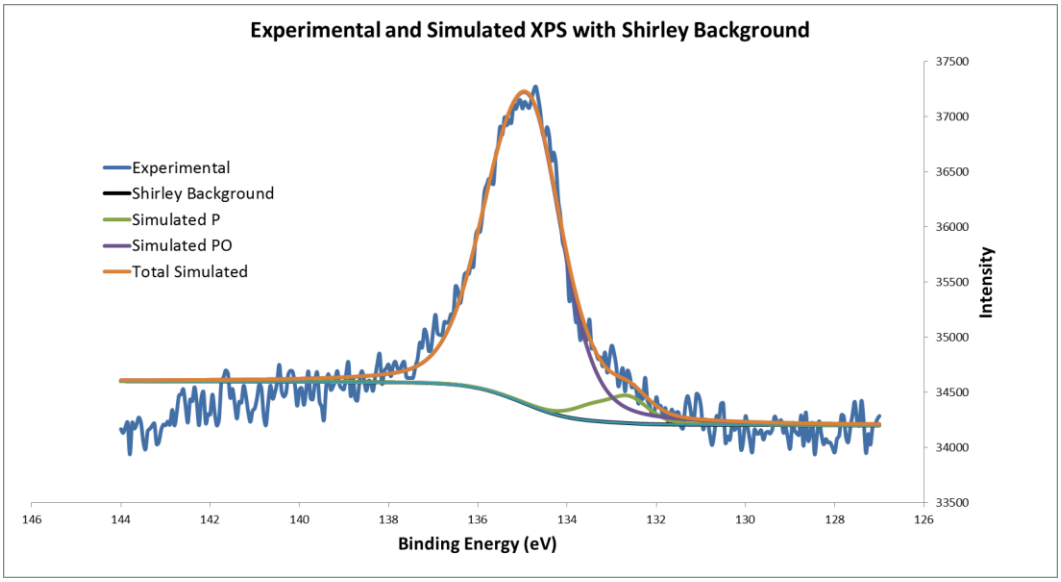

Figure 5.16 P 2p XP spectrum of 0.17 wt% Au_8/TiO_2 calcined under O_2. Courtesy of Professor Gunther Andersson.

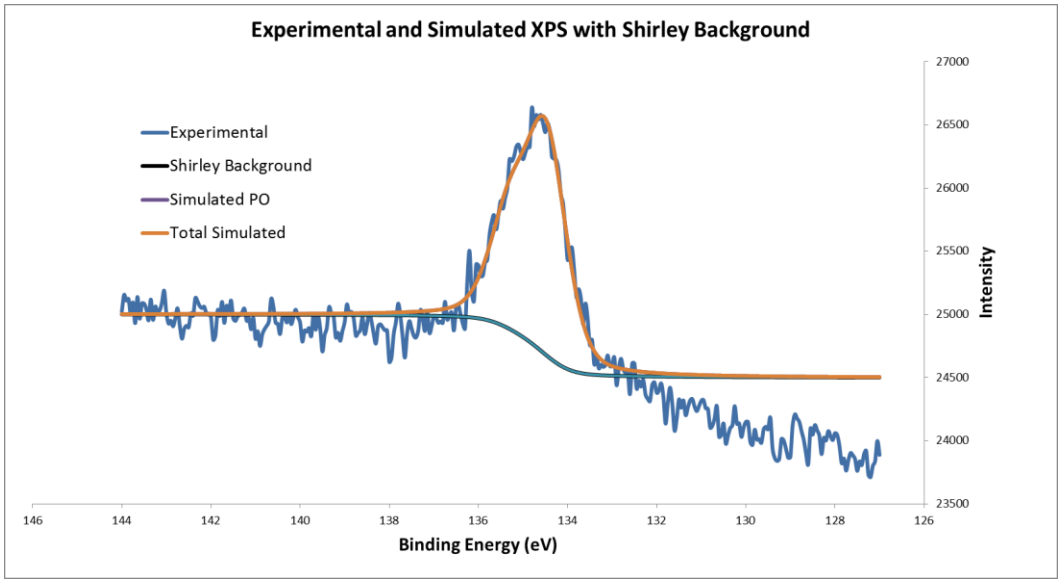

Figure 5.17 P 2p XP spectrum of 0.17 wt% Au_9/TiO_2 calcined under O_2. Courtesy of Professor Gunther Andersson.

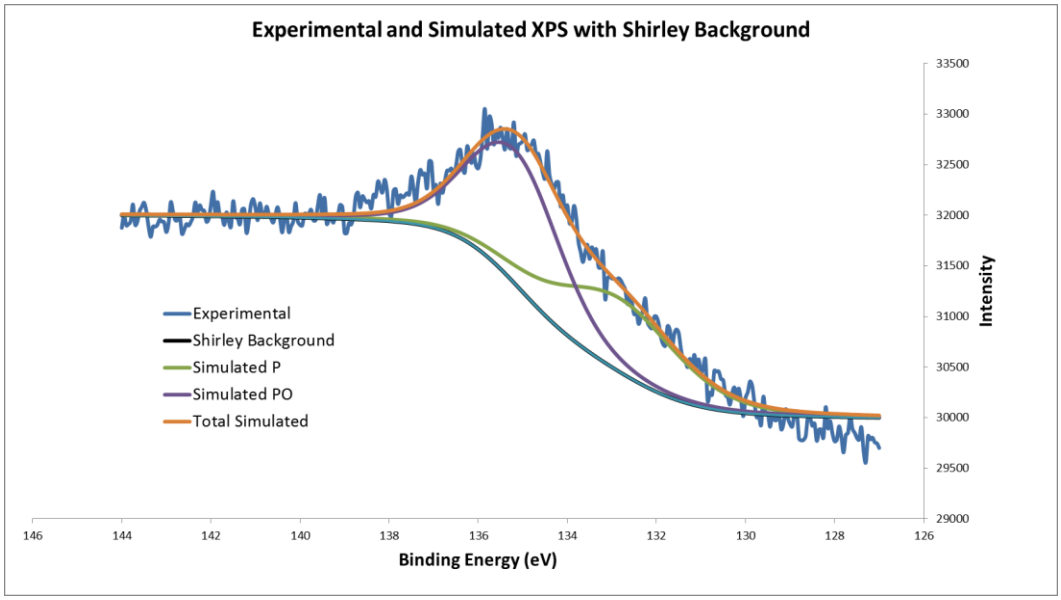

Figure 5.18 P 2p XP spectrum of 0.17 wt% Au_{101}/TiO_2 calcined under O_2. Courtesy of Professor Gunther Andersson.

HRTEM study confirms XPS findings for these series: Au_8 clusters aggregate to form Au nanoparticles with mean size of 2.2 ± 1.5 nm (Figure 5.19), Au_9-based catalyst contains 2.4 ± 0.5 nm particles (Figure 5.20), whereas for Au_{101} cluster, Au nanoparticles around 3.5 ± 0.8 nm are formed (Figure 5.21). For Au_8 clusters on TiO_2 consisting of nanoparticles and clusters, the ultra-small clusters are barely observed using available to us HRTEM system due to the instrument limitations (poor contrast) mentioned above. Despite its mean size of 2.2 nm, the standard deviation is 1.5 nm and the smallest size observed under HRTEM is 1.3 nm; the HRTEM images justify the presence of the Au-HBP for Au $4f_{7/2}$ component due to small Au clusters for the Au_8. It is worth noting that after the heat treatment under O_2, not only does the particle size increase (*cf*. untreated materials), but also a non-uniform aggregation occurs to form particles of different sizes, contributing to the wider size distribution of Au nanoparticles (as shown by the statistical histograms, Figures 5.19-5.21). The increase in Au cluster size is 175 % (2100 % by volume) for Au_8, 140 % (1800% by volume) for Au_9, and 75 % (960% by volume) for Au_{101} clusters as compared to the untreated Au_x/TiO_2 catalysts (x = 8, 9 and 101). This finding is not surprising and correlates with an earlier report by Coutts *et al.* that under oxidative environment, the temperature of sintering is lowered, promoting rapid growth of Au nanoparticles.[283]

With regard to the chemical state of Au clusters on TiO_2, the XPS analysis reveals that Au clusters are in zero oxidation state for all Au_x/TiO_2 (x=8,9 and 101) catalysts calcined under O_2. The characteristic signatures of oxidised gold species such as Au^+ and Au^{3+} appear as $4f_{7/2}$ peaks with binding energies of 85.2 - 85.7 eV (in $AuPPh_3Cl$) and 85.5 - 86.3 eV (in Au_2O_3) respectively.[134, 284] It was reported previously that the oxidation of gold could occur under harsh conditions, such as oxygen plasma or reaction with a strong oxidising agent.[257, 263] The calcination temperature used in this work (200 °C) is much higher than the temperature range of Au_2O_3 decomposition.[285, 286] With regard to Au^{3+} or/and Au^+ in the supported Au clusters, the presence of these species based on conditions alone could not be ruled out as during cooling down stage samples were still exposed to pure O_2 atmosphere. Hence, XPS provides evidence of absence of such oxidized species in these materials. Specifically, no Au-HBP for Au_9 and Au_{101} was observed, while some Au-HBP observed in the case of Au_8 correlates better with unaggregated clusters as it coincides with existence of P-LBP corresponding to phosphine ligands still bonded to Au cluster cores.

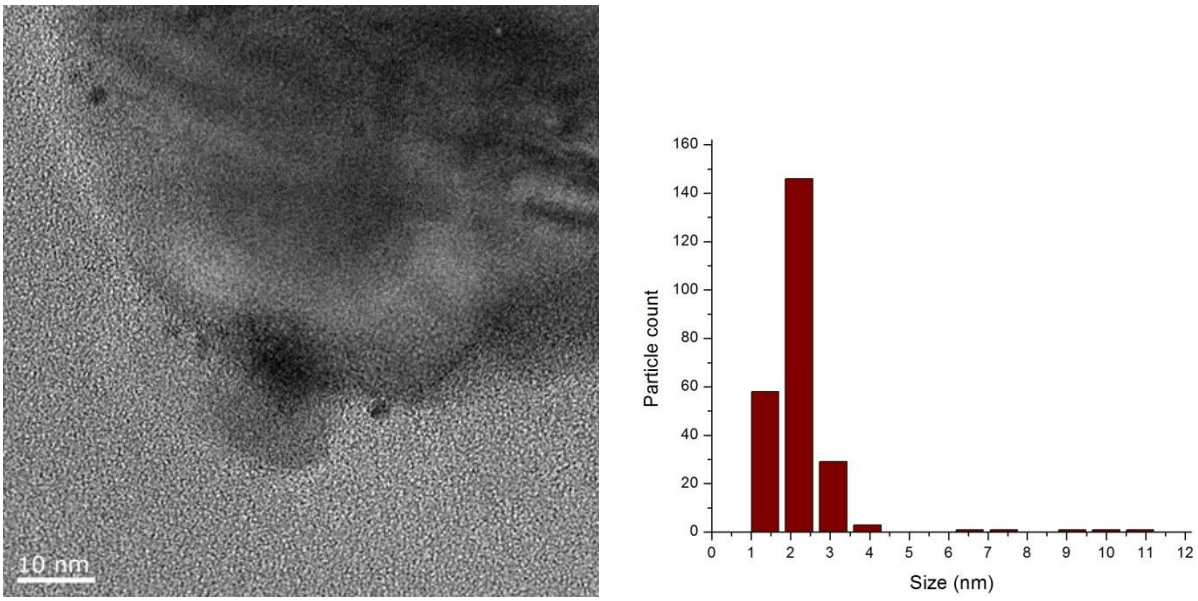

Figure 5.19 A representative TEM image of 0.17 wt% Au_8/TiO_2 catalyst calcined under O_2 (left) and the corresponding statistical Au particle size distribution histogram (right).

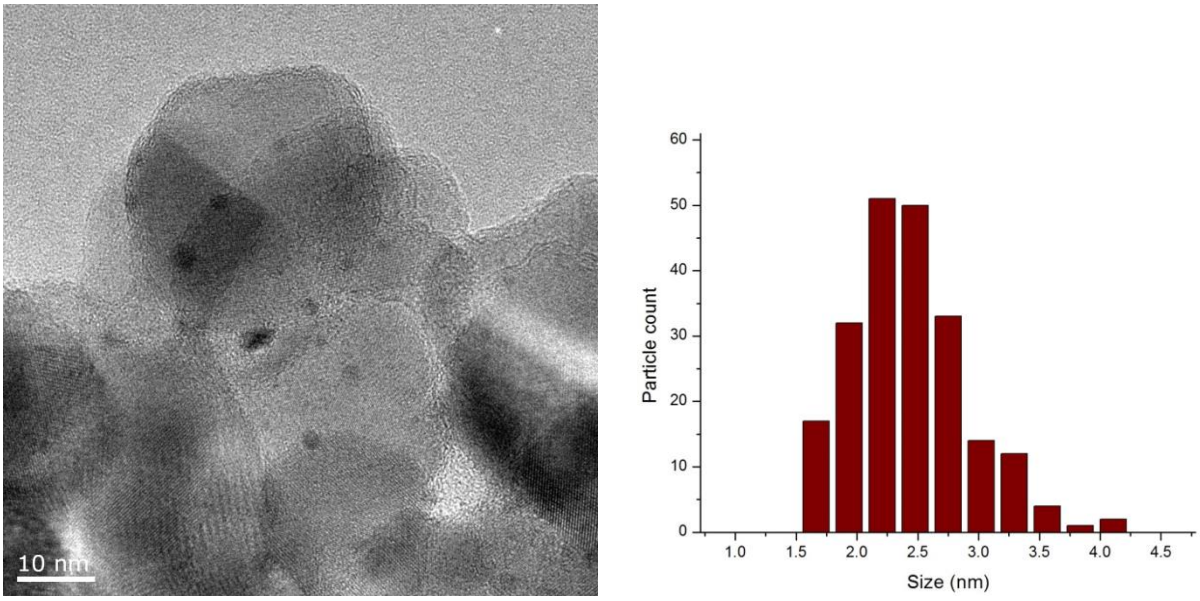

Figure 5.20 A representative TEM image of 0.17 wt% Au_9/TiO_2 catalyst calcined O_2 (left) and the corresponding statistical Au particle size distribution histogram (right).

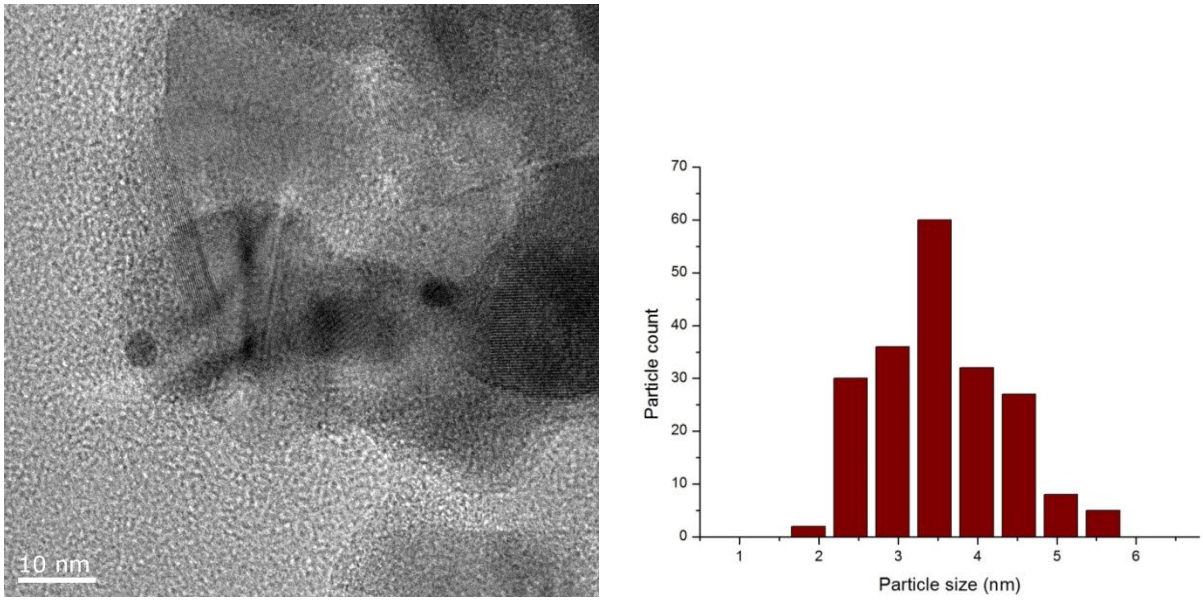

Figure 5.21 A representative TEM image of 0.17 wt% Au_{101}/TiO_2 catalyst calcined under O_2 (left) and the corresponding statistical Au particle size distribution histogram (right).

UV-vis DR spectra (Figure 5.10-5.12, middle, red spectra) displays the presence of LSPR peak maximum for Au_8 (552 nm), Au_9 (555 nm) and Au_{101} (533 nm) clusters. The appearance of LSPR peak maximum indicates that the Au particle size evolves from the cluster regime (< 2 nm) to nanoparticle regime (> 2 nm). UV-vis DR spectra reinforce the aggregation of all untreated Au_x/TiO_2 (x=8,9 and 101) catalysts after calcination under O_2. The broad tail of the LSPR peaks is attributed to the electronic modulation of Au nanoparticles when adsorbed onto TiO_2 supports and a wide distribution of Au particles size.[106] It is worth to notice that the typical colloidal Au nanoparticles (e.g. citrate-stabilized Au nanoparticles having particle size of ~13 nm) have the LSPR peak at ~525 nm.[162, 287] While in this case, TiO_2-supported Au nanoparticles have particle size around 2-4 nm, yet the LPSR peaks are around 530-555 nm. Tsukuda and co-workers found that the LSPR peak was red-shifted when deposited onto supports and attributed such observation to the electronic interaction between Au nanoparticles and supports.[106]

5.2.4 Catalysts calcined under O_2 followed by calcination under H_2

Calcination under H_2 is normally performed to reduce the oxidized Au^{3+} and/or Au^{+} species to metallic Au^0.[288, 289] Zanella and Louis observed that the growth of Au nanoparticles on TiO_2, prepared *via* deposition-precipitation method, can be impeded by heating under the flow of H_2 at 300 °C as compared to heating under air.[280] In their study, the reported that Au/TiO_2 calcined under H_2 had a mean diameter of 1.7 ± 0.5 nm, smaller than that of calcined under air, 2.3 ± 0.7 nm. Tsubota *et al*. also showed that Au/TiO_2 catalysts calcined under H_2 led to a smaller Au size (2.1 nm) than calcined under air (3.3 nm) at 250 °C.[290] In this study, the Au_x/TiO_2 (x = 8, 9 and 101) catalysts that had been calcined under O_2 earlier were calcined further under H_2 flow (referred to as catalysts under combined O_2-H_2 calcination for convenience) at 200 °C for 2 hours. The XP Au 4f spectra for Au_x/TiO_2 (x=8, 9 and 101) catalysts under combined O_2-H_2 calcination show only one characteristic peak at Au-LBP position, with $4f_{7/2}$ peak at 83.7-84.0 eV (Figure 5.22-5.24). The disappearance of Au-HBP (85.3 ± 0.2 eV) in the XP spectra indicates that Au clusters in all samples (Au_8, Au_9 and Au_{101}) have completely aggregated forming bulk-like in nature Au nanoparticles. The Au $4f_{7/}2$ peak at 83.7-84.0 eV also indicates that Au nanoparticles are in zero oxidation state. Table 5.4 summarize the peak position of Au catalysts calcined under combined O_2-H_2 condition.

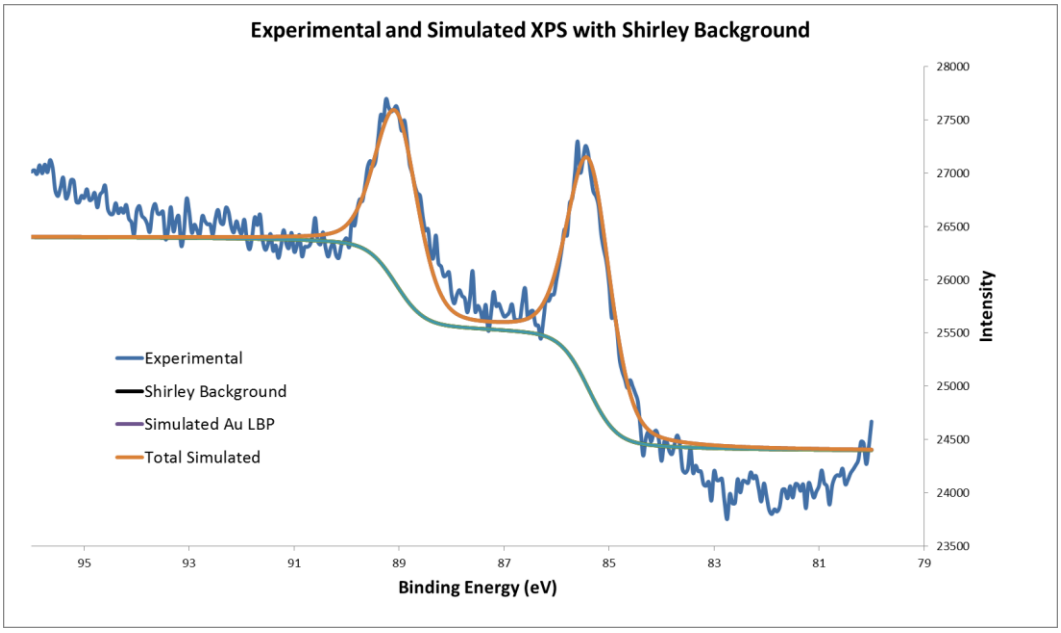

Figure 5.22 Au 4f XP spectrum of 0.17 wt% Au_8/TiO_2 calcined under O_2 followed by H_2. Courtesy of Professor Gunther Andersson.

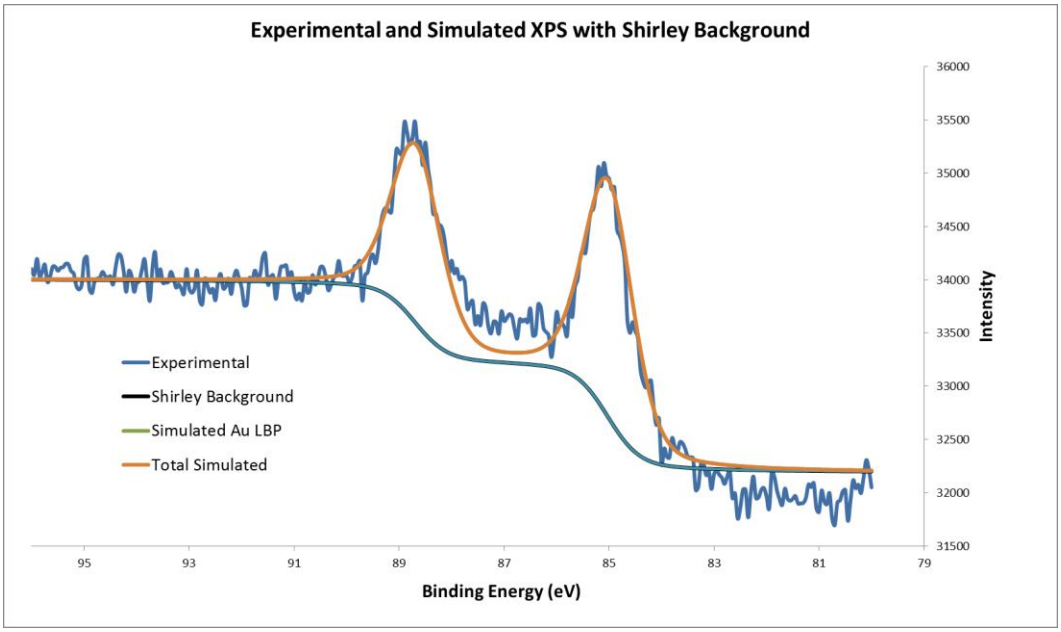

Figure 5.23 Au 4f XP spectrum of 0.17 wt% Au_9/TiO_2 calcined under O_2 followed by H_2. Courtesy of Professor Gunther Andersson.

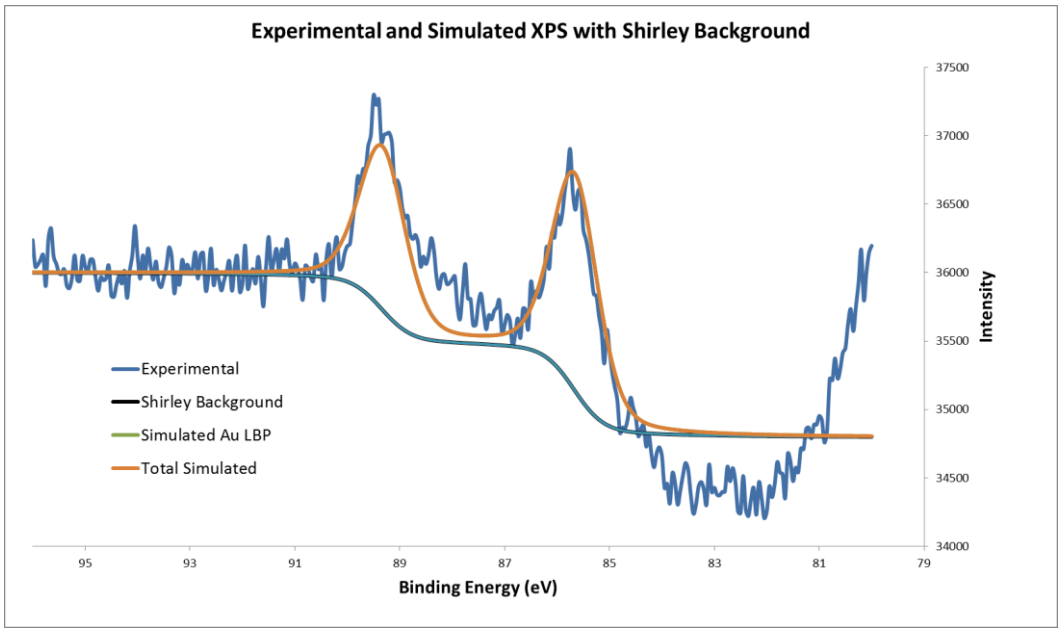

Figure 5.24 Au 4f XP spectrum of 0.17 wt% Au_{101}/TiO_2 calcined under O_2 followed by H_2. Courtesy of Professor Gunther Andersson.

The P 2p spectra for Au_8, Au_9 and Au_{101} cluster-based materials can be mostly fitted with a single peak at P-HBP although a small peak area due to the contribution from the P-LBP is needed for Au_8 albeit at large uncertainty (0.9 ± 1.0 eV). The ratio intensity of total Au/total P shows a much smaller value than the stoichiometric ratio of Au/P in the pristine clusters (Table 5.2), which is due to attenuation of XP signal from large Au a particle due to limited mean free path of photoelectrons. Combining the interpretation of P 2p and Au $4f_{7/2}$ spectra one could show that the phosphorous ligands are entirely dislodged from the Au cluster cores and re-deposited on the TiO_2 surface while the Au clusters completely sinter.

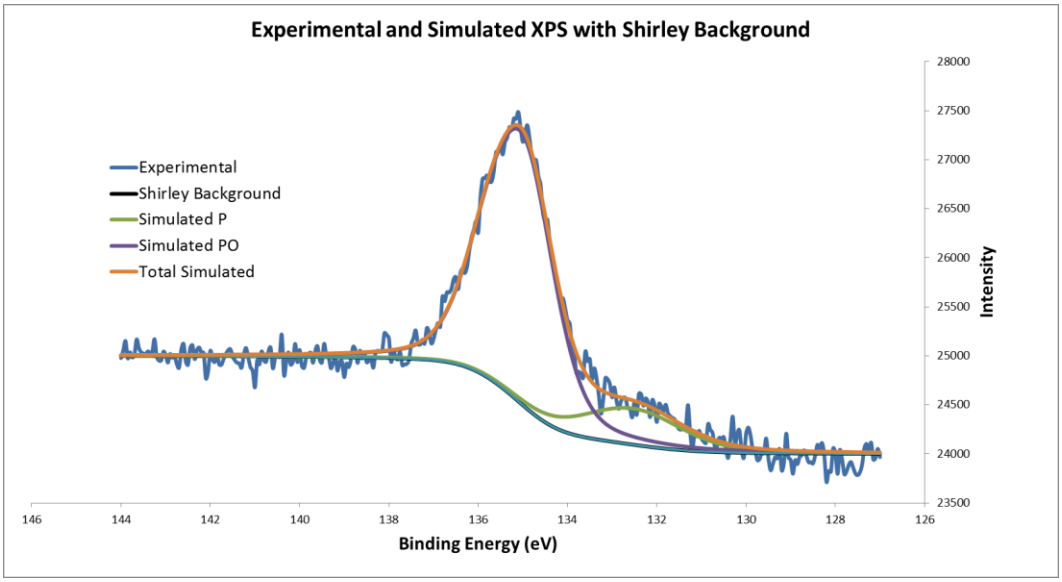

Figure 5.25 P 2p XP spectrum of 0.17 wt% Au_8/TiO_2 calcined under O_2 followed by H_2. Courtesy of Professor Gunther Andersson.

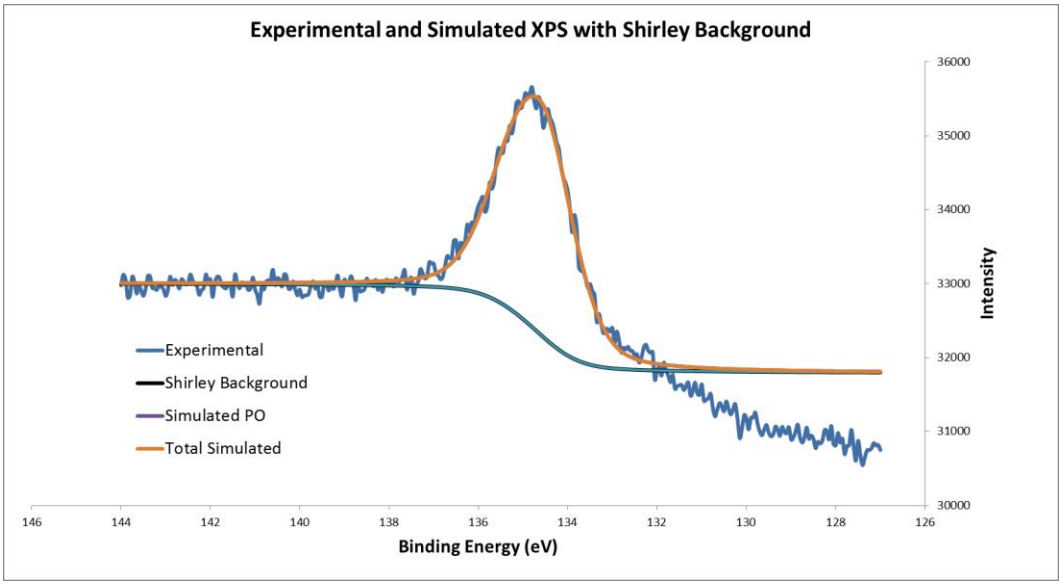

Figure 5.26 P 2p XP spectrum of 0.17 wt% Au_9/TiO_2 calcined under O_2 followed by H_2. Courtesy of Professor Gunther Andersson.

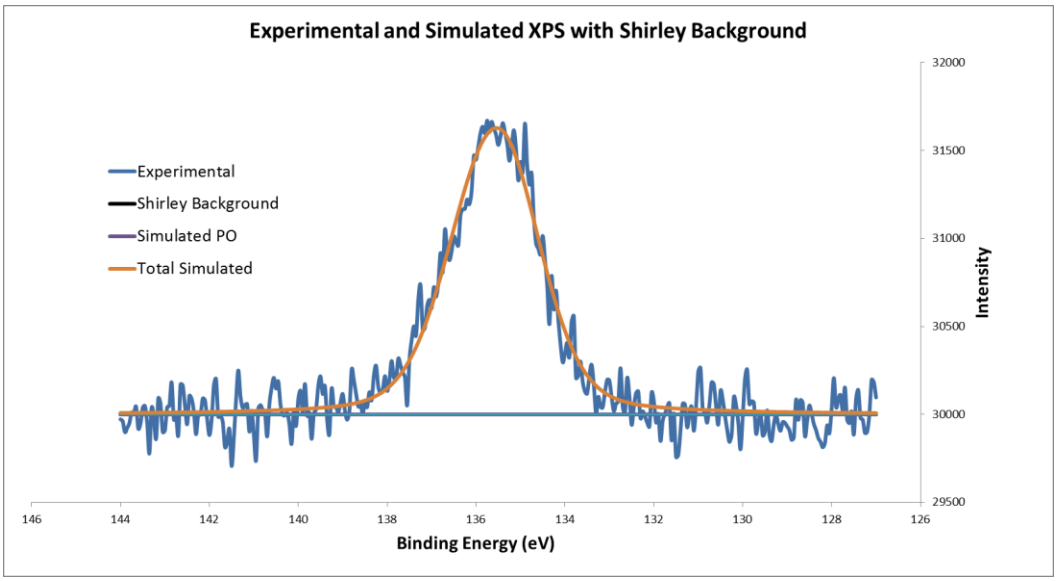

Figure 5.27 P 2p XP spectrum of 0.17 wt% Au_{101}/TiO_2 calcined under O_2 followed by H_2. Courtesy of Professor Gunther Andersson.

Table 5.4. Position and FWHM of the Au $4f_{7/2}$ XP peaks for catalysts calcined under O_2-H_2

Catalyst	Peak	Energy (eV)	FWHM (eV)	Intensity HBP/LBP
0.17 wt% Au_8/TiO_2	Au-LBP	83.7 ± 0.1	1.0 ± 0.2	
	Au-HBP	-	-	
				0
0.17 wt% Au_9/TiO_2	Au-LBP	83.7 ± 0.1	1.0 ± 0.2	
	Au-HBP	-	-	
				0
0.17 wt% Au_{101}/TiO_2	Au-LBP	84 ± 0.1	1.1 ± 0.2	
	Au-HBP	-	-	
				0

Analysis of representative TEM images shows the increase in particle sizes to 2.5 ± 1.7 nm for Au_8 (Figure 5.28), 2.9 ± 0.9 nm for Au_9 (Figure 5.29) and 4.4 ± 1.2 nm for Au_{101} (Figure 5.30) respectively. The size distribution of gold clusters also widens after combined O_2-H_2 calcination as can be seen from the statistical particle size distribution histograms (right images in Figures 12-14). It is worth to note here that combined O_2-H_2 calcination at 200 °C results in smaller incremental increase of Au particle sizes as compared to the calcination under O_2 at 200 °C. Specifically, for Au_8 combined O_2-H_2 treatment resulted in growth of particles - 14 % by size (44 % by volume) compared to untreated material (*cf*. the case of O_2-only treatment resulting in increase of 175 % by size and 2150 % by volume). Similarly, in the case of Au_9 combined O_2-H_2 calcination increased particle size by 21 % (76 % by volume) *vs*. 140% by size (800% by volume) increase calcination under O_2. Finally, increase for Au_{101} clusters was 26% by size (98% by volume) which is again lower than that under O_2 (75% by size and 960% by volume). These findings show a small increment of Au size sequentially calcined under O_2 followed by H_2 atmosphere as compared to those calcined under O_2 alone are in agreement as with the reports by Zanella and Louis,[280] and Tsubota *et al*.[290]

To explain the suppression of Au nanoparticle aggregation calcined under H_2, Haruta and co-workers suggested that H_2 might remove the remaining Cl^- species (from the $HAuCl_4$ precursor) on the surface of supports as HCl.[291] Cl^- ion is known to promote sintering of Au nanoparticles, and thus its removal is highly desirable.[135] Oxygen defect sites could be created on the TiO_2 surface in reductive environments (H_2 or CO), and thus these defects, if formed, could impede the diffusion of gold atoms and particles because the adhesion energy is larger on oxygen-defective surfaces.[292, 293] Lopez *et al*. estimated

the number of the defects for rutile TiO_2(110) produced under H_2 and CO using the formation energies of oxygen vacancies and found that the number of defects increases with increasing temperature and the amount of gas (CO or H_2).[293] Okazaki *et al*. calculated the adhesion energy of Au monolayer on rutile TiO_2(110) surface using the *ab initio* pseudopotential method based on the DFT.[292] They found that the adhesion energy (E_{ad}) for nonstoichiometric TiO_2(110) surface with oxygen vacancies is 1.90 eV/adatom and for stoichiometric TiO_2(110) surface is 0.10 eV/adatom. This indicates that Au nanoparticles resist sintering when defects (in this case oxygen vacancies) are present.

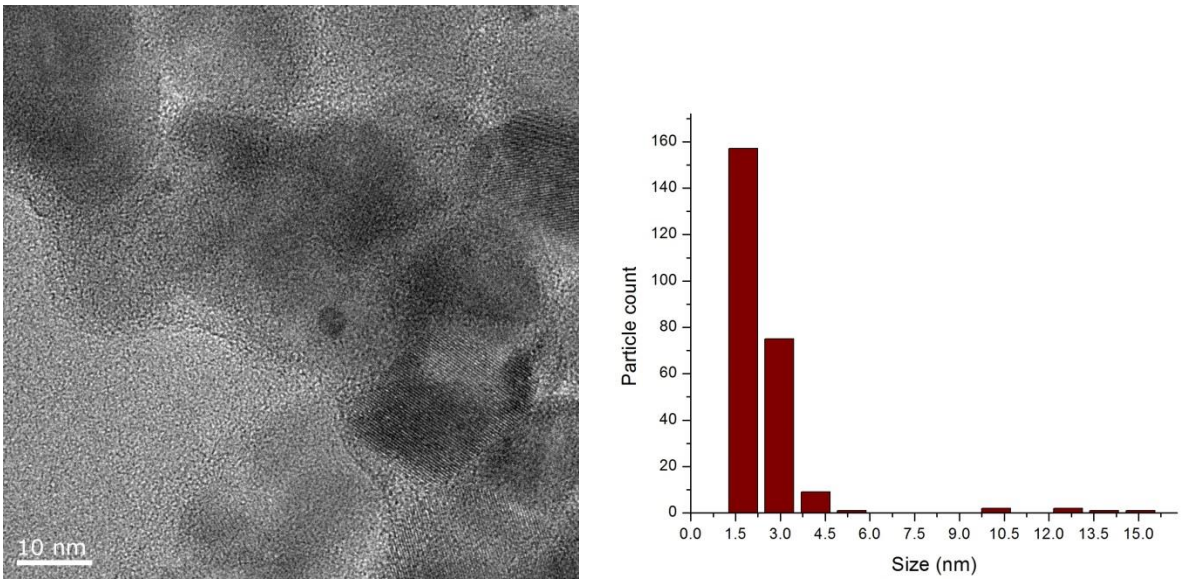

Figure 5.28 A representative TEM image of 0.17 wt% Au_8/TiO_2 catalyst calcined under combined O_2-H_2 (left) and the corresponding statistical Au particle size distribution histogram (right).

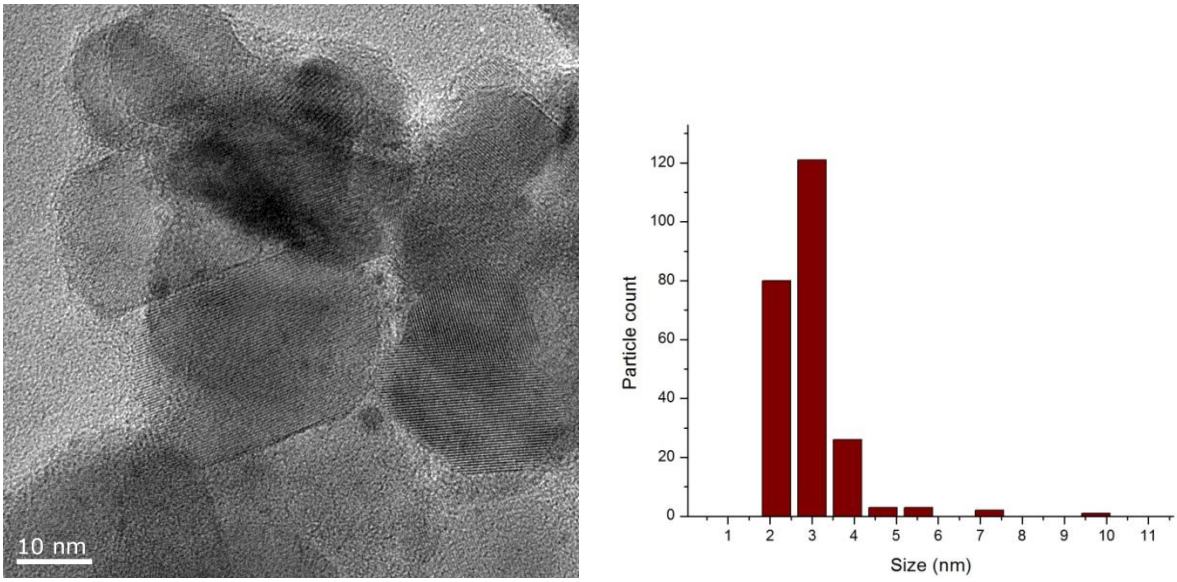

Figure 5.29 A representative TEM image of 0.17 wt% Au_9/TiO_2 catalyst calcined under combined O_2-H_2 (left) and the corresponding statistical Au particle size distribution histogram (right).

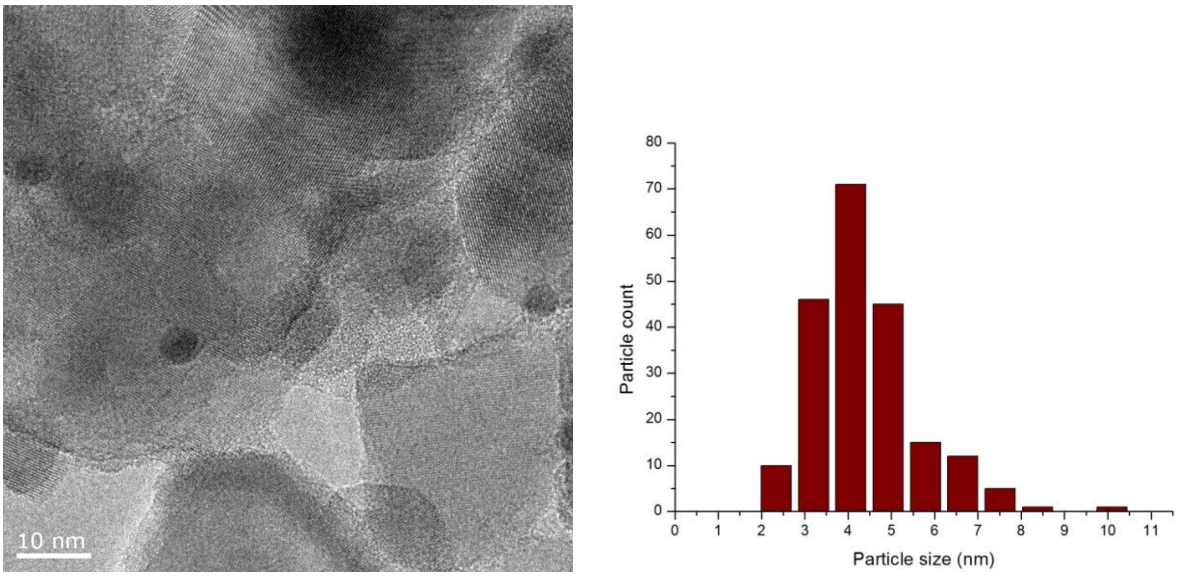

Figure 5.30 A representative TEM image of 0.17 wt% Au_{101}/TiO_2- catalyst calcined under combined O_2-H_2 (left) and the corresponding statistical Au particle size distribution histogram (right).

UV-vis DR spectra for Au_9 and Au_{101} (Figure 5.10-5.12, top, blue spectra) showed that LSPR peak maxima are red-shifted for samples calcined in O_2 followed by H_2 at 200 °C (*cf*. as made samples) and maintained broad tails further corroborating the particle size distribution observed by TEM. This shift of the LSPR peak is consistent with the increase of Au particle sizes as observed in TEM.

5.2.5 XAS study of Au_9 cluster

Au L_{III}-edge XANES spectra for unsupported Au_9 cluster, supported Au_9 cluster and bulk gold metal are shown in Figure 5.31. L-edge is chosen because it provides a more sensitive measurement and useful information about the local structure, symmetry, coordination number and bond length. L_{III}-edge gives the most intense transition from 2p states to d-like final states.[189] Pristine Au_9 clusters (in the form of a microcrystalline powder of pure cluster diluted in sample preparation matrix, such as cellulose, as described in the Experimental) have a distinct peak at ~ 11925 eV and broad peaks at ~11947 and ~11970 eV. The peak intensity at 11925 eV is reduced and the broad peaks at 11947 and 11970 eV are intensified in the case of samples of supported clusters ("as deposited") and calcined. These features become more pronounced for the samples calcined under O_2 and O_2 followed by H_2 and eventually resemble the features observed in the spectrum of the bulk gold metal (spectrum e in Figure 5.31). A linear regression fit of the spectra for the calcined Au_9 clusters in the energy range 11880 - 11980 eV further supports the conclusions based on the analysis on XPS spectra and TEM images of the heat treated samples that aggregated Au_9 clusters are chemically equivalent to the bulk gold (Figure 5.32 and 5.33). The best fit of a linear regression for untreated supported-immobilized Au_9 clusters is achieved with 61 ± 3% of pure Au_9 (unsupported, spectrum obtained by mixing Au_9 with cellulose) and 39 ± 3% of bulk gold (a comparison of the data and the fit including a residual as shown in Figure 5.34).

Overbury and co-workers performed an XAS study on Au/TiO_2 catalysts prepared *via* deposition-precipitation and impregnation method to investigate the oxidation state of Au in the XANES region and the coordination number and bond length in the EXAFS region.[294] From XANES analysis, the authors found that Au/TiO_2 catalysts calcined under H_2 (4 v/v% in He) at 100 and 200 °C for 1 hour were completely reduced to Au^0 state and the aggregation of Au nanoparticles to form large particles resembling bulk gold was also observed. The author also estimated the Au nanoparticle size using the Au-Au first shell coordination number obtained from the EXAFS spectra concluding that the XAS technique can be used to probe the size of Au nanoparticles. Unfortunately, the authors did not provide TEM images of the catalysts, which could reinforce their findings.

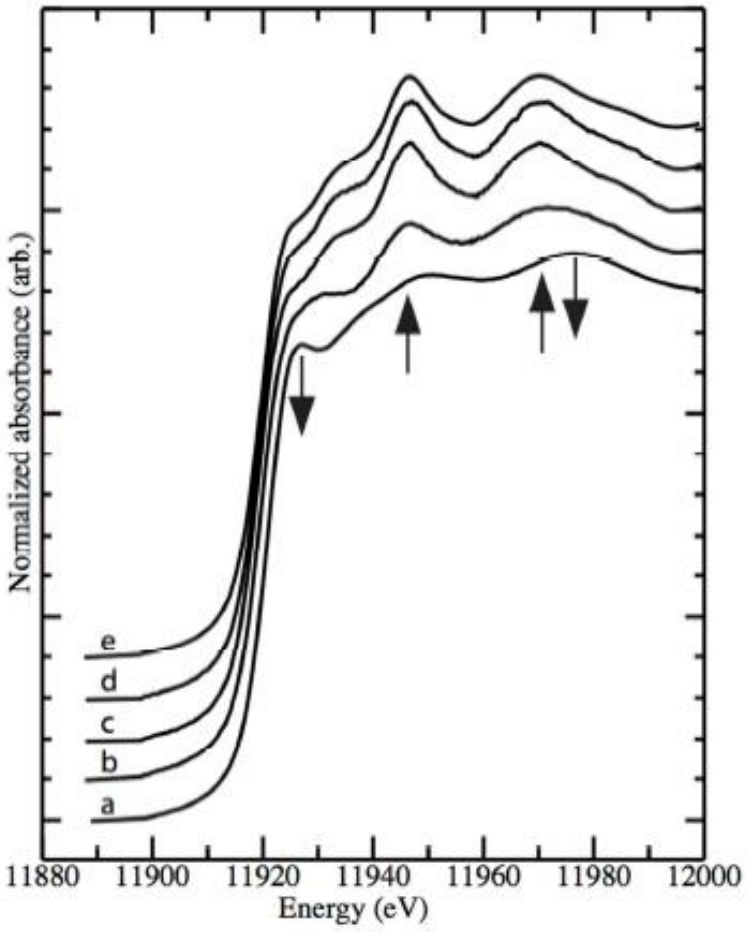

Figure 5.31 Au LIII-edge X-ray absorption spectra of: a) pristine, unsupported Au_9 clusters diluted in cellulose; b) untreated Au_9/TiO_2 catalyst; c) Au_9/TiO_2 catalyst calcined under O_2, d) Au_9/TiO_2 catalyst calcined under combined O_2-H_2, and e) bulk gold. The arrow indicates the features that are observed to change as the samples progress from clusters to aggregated nanoparticles.

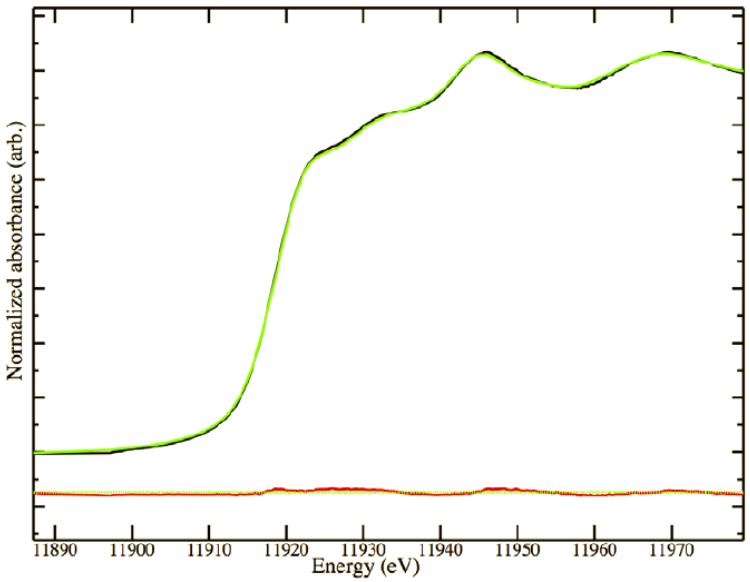

Figure 5.32 A comparison of Au LIII-edge XAS spectra for the Au_9/TiO_2 catalyst calcined under O_2 at 200 °C (black curve) and bulk gold (green curve). The difference between the spectra is shown in red and is very close to the base line (green) at the bottom of the figure.

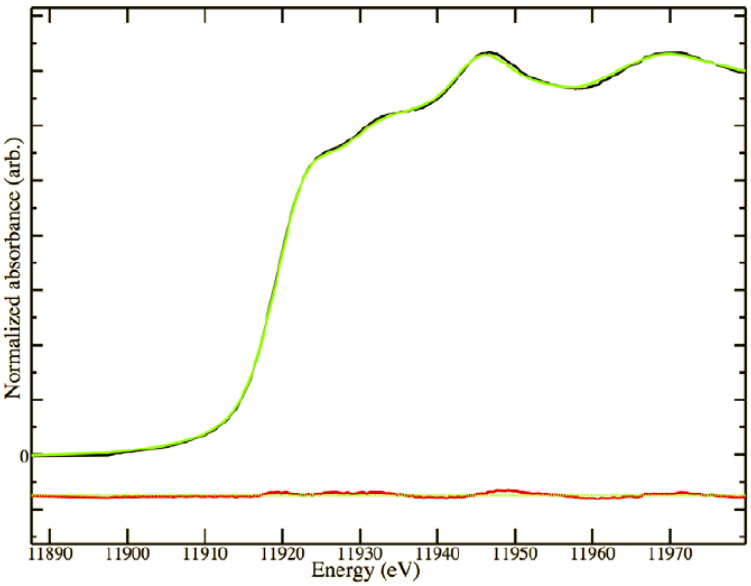

Figure 5.33 A comparison of Au LIII-edge XAS spectra for the Au_9/TiO_2 catalyst calcined under combined O_2-H_2 at 200 °C (black curve) and bulk gold (green curve). The difference between the spectra is shown in red and is very close to the base line (green) at the bottom of the figure.

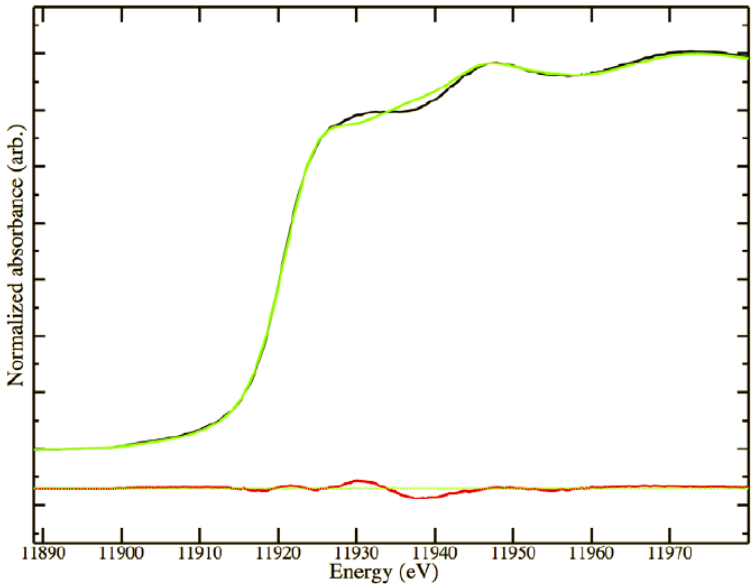

Figure 5.34 Au LIII-edge XAS spectra for the untreated Au_9/TiO_2 catalyst (black curve), against the fitted linear combination of the spectra with 61±3% pure Au_9 cluster diluted in cellulose and 39±3% bulk gold. The residual (red) is close to the base line (green).

5.2.6 TEM and UV-vis DRS study of Au_{101}/SiO_2 catalysts

Due to the charging problem during XPS measurements at the Australian Synchrotron, the obtained XP spectra did not provide accurate information on the nature of Au species in Au_{101}/SiO_2 catalysts. Here, only TEM images and UV-vis DR spectra are discussed in an attempt to investigate the nature of these catalysts. Figures 5.35, 5.36, 5.37 show the TEM images and corresponding particle size distribution histograms for 0.5 wt% Au_{101}/SiO_2 catalysts (untreated, calcined under O_2, and calcined under combined O_2-H_2 respectively). It is worth reminding at this stage that the metal loading of 0.5 wt% for Au/SiO_2 catalysts was chosen to ensure the same surface density in cluster coverage on both SiO_2 and TiO_2. It is evident from Figure 5.35 that despite the large surface area of SiO_2 (*ca.* 200 m^2/g) there is a severe aggregation of Au_{101} clusters after deposition on SiO_2: the mean Au size is 3.6 ± 1.2 nm with the largest observed particle is 8 nm. Calcination under O_2 promotes further aggregation to particles with the mean Au size of 4.7 ± 1.6 nm with the largest observed particle of 11 nm (Figure 5.36). A combined O_2-H_2 calcination increases the mean Au size further to 5.7 ± 2.9 nm (Figure 5.37). Apart from the increase in Au size, a noticeable broadening of size distribution (*cf.* as deposited, untreated samples) was observed in the case of calcined catalysts. Since the Au cluster surface coverage density on the SiO_2 support is the same as for the analogues fabricated on the TiO_2 (normalization of the Au loading by the surface area of supports), the above findings suggest that Au_{101} clusters interact only weakly with the inert SiO_2 supports

as opposed to the interacting, reducible TiO_2 support. An observation of the related effect in a MIES study showed that during deposition process, Au clusters did not absorb from solutions of various concentrations onto SiO_2 support while did absorb onto TiO_2 surface (under dip-coating conditions).[295] . Strength of metal-support interaction was the key argument used to justify the inferior catalytic activity of Au/SiO_2 (*vs.* Au/TiO_2) catalysts by several authors.[128, 296-298] Nevertheless, the evidence of charge transfer from Au clusters/nanoparticles to TiO_2 in the XPS study mentioned above was not observed.

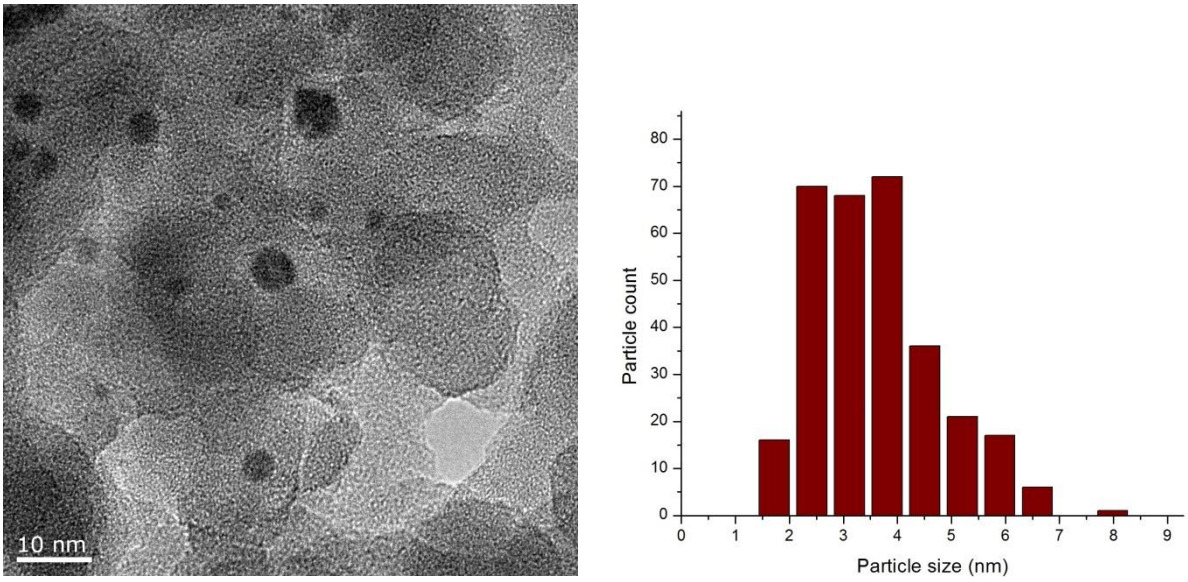

Figure 5.35 A representative TEM image of untreated 0.5 wt% Au_{101}/SiO_2 catalyst and the corresponding statistical Au particle size distribution histogram (right).

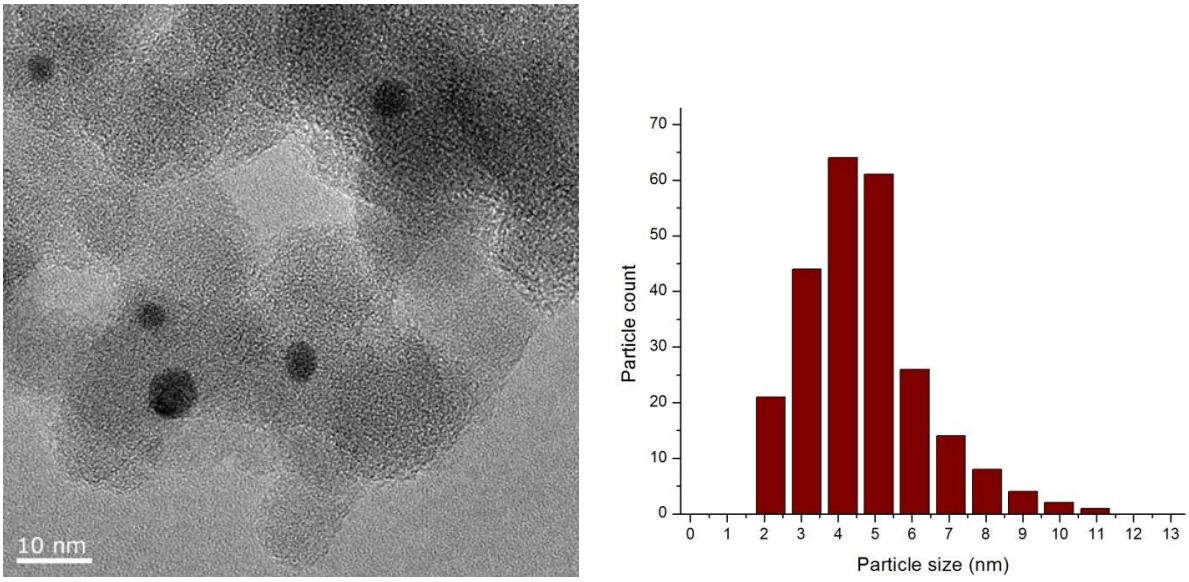

Figure 5.36 A representative TEM image of 0.5 wt% Au_{101}/SiO_2 catalyst calcined under O_2 and the corresponding statistical Au particle size distribution histogram (right).

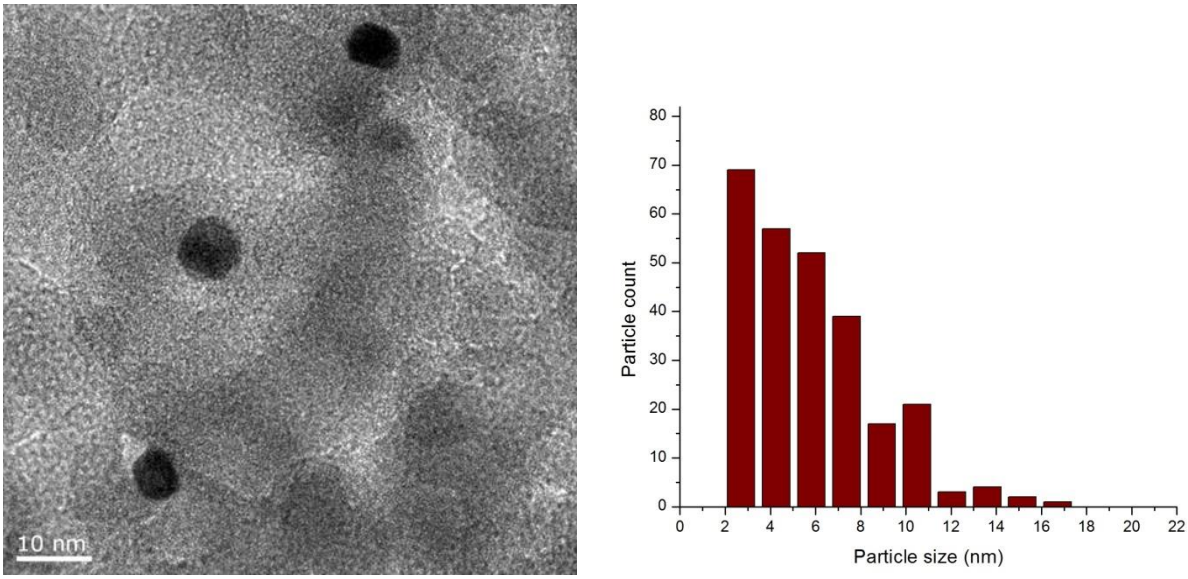

Figure 5.37 A representative TEM image of 0.5 wt% Au_{101}/SiO_2 catalyst calcined under combined O_2-H_2 and the corresponding statistical Au particle size distribution histogram (right)

Figure 5.38 shows the UV-vis DR spectra of 0.5 wt% Au_{101}/SiO_2 catalysts. The spectra display the trend of decreasing wavelength of the LSPR peak maxima (*i.e*. blue-shift) as the Au particle size increases (according to the TEM study). This finding is in contrast with the trend observed for Au_x/TiO_2 catalysts (x = 8, 9 and 101) and most other studies reported in the literature in which increase in the particle correlates with red-shift of LSPR peak position. It is worth mentioning that the LSPR peak

maximum is highly sensitive the size and morphology of Au nanoparticles, the interaction between Au nanoparticle and support, and the dielectric constant of the surrounding medium (*e.g.* solution/support) and it could be that in the case of this particular Au/SiO_2 system other factors (*cf.* MNP size) dominate.[122, 161, 299, 300]

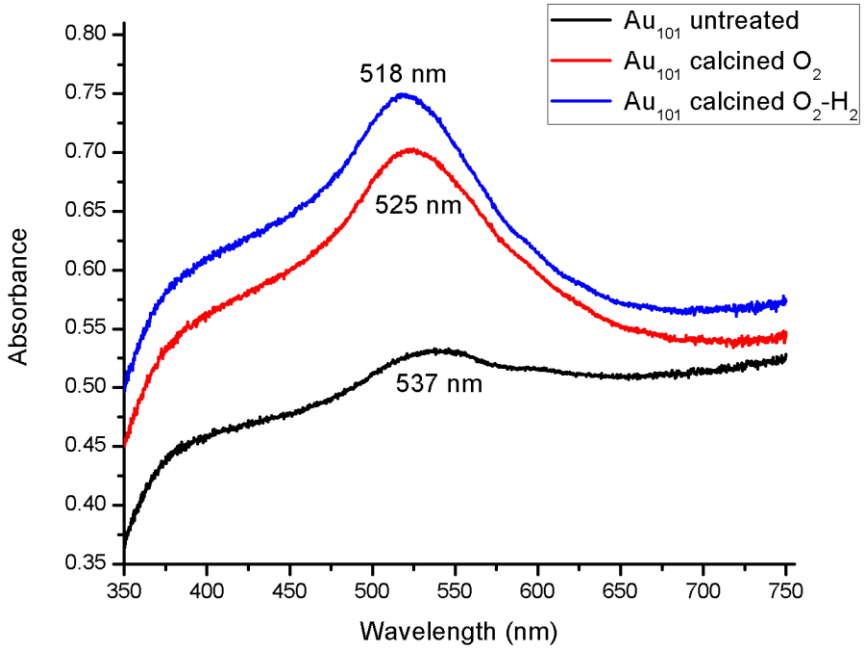

Figure 5.38 UV-vis DR spectra of 0.5 wt% Au_{101}/SiO_2 catalysts.

Another set of Au_{101}/SiO_2 catalysts was prepared at a lower loading (0.17 wt% Au) and activated under the same conditions to compare with the Au_{101}/TiO_2 analogue. Is it shown that the untreated 0.17 wt% Au_{101}/SiO_2 catalyst contains a significant proportion of small clusters (< 2 nm) and a small fraction of large agglomerates (Figure 5.39). Furthermore, UV-vis DR spectrum of the "as deposited" sample does not exhibit LSPR peak (bottom, black pattern in Figure 5.42), indicating that untreated Au_{101} nanoparticles on SiO_2 immediately after deposition (at 0.17 wt% loading) are below 2 nm in their vast majority (similarly to the mentioned earlier "as deposited, untreated" Au_8 and Au_9 on TiO_2). The 0.17 wt% Au_{101}/SiO_2 catalysts calcined under O_2 contain aggregated particles with mean size 3.6 ± 2.7 nm (Figure 5.40), similar to the case of 0.17 wt% Au_{101}/TiO_2 catalyst calcined under O_2 (3.5 ± 0.8 nm) while the Au particle size distribution on SiO_2 is broader. Taking into account much higher surface area of SiO_2 (*cf.* TiO_2) this finding once again proves weaker metal-support interaction, resulting in greater Au particle mobility and propensity to aggregate. The 0.17 wt% Au_{101}/SiO_2 after combined O_2-H_2 calcination has a mean Au particle size of 4.5 ± 2.5 nm, again, similar to the Au_{101}/TiO_2 analogue yet with a broader Au particle size distribution (Figure 5.41).

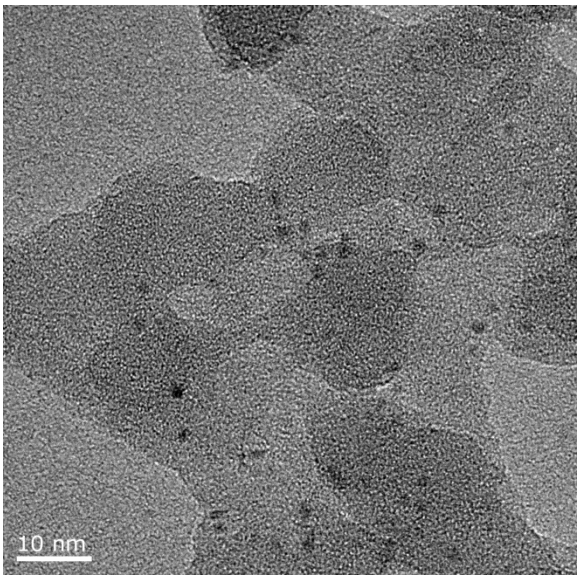

Figure 5.39 A representative TEM image of untreated 0.17 wt% Au_{101}/SiO_2 catalyst.

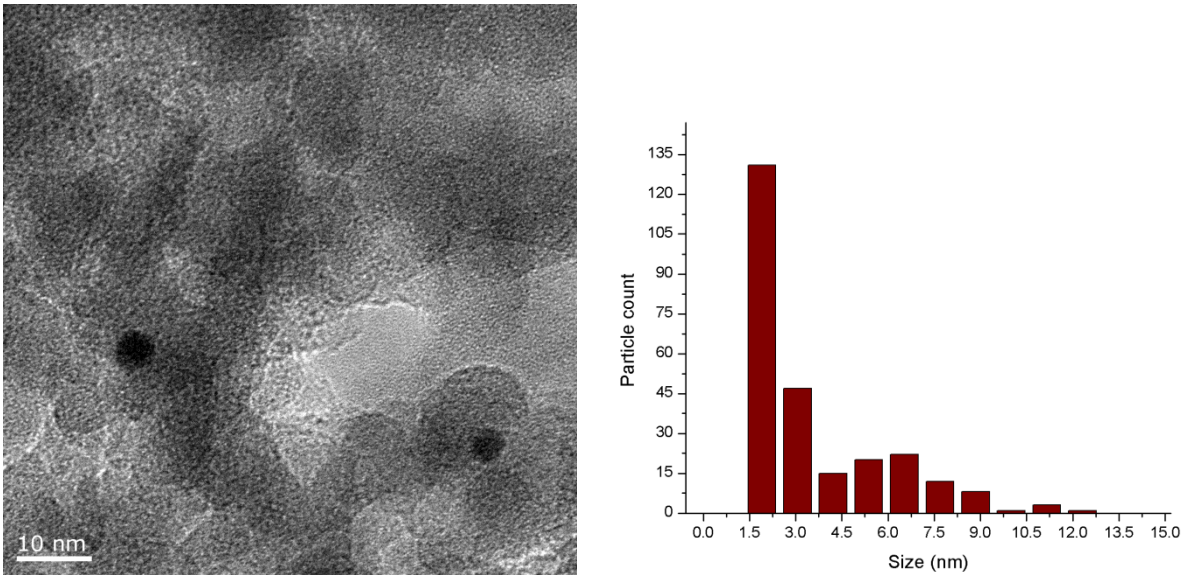

Figure 5.40 A representative TEM image of 0.17 wt% Au_{101}/SiO_2 catalyst calcined under O_2 and the corresponding statistical Au particle size distribution histogram (right).

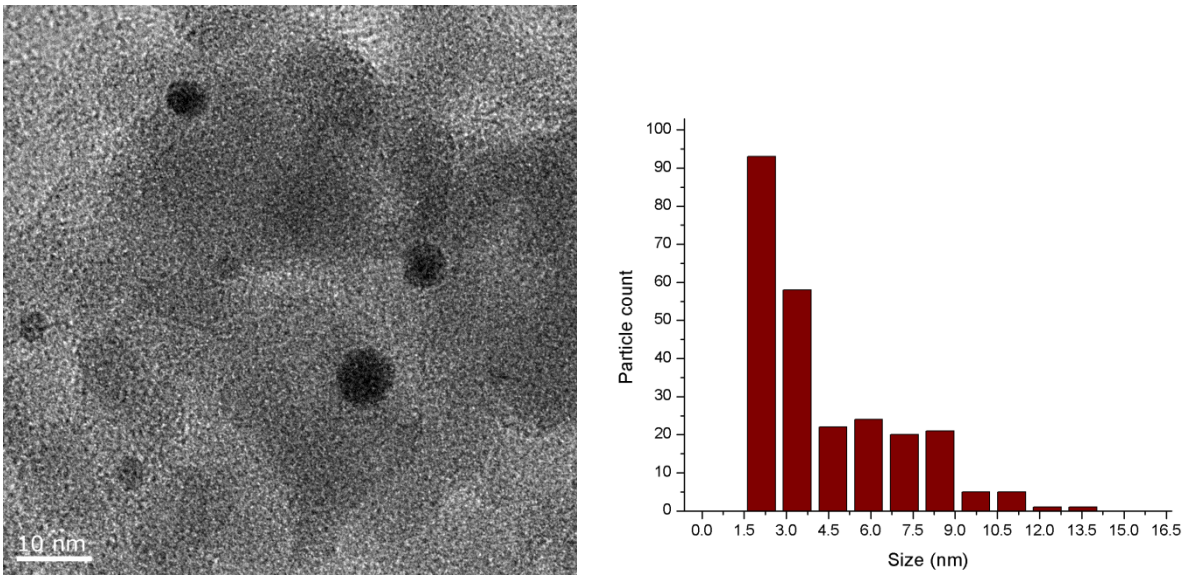

Figure 5.41 A representative TEM image of 0.17 wt% Au_{101}/SiO_2 catalyst calcined under combined O_2-H_2 and the corresponding statistical Au particle size distribution histogram (right).

UV-vis DR spectra for 0.17 wt% Au_{101}/SiO_2 catalysts are shown in Figure 26. Similarly to the case of 0.5 wt% Au_{101}/SiO_2 catalysts, the LSPR peaks show the unique trend towards shorter wavelength (blue-shift) as the Au nanoparticle size increases; 529 nm for catalyst calcined under O_2 and 524 nm under combined O_2-H_2 calcination (while there is no observable LSPR band in the case of as deposited samples as particles are below lower LSPR size threshold and are not plasmonic).

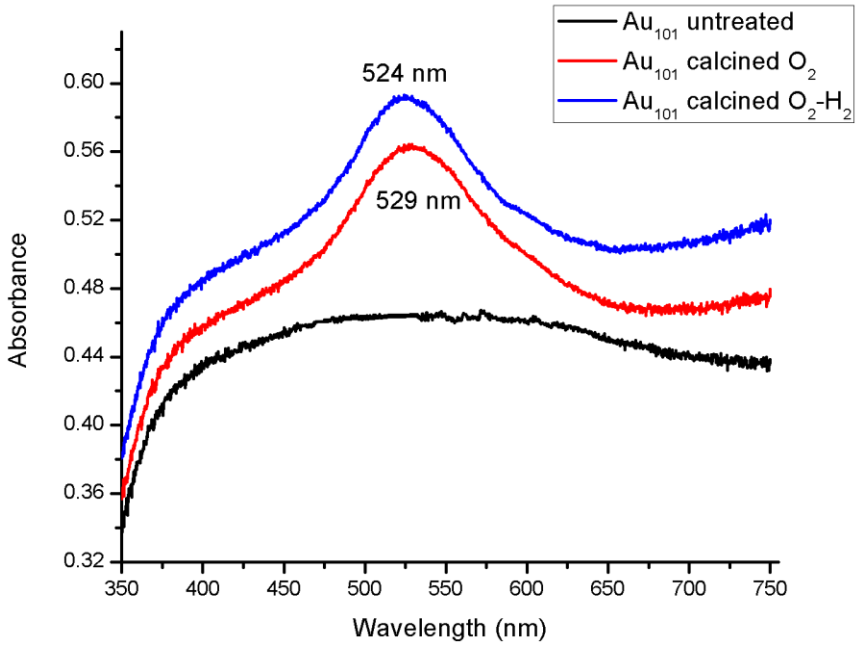

Figure 5.42 UV-vis DR spectra of 0.17 wt% Au_{101}/SiO_2 catalysts.

5.2.7 TEM images and UV-vis DR spectra of Au_{101} clusters on ZrO_2 and ZnO calcined under O_2

Supports are shown to influence the performance of Au supported catalysts in catalysis.[301, 302] For example, Choudhary *et al*. prepared Au nanoparticles on various metal oxide support including ZnO, ZrO_2, CuO and Sm_2O_3 by the homogeneous deposition precipitation method to test the effect of support in the catalytic oxidation of benzyl alcohol.[303] The authors observed that the activity and selectivity of the products are highly dependent on the supports yet they concluded the comparison was not equivalent because the Au loadings were different on each support, which complicated the elucidation of the active site. Comotti *et al*. prepared PVA-capped Au nanoparticles on different transition metal oxides (TiO_2, ZrO_2, ZnO and Al_2O_3) by sol immobilization method for CO oxidation.[302] They were able to produce similar Au loading and particle size on different metal oxides and observed the support effect played a crucial role in determining the catalytic activity of CO oxidation. Here d Au_{101} clusters were depositedon ZrO_2 and ZnO_2 supports at 0.17 wt% Au loading, in addition to TiO_2 (anatase) and SiO_2 (fumed), in order to study the effect of support in catalysis (later in Chapter 6). The catalysts were calcined under O_2 atmosphere. Figure 5.43 displays the TEM image and particle size distribution histogram of Au_{101}/ZrO_2 calcined under O_2 having a mean size 3.5 ± 1.4 nm. The UV-vis DR spectrum (Figure 5.44) displays the LSPR peak maximum for Au_{101}/ZrO_2 appears at 536 nm. The TEM image and particle size distribution histogram for Au_{101}/ZnO are shown Figure 5.45. The mean Au particle size on ZnO is 3.3 ± 1.0 nm. The LSPR peak maximum for Au_{101}/ZnO appears at 534 nm in UV-vis DR spectrum (Figure 5.46).

Interestingly, the mean Au_{101} size on ZrO_2 and ZnO supports after calcination under O_2 is comparable to that of Au_{101}/TiO_2 calcined under O_2 (3.5 ± 0.8 nm).

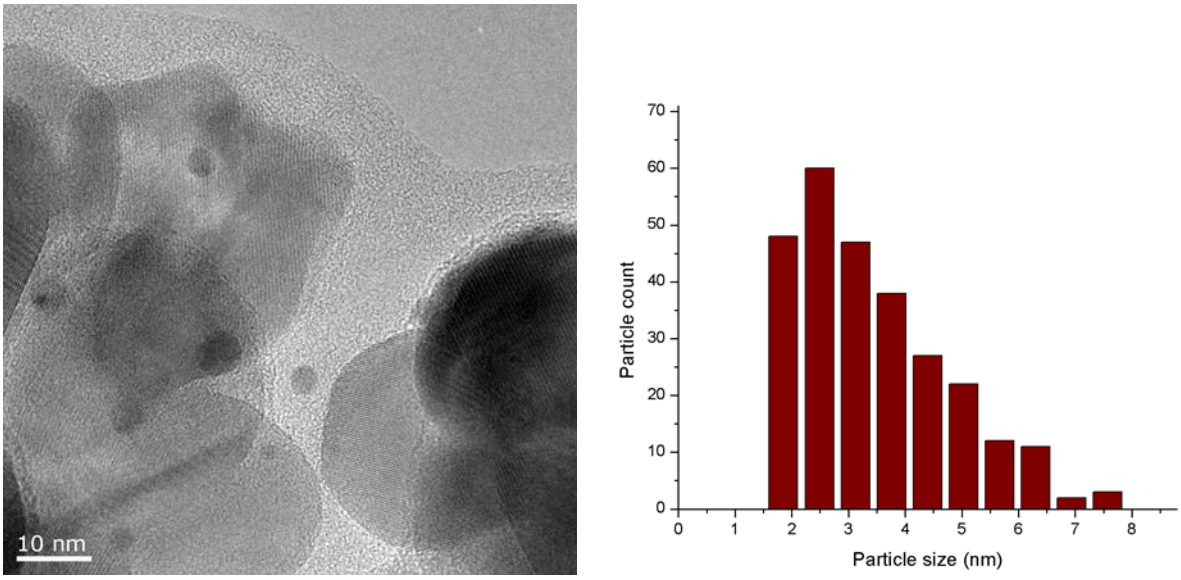

Figure 5.43 A representative TEM image of 0.17 wt% Au_{101}/ZrO_2 catalyst calcined under O_2 (left) and the corresponding statistical Au particle size distribution histogram (right).

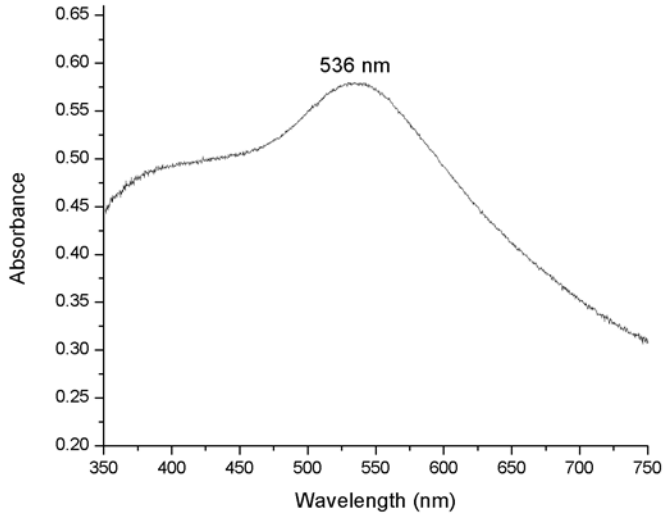

Figure 5.44 UV-vis DR spectrum of 0.17 wt% Au_{101}/ZrO_2 catalyst.

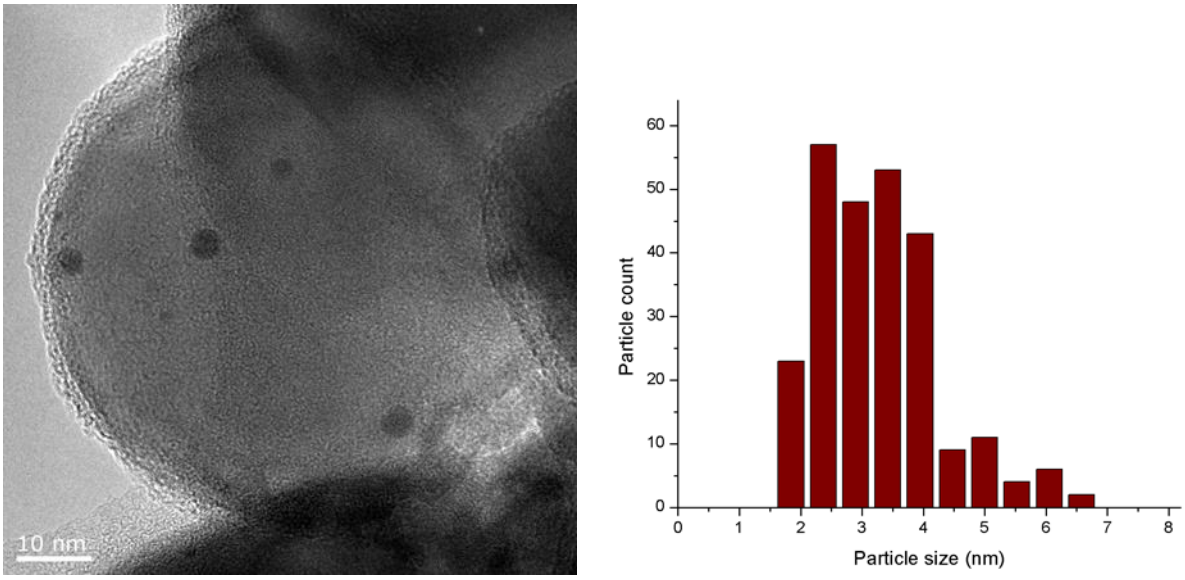

Figure 5.45 A representative TEM image of 0.17 wt% Au_{101}/ZnO catalyst calcined under O_2 (left) and the corresponding statistical Au particle size distribution histogram (right).

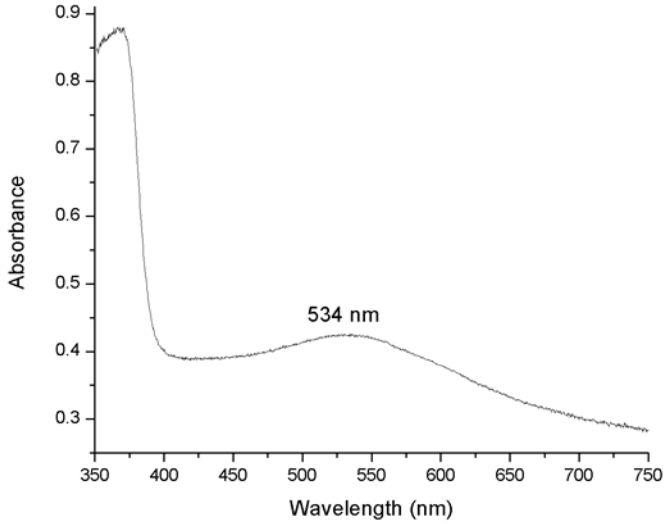

Figure 5.46 UV-vis DR spectrum of 0.17 wt% Au_{101}/ZnO catalyst

5.3 Conclusion

In summary, synchrotron XPS and XAS, TEM and UV-vis DRS studies allowed to shed light on the electronic structure and particle size of phosphine-stabilized Au clusters supported and activated on TiO_2. Calcination under O_2 and combined O_2-H_2 conditions resulted in partial removal of phosphine ligands. P XP spectra indicate that phosphine ligands were oxidized to form phosphine oxide (possibly by interacting with oxygen from the TiO_2 surface). Combined O_2-H_2 calcination under results in a complete sintering of Au_8, Au_9 and Au_{101} clusters on TiO_2 and complete removal of phosphine ligands from the Au cores and oxidation of phosphine ligands (possibly by interacting with oxygen from TiO_2 surfaces). There is clear correlation between results of TEM and UV-vis DRS study of Au/TiO_2 systems indicating gradual growth of Au particle sizes in the series (pure, pristine clusters)<<(as deposited, untreated)<(calcined under O_2)<(calcined under O_2-H_2). Au_{101}/SiO_2 catalysts also show similar Au_{101} particle aggregation upon calcination (according to TEM), yet observed trends in position of LSPR band are impossible to explain based on trends in Au particle size alone. Using sol-immobilisation method, Au_{101} clusters deposited onto TiO_2, SiO_2, ZrO_2 and ZnO support followed calcination under O_2 display almost a similar mean Au particle size (*ca*. 3.5 nm).

Chapter 6

Benzyl alcohol oxidation using supported Au and Ru clusters

This chapter discusses about the catalytic performance of supported Au and Ru clusters on metal oxide supports. Part of this work has been recently published in the journal *Catalysis Science & Technology*. All experiments in this chapter were performed by the author of this thesis with Dr. Meike Holzenkaempfer helped with the development of HPLC methodology.

Abstract

A series of metal clusters containing Au and Ru metal stabilized by organic ligands (Au_8, Au_9, Au_{101}, $AuRu_3$, Ru_3, Ru_4) were deposited and activated on TiO_2 (anatase) and fumed SiO_2 (fumed). Au_{101}-based catalysts showed almost a complete oxidation of benzyl alcohol (>90 %) within 3 hours at 80 °C and 3 bar O_2 in methanol with a high substrate-to-metal molar ratio of 5800 and turn-over frequency of 0.69 s^{-1}. Factors influencing catalytic activity were investigated, including metal-support interaction, effects of heat treatments, chemical composition of Au clusters, the size of Au nanoparticles and catalytic conditions. It was found that the anions present in triphenylphosphine Au clusters played a critical role in determining the catalytic activity in this reaction, with NO_3^- diminishing the catalytic activity. High catalytic activity was attributed to the formation of large Au nanoparticles (> 2 nm) that coincides with partial removal of ligands which occurs during heat treatment and catalysis. Selectivity towards the formation of methyl benzoate can be tuned by selection of the reaction temperature. Au_{101} clusters on different metal oxides (TiO_2, ZrO_2 and ZnO) showed a similar catalytic activity and selectivity, suggesting that the influence of different metal oxide supports in benzyl alcohol oxidation is minimal. Ru clusters on TiO_2 show no activity in benzyl alcohol oxidation.

6.1 Introduction

For centuries, Au was considered to be chemically inert and catalytically inactive, making it valuable in jewellery and as coinage metal but worthless for applications in catalysis. However, this perception has changed since the early report by Haruta *et al*. that small Au particles were catalytically active in CO oxidation at low temperature[16] and discovery by Hutchings *et al.* that a gold-based catalyst could be used in the hydrochlorination of acetylene.[304] These discoveries triggered a revolution in Au-

based catalysis, with numerous follow-up papers demonstrating the superiority of Au-based catalysts over the more expensive Pt group metals in various catalytic processes, with improvements in activity, selectivity and stability against deactivation paving a pathway to numerous commercially-oriented patents.[24, 25] Gold catalysts are now commercially used for eliminating odours in restrooms and air purification.[24] The number of studies on nanoparticulate Au-based catalysts for a broad range of bulk and fine chemical synthesis processes has grown exponentially.[26, 305, 306]

Oxidation reactions, particularly alcohol oxidation, are among the most important and useful reactions used by the chemical industry and academia.[30, 124] The most common commercial methods of alcohol oxidation use stoichiometric oxidants, such as chromates, permanganates or peroxides, that often yield a large amount of environmentally dangerous waste.[307] The use of harmful organic solvents (*e.g.* chlorinated solvents) may also have a negative environmental impact.[303] There is an urgent need to move towards environmentally benign and cost-effective processes involving renewable, environmentally friendly and cheap oxidants, such as molecular oxygen or atmospheric air as opposed to peroxides (*e.g.* H_2O_2 and *tert*-butyl hydroperoxide) with the help of suitable catalysts.[308] In recent years, liquid phase oxidation of alcohols has become popular as a model catalytic test, due to simple setup and handling procedures and relatively mild reaction conditions.[303, 309] Supported platinum group catalysts are widely used in oxidation of alcohols, yet they often require a secondary metal as a promoter to increase the selectivity and stability of such catalysts.[310-314] Hence, gold-based catalysts could be advantageous if such systems would not suffer from the stability and selectivity issues.[18]

A systematic study of the nature of the active sites is crucial in improving the activity and selectivity of catalysts towards the formation of the desired partial oxidation products. In the case of heterogeneous Au-based catalysts the following factors are often considered to define the catalytic activity and selectivity: gold particle size and morphology, oxidation state of Au species, metal-support interaction and specific parameters of catalytic testing conditions. The nature of the active site in the liquid phase oxidation of alcohols currently is still unclear, with both ultra-small particles (< 2 nm)[164, 315] and larger particles (> 2 nm)[316] reported as active catalysts. Tsukuda *et al*. reported that as the size of Au nanoparticles reduced below 2 nm, the turnover frequency (TOF) for the aerobic oxidation of p-hydroxybenzylalcohol increased significantly.[112] The authors proposed that the catalytic activity of these small Au nanoparticles was due to the increased electron density on the Au core and also charge transfer from the poly(N-vinyl-2-pyrrolidone) ligands. However, Haider *et al*. observed that smaller size was not necessarily responsible for higher activity – the authors reported that the optimum size of the Au nanoparticles for ethanol oxidation is *ca*. 7 nm, irrespective of the supports.[316] Zheng *et al*. also observed

a similar trend in ethanol oxidation in which the most active catalyst contained Au nanoparticles of around 6 nm.[242]

There are currently only very few studies on the effects of the Au nanoparticle precursor (size, composition *etc*.) on the performance of resulting catalysts since the majority of reports in the literature are focused predominantly on the morphology and size of Au nanoparticles.[164, 203, 254, 317] Colloidal Au nanoparticles are usually stabilized by organic molecules or polymers which prevent aggregation (further growth) by stabilizing the high-energy surface of Au nanoparticles.[158, 318] It was previously thought that ligand removal was necessary to allow for the access of reactants to the surface of catalysts.[319, 320] Only recently, several studies on the effects of ligands, such as citrate, polyvinylpyrrolidone and polyvinyl alcohol, on the performance of gold-based catalysts have been reported in a wide range of catalytic reactions - glycerol oxidation,[252] hydrogenation of cinnamaldehyde[321] and reduction of p-nitrophenol.[318] Chen *et al*. reported that PVP-stabilized Au nanoparticles greatly enhanced the selectivity towards benzaldehyde in benzyl alcohol oxidation.[322] The authors proposed that PVP might act to isolate chemisorb benzaldehyde and benzyl alcohol to stop further reaction to produce benzyl benzoate; hence the benzaldehyde selectivity reached ~100%. A similar observation of ligand tuning selectivity was also reported by Tsukuda and co-workers in benzyl alcohol oxidation using thiolate-stabilized Au_{25} clusters on porous carbon.[323] The authors suggested that the residual thiol ligands on the surface of Au nanoparticles prevent the esterification of benzyl alcohol and benzaldehyde by site isolation, retaining high selectivity of benzaldehyde. These findings clearly suggest that the nature of ligands plays a critical role in determining the performance of a catalytically active Au particles in a particular reaction, perhaps, similarly to the role of support.[192] Hence, it is important to study the effect of the composition (size of the Au core, neutral organic ligands and anionic ligands or counter-ions) of precursors used in fabrication of gold-based catalysts in order to design catalysts with high activity and improved selectivity.

Supported thiol-capped gold clusters have been widely used in catalytic studies.[324-326] For example, Jin *et al.* supported $Au_{25}(SR)_{18}$, $Au_{38}(SR)_{24}$ and $Au_{99}(SPh)_{42}$ clusters on various metal oxides and tested them in selective oxidation and hydrogenation reactions.[48, 204, 327, 328] Tsukuda *et al.* used $Au_{10}(SG)_{10}$, $Au_{18}(SG)_{14}$, $Au_{25}(SG)_{18}$ and $Au_{39}(SG)_{24}$ deposited on hydroxyapatite in styrene oxidation.[329] In contrast, very few studies have focussed on using phosphine-capped Au nanoparticles in catalysis.[330, 331] Phosphine ligands have weaker bonding interaction between Au and phosphorous (P) atoms compared to the Au-S interactions in thiol-capped Au nanoparticles.[110]

Building on the recent X-ray spectroscopy studies of supported triphenylphosphine-stabilised Au nanoparticles (published in *PCCP*),[153, 154] the aim of this chapter is to study the catalytic performance of materials derived from selected phosphine-capped Au clusters, supported and activated on titania and silica using liquid phase benzyl alcohol oxidation as a model catalytic test. Herein, a series of Au clusters: $Au_{101}(PPh_3)_{21}Cl_5$ (denoted as Au_{101} with mean size of 1.6 ± 0.3 nm) and $Au_9(PPh_3)_8(NO_3)_3$ (denoted as Au_9 with mean size of 0.8 nm) and Ru clusters: $Ru_3(CO)_{12}$ (denoted as Ru_3), $Ru_4H_4(CO)_{12}$ (denoted as Ru_4) and $Ru_3(AuPPh_3)(Cl)(CO)_{10}$ (denoted as $AuRu_3$) were prepared. These clusters were then deposited and activated on TiO_2 (anatase), SiO_2 (fumed), ZrO_2 and ZnO using sol-immobilisation method;[153, 154]; a well-established method developed earlier by Rossi,[30] Jin[204] and Hutchings[332] for immobilising pre-synthesized gold nanoparticles or clusters onto supports. Sol-immobilisation method was shown to give minimal aggregation and high dispersion of Au nanoparticles on the supports.[333] The catalysts were then calcined under different atmospheres: oxygen (O_2) and oxygen and subsequently hydrogen (O_2-H_2) at 200 °C to dislodge the phosphine ligands and expose the metal core adsorbed on the support to facilitate access by the substrate.[153]

6.2 Results and Discussions

6.2.1 Catalyst characterization

Au_{101} nanoparticles and Au_9 clusters are smaller than 2 nm, are highly monodisperse, have a high surface area to volume ratio, and do not have a localised surface plasmon resonance (LSPR) due to their non-metallic surface state.[108, 110] We prepared heterogeneous Au catalysts derived from Au_{101} and Au_9 clusters deposited onto the surface of TiO_2 (anatase) and SiO_2 (fumed) nanopowders. The 0.17 wt% Au_{101}/TiO_2-untreated and 0.17 wt% Au_9/TiO_2-untreated catalysts made *via* sol-immobilisation method show minimal cluster aggregation (Table 6.1). Although, in the case of Au_8 and Au_9 clusters, poor contrast did not allow precise particle size determination, absence of larger, easily visible in HRTEM aggregates is evident. Our earlier study using synchrotron XPS and NEXAS also confirmed presence of significant fraction of supported Au_9 clusters on TiO_2.[153] The Au loading of 0.17 wt% on TiO_2 was chosen to minimize the aggregation of gold nanoparticles, yet still to be able to obtain discernible signals in X-ray photoelectron spectroscopy (XPS) and UV-vis diffuse reflectance spectroscopy (UV-vis DRS) studies. In the case of clusters supported on fumed SiO_2, the Au loading was normalised based on the surface area (to be 0.5 wt%) in order to obtain equivalent (to TiO_2) surface coverage by clusters.

A careful heat-treatment was employed in order to remove the capping ligands and expose gold core to the substrate, yet to minimise aggregation. Here, calcination of the catalysts was done at 200 °C

under different environments: under pure oxygen (O_2) and oxygen followed by hydrogen (O_2-H_2).[203, 329] After calcination, the Au clusters aggregated to form larger nanoparticles. TiO_2-based catalysts showed minimal aggregation and narrower particle size distributions as compared to SiO_2-based catalysts, suggesting that gold formed stronger metal-support interaction with TiO_2 *cf.* SiO_2 (Table 6.1). UV-vis DR spectra showed the absence of LSPR bands in the cases of untreated catalysts allowing inferring that the Au clusters were predominantly with sizes below 2 nm and retained their non-metallic state. The appearance of an LSPR band in the UV-vis DR spectra of the TiO_2-supported samples after calcination indicated formation of the plasmonic Au nanoparticles which is indicative of the increase in particle size to greater than 2 nm.[160, 334, 335] It was previously reported that the position of the maximum of the LSPR peak moves to longer wavelength as the size of Au particles increases, although in some cases this general trend broke down due to the effect of the dielectric constant of the surrounding environment.[61, 267, 268, 336] Interestingly, the 0.17 wt% Au_{101}/TiO_2 catalysts showed very minimal aggregation after catalytic reaction. Particle size analysis based on the statistical evaluation of numerous TEM images (Table 6.1) confirms that the increase in particle size after heat-treatments and after catalytic reactions for Au_x/TiO_2 catalysts (x=8,9, 101) was consistent with the red shift in the peak maximum position of the LSPR bands observed in UV-vis DR spectra.

For 0.5 wt% Au_{101}/SiO_2 catalyst, a significant agglomeration occurred. It was obvious that Au clusters even in the 0.5 wt% Au_{101}/SiO_2-untreated catalyst aggregated to form gold nanoparticles of mean size 3.6 ± 1.2 nm, almost twice the size of pristine Au_{101} cluster. The Au cluster also grew non-uniformly to yield a wide particle size distribution with the largest particle found under TEM being *ca.* 8 nm and the smallest was *ca.* 2 nm. (entry 20 in Table 6.1). After calcination under O_2 and O_2 followed by H_2 at 200 °C, the agglomeration progressed further resulting in formation of larger Au nanoparticles and wider particle size distributions (entry 21 and 22 in Table 6.1). A summary of supported Au particle mean sizes and positions of the LSPR peak maxima are given in Table 6.1.

Table 6.1 Summary of the Au particle size and the LSPR peak position of supported Au catalysts.

Entry	Catalysts	Condition	Size (nm)[a]	LSPR peak position (nm)[b]
1	0.17% Au_{101}/TiO_2-untreated	Before reaction	2.0 ± 0.4	No peak
2	0.17% Au_{101}/TiO_2-O_2	Before reaction	3.5 ± 0.8	533
3	0.17% Au_{101}/TiO_2-O_2-H_2	Before reaction	4.4 ± 1.2	540
4	0.17% Au_{101}/TiO_2-untreated	After reaction	3.6 ± 1.2	540
5	0.17% Au_{101}/TiO_2-O_2	After reaction	3.9 ± 1.0	541
6	0.17% Au_{101}/TiO_2-O_2-H_2	After reaction	4.6 ± 1.5	546
7	0.17% Au_{101}/TiO_2-untreated	After recycle	4.6 ± 2.5	541
8	0.17% Au_{101}/TiO_2-O_2	After recycle	4.2 ± 1.2	547
9	0.17% Au_{101}/TiO_2-O_2-H_2	After recycle	5.0 ± 1.5	551
10	1.3% Au_{101}/TiO_2-untreated	Before reaction	2.7 ± 0.6	530
11	0.17% Au_9/TiO_2-untreated	Before reaction	< 2[c]	No peak
12	0.17% Au_9/TiO_2-O_2	Before reaction	2.4 ± 0.5	555
13	0.17% Au_9/TiO_2-O_2-H_2	Before reaction	2.9 ± 0.9	558
14	0.17% Au_8/TiO_2-untreated	Before reaction	< 2[c]	No peak
15	0.17% Au_8/TiO_2-O_2	Before reaction	2.2 ± 1.5	552
16	0.17% Au_8/TiO_2-O_2-H_2	Before reaction	2.9 ± 0.9	555
17	0.17% Au_{101}/SiO_2-untreated	Before reaction	< 2[c]	No peak
18	0.17% Au_{101}/SiO_2-O_2	Before reaction	3.6 ± 2.7	529
19	0.17% Au_{101}/SiO_2-O_2-H_2	Before reaction	4.4 ± 2.5	524
20	0.5% Au_{101}/SiO_2-untreated	Before reaction	3.6 ± 1.2	537
21	0.5% Au_{101}/SiO_2-O_2	Before reaction	4.7 ± 1.6	525
22	0.5% Au_{101}/SiO_2-O_2-H_2	Before reaction	5.7 ± 2.9	518
23	0.17% Au_{101}/ZrO_2-O_2	Before reaction	3.5 ± 1.4	536
24	0.17% Au_{101}/ZnO-O_2	Before reaction	3.3 ± 1.0	534

[a]Measured using TEM; [b]Measured using UV-vis DRS; [c]Estimated based on the absence of LSPR peak in the UV-vis DR spectra.

The recent XPS study of phosphine-capped Au clusters on TiO_2 showed that for untreated Au_8/TiO_2, Au_9/TiO_2 and Au_{101}/TiO_2, a significant fraction of phosphine ligands were dislodged from the gold core and they formed phosphine oxide-like species by interaction with oxygen on TiO_2 surface.[153] When the catalysts were calcined at 200 °C under O_2 or O_2 followed by H_2, the majority of the phosphine ligand were detached from the gold core, leaving a very tiny amount of phosphine ligand remained intact and associated with the gold core. The fact that only a small amount of residual phosphine ligand bound to gold was found in XPS study is consistent with thermogravimetric analysis data: the complete removal of ligands occurred at 250 °C for Au_{101} clusters, at 240 °C for both Au_9 and Au_8 clusters (Figure 6.1-6.3).

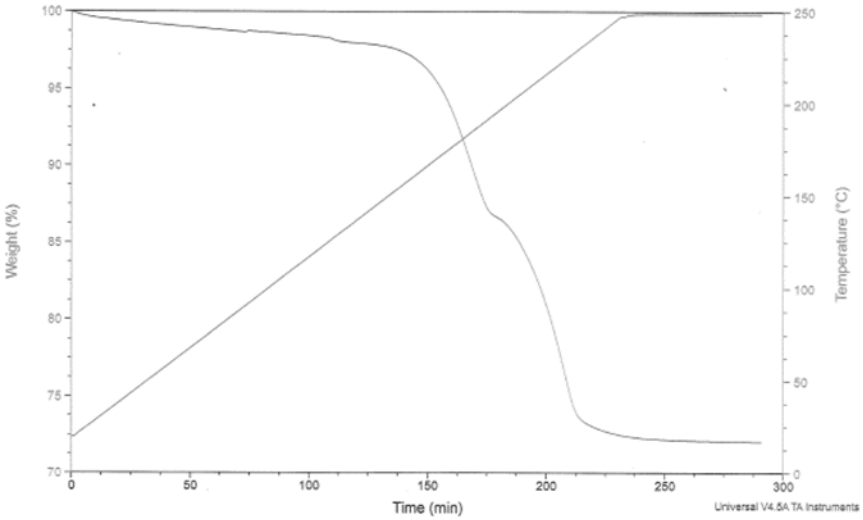

Figure 6.1 Thermogravimetric analysis of Au_{101} cluster.

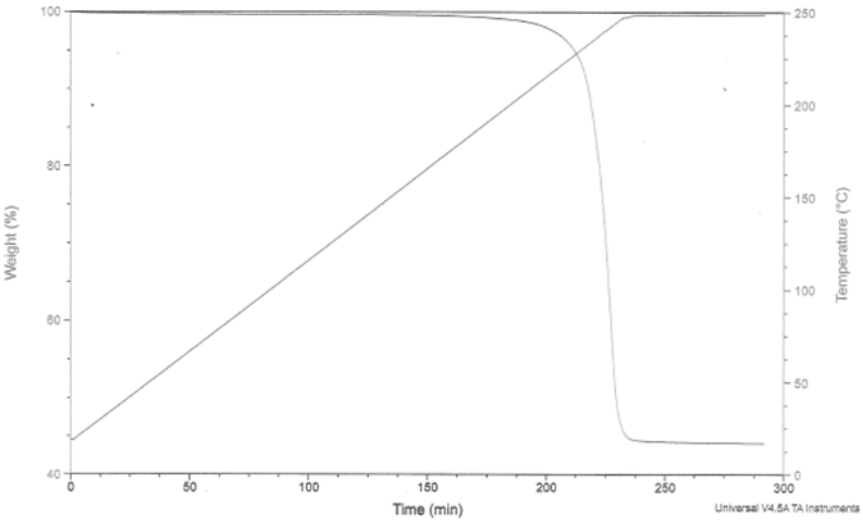

Figure 6.2 Thermogravimetric analysis of Au_9 cluster.

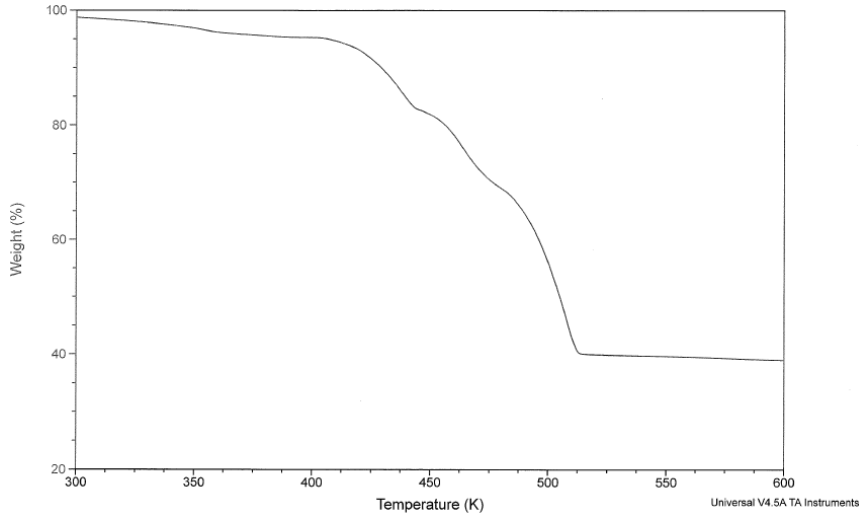

Figure 6.3 Thermogravimetric analysis of Au_8 cluster.

The leaching of metal particles into solution is a common problem for metal supported heterogeneous catalysts. However, our phosphine-stabilised Au clusters did not show signs of leaching during our catalytic studies according to Au loading analysis by AAS (Table 6.2).

Table 6.2 The Au content of the Au_{101}/TiO_2 catalysts as measured by AAS.

Catalyst	**Target loading (%)**	**Experimental measurement (%)**		
		Before reaction	**After 1st test**	**After 2nd test (recycled)**
0.17% Au_{101}/TiO_2-untreated	0.17	0.14 ± 0.01	0.11 ± 0.02	0.11 ± 0.02
0.17% Au_{101}/TiO_2-O_2	0.17	0.13 ± 0.01	0.13 ± 0.02	0.13 ± 0.02
0.17% Au_{101}/TiO_2-O_2-H_2	0.17	0.13 ± 0.01	0.11 ± 0.02	0.13 ± 0.01
0.17% Au_9/TiO_2-untreated	0.17	0.17 ± 0.01	0.15 ± 0.02	0.14 ± 0.02
0.17% Au_9/TiO_2-O_2	0.17	0.15 ± 0.01	0.16 ± 0.01	0.15 ± 0.02
0.17% Au_9/TiO_2-O_2-H_2	0.17	0.17 ± 0.01	0.16 ± 0.02	0.16 ± 0.02
0.17% Au_{101}/SiO_2-untreated	0.17	0.18 ± 0.01	0.17± 0.01	0.17 ± 0.02
0.17% Au_{101}/SiO_2-O_2	0.17	0.19 ± 0.01	0.17 ± 0.02	0.18 ± 0.02
0.17% Au_{101}/SiO_2-O_2-H_2	0.17	0.18 ± 0.02	0.18 ± 0.01	0.17 ± 0.02
0.5% Au_{101}/SiO_2-untreated	0.5	0.50 ± 0.01	0.49 ± 0.01	0.48 ± 0.02
0.5% Au_{101}/SiO_2-O_2	0.5	0.48 ± 0.02	0.49 ± 0.02	0.48 ± 0.01
0.5% Au_{101}/SiO_2-O_2-H_2	0.5	0.46 ± 0.02	0.45 ± 0.02	0.47 ± 0.01

6.2.2 Catalytic testing

The liquid phase oxidation of benzyl alcohol using Au nanoparticle-based catalysts reported here yielded benzoic acid and methyl benzoate as the major products, which were identified using HPLC-MS and quantified using HPLC-UV (using internal standard and solutions of known concentrations of reference compounds for calibration). The untreated catalysts with 0.17 wt% Au loading were inactive, showing no conversion while heat treated catalysts showed almost complete (> 92 %) conversion of benzyl alcohol after 4 hours (see Table 6.3). The most active catalysts gave very high catalytic activity with a molar substrate to metal ratio of 5800 and turnover frequency up to 0.69 s^{-1} (which is orders of magnitude greater than in any of the related earlier reports).

Table 6.3 Comparison of catalytic performance of gold nanoparticles in the oxidation of benzyl alcohol.

Catalysts	**Au content (mol %)**	**Au size (nm)**	**T (K)**	**Pressure (bar)**	**Solvent**	**Time (h)**	**Conversion (%)**	**TOF (s^{-1})**	**Refs.**
Au/MOF-5	1	4.8	353	5	Methanol	3	>99	0.01	337
Au/Al-MIL53	1	~1.0	353	5	Methanol	23	98	0.001	337
Au/CPL-2	1	2.1	353	5	Methanol	23	55	0.0007	337
Au_{25}/CNT calcined 370 °C	1	n/d	353	5	Toluene	8	33	0.011	338
$Au_{13}Cu_8$/CNT calcined 370 °C	1	n/d	353	5	Toluene	8	47	0.016	338
Au_{101}/TiO_2 calcined O_2	0.13	3.5	353	3	Methanol	3	93	0.65	This work
Au_{101}/TiO_2 calcined O_2	0.13	3.5	353	5	Methanol	4	96	0.51	This work
Au_{101}/TiO_2 calcined O_2-H_2	0.13	4.4	353	5	Methanol	4	97	0.51	This work
Au_{101}/SiO_2 calcined O_2-H_2	0.46	5.7	353	5	Methanol	4	99	0.15	This work
Au_{101}/ZrO_2 calcined O_2	0.69	3.5	353	3	Methanol	3	98	0.69	This work
Au_{101}/ZnO calcined O_2	0.67	3.3	353	3	Methanol	3	95	0.67	This work

There are several factors contributing to the high activity of our catalysts. Firstly, the water soluble base (K_2CO_3) is known to be a promoter in liquid phase oxidation of alcohols.[296] Rossi proposed that alcohols cannot adsorb directly onto gold and a base was required to deprotonate the hydroxyl group forming a metal alkoxide prior to adsorption onto gold.[18] The indispensable role of the base was shown when no conversion of benzyl alcohol was achieved in its absence (entry 1 and 2 in Table 6.4). There are studies of benzyl alcohol oxidation using supported-Au catalysts under base-free conditions, however, in those studies, high conversions (> 90 %) were not achieved.[303, 309, 337]

Secondly, the nature of the support and metal-support interaction dictated the performance of the catalysts. The nature of metal-support interaction depends on the type of metal nanoparticles and supports and this could involve electronic modulation of metal nanoparticles and/or supports, charge transfer and bonding between metal nanoparticle and support and physical encapsulation of metal nanoparticles by the supports.[56, 192, 339, 340] For example, catalysts with similar gold loading on different supports, Au_{101} on TiO_2 (0.13 wt% Au by AAS) showed superior performance (Table 6.4) when compared with to analogous catalyst systems made using SiO_2 as a support (with 0.18 wt% Au by AAS). Typically, SiO_2 is considered an inert, non-reducible support whereas TiO_2 is an activating, reducible support due to the ability of Ti centers to be reduced (e.g. from Ti^{4+} to Ti^{3+}) and the presence of defects notably oxygen vacancies.[341, 342] The higher catalytic activity of Au/TiO_2 catalysts over Au/SiO_2 was also observed in CO oxidation in many studies.[128, 296-298] Hence, the size effect of Au nanoparticles alone is not sufficient to explain the activity of supported gold catalysts. Metal-support interactions (MSI) play crucial role in defining reactivity and selectivity of supported Au catalysts. Haruta *et al.* and Hassan *et al.* hypothesized that the oxygen activation occurs at the perimeter (*i.e.* interface) of the gold nanoparticles and metal oxide supports.[26, 271, 343] This hypothesis could explain the lower activity of Au_{101}/SiO_2 catalysts as compared to Au_{101}/anatase in benzyl alcohol oxidation observed in this study, since silica based catalysts with much larger particles will have much smaller surface area corresponding to the gold-support interface.

Table 6.4 Performance of catalysts in the liquid phase oxidation of benzyl alcohol.

Catalysts	Time (h)	Conversion (%)	Selectivity to methyl benzoate (%)	Selectivity to benzoic acid (%)	TOF (s^{-1})
Blank[a]	4	0	0	0	0
TiO_2[a]	4	0	0	0	0
TiO_2	4	0	0	0	0
0.17% PPh_3/ TiO_2	4	0	0	0	0
0.17% $OPPh_3$/ TiO_2	4	0	0	0	0
0.17% $AuPPh_3Cl/TiO_2$	4	0	0	0	0
0.17% Au_{101}/TiO_2-untreated	4	0	0	0	0
0.17% Au_{101}/TiO_2-O_2	4	96	79	21	0.51
0.17% Au_{101}/TiO_2-O_2-H_2	4	97	75	23	0.51
0.17% Au_{101}/TiO_2-untreated[b]	4	29	65	15	0.12
0.17% Au_{101}/TiO_2-O_2[b]	4	96	73	20	0.51
0.17% Au_{101}/TiO_2-O_2-H_2[b]	4	98	70	23	0.51
0.01% Au_{101}/TiO_2-untreated[c]	4	0	0	0	0
0.01% Au_{101}/TiO_2-O_2[c]	4	0	0	0	0
0.01% Au_{101}/TiO_2-O_2-H_2[c]	4	0	0	0	0
1.3% Au_{101}/TiO_2-untreated	4	99	87	13	0.05
0.17% Au_{101}/TiO_2-O_2	3	93	78	22	0.65
0.17% Au_{101}/TiO_2-O_2-H_2	3	92	76	24	0.65
0.17% Au_9/TiO_2-untreated	4	0	0	0	0
0.17% Au_9/TiO_2-O_2	4	0	0	0	0
0.17% Au_9/TiO_2-O_2-H_2	4	20	23	18	0.08
0.17% Au_8/TiO_2-untreated	4	0	0	0	0
0.17% Au_8/TiO_2-O_2	4	0	0	0	0
0.17% Au_8/TiO_2-O_2-H_2	4	30	37	48	0.13
0.17% Au_{101}/SiO_2-untreated	4	0	0	0	0
0.17% Au_{101}/SiO_2-O_2	4	69	72	24	0.25
0.17% Au_{101}/SiO_2-O_2-H_2	4	69	70	26	0.25
0.5% Au_{101}/SiO_2-untreated	4	63	74	16	0.09
0.5% Au_{101}/SiO_2-O_2	4	95	63	31	0.13
0.5% Au_{101}/SiO_2-O_2-H_2	4	99	65	32	0.14

0.17% Au_{101}/ZrO_2-O_2	3	98	78	22	0.69
0.17% Au_{101}/ZnO-O_2	3	95	77	23	0.67
0.17% Ru_3/TiO_2-untreated	4	0	0	0	0
0.17% Ru_4/TiO_2-untreated	4	0	0	0	0
0.17% Ru_3/TiO_2-vacuum[e]	4	0	0	0	0
0.17% Ru_3/TiO_2-vacuum[e]	4	0	0	0	0
0.17% $AuRu_3/TiO_2$-untreated	4	0	0	0	0
0.17% $AuRu_3/TiO_2$-vacuum[e]	4	66	72	21	0.24
0.17% Au_{101}/TiO_2-O_2 + KNO_3	4	85	78	21	0.46
0.17% Au_9/TiO_2-O_2 + KCl	4	0	0	0	0

Reaction conditions: 50 mg catalyst, 2.5 mmol benzyl alcohol, 25 mL methanol (solvent), 1.25 mmol anisole (internal standard), 2.5 mmol K_2CO_3, 5 bar O_2 pressure, 80 °C. [a]Without base (K_2CO_3) and catalysts. [b]Recycled catalysts. [c]850 mg of a catalyst was used to retain the same total amount of metal as in the case of 0.17 wt% Au catalyst. [d]KNO_3 (or KCl) was added according to equivalent molar percentage by impregnation method. [e]The catalysts were calcined under vacuum at 200 °C.

The high activity of heat treated catalysts can be attributed to stronger metal-support interaction established during calcination. Haruta *et al.* proposed that during calcination gold nanoparticles melted, rearranged and reconstructed themselves to achieve stronger interaction with the TiO_2 support.[344] This hypothesis is in line with report by Buffat and Borel that 2 nm Au nanoparticles melt around 600 K,[345] which is significantly lower than the melting point of the bulk gold (1337 K). Yiliang *et al*. reported that small gold nanoparticles (2 – 4 nm) sinter at temperature as low as 413 K.[346] The sintering of gold nanoparticles around 423 K was also reported by Coutts *et al.*[283] The mechanism in which sintering of Au nanoparticles occurs is still under debate. Tilley and co-workers investigated the sintering of oleylamine-capped Au nanoparticles below 250 °C.[249] They author reported that ligands were first desorbed from the Au core followed by the aggregation of separate Au nanoparticles and finally the grain growth occur. Hence, it is experimentally observed that small Au nanoparticles could aggregate below the melting point. Analysis of supported-gold particle sizes as measured by TEM (Table 6.1) showed that the particle size distribution of gold nanoparticles was wider (indicated by larger standard deviation) on SiO_2 support as compared to TiO_2 for the same Au loading (target 0.17 wt%), suggesting that weaker metal-support interaction in Au_{101}/SiO_2 catalysts facilitates aggregation resulting in wider particle size distributions despite the significantly higher surface area of SiO_2 support. Interestingly, for Au_{101} clusters deposited on TiO_2, ZrO_2 and ZnO supports and calcined under O_2 show similar activity and selectivity, indicating that these metal oxide (MOX) supports have very little influence on catalytic performance of Au_{101}-based

catalysts. This type of metal oxides (TiO_2, ZrO_2 and ZnO) is known to be reducing supports and to have naturally occurring defects such as oxygen vacancies as well as similar isoelectric point (~ pH 7)[276, 301] and thus, could explain the similar catalytic activity.

For the same Au loading (0.17 wt%) and support (TiO_2), Au_{101} cluster-based catalysts showed much higher catalytic activity compared to Au_8-based and Au_9-based catalysts even though the Au particle sizes were smaller in the case of Au_9/TiO_2 (*cf.* Au_{101}/TiO_2 analogues, Table 6.1). We hypothesize that the presence of anionic species within the gold cluster (Cl^- in Au_{101} *vs.* NO_3^- in Au_8 and Au_9) strongly affected the catalytic activity. To identify the anionic component of the cluster precursor responsible for quenching of the catalytic activity, we investigated the role of such anionic component in benzyl alcohol oxidation. Firstly, we added KCl calculated according to the weight percentage of Cl^- in $Au_{101}(PPh_3)_{21}Cl_5$ (0.08 wt%) to mimic the presence of Cl^- anion to Au_9/TiO_2 catalyst and calcined under O_2 to resemble Au_{101}/TiO_2-O_2, and we found no increase in the catalytic activity (Table 2, last entry). When KNO_3 (amount estimated to mimic the amount of NO_3^- from Au_9, 4.6 wt%) was added to the Au_{101}/TiO_2 catalysts, a noticeable reduction in the catalytic activity was observed (Table 6.4, penultimate entry). Hence, it appears that the presence of NO_3^- lowers the catalytic activity of Au_{101}-based catalysts and could be the reason for the significantly lower activity of Au_8-based and Au_9-based analogues. To the best of the author's knowledge this is the first report of the effect of NO_3^- on activity of gold-based heterogeneous catalysts. While numerous studies report that ultra-small gold nanoparticles (< 2 nm) are the key active site,[106, 112, 164] these results demonstrate that the size of gold nanoparticles alone is not sufficient to explain the catalytic activity of catalysts made using phosphine-capped Au nanoparticles as it is strongly affected by the type of anions present in the supported gold cluster catalysts, type of support and activation treatment protocols.

The effect of different calcination conditions is negligible for Au_{101}-based catalysts but has significant impact on Au_8/TiO_2 and Au_9/TiO_2 catalysts (see Table 2). Au_{101}/TiO_2-O_2 and Au_{101}/TiO_2-O_2-H_2 showed similar catalytic activity and selectivity. However, Au_9/TiO_2-O_2-H_2 (similar for Au_8/TiO_2-O_2-H_2 catalyst) showed significantly higher activity as compared to Au_9/TiO_2-O_2 and Au_9/TiO_2-untreated (similar for Au_8/TiO_2-O_2 and Au_8/TiO_2-untreated) which were inactive. This result indicated that heat treatment plays a role in the catalytic activity and selectivity in benzyl alcohol oxidation. Youzhu *et al.* prepared Au_9/TiO_2 for CO oxidation.[347] The authors observed that untreated Au_9/TiO_2 catalyst was inactive for CO oxidation while heat treated Au_9/TiO_2 catalyst under 5% H_2/Ar was active. However, they did not comment on the difference of catalytic activity of those catalysts. However, it is worth mentioning that at this stage the true nature of NO_3^- after a combined O_2-H_2 calcination could not be established

because the present XPS analysis provides no evidence of how and the nature of NO_3^- changes after such calcination.[348]

All Ru-based catalysts were inactive in benzyl alcohol oxidation except for $AuRu_3/TiO_2$ treated under vacuum at 200 °C. $AuRu_3/TiO_2$-vacuum shows a significant conversion at 66%. It is believed that the addition of Au metal into Ru cluster promotes the catalytic activity *via* synergistic effect between the metals. Such synergistic effect contributing to the catalytic activity of mixed-metal nanoparticles has been observed in catalysis.[349, 350] For example, Garcia et al. showed that bimetallic AuAg/C catalysts showed superior performance as compared to the monometallic (Au/C and Ag/C) catalysts in electro-oxidation of glycerol.[349] In this study, the monometallic catalyst $AuPPh_3Cl/TiO_2$ and Ru_3/TiO_2 were inactive in benzyl alcohol oxidation. However, the bimetallic catalyst $AuRu_3/TiO_2$ (which was synthesized from $AuPPh_3Cl$ and $Ru_3(CO)_{12}$ precursors) displayed an a high catalytic activity, which could be attributed to the synergistic effect between Au and Ru metals. This synergistic effect is subjected to the surface electronic states which is altered by the geometric parameters such as local strain, atomic coordination numbers at the surface.[351] Shastri and Schwank found that O_2 adsorbed at lower temperature than Au.[352] Chavadej and co-workers attributed the increased activity of Ru-Au catalysts in methanol oxidation due to the creation of different types of adsorption/desorption sites in the system.[353] Based on these findings, it could be inferred that the synergistic effect in $AuRu_3/TiO_2$ catalysts resulted in a higher catalytic activity over their monometallic counterparts.

The proposed reaction pathway of benzyl alcohol oxidation in methanol in the presence of base is shown in Figure 6.4. Benzyl alcohol is first oxidized to benzaldehyde, which serves as an intermediate in this catalytic system. In the presence of base, benzaldehyde is preferentially oxidized further to benzoic acid.[113, 124] The formation of methyl ester resulted from the reaction between benzaldehyde and methanol (the solvent). We carried out a control reaction using benzaldehyde and benzoic acid as substrates (instead of benzyl alcohol). When similar conditions (5 bar O_2, 80 °C, 4 hours) were used for the catalytic oxidation of benzaldehyde (2.5 mmol) in methanol (25 mL) using Au_{101}/anatase catalysts, a complete transformation of benzaldehyde to benzoic acid and methyl benzoate with the same distribution of products (*i.e.* benzoic acid:methyl benzoate of 70:30) was observed. However, any reaction when benzoic acid was used as a substrate was not found. Here, the observations excluded the formation of the methyl ester *via* the benzoic acid route. Sedigheh Ghadamgahi (Golovko group) performed a catalytic oxidation of benzyl alcohol in ethanol as solvent and found that the ethyl benzoate was formed as one of the products.[354] Hence, it could be generalized that alcoholic solvents contribute to the formation of ester in benzyl alcohol oxidation.

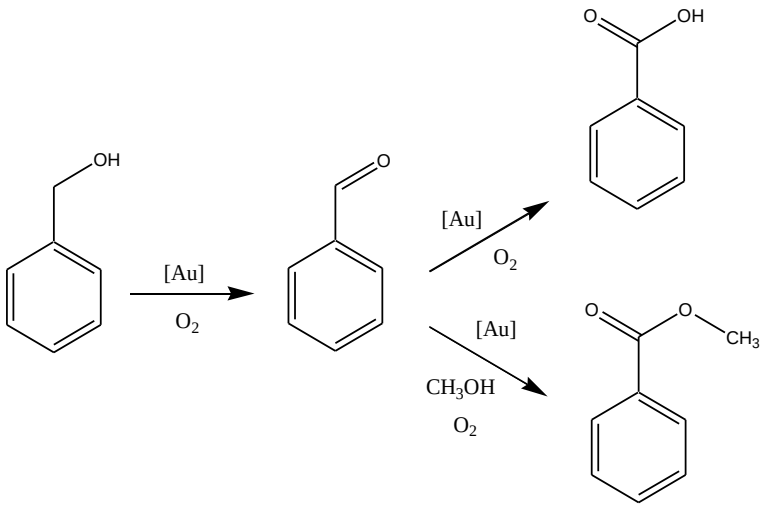

Figure 6.4 Proposed reaction pathway of oxidation of benzyl alcohol in methanol

The Au nanoparticles in Au_{101}/TiO_2 catalysts agglomerated slightly after the catalytic tests (Table 6.1). The Au_{101}/TiO_2-untreated catalyst was active upon recycling (*i.e.* in the 2nd consecutive catalytic test) and showed significant conversion (29%), and formed considerable amount of benzaldehyde as compared to other catalytic tests in this study (Figure 6.5). The increased in activity of 0.17 wt% Au_{101}/TiO_2-untreated could be attributed to the increase in size of the gold nanoparticles and the loss of phosphine ligands from the gold core. ^{31}P NMR spectrum of the reaction mixture showed the presence of triphenylphosphine oxide, which originated from phosphine ligands dislodged from the Au core, which then oxidized during the catalytic reaction. Both heat treated Au_{101}/TiO_2 catalysts under O_2 and O_2-H_2 showed no significant loss of catalytic activity and selectivity after the first catalytic test.

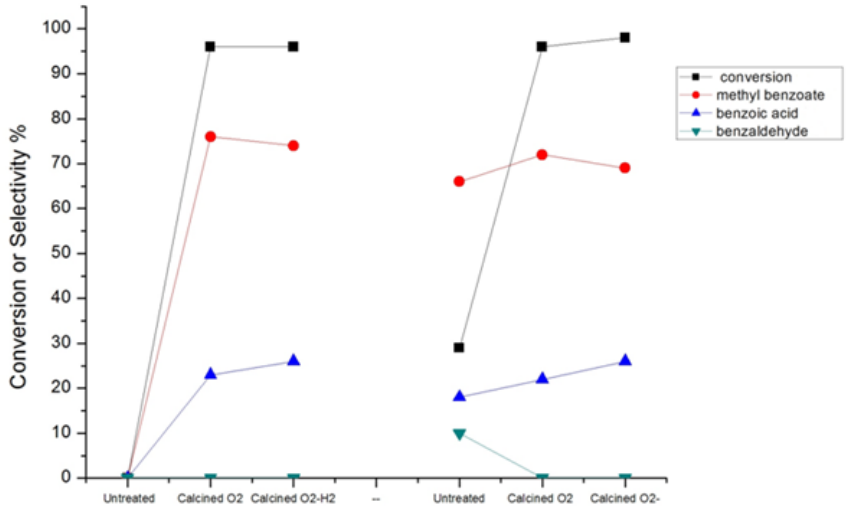

Figure 6.5 Recycling of the 0.17% Au_{101}/anatase calcined O_2 (left: fresh catalysts, right: recycled catalysts). Reaction conditions: 2.5 mmol benzyl alcohol, 25 ml MeOH (solvent), 1.25 mmol anisole (internal standard), 2.5 mmol K_2CO_3, 5 bar O_2, 80 °C, 4 hrs.

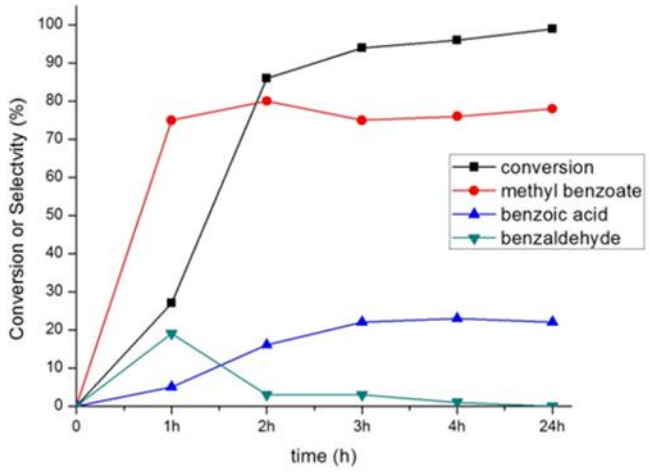

Figure 6.6 Time-dependent profile of benzyl alcohol oxidation using 0.17% Au_{101}/TiO_2-O_2. Reaction conditions: 2.5 mmol benzyl alcohol, 25 mL methanol, 1.25 mmol anisole, 2.5 mmol K_2CO_3, 5 bar O_2 pressure at 80 °C.

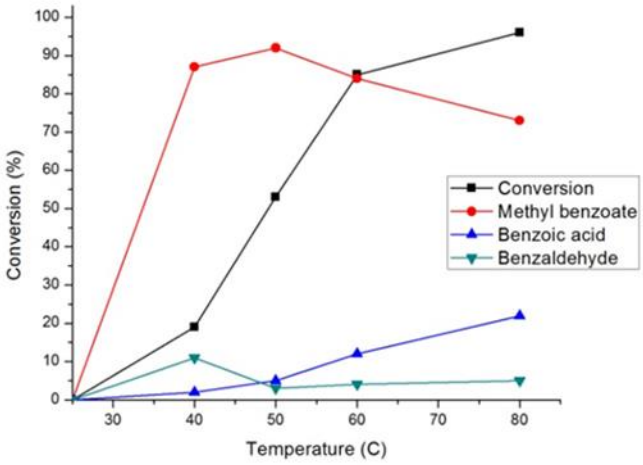

Figure 6.7 Effect of the temperature on the conversion and profile of benzyl alcohol oxidation products using 0.17% Au_{101}/TiO_2-O_2. Reaction conditions: 2.5 mmol benzyl alcohol, 25 mL methanol, 1.25 mmol anisole, 2.5 mmol K_2CO_3, 5 bar O_2 pressure and 4 hours.

The evolution of conversion and selectivity of benzyl alcohol oxidation as a function of time is presented in Figure 6.6 above. The high conversion of benzyl alcohol (80- 90 %) was observed after the first two to three hours. The selectivity towards the formation of methyl benzoate and benzoic acid are independent of reaction time but primarily dependent on the reaction temperature, as shown in Figure 6.7 above. A considerable amount (*ca*. 20%) benzaldehyde was formed after one hour and then depleted over time (Figure 6.6), suggesting that benzaldehyde is the intermediate in for the formation of benzoic acid and methyl benzoate in benzyl alcohol oxidation.[355-357] The effect of the temperature in this reaction was studied from room temperature (25 °C) up to 80 °C (Figure 6.7). Reduction in the temperature of the catalytic reaction results in the reduction of the catalytic activity. However, the product selectivity showed non-linear behaviour. The highest selectivity towards methyl benzoate (93 %) was observed at 50 °C with 53 % conversion of benzyl alcohol, suggesting the selective formation of methyl benzoate is possible by manipulating the reaction temperature.

6.3 Conclusion

In summary, a high catalytic activity (conversions of > 90 %) is achieved using Au_{101}-based catalysts whereas Au_9-based catalysts are barely active. In this study, that the catalytic performance in benzyl alcohol oxidation is strongly affected by the presence of anions in gold clusters: the presence of NO_3^- anion lowers the catalytic activity in catalytic oxidation of benzyl alcohol. For Au_{101}-based catalysts on TiO_2, SiO_2, ZrO_2 and ZnO, the catalytic activity appears with the formation of large (> 2 nm) gold nanoparticles which coincides with the partial removal of phosphine ligands. A higher catalytic activity of TiO_2-supported catalysts as compared to that of SiO_2-supported catalysts could be due to the stronger metal-support interaction effect as proposed by Haruta. Au_{101} clusters deposited on TiO_2, ZrO_2 and ZnO, and calcined under O_2 exhibit a similar catalytic activity and selectivity. The effect of heat treatment on under different atmospheres on catalytic performance is less pronounced in the case of Au_{101}/TiO_2 catalysts, but significantly affects Au_9/TiO_2 catalysts with noticeable catalytic activity (20 % conversion) observed only for Au_9/TiO_2-O_2-H_2. The selectivity of toward the formation of methyl benzoate can be tuned by manipulating the reaction temperature. The highest selectivity towards methyl benzoate is achieved at 50 °C with 93%. The bimetallic catalyst $AuRu_3/TiO_2$ displays a remarkable catalytic activity as compared to the monometallic $AuPPh_3Cl/TiO_2$ and Ru_3/TiO_2 catalysts, which could be due to the synergistic effect between Au and Ru metal.

Chapter 7

Hydrogen gas sensing using gold nanoparticles on WO_3 thin films

This chapter reports the results of a side-project to the main aims of the thesis, conducted as a joint project with our collaborators, Prof. Wojtek Wlodarski and his group at the Electrical Engineering Department, RMIT University, Melbourne, Australia. The objective of the project was to fabricate gold clusters as a catalytic material on thin film supports deposited on the transducers for hydrogen gas sensing. The author specific role in this project were to synthesize gold clusters, namely $(Au_9(PPh_3)_8)(NO_3)_3$ and deposit them on transducer thin films. The thin films were then characterized using electron microscopy techniques for particle imaging and statistical analysis (performed by the author). The sensing elements (thin films with clusters) were sent to the collaborators at RMIT (Muhammad Zamharir and Professor Wojtek Wlodarski) for hydrogen gas sensing testing using conductometric sensing system. This chapter discusses the results of H_2 sensing using produced materials in the light of their fabrication and characterization. Results of this study had been published in the *International Journal of Hydrogen Energy* ***38****(29): 12865-12877*.

Abstract

Atomically precise gold clusters, $Au_9(PPh_3)_8(NO_3)_3$ (referred to as Au_9) prepared *via* a wet-chemistry method, were deposited onto tungsten oxide (WO_3) thin films using dip-coating into solutions of clusters at two concentrations, and then annealed at 400 °C to remove the organic ligands and produce activated transducer thin films as sensors for hydrogen gas. Two sensors, S1 and S2, used in this study were deposited from the Au_9 solution at the cluster concentrations of 0.01 mg/mL and 0.1 mg/mL, respectively. The Au/WO_3 sensors were tested in hydrogen detection at varying H_2 concentration from 0.06 to 1.0 v/v % in synthetic air at operating temperatures ranging from ambient up to 450 °C. It was found that the optimal temperature for the sensor S1 occurred at 300 °C and for the sensor S2 at 350 °C. The sensor with a lower Au loading was identified to give resistance changes of greater magnitude in response to exposure to H_2, excellent baseline stability and more active dynamic performance. The HRTEM images provide the evidence that the more active sensor, S1, was enriched with sub-5 nm Au particles. Finally, the sensing mechanism was also suggested based on several earlier reports on related systems in the literature.

7.1 Introduction

Hydrogen typically exists as a diatomic gas in nature and its content in atmospheric air at sea level is 0.5 ppm.[358, 359] Its characteristics include low density (0.09 kg/m^3), low minimum ignition energy (MIE = 0.02 mJ), high enthalpy of combustion ΔH = -286 kJ/mol), high diffusion coefficient (0.61 cm^2/s in air) and a wide flammable range (4-75 v/v/%).[360, 361] The hydrogen gas is attractive as a source of energy in a wide range of industrial and scientific applications due to its non-toxicity (water as the only product of combustion) and abundant source (*via* splitting water).[362] Currently, hydrogen (derived predominantly from natural gas) plays a crucial role in hydrogenation reactions (particularly of unsaturated hydrocarbons) performed by chemical industry in the presence of catalysts like nickel, gold, platinum and palladium.[204, 363-365] Owing to its reducing property, it has been employed as a reducing agent in many chemical reactions, notably in metal nanoparticle syntheses.[366]

From an environmental point of view, hydrogen burns in air to form water without producing harmful products or by-products, including the important greenhouse gas, CO_2.[367] Therefore, the use of hydrogen as fuel (replacing currently common hydrocarbons) is expected to reduce CO_2 emissions. Unlike most combustible hydrocarbon-based fuels, hydrogen has high energy per mass content, 143 MJ kg^{-1} (*cf.* gasoline 47 MJ kg^{-1} and methane 56 MJ kg^{-1}).[368] The impending energy crisis resulting from a depletion of petroleum fuel source has led to consideration and utilization of hydrogen as an alternative clean and renewable energy source for the future.[369] The potential use of hydrogen as future energy has been demonstrated earlier on an example of using it as a rocket fuel.[370, 371] More crucially, numerous studies have demonstrated that electro/photo/catalytic water splitting process could produce hydrogen from water allowing to a complete green cycle of H_2-H_2O-H_2 in energy storage and conservation.[372-374]

Despite the compelling attractions of hydrogen as an alternative fuel, it entails some risk as a highly flammable gas because of its wide range of flammable mixtures (v/v %) with air and very low flash point.[375] Hence, extreme precautions are taken when dealing with hydrogen including its safe production, storage and transportation. Currently, the most common method for hydrogen production is stream-methane reforming (SMR) process, which is also the most economical method in the case of hydrogen produced using hydrocarbon feedstock.[376, 377] Methods of the safe storage of hydrogen include high-pressure storage, adsorptive storage on high surface area adsorbents, chemical storage in metal and complex hydrides as well as in boranes and their analogues.[378-382] However, storage and use of even a small quantity of H_2 typically needed for operation of portable fuel cells (e.g. fuel cell based car system) raise concerns about and require implementation of an adequate safety (leak detection) system due high flammability of H_2 even at low concentrations (4 v/v%).[383]

With its characteristics (odourless, colourless and tasteless gas) it can be difficult to detect hydrogen leaks in a closed or open area. In regards to this issue, there is an urgency to develop a H_2 sensing system with low cost, high sensitivity and fast response to minimize the risk of explosion. The characteristics of a successful hydrogen sensor are small size, low cost, high sensitivity as well as thermal and chemical stability.[384]

A chemical sensor is a device that exploits a chemical reaction or process between the analyte gas and the sensor device to transform the quantitative or qualitative chemical information into a useful analytical electronic signal.[385, 386] The typical electronic signal includes current (I), voltages (V), resistance (R), frequency (Hz) and optical absorbance.[370] Many commercially available hydrogen sensors use a transducer device that produce electrical signals with a magnitude corresponds to the concentration of the analyte gas.[386] A market survey performed by Banach and co-workers stated that commercially available H_2 sensors are based primarily on semiconductor metal oxides (MOX) materials capable of detecting hydrogen by means of electrochemical H_2 oxidation, catalytic response and optical response.[387]

Conductometric sensors based on semiconductor metal oxides (MOX) involve use of a wide band gap semiconductor material, such as titanium dioxide (TiO_2), zinc oxide (ZnO), tungsten oxide (WO_3), tin oxide (SnO_2), as the active element of the sensor.[388-390] This type of a sensor requires operating at elevated temperature in order to obtain a stable measurable change in resistance.[391] The variation of hydrogen concentration affects the magnitude of a change in resistance and should exhibit a linear relationship for a propitious hydrogen sensor. The performance of a gas sensor is characterized by the sensor response, baseline stability and the dynamic performance. The sensor response (S) reflects the sensitivity and linearity of a sensor and is calculated as the ratio of the resistance of the sensor in air to the resistance in the presence of the gas analyte.[392] The baseline stability refers to the recovery of the resistance of the sensor to the initial value.[393] The dynamic performance of sensor is characterized by taking into account its response time, recovery time and sensor response. For a MOX-based conductometric sensor system, the response time is defined as the time required for the resistance to reach 90% of the equilibrium value after the injection of the analyte gas and the recovery time is the time needed to achieve 90% of the maximum change in the resistance upon removal of analyte.[394] The advantage of MOX sensor platform is that it is small, low cost and highly sensitive for detecting an extremely low concentration of hydrogen (~ 1% concentration level).[393, 395] Figure 7.1 shows the common design of the MOX-based conductometric sensor element.

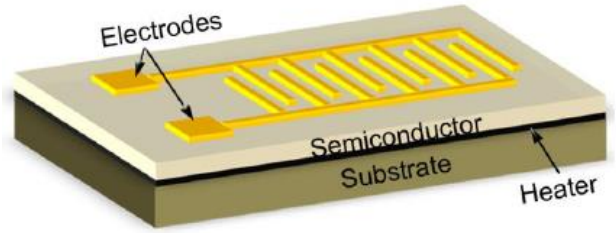

Figure 7.1 The schematic design of MOX hydrogen sensor.

Nanostructured metal oxides exhibit promising performance for a wide range of different gases due to high surface area to volume ratio, enabling a higher diffusion rate of an analyte in and out of metal oxide surface.[85, 384, 388] Tungsten oxide (WO_3) is an n-type semiconductor with band gap of 3.36 eV; it is very robust against chemical (acids *etc*.) poisoning and is a hydrogen-sensitive and colorimetric material.[396, 397] Hence, WO_3-based sensors would be an ideal choice of sensing materials for long-term stability and increased sensitivity. WO_3-based sensors have been employed by Prof. Wojtek Wlodarsky's group at RMIT for H_2 sensing at concentrations of less than 1 v/v% in air.[398, 399] Furthermore, Wlodarsky's group has demonstrated that a significant improvement in response could be achieved by careful addition of metal nanoparticle catalysts, such as platinum (Pt) and palladium (Pd), which speed up chemical reactions (in this case - hydrogen adsorption and dissociation) by reducing the associated activation energy.

Unlike Pt and Pd, the catalytic activity of Au was unknown prior to the 1970s.[27, 400] The first discovery of catalytic activity of Au was reported by Bond and Sermon in 1973 when they observed Au nanoparticles (NPs) were active in hydrogenation of olefins.[401, 402] In spite of the exciting results, their report remained ignored for several years until Haruta and co-workers reported in 1987 that small Au NPs on transition metal oxide catalysed CO oxidation at low temperature.[134] A remarkable work by Bus and Bokhoven reported that small Au clusters were able to chemisorb and dissociate hydrogen molecules.[403] Based on these startling findings, there has been a growing interest in using Au NPs as catalytic materials in gas sensing.[140, 404, 405]

The aim of work reported in this chapter is to investigate the sensing performance of H_2 sensors based on Au clusters deposited onto MOX thin films. In this work, sub-nanometer $Au_9(PPh_3)_8](NO_3)_3$ clusters were prepared through a wet-chemistry method and deposited onto RF sputtered WO_3 transducer thin films using a dip-coating method at two different concentrations in order to study the effect of concentration and Au particle size on the response and dynamic performance of the resulting sensors. The thin films were annealed at 400 °C in air (typical temperature used to remove the organic ligands)

and expose the metal core to the analyte/gas. The hydrogen-sensing performance was tested at industrially relevant H_2 concentrations from 0.06 - 1.0 v/v% in synthetic air with temperature ranging from 100 to 450 °C (the temperature of the sensing element of the sensor, not H_2 or air). The sensor response, response time and recovery time were measured to identify the optimal conditions.

7.2 Results and discussion

7.2.1 Au/WO_3 thin film characterization

Although SEM is not suitable for imaging small Au clusters, it is nevertheless a non-destructive and useful technique for imaging over large areas. At low magnification, SEM images of the sample surface after Au_9 cluster deposition display a high degree of uniformity of the WO3 thin films over large area in which large Au nanoparticles are absent (Figure 7.2a). At high magnification, SEM images of WO_3 thin films after Au_9 cluster deposition for the sample S1 and S2 show no evidence of aggregation of Au_9 clusters (Figure7.2b-c). After the annealing process at 400 °C, low magnification SEM images indicate the evidence of few large Au nanoparticles (10-30 nm) corresponding to agglomerated Au clusters, which are uniformly scattered at the surface of thin films (Figure 7.2d-e). Crucially, higher magnification SEM images of the samples after annealing (Figure 7.2f-g) reveal that the sample S1 contain fewer large aggregate of Au nanoparticles, in comparison with the sample S2, which contains a higher proportion of large Au nanoparticles (10 nm or larger). Unfortunately, the SEM used in this work was incapable of EDS mapping at nanoscale needed to observe the distribution of Au on WO_3. However, it is worth mentioning that SEM images only provide an estimate for such small particles. The more accurate particle size imaging is performed using a HRTEM and discussed in the next paragraph.

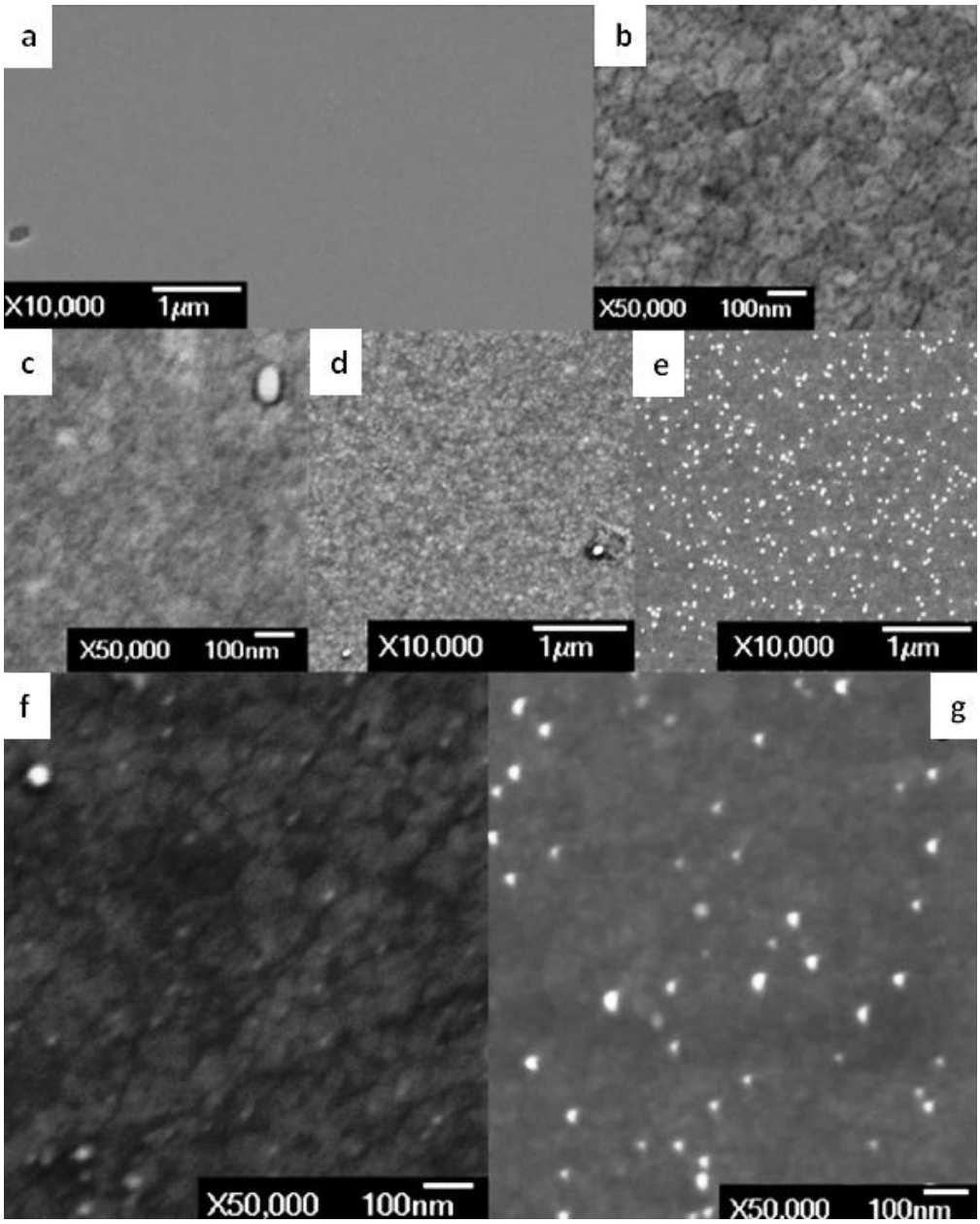

Figure 7.2 SEM images: a) low magnification image of WO_3 thin film after Au_9 cluster deposition for the sample S2, b) and c) show higher magnification images of WO_3 thin film after Au_9 cluster deposition for the sample S1 (b) and S2 (c); d) and e) show low magnification images of WO_3 thin film after Au_9 cluster deposition and annealing at 400 °C for the sample S1 (d) and S2 (e), f) and g) show high magnification images for the sample S1 (f) and S2 (g) after Au_9 cluster deposition and annealing at 400 °C. Adapted from the *International Journal of Hydrogen Energy, 2013, **38**, 12865*. Copyright Elsevier.

The TEM images and histograms of the samples S1 (0.01 mg/mL) and S2 (0.1 mg/mL) after annealing at 400 °C are shown in Figures 7.3 and 7.4 respectively. It can be clearly observed that the sample S1 contains small Au particles with a mean size of 3.7 ± 1.2 nm with the smallest and largest particles observed are 1.4 nm and 9 nm, respectively. Whereas the sample S2 has larger particles of a mean size of 4.9 ± 2.1 nm with smallest and largest particles observed are 2.1 nm and 19.3 nm, respectively. The pristine (non-sintered) Au_9 cluster has a core size of *ca*. 0.8 nm.[144] The extent of the growth of the Au particle sizes in both samples can be explained by using the Au concentration in the samples. Having a smaller concentration in the S1 (0.01 mg/mL) sample, Au particles aggregate less because of a smaller number of Au clusters adsorbed per unit area of support and a larger interparticle distance. Meanwhile a higher concentration of Au clusters adsorbed onto support in the case of S2 (0.1 mg/mL) sample leads to a more pronounced aggregation into much larger Au particles (as big as 20 nm) due to the smaller interparticle distance.

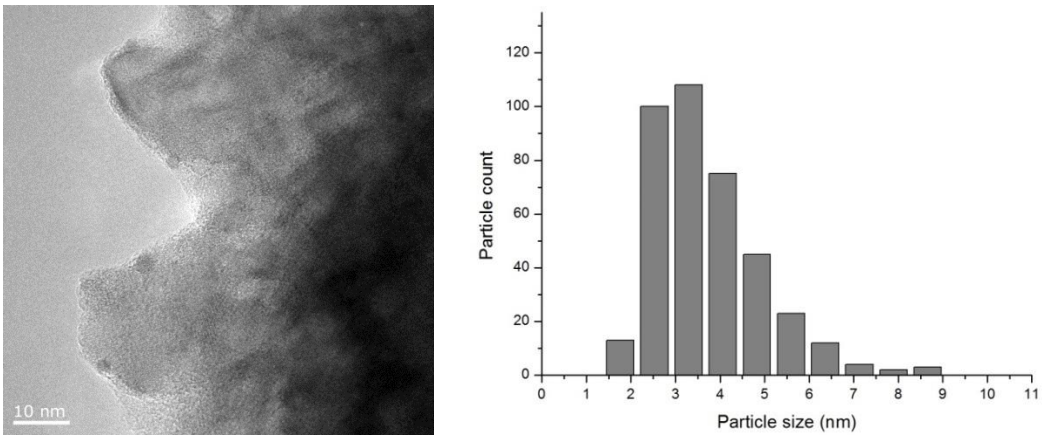

Figure 7.3. A representative TEM image of the S1 sample (left) and particle size distribution histogram (right); mean Au particle size is 3.7 ± 1.2 nm.

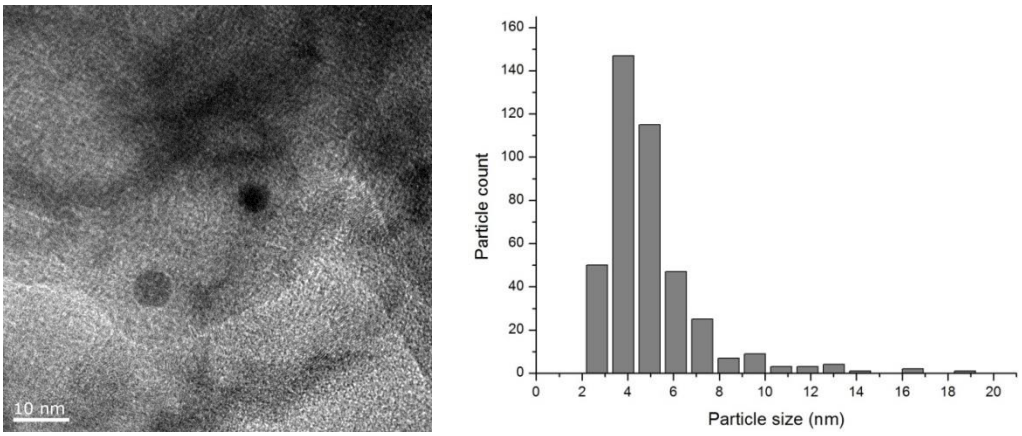

Figure 7.4. A representative TEM image of the S2 sample (left) and particle size distribution histogram (right); mean Au particle size is 4.9 ± 2.1 nm.

While large Au particles (> 2 nm) are seen in the representative TEM images of both samples, the presence of small clusters (sub-1 nm) cannot be excluded based on these images. Imaging such ultra-small clusters using a conventional HRTEM proves to be very challenging due to the inherent instrument limitations. Specifically, the difficulty in imaging such small clusters is associated with poor, minimal contrast between the Au clusters (of just nine Au atoms) and the WO_3 support (*ca*. 500 nm thick); thus, such ultra-small clusters on the metal oxide cannot be detected using conventional HRTEM.[165] Nevertheless, the statistical histograms of both S1 and S2 samples are skewed towards the small particle size region indicating that the majority of Au particles are sub-5 nm regime. Moreover, the larger particles (> 10 nm) are very infrequently seen in the TEM images taken from several different areas, except for very few particles in both sensors S1 and S2. Therefore, it is very compelling to suggest that the significant population of sub-5 nm Au plays a crucial role in defining the dynamic performance and response of these sensors as described in the next section. This conclusion was arrived at by comparing two related sensors made of using different concentrations of Au_9 clusters and evidence based on results of HRTEM and SEM studies.

The X-ray diffraction patterns of the as-deposited WO_3, annealed WO_3, and annealed Au/WO_3 are displayed in Figure 7.5 below. WO_3 exists in three different phases depending on the temperature: triclinic (-43 – 17 °C), monoclinic (17 – 330 °C) and orthorhombic (330 – 740 °C).[155] Fitting with the fact that at room temperature the monoclinic structure is the most stable phase,[406] all as-deposited WO_3 thin films show the presence of the monoclinic WO_3 (JCPDS 83-0950) structure. The top pattern (in black) shows the intensified peaks of monoclinic WO_3 (JCPDS card 83-0950) and triclinic WO_3 (JCPDS card 83-0947) structures together with possibly the Au cubic structure (JCPDS No. 03-0921) after the annealing process at 400 °C (observed for both Au/WO_3 sensor S1 and S2). However, it is worth

mentioning that small Au clusters (< 3 nm) are not visible in the XRD patterns due to the line broadening.[288] Hence, the presence of Au peaks here is attributed to the large Au nanoparticles, which are evident in the SEM and TEM images for both sensor S1 and S2 (see Figure 7.2-7.4).

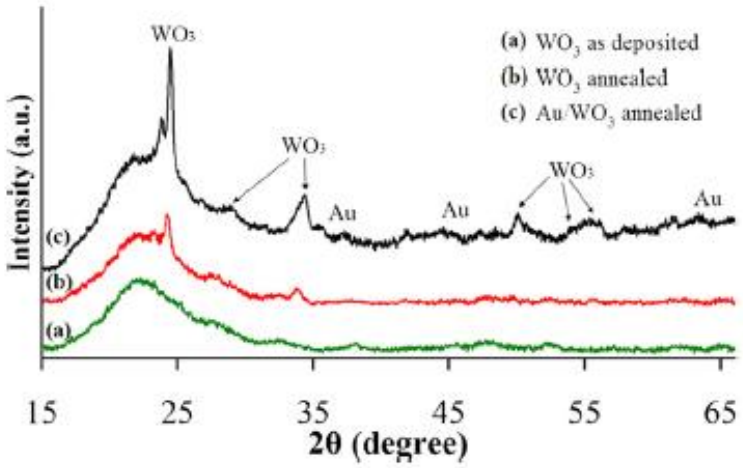

Figure 7.5 XRD patterns of a) as-deposited WO_3, b) annealed WO_3, and c) annealed Au/WO_3. Adapted from the *International Journal of Hydrogen Energy, 2013, **38**, 12865*. Copyright Elsevier.

Figure 7.6 displays the XP spectra of a) tungsten 4f, b) gold 4f and c) oxygen 1s. The binding energy (BE) of tungsten $4f_{7/2}$ electrons for both sensor S1 and S2 is 36.0 ± 0.1 eV, similar to the value reported in the literature.[407, 408] However, the BE of tungsten for both sensor S1 and S2 after H_2 sensing displays a shift of -0.3 eV which could be due to the loss of oxygen during the sensing test, forming moisture when reacts with hydrogen ($H_2 + O_2 \rightarrow H_2O$).[409, 410] Other authors also reported the same peak positions for WO_3 thin films deposited using different techniques such as chemical vapour deposition[411] and thermal evaporation.[412] The film thickness and the evolution of band-bending due to the WO_3-Au interaction could also influence the shift of tungsten $4f_{7/2}$ peak position.[413] However, the formation of oxygen vacancies can be ruled out because the broadening of the peaks associated with the change in stoichiometry of the WO_3 films is not observed.[414]

The O 1s peak position appear at 531.0 eV for both untested sensors S1 and S2 and show a shift to 530.6 eV after H_2 sensing test (Figure 6c). The reported in the literature value of binding energy for O 1s electrons differs from 530.7 to 530.4 eV depending on the sample thickness, the nature of the materials and deposition conditions (annealing temperature, duration *etc.*).[415] It is important to note that a very small shoulder appears at 532.1 eV and becomes apparent as the sensors undergo thermal heating, which could be either due to the annealing process or H_2 sensing test (following annealing process). This

shoulder could be attributed to the chemisorbed or dissociated oxygen or hydroxyl species on the WO_3 surfaces. [416]

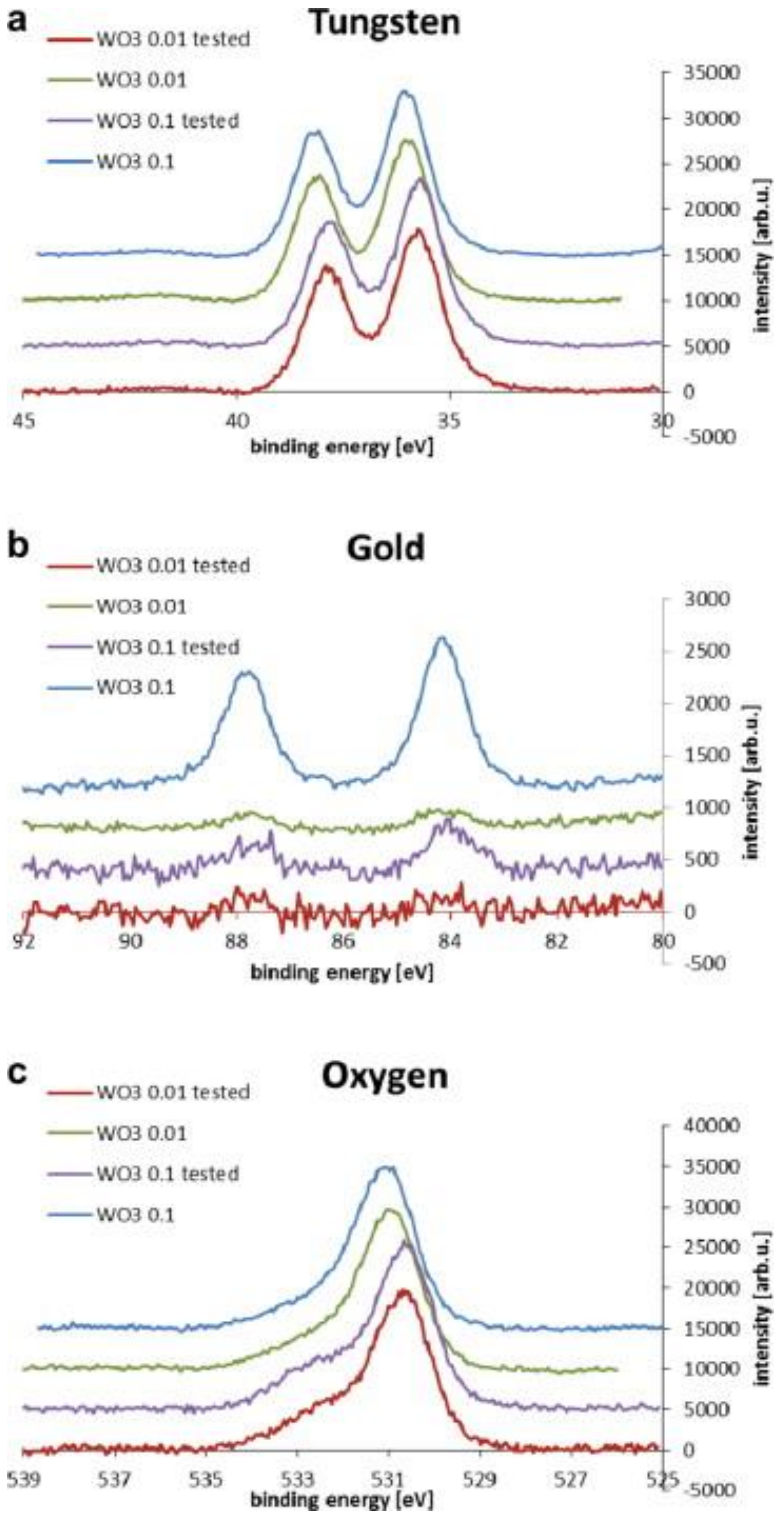

Figure 7.6 XP spectra of annealed Au/WO_3 sensors: a) tungsten 4f, b) gold 4f, and c) oxygen 1s. Spectra are colour-labelled according to the legend (inset). Adapted from the *International Journal of Hydrogen Energy, 2013, **38**, 12865*. Copyright Elsevier.

The intensity of Au signals in the XP spectrum could provide a good indication of the Au content on the WO_3 surface since the XPS technique is a surface-sensitive technique.[154] By assuming that Au nanoparticles are located at the outermost layer of the sensor thin film, photoelectrons generated passing through the sample undergo an inelastic interaction within the atoms in the sample. The photoelectrons emitted from the sample have an intensity that decreases exponentially with the path length. The mean free path of the electrons emitted from Au 4f orbitals is calculated to be 1.5 ± 0.2 nm while the Au-Au bond length is assumed to be 0.25 nm. [417] Hence, a single monolayer of gold yields 16% of the total intensity in the XPS spectrum based on these data. The as-made Au/WO_3 sensor S1 (coated with 0.01 mg/mL Au_9 solution) and S2 (coated with 0.1 mg/mL Au_9 solution) have gold intensities of 0.03 ± 0.02 and 0.39 ± 0.02, respectively. Using these values, the sample S1 is calculated to have 0.15% fraction of the monolayer while the sample S2 has 2.4% fraction of the monolayer. These data also allow us to estimate the particle density (the number of particles per unit area in cm^2) depending on the Au particle size. For example, by assuming the Au particle size to be 1.5 nm in both sensors S1 and S2, the particle density for the sensor S1 and S2 would be $2.2x10^{10}$ and $2.8x10^{11}$ cm^{-2}, respectively.

The estimates given above confirm our hypothesis that the significant sintering of Au particles (as observed in the TEM images) in the case of the sensor fabricated using an Au_9 solution with higher concentration (S2) is related to the density of adsorbed clusters. Similarly, the sensor fabricated using Au_9 solution with lower concentration (S1) has a significantly greater population of smaller Au nanoparticles (not all of which may be large enough to be observed using TEM). In summary, the observed intensities of Au signals reflect the Au concentration on the WO_3 surface and account for the extent of aggregation of Au nanoparticles.

7.2.2 H_2 sensing performance

The sensing performance of Au/WO_3 toward H_2 was initially performed at 0.06 v/v% at the operating temperature ranging from 100 to 400 °C to identify the optimum operating temperature. The optimal temperature for both sensors to yield the best performance is chosen by considering a combination a high sensitivity, as indicated by the sensor response (S) and a fast response and recovery time. For a systematic study of the H_2 sensing, the optimized temperatures for the sensors S1 and S2 were selected to be 300 °C and 350 °C, respectively (Figure 7.7 and 7.8). The H_2 sensing performances at other temperatures resulted in slower response and/or recovery time or lower sensor response. For example, at 200 °C, the sensor S1 showed the response time of about 40 s, but the recovery time was much longer (350 s) and the sensor response was 3. The sensor S2 showed the highest sensor response (4.6) at 150 °C, yet *both* the response and recovery times at this temperature were slow (both around 100 s). Table 7.1

displays a comparison of the performance between the sensors at their optimized operating temperatures. It is generally observed that a higher operating temperature is required for a higher performance of semiconductor metal oxide based sensors due to the lowering of activation energy for gas adsorption and desorption.[361]

Table 7.1 A comparison of the sensing performance of Au/WO_3-based hydrogen sensors.

Au/WO_3 sensor	**Optimized temperature, °C**	**Sensor response, S**	**Response time, τ_{res}**	**Recovery time, τ_{rec}**
S1 (0.01 mg/mL)	300	4.6	20	300
S2 (0.1 mg/mL)	350	2.3	30	100

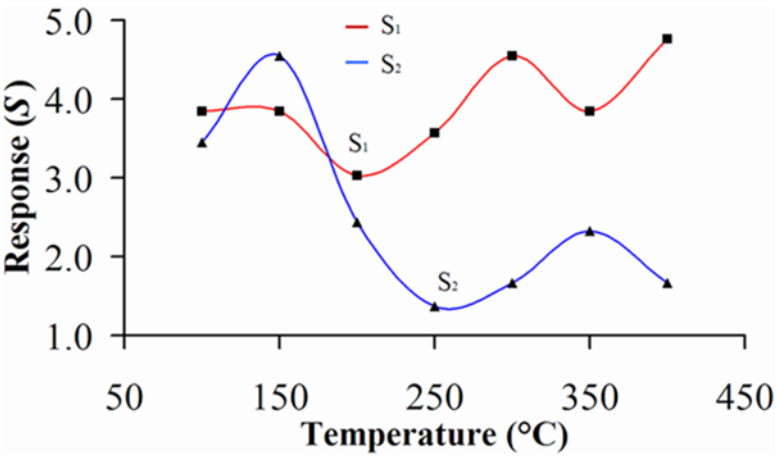

Figure 7.7 The response of Au/WO_3 sensors S1 and S2 across the temperature range from 100 to 400 °C. Adapted from the *International Journal of Hydrogen Energy*, *2013*, ***38***, *12865*. Copyright Elsevier.

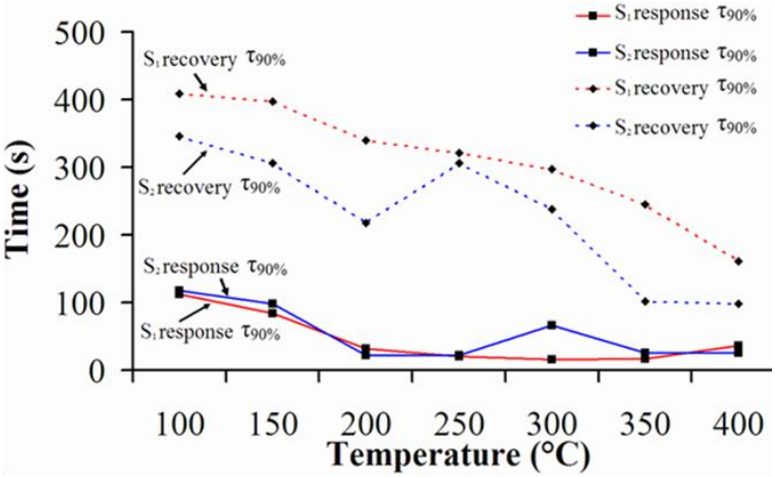

Figure 7.8 The response and recovery times for both S1 and S2 sensors exposed to the H_2 gas at 0.06 (v/v% in air) at operating temperature from 100 to 400 °C. Adapted from the *International Journal of Hydrogen Energy, 2013, **38**, 12865*. Copyright Elsevier.

A comparison of the sensor response for RF sputtered WO_3, Au/WO_3 sensors S1 and S2 are shown in Figure 7.9. The Au-free WO_3 sensor does not show noticeable response while both Au/WO_3 sensors display enhanced responses towards H_2. It is well known that the addition of catalytic materials, such as noble metals (Au, Pd, Pt), results in increase of the response and dynamic performance of the sensor.[392, 393, 418, 419] For example, Shim *et al.* reported that WO_3 nano-igloos decorated with noble metals (Au, Ag, Pd) by electron beam evaporator showed improved in sensor response as compared to bare WO_3 nano-igloos in H_2 sensing.[393] A similar increase in response towards H_2 sensing was also observed by Xiang *et al*. using Au NPs deposited on WO_3 nanorods.[394] Ippolito *et al.* reported that Au/WO_3 and Pt/WO_3 sensors were 160 and 40 times more sensitive than the bare WO_3 film respectively.[397] Penza *et al.* evaporated noble metals (Pt, Pd, Au) onto WO_3 thin films and found that the addition of noble metal increased the response towards different reducing gases including H_2.[405] Apart from WO_3-based sensors, more complex systems utilizing the synergistic effect metal NPs and other metal oxide components have been developed to detect H_2. For example Barreca *et al.* prepared a hybrid Au-TiO_2-CuO and observed an increased response in ethanol, H_2 and ozone sensing.[420] The authors attributed the increased response to the formation of a high areas of interfacial p-n heterojunctions between p-type CuO and n-type TiO_2 as well as the catalytic activity of TiO_2 and Au NPs. De Luca *et al*. fabricated Pt/TiO_2/MWCNTs composite by sol-gel method and observed that all three components (Pt, TiO_2 and MWCNT) were essential for H_2 detection at room temperature.[421] It is obvious from the results of this study that the Au nanoparticles are the key component that improves the performance toward H_2 sensing. At their optimal operating temperatures both sensor S1 and S2 show linear relationships between their sensor responses and the H_2

concentration across the range of 0.06 – 1.0 v/v% (Figure 7.9). The higher sensitivity of sensor S1 over S2 indicates that Au/WO_3 sensors exhibit "the less is more" principle with regard to the effect of Au concentration in H_2 sensing which might help to design a highly sensitive and lower cost sensor.

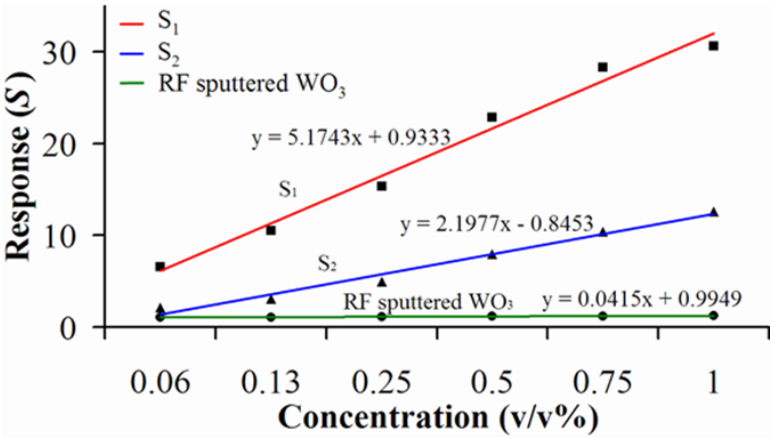

Figure 7.9 The response of RF-sputtered WO_3 and Au/WO_3 sensors S1 and S2 at different H_2 concentrations ranging from 0.06 to 1.0% v/v in air. Adapted from the *International Journal of Hydrogen Energy, 2013, **38**, 12865*. Copyright Elsevier.

The same optimal temperatures were used to investigate the dynamic performance of both sensors in a wide, industrially relevant range of H_2 concentrations in air (0.06 to 1.0 v/v%). Figures 7.10-7.11 show the dynamic performance of the sensors S1 and S2, respectively. A dynamic performance experiment was carried out by sequentially introducing the H_2 flow pulses to yield six different concentrations (0.06, 0.13, 0.25, 0.5, 0.75 and 1 v/v%) within the chamber and measuring the response and recovery times at onset and at the end of each flow pulse. When H_2 flow is introduced in the sensing system, a drop in resistance of the sensor element is observed. Once the H_2 flow is stopped by switching it to the air flow (in the absence of H_2), the resistance returns to the level corresponding to the baseline. Both Au/WO_3 S1 and S2 sensors show that the resistance returns to its original value during each cycle of exposure to the different concentrations of H_2. Thus both sensors display good baseline stability (less than 10% deviation) as shown in the Figures 7.10-7.11.

The Au/WO_3 sensor S2 shows a lower initial resistance as compared to sensor S1, indicating that the former should contain more metallic Au particles.[422] However, the change in resistance for the sensor S2 is significantly less pronounced (tens of kilo ohms) than that of the sensor S1 (hundreds of kilo ohms), indicating that the response of the sensor S2 is inferior as compared to that of S1 despite the higher concentration of Au nanoparticles in the sensor S2 (Figure 7.9 and 7.10); since the sensor response (S) is

defined as $S = R_a/R_g$ where R_a is the resistance in air and R_g is the resistance under H_2 exposure). This observation can be explained by presence of Au nanoparticles sizes in the sensors. Haruta and co-workers conducted an hydrogen dissociation study, H_2-D_2, on Au nanoparticles supported on rutile TiO_2(110) surfaces.[423] The authors found that the rate of HD formation and the H_2-D_2 exchange rate increased monotonically when the Au particle size decrease from 5.5 to 1.3 nm. The similar argument could be applied to explain the superior performance of the sensor S1 over S2 since the mean particle size in the sensor S1 is much smaller (3.7 nm) than that of in the sensor S2 (4.9 nm) based on the rate of H_2 dissociation on the sensors. In addition to the Au particle size effect, the Au concentration might contribute to the difference in sensing performance. Xu and co-workers, who observed an optimum Au concentration on WO_3 surfaces for the best sensor response, proposed that a higher concentration Au nanoparticles blotted the active sites of WO_3 surfaces and lowered the sensor response toward H_2 sensing.[394] Interestingly, Yamazoe and co-workers also reported that a higher Au loading reduced the sensor response of the Au/ZnO sensor in ethanol sensing.[424] Out of a few different Au loading (0.5, 1.0 and 1.5 mol/mol %), the authors found that 1.0 mol/mol % Au in the Au/ZnO sensor yielded the highest sensor response.

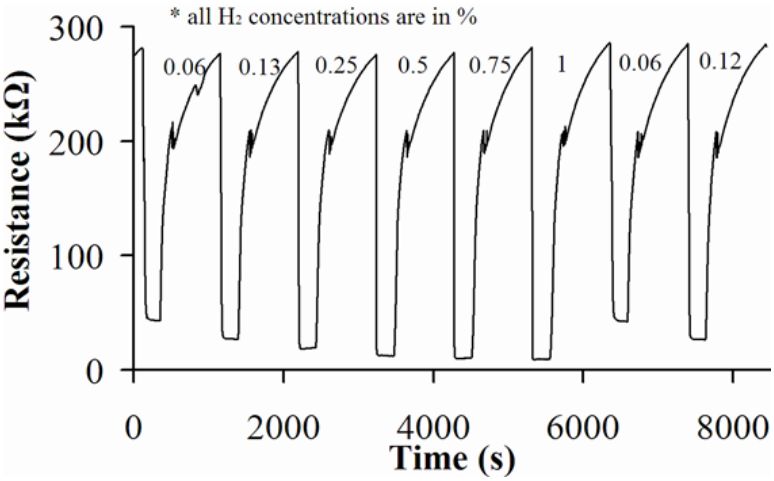

Figure 7.10 The dynamic performance for the Au/WO_3 sensor S1 at 300 °C in the H_2 concentration range from 0.06 to 1.0 v/v% in air. Adapted from the *International Journal of Hydrogen Energy, 2013, **38**, 12865*. Copyright Elsevier.

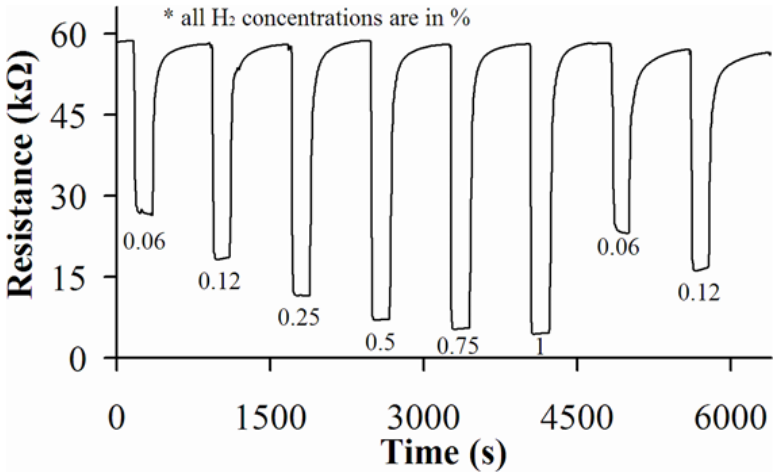

Figure 7.11 The dynamic performance for the Au/WO_3 sensor S2 at 350 °C in the H_2 concentration range from 0.06 to 1.0 v/v% in air. Adapted from the *International Journal of Hydrogen Energy, 2013, **38**, 12865*. Copyright Elsevier

The sensing mechanism for H_2 detection is still poorly understood, yet several possible mechanisms have been proposed in the literature based on the redox reactions between hydrogen and a few types of oxygen species present at the WO_3 surface.[399, 409, 421, 425] Humidity of the environment as a contributing factor to the sensing performance can be excluded due to the high operating (optimized) temperature of the sensors (not temperature of H_2 or air) used here (300 – 350 °C) because the water desorption rate is higher under these conditions than that of H_2.[410] The proposed reaction between H_2 and Au/WO_3 sensor could involve the following steps[399, 425] (also see Figure 7.12 for the schematic diagram):

1. When the sensor is exposed to air , oxygen molecules adsorb on WO_3 layer and form oxygen ion species by extracting electrons from the conduction band of WO_3 according to the equations:

   O_2 (g) ↔ O_2 (ad) 6.1

   O_2 (ad) + e^- (conduction band) → O_2^- (ad) 6.2

2. When the sensor is exposed to a H_2 molecule, H_2 is dissociated on the Au nanoparticles:

   $H_2 \xrightarrow{Au} 2H^+ + 2e^-$ 6.3

3. The H^+ ions then diffuse to the surface of WO_3 and react with adsorbed O_2^- species to reduce W^{6+} to W^{5+} followed by the formation of H_2O. The transfer of the electrons to WO_3 (in the case referred as W_2O_6) leads to a measured decrease in resistance:

$$W_2O_6 + 2H^+ + 2e^- \leftrightarrow W_2O_5 + H_2O \qquad 6.4$$

The forward reaction is limited by the amount of H^+ and e^- while the backward reaction is limited by the amount of H_2O.

4. Finally, the reversal to the original state of the sensor occurs with the formation of H_2. When the stoichiometry of tungsten oxide layer is restored, an increase in the resistance is observed:

$$W_2O_5 + H_2O \xrightarrow{Au} W_2O_6 + H_2 \qquad 6.5$$

When oxygen molecules from air adsorb on the WO_3 surface, they extract electrons from the conduction band to form oxygen ion species as pointed in equations 6.1 and 6.2. This reaction leads the formation of an electron depletion region near the WO_3 surface.[361] When hydrogen is introduced, the hydrogen molecules are dissociated into H^+ ions and electrons are generated according to equation 6.3. The transfer of the electrons to the WO_3 surface reduces the thickness of the depletion region and results in a decrease in the resistance of the sensor.[394]

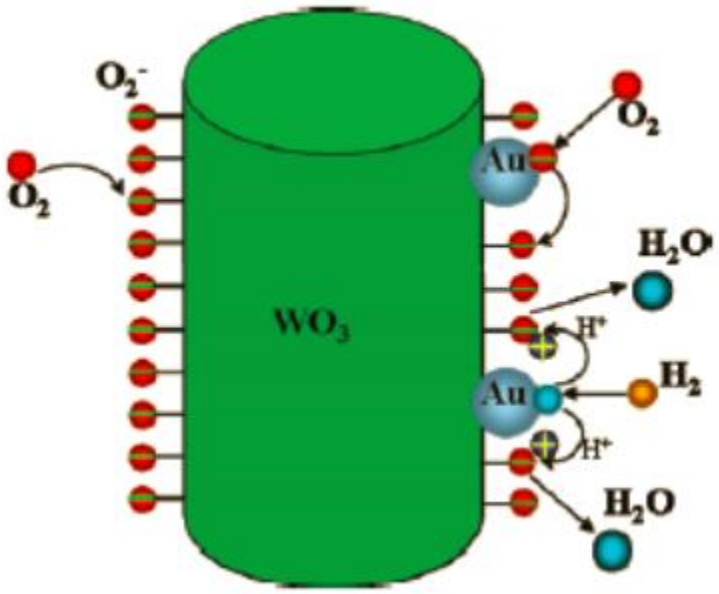

Figure 7.12 The proposed mechanism of the reactions involving H_2 at the surface of the Au/WO_3 sensor. Adapted from the *Journal of Physical Chemistry C, 2010, 114, 2049*. Copyright American Chemical Society.

While this work highlights the Au NPs as the key component of the active sensing element, there are some reports about the active response of bare WO_3 films. For example, Ahsan *et al*. prepared nanostructured WO_3 thin film by thermal evaporation and found that the WO_3 films only showed a noticeable response after annealing at 300 or 400 °C, which was attributed to the improved crystallinity of WO_3 films and transition from amorphous to monoclinic structure.[426] A similar observation that improved crystallinity and transition from amorphous to monoclinic structure of WO_3 led to an increase in the sensor response in CO, H_2 and NO sensing was also reported by Kukkola *et al*.[427] Despite the sufficiently good performance of bare WO_3 thin films, the addition of noble metal NPs could improve the dynamic performance (response time and recovery time) or/and sensitivity (response) of H_2 sensor based on the catalytic action of noble metal NPs.[163, 405] Table 7.2 compares the performance of H_2 sensors used in this work with other MOX sensors reported in the literature. Au nanoparticles deposited on different type of nanostructured WO_3 (needle, igloo) and TiO_2 show relatively higher response, yet their response and recovery are slower than Au/WO_3 sensors used in this work (entry 3, 4 and 10 in Table 7.2). Au/WO_3 nano-rods (entry 5 in Table 7.2) show the fastest response and recovery time as well as highest response among Au-based H_2 sensors presented here (Table 7.2). Tungsten oxide decorated with other noble metal particles, Pt and Pd, displays higher response towards H_2 detection, yet their response and recovery are slower than Au/WO_3 sensors used in this work, making Au nanoparticles as a catalytic layer more suitable for commercial H_2 sensors (N.B.: currently many commercial H_2 sensors employ Pd as a catalytic

layer).[370, 388] This work introduces a simple and low-cost method of fabrication Au/WO_3 sensors using dip-coating method of chemically synthesized Au_9 clusters. In particular, Au_9 clusters can be prepared in large-scale (grams, while micrograms are required per sensor) and crystallized (purified) and stored as air-stable powder.

Table 7.2 A comparison of the performance of H_2 sensors.

Entry	Sensor thin films	Operating temperature, °C	Sensor response, S	Response time, s	Recovery time, s	Ref.
1	WO_3 nanoparticles	150	10	140	80	426
2	WO_3 nano-igloos	200	1.2	24	n/a	393
3	Au/WO_3 nano-needles	150	35	329	5069	428
4	Au/WO_3 nano-igloos	200	9.3	77	n/a	393
5	Au/WO_3 nano-rods	290	6.6	8	10	394
6	Au/WO_3 (S1)	300	4.6	20	300	This work
7	Au/WO_3 (S2)	350	2.3	30	100	This work
8	Pd/WO_3	100	10000	80	100	429
9	Pt/$W_{18}O_{49}$	200	2.1	42	n/a	430
10	Au/TiO_2	25	n/a	180	600	163

7.3 Conclusions

A novel approach to fabricate H_2 sensors is demonstrated by depositing pre-synthesized Au_9 clusters onto WO_3 transducer thin films *via* a dip-coating method. Au/WO_3 sensors exhibit enhanced performance compared to pure WO_3 in terms of the sensor response, response time and recovery time across a wide range of industrially relevant H_2 concentrations, from 0.06 to 1 v/v%. Both sensors S1 and S2 show excellent baseline stability at optimized operating temperatures of 350 and 300 °C, respectively. The sensor S1 with lower Au nanoparticle density at the surface and smaller Au particle sizes displays much higher sensor response than that of sensor S2, leading to the conclusion that principle "the less is more" observed in this case and truly ultra-small particles outperform their larger analogues even when present in significantly lower numbers. Detailed material characterization results suggest that the superior performance of sensor S1 is attributed to the small Au clusters, most likely due to the higher rate of H_2 activation (dissociation) according to earlier reports in the literature. These findings pave the pathway to knowledge-based design of the low cost, highly sensitive and stable H_2 sensors.

Chapter 8

Conclusions and an outlook

Abstract

This final chapter of this thesis concludes the results presented here. An overarching summary of the outcomes and suggestions for possible future work are also presented.

8.1 Summary of the work and conclusions

The research project carried out in over the course of the PhD study is inspired by the discoveries of catalytic activity of small Au nanoparticles in hydrogenation and oxidation reactions since the 1970s. These discoveries offer opportunities to replace the more expensive and often less active and selective Pt group metals (Rh, Pt, Pd) in catalysis. Moreover, the Pt group metals are not stable over a long term due to metal leaching and sintering. Despite the enormous and rapidly growing number of reports in the literature focused on the investigation of the catalytic activity of Au-based catalysts, the true nature of the active sites remains elusive and constitutes one of the hottest topics in research in this area. Various research teams had investigated effects of various factors, such as the oxidation state of Au species, the Au particle size, the effect of electronic and geometric structure of Au nanoparticles, metal support interactions, presence of ligands or effects of catalyst activation treatments *etc*. One possible way to elucidate the nature of the active sites of Au-based catalysts is to employ atomically precise Au clusters supported on solid supports such as metal oxides – an approach which was implemented in this thesis.

This thesis begins with the synthesis of atomically precise Au and Ru clusters using the established protocols reported in the literature. Among the clusters prepared in this project are clusters containing Au_8, Au_9, Au_{101}, Ru_3, Ru_4, $AuRu_3$ metal cores. Phosphine stabilized Au clusters are chosen because:

a) phosphine ligands are weakly bonded to Au, allowing the possibility of easy ligand removal,

b) phosphine-stabilized Au clusters can be prepared on the large scale, purified and isolated in the form of microcrystalline powder or crystals suitable for single crystal X-ray crystallography studies, and

c) the synthetic protocols are milder and less tedious as compared to thiol-stabilized Au clusters, which normally involve chromatographic separation and gel electrophoresis.

In addition to Au clusters, Ru carbonyl clusters were also prepared for comparison with the Au clusters and with an ambition to investigate possible synergistic effect between Au and Ru.

The next phase in this thesis is to investigate the electronic structure of these atomically precise metal clusters. It has been known that small clusters show deviations from the scaling laws. Addition or removal of one atom results in abrupt changes of chemical and physical properties of the clusters. Moreover, the catalytic activity of small clusters is strongly influenced by their electronic and geometric structure. The vibrational modes including metal-metal core and metal-ligand vibrations are investigated using the synchrotron far-IR spectroscopy. The vibrational modes are very sensitive to the geometric structure and the elements constituting the cluster. The work in this thesis is the first to assign the vibrational modes of atomically precise metal clusters at low frequency region where metal-metal core vibrations occur by comparing with the quantum mechanical DFT calculations, with a series of visits to the Australian Synchrotron (AS) to employ the far-IR beamline to study the vibrational modes of a series metal clusters including Au_9, Ru_3, Ru_4 and mixed-metal $AuRu_3$ clusters. The high flux beamline at the AS allows probing the low intensity and low frequency metal-metal core vibrations. The unambiguous assignment of the key peaks in the experimentally obtained spectra is achieved by comparing with the predicted by computational calculations spectra.

The study reveals that significant Au cluster core vibrations occur at 157, 177 and 197 cm^{-1} due to core distortion for the Au_9 cluster. For the Ru_3 cluster, only a single core vibration appears at 150 cm^{-1} which is attributed to the asymmetric distortion. The Ru_4 cluster displays two asymmetric core distortions at 153 and 170 cm^{-1}. Interestingly, the mixed-metal $AuRu_3$ cluster (which could be seen as Ru_4 with a substitution by an Au atom or Ru_3 with addition of one Au atom), exhibits a shift of the cluster core centered vibrations towards higher wavenumbers at 177 and 299 cm^{-1} which is attributed to the change in chemical composition and geometry of the metal core. These important findings of the key transitions in atomically precise metal clusters are reported in the high impact journals, *RSC Advances* and *Inorganic Chemistry*.

At the moment of thesis submission, the teams in the University of Adelaide are still working on the DFT calculations of few other metal clusters such as Au_3O, Ru_6 and $Ru(H)_2(CO)(PPh_3)_3$ clusters, for which experimental far-IR spectra have been obtained recently.

The size of small clusters can be probed using an HAADF-STEM. However, the instrument is not easily accessible. Fortunately, XPS and XAS are other tools that can probe the relative size of such ultra-small clusters by taking into account the bond length (metal-ligand, metal-metal), symmetry, molecular structure, stabilizing ligands and chemical nature. The electronic structure of a series of phosphine-stabilized Au clusters (Au_8, Au_9 and Au_{101}) deposited and activated (by calcination) onto TiO_2 (anatase) are investigated by means of XPS. The useful signal for analyzing the electronic structure of gold comes from the Au $4f_{7/2}$ orbital. In the case of the "as deposited" Au_8 and Au_9 clusters, a significant fraction of non-agglomerated clusters is retained – a result that is confirmed further by a detailed HRTEM study. Interestingly, Au_{101} already resembles bulk-like gold upon deposition as evident from the position of Au $4f_{7/2}$ peak in XP spectra (in line with results of the earlier studies by our group), yet the particles are too small to show pronounced LSPR band in UV-vis DR spectrum. During calcination under different conditions (O_2 and combined O_2-H_2), the size of Au clusters evolve, forming larger Au particles. The results of the XPS study of such activated catalysts correlated well with observations by HRTEM. The size evolution of Au clusters to form nanoparticles after calcinations is additionally confirmed by means of UV-vis DRS study. The P XP spectra reveal that the phosphine ligands are initially bound to the Au core in the case of "as deposited" samples confirming the hypothesis based on other studies that clusters stay mostly intact, with only a minority of phosphine ligands forming phosphine oxide-like species possibly by interacting with the oxygen from TiO_2 surface. Activation treatments by calcination result in removal of the vast majority of phosphine ligands from the Au core and formation of phosphine oxide-like species anchored on TiO_2.

The XAS study of Au_9/TiO_2 reveals the evolution of the particle size starting from the pristine Au_9 clusters and resulting in the formation of bulk-like gold after the calcination processes (O_2 and then combined O_2-H_2 condition) employed in this thesis. A TEM study demonstrates that aggregation also occurs even easier in the case of Au_{101}/SiO_2 catalysts after deposition and calcination despite significantly higher surface area of SiO_2. In summary, calcination of Au clusters on TiO_2 supports results in aggregation of Au clusters (< 2 nm) to form nanoparticles (> 2 nm) and removal of phosphine ligands. Part of this study is published in the journal *Physical Chemistry Chemical Physics*.

Using the prepared Au and Ru clusters on different metal oxides (TiO_2, SiO_2, ZrO_2 and ZnO), a catalytic test in aerobic oxidation of benzyl alcohol is undertaken. The results reveal that the most active catalyst is based on the Au_{101} cluster, while supported Au_8 and Au_9 clusters show no activity. Further study reveals that the nature of the counter anions (Cl^- *vs.* NO_3^-) plays an important and non-trivial role in determining the catalytic activity in benzyl alcohol oxidation. The results indicate that the presence of NO_3^- ions accompanying Au_8 and Au_9 clusters seem to diminish their catalytic activity. It is shown that in

liquid phase catalytic oxidation of benzyl alcohol, complex factors are involved in determining the catalytic activity including the effect of counter anions, nature of supports (defining metal-support interaction) and effect of the Au particle size. In this work, Au_{101}-based catalysts are able to catalyze benzyl alcohol with a high substrate to molar ratio of 5800 and turn-over frequency of 0.65 cm^{-1}, outperforming many of supported Au nanoparticle-based catalysts reported in the literature. This study also shows that the selectivity towards methyl benzoate can be tuned by manipulating the temperature of catalytic reaction. Ru clusters on TiO_2 supports are found to be inactive in this reaction. To the best of the author's knowledge, this work demonstrates the effect of counter anions in catalytic oxidation of benzyl alcohol for the first time. The result of this study is reported in the journal *Catalysis Science & Technology*.

Finally, the catalytic activity study of Au clusters is extended into hydrogen sensing. Au_9 clusters are deposited onto WO_3 thin films using the dip-coating method at two different concentrations (0.01 and 0.1 mg/mL Au_9 clusters solutions). The result of this study reveals that the sensor with a lower Au cluster loading exhibits higher sensitivity and faster response and recovery time, confirming "less is more" principle in terms of effect of Au concentration in WO_3 thin films on their sensing performance. Detailed characterization of studied materials suggest that the superior performance of the sensor with a lower Au loading is due to the presence of significant majority of sub-5 nm Au clusters, which is hypothesized to (based on relevant recent studies) adsorb and dissociate H_2 molecules easily. It is clearly shown that the presence of Au nanoparticles on WO_3 films is the key to improved performance in H_2 sensing. With the superior sensing performance of WO_3 thin films containing tiny amounts of Au cluster, this study indicates that a highly sensitive and low cost H_2 sensor could be fabricated by employing Au_9 clusters onto MOX thin films as the key component. The result of this study is published in the *International Journal of Hydrogen Energy*.

8.2 Future work

While this PhD thesis has resulted in many high impact publications, there is still some room for improvement and follow-up studies. Therefore, the author would like to suggest several possible and practical research directions that could be worth implementing in the future.

In addition to the far-IR studies of atomically precise metal clusters, Raman spectroscopy is also a complementary tool to investigate the vibrational modes of metal clusters. IR and Raman spectroscopy are governed by different selection rules – any transition that in active in IR is never active in Raman spectroscopy. For example, Varnholt *et al*. reported the use of far-IR and Raman spectroscopy of

atomically precise thiolate-stabilized Au clusters recently.[55, 195] The authors assigned the difference in the spectra of different Au clusters are due to the different configuration of the Au clusters, yet they did not assign the metal-metal core vibrations the peak in both Raman and far-IR spectra. It is an opportunity, if possible, to proceed with the investigation of vibrational modes of atomically precise phosphine-stabilized Au clusters using Raman spectroscopy.

All the supported Au clusters on metal oxides were tested in catalytic oxidation of benzyl alcohol and Au_{101}-based catalysts showed the highest catalytic activity. These catalysts could be tested in other catalytic reactions that use bio-derived raw materials, such as glycerol and hydroxymethylfurfural (HMF), as the substrate.[333, 431] These bio-derived raw materials are readily available and their conversion to high-added value products would be of interest for the development of sustainable feedstock–based chemical industry. For example, HMF is considered as a industrially relevant precursor for the production of derivatives that have applications in pharmaceuticals, antifungals and polymers.[432] Glycerol could be catalytically converted into glyeric acid or dihydroxyacetone which are the starting material for DL-serine synthesis.[312]

The study on H_2 sensing using Au clusters on WO_3 thin films reveals that Au clusters are the key component that improves the sensor response magnitude and reduces the response and recovery times in H_2 sensing. Another potential prospect that is worth looking into is to employ Ru clusters (Ru_3 and Ru_4) or mixed-metal clusters containing Au atoms such as ($AuRu_3$ or $AuPd_6$). Mulvaney and co-workers showed that Au@Pt (core@shell) nanoparticles embedded in TiO_2 thin films resulted in a superior performance (faster response and recovery times) in H_2 sensing as compared to Pt or Au nanoparticles alone.[163] The authors attributed the superior performance due to the catalytic effect of Pt metal, which is well-known to chemisorb and dissociate H_2 molecules.[433] The use of other metal clusters, especially mixed-metal clusters, might contribute to the superior performance in terms of sensor response, and response and recovery time in H_2 sensing.

References

1. A. T. Bell, *Science*, 2003, **299**, 1688-1691.
2. G. Centi and S. Perathoner, *Catal. Today*, 2008, **138**, 69-76.
3. V. Polshettiwar and R. S. Varma, *Green Chemistry*, 2010, **12**, 743-754.
4. J. Grunes, J. Zhu and G. A. Somorjai, *Chem. Commun.*, 2003, 2257-2260.
5. I. Langmuir, *Transactions of the Faraday Society*, 1922, **17**, 607-620.
6. Y. Li and G. A. Somorjai, *Nano Lett.*, 2010, **10**, 2289-2295.
7. D. M. Kiefer, *Today's chemist at work*, 2001, **10**, 57.
8. J. Berzelius, *H. Laupp, Tubingen*, 1836.
9. E. K. Rideal, *Journal of the Chemical Society (Resumed)*, 1951, 1640-1647.
10. M. Kollár, A. De Stefanis, H. E. Solt, M. R. Mihályi, J. Valyon and A. A. G. Tomlinson, *J. Mol. Catal. A: Chem.*, 2010, **333**, 37-45.
11. I. Fechete, Y. Wang and J. C. Védrine, *Catal. Today*, 2012, **189**, 2-27.
12. D. Astruc, F. Lu and J. R. Aranzaes, *Angew. Chem. Int. Ed.*, 2005, **44**, 7852-7872.
13. I. V. Yentekakis, M. Konsolakis, I. A. Rapakousios and V. Matsouka, *Top. Catal.*, 2007, **42-43**, 393-397.
14. G. Ertl, *Angew. Chem. Int. Ed.*, 2008, **47**, 3524-3535.
15. I. K. Kalavrouziotis and P. H. Koukoulakis, *Water, Air, Soil Pollut.*, 2009, **196**, 393-402.
16. M. Haruta, T. Kobayashi, H. Sano and N. Yamada, *Chem. Lett.*, 1987, **16**, 405-408.
17. G. J. Hutchings, *J. Catal.*, 1985, **96**, 292-295.
18. L. Prati and M. Rossi, *J. Catal.*, 1998, **176**, 552-560.
19. J. E. Bailie and G. J. Hutchings, *Chem. Commun.*, 1999, 2151-2152.
20. H. Tsunoyama, H. Sakurai, N. Ichikuni, Y. Negishi and T. Tsukuda, *Langmuir*, 2004, **20**, 11293-11296.
21. S. K. Klitgaard, K. Egeblad, U. V. Mentzel, A. G. Popov, T. Jensen, E. Taarning, I. S. Nielsen and C. H. Christensen, *Green Chemistry*, 2008, **10**, 419-423.
22. S. Bawaked, Q. He, N. F. Dummer, A. F. Carley, D. W. Knight, D. Bethell, C. J. Kiely and G. J. Hutchings, *Catalysis Science & Technology*, 2011, **1**, 747-759.
23. F.-Z. Su, L. He, J. Ni, Y. Cao, H.-Y. He and K.-N. Fan, *Chem. Commun.*, 2008, 3531-3533.
24. M. Haruta, *Angew. Chem. Int. Ed.*, 2014, **53**, 52-56.
25. M. Haruta and M. Daté, *Applied Catalysis A: General*, 2001, **222**, 427-437.
26. M. Haruta, *The Chemical Record*, 2003, **3**, 75-87.
27. M. Haruta, *Catal. Today*, 1997, **36**, 153-166.

28. G. Bond, *Gold Bulletin*, 2001, **34**, 117-119.
29. A. S. K. Hashmi and G. J. Hutchings, *Angew. Chem. Int. Ed.*, 2006, **45**, 7896-7936.
30. C. Della Pina, E. Falletta, L. Prati and M. Rossi, *Chem. Soc. Rev.*, 2008, **37**, 2077-2095.
31. R. P. Feynman, *Talk at American Physical Society in Pasadena*, 1959.
32. N. Taniguchi, *Proc. Intl. Conf. Prod. Eng.*, 1974, **Part II**.
33. V. Vinod Kumar and S. Philip Anthony, *RSC Advances*, 2014, **4**, 18467-18472.
34. M. Rahman, S. Khan and A. Asiri, *Microchimica Acta*, 2014, **181**, 553-563.
35. X. Niu, D. Xu, Y. Yang and Y. He, *Analyst*, 2014, **139**, 2691-2694.
36. Y.-S. Nam, K.-C. Noh, N.-K. Kim, Y. Lee, H.-K. Park and K.-B. Lee, *Talanta*, 2014, **125**, 153-158.
37. E. Yasun, H. Kang, H. Erdal, S. Cansiz, I. Ocsoy, Y.-F. Huang and W. Tan, *Interface Focus*, 2013, **3**.
38. N. Li, L. Yu and J. Zou, *Journal of Laboratory Automation*, 2014, **19**, 82-90.
39. M. Sanders, Y. Lin, J. Wei, T. Bono and R. G. Lindquist, *Biosens. Bioelectron.*, 2014, **61**, 95-101.
40. P. T. Burks and P. C. Ford, *Dalton Transactions*, 2012, **41**, 13030-13042.
41. B. Hua, Q. Lin, Q. Zhang and Z. Fan, *Nanoscale*, 2013, **5**, 6627-6640.
42. H. Fu and S.-W. Tsang, *Nanoscale*, 2012, **4**, 2187-2201.
43. J. Panyam and V. Labhasetwar, *Advanced Drug Delivery Reviews*, 2003, **55**, 329-347.
44. J. Liu, C. Detrembleur, A. Debuigne, M.-C. De Pauw-Gillet, S. Mornet, L. Vander Elst, S. Laurent, E. Duguet and C. Jerome, *Journal of Materials Chemistry B*, 2014, **2**, 1009-1023.
45. C. Wang, M. Waje, X. Wang, J. M. Tang, R. C. Haddon and Yan, *Nano Lett.*, 2003, **4**, 345-348.
46. W. Li, C. Liang, W. Zhou, J. Qiu, Zhou, G. Sun and Q. Xin, *The Journal of Physical Chemistry B*, 2003, **107**, 6292-6299.
47. M. Haruta, *Faraday Discuss.*, 2011, **152**, 11-32.
48. Y. Zhu, H. Qian and R. Jin, *Chemistry – A European Journal*, 2010, **16**, 11455-11462.
49. F. Porta, L. Prati, M. Rossi, S. Coluccia and G. Martra, *Catal. Today*, 2000, **61**, 165-172.
50. E. Roduner, *Chem. Soc. Rev.*, 2006, **35**, 583-592.
51. M. Faraday, *Philosophical Transactions of the Royal Society of London*, 1857, **147**, 145-181.
52. G. Mie, *Annalen der Physik*, 1908, **330**, 377-445.
53. U. K. a. M. Vollmer, *Springer-Verlag: New York*, 1995.
54. Y. Yamamoto, S. Arai, A. Esaki, J. Ohyama, A. Satsuma and N. Tanaka, *Microscopy*, 2014.
55. B. Varnholt, P. Oulevey, S. Luber, C. Kumara, A. Dass and T. Bürgi, *The Journal of Physical Chemistry C*, 2014, **118**, 9604-9611.

56. B. C. Gates, *Chem. Commun.*, 2013, **49**, 7876-7877.
57. O. Varnavski, G. Ramakrishna, J. Kim, D. Lee and T. Goodson, *J. Am. Chem. Soc.*, 2009, **132**, 16-17.
58. A. C. Templeton, W. P. Wuelfing and R. W. Murray, *Acc. Chem. Res.*, 1999, **33**, 27-36.
59. R. Kubo, A. Kawabata and S. Kobayashi, *Annu. Rev. Mater. Sci.*, 1984, **14**, 49-66.
60. R. Jin, *Nanoscale*, 2010, **2**, 343-362.
61. E. A. Coronado, E. R. Encina and F. D. Stefani, *Nanoscale*, 2011, **3**, 4042-4059.
62. A. Urbieta, P. Fernández and J. Piqueras, *J. Appl. Phys.*, 2004, **96**, 2210-2213.
63. J. Zhang, J. Worley, S. Dénommée, C. Kingston, Z. J. Jakubek, Y. Deslandes, M. Post, B. Simard, N. Braidy and G. A. Botton, *The Journal of Physical Chemistry B*, 2003, **107**, 6920-6923.
64. H. Usui, Y. Shimizu, T. Sasaki and N. Koshizaki, *The Journal of Physical Chemistry B*, 2004, **109**, 120-124.
65. Y. Jouane, S. Colis, G. Schmerber, P. Kern, A. Dinia, T. Heiser and Y. A. Chapuis, *J. Mater. Chem.*, 2011, **21**, 1953-1958.
66. S. H. Xin, P. D. Wang, A. Yin, C. Kim, M. Dobrowolska, J. L. Merz and J. K. Furdyna, *Appl. Phys. Lett.*, 1996, **69**, 3884-3886.
67. S. V. Ivanov, A. A. Toropov, S. V. Sorokin, T. V. Shubina, I. V. Sedova, A. A. Sitnikova, P. S. Kop'ev, Z. I. Alferov, H.-J. Lugauer, G. Reuscher, M. Keim, F. Fischer, A. Waag and G. Landwehr, *Appl. Phys. Lett.*, 1999, **74**, 498-500.
68. J. Song, D. Kim and D. Lee, *Langmuir*, 2011, **27**, 13854-13860.
69. B. Xia, F. He and L. Li, *Langmuir*, 2013, **29**, 4901-4907.
70. Q. Zhang, J. Xie, J. Yang and J. Y. Lee, *ACS Nano*, 2008, **3**, 139-148.
71. Z. Yin, D. Ma and X. Bao, *Chem. Commun.*, 2010, **46**, 1344-1346.
72. Y. Wu, D. Wang and Y. Li, *Chem. Soc. Rev.*, 2014.
73. J. Turkevich, P. C. Stevenson and J. Hillier, *Discussions of the Faraday Society*, 1951, **11**, 55-75.
74. G. Frens, *Nature (London), Phys. Sci.*, 1973, **211**, 20.
75. M. K. Chow and C. F. Zukoski, *J. Colloid Interface Sci.*, 1994, **165**, 97-109.
76. X. Ji, X. Song, J. Li, Y. Bai, W. Yang and X. Peng, *J. Am. Chem. Soc.*, 2007, **129**, 13939-13948.
77. B.-K. Pong, H. I. Elim, J.-X. Chong, W. Ji, B. L. Trout and J.-Y. Lee, *The Journal of Physical Chemistry C*, 2007, **111**, 6281-6287.
78. J. Polte, T. T. Ahner, F. Delissen, S. Sokolov, F. Emmerling, A. F. Thünemann and R. Kraehnert, *J. Am. Chem. Soc.*, 2010, **132**, 1296-1301.

79. S. Kumar, K. S. Gandhi and R. Kumar, *Industrial & Engineering Chemistry Research*, 2006, **46**, 3128-3136.
80. W. Patungwasa and J. H. Hodak, *Mater. Chem. Phys.*, 2008, **108**, 45-54.
81. A. Rohiman, I. Anshori, A. Surawijaya and I. Idris, AIP Conference Proceedings, 2011.
82. K. Jun-Hyun, W. L. Brian, D. B. Roarke and W. B. Brett, *Nanotechnology*, 2011, **22**, 285602.
83. C. H. Su, P. L. Wu and C. S. Yeh, *J. Phys. Chem. B*, 2003, **107**, 14240-14243.
84. K. Gawlitza, S. T. Turner, F. Polzer, S. Wellert, M. Karg, P. Mulvaney and R. v. Klitzing, *PCCP*, 2013, **15**, 15623-15631.
85. D. Buso, L. Palmer, V. Bello, G. Mattei, M. Post, P. Mulvaney and A. Martucci, *J. Mater. Chem.*, 2009, **19**, 2051-2057.
86. D. Maity, A. Kumar, R. Gunupuru and P. Paul, *Colloids and Surfaces A: Physicochemical and Engineering Aspects*, 2014, **455**, 122-128.
87. M. Giersig and P. Mulvaney, *Langmuir*, 1993, **9**, 3408-3413.
88. L. H. Dubois and R. G. Nuzzo, *Annu. Rev. Phys. Chem.*, 1992, **43**, 437-463.
89. M. Brust, M. Walker, D. Bethell, D. J. Schiffrin and R. Whyman, *J. Chem. Soc., Chem. Commun.*, 1994, 801-802.
90. M. Brust, J. Fink, D. Bethell, D. J. Schiffrin and C. Kiely, *J. Chem. Soc., Chem. Commun.*, 1995, 1655-1656.
91. M. J. Hostetler, J. E. Wingate, C.-J. Zhong, J. E. Harris, R. W. Vachet, M. R. Clark, J. D. Londono, S. J. Green, J. J. Stokes, G. D. Wignall, G. L. Glish, M. D. Porter, N. D. Evans and R. W. Murray, *Langmuir*, 1998, **14**, 17-30.
92. P. J. G. Goulet and R. B. Lennox, *J. Am. Chem. Soc.*, 2010, **132**, 9582-9584.
93. Y. Li, O. Zaluzhna, B. Xu, Y. Gao, J. M. Modest and Y. J. Tong, *J. Am. Chem. Soc.*, 2011, **133**, 2092-2095.
94. M. M. Alvarez, J. T. Khoury, T. G. Schaaff, M. Shafigullin, I. Vezmar and R. L. Whetten, *Chem. Phys. Lett.*, 1997, **266**, 91-98.
95. M. Zhu, C. M. Aikens, F. J. Hollander, G. C. Schatz and R. Jin, *J. Am. Chem. Soc.*, 2008, **130**, 5883-5885.
96. P. R. Nimmala and A. Dass, *J. Am. Chem. Soc.*, 2011, **133**, 9175-9177.
97. H. Qian, W. T. Eckenhoff, Y. Zhu, T. Pintauer and R. Jin, *J. Am. Chem. Soc.*, 2010, **132**, 8280-8281.
98. H. Qian and R. Jin, *Nano Lett.*, 2009, **9**, 4083-4087.
99. H. Tsunoyama, Y. Negishi and T. Tsukuda, *J. Am. Chem. Soc.*, 2006, **128**, 6036-6037.

100. T. G. Schaaff, M. N. Shafigullin, J. T. Khoury, I. Vezmar, R. L. Whetten, W. G. Cullen, P. N. First, C. Gutiérrez-Wing, J. Ascensio and M. J. Jose-Yacamán, *The Journal of Physical Chemistry B*, 1997, **101**, 7885-7891.
101. Y. Negishi, Y. Takasugi, S. Sato, H. Yao, K. Kimura and T. Tsukuda, *J. Am. Chem. Soc.*, 2004, **126**, 6518-6519.
102. Z. Wu, J. Suhan and R. Jin, *J. Mater. Chem.*, 2009, **19**, 622-626.
103. Y. Shichibu, Y. Negishi, H. Tsunoyama, M. Kanehara, T. Teranishi and T. Tsukuda, *Small*, 2007, **3**, 835-839.
104. M. McPartlin, R. Mason and L. Malatesta, *Journal of the Chemical Society D: Chemical Communications*, 1969, 334-334.
105. B. K. Teo, X. Shi and H. Zhang, *J. Am. Chem. Soc.*, 1992, **114**, 2743-2745.
106. Y. Liu, H. Tsunoyama, T. Akita and T. Tsukuda, *The Journal of Physical Chemistry C*, 2009, **113**, 13457-13461.
107. J. W. A. Van der Velden, J. J. Bour, W. P. Bosman and J. H. Noordik, *Inorg. Chem.*, 1983, **22**, 1913-1918.
108. W. W. Weare, S. M. Reed, M. G. Warner and J. E. Hutchison, *J. Am. Chem. Soc.*, 2000, **122**, 12890-12891.
109. P. M. Shem, R. Sardar and J. S. Shumaker-Parry, *Langmuir*, 2009, **25**, 13279-13283.
110. G. H. Woehrle, L. O. Brown and J. E. Hutchison, *J. Am. Chem. Soc.*, 2005, **127**, 2172-2183.
111. H. Tsunoyama and T. Tsukuda, *J. Am. Chem. Soc.*, 2009, **131**, 18216-18217.
112. H. Tsunoyama, N. Ichikuni, H. Sakurai and T. Tsukuda, *J. Am. Chem. Soc.*, 2009, **131**, 7086-7093.
113. C. Bianchi, F. Porta, L. Prati and M. Rossi, *Top. Catal.*, 2000, **13**, 231-236.
114. H. Parab, C. Jung, M.-A. Woo and H. Park, *J. Nanopart. Res.*, 2011, **13**, 2173-2180.
115. M. S. Onses and P. F. Nealey, *Small*, 2013, **9**, 4168-4174.
116. G. R. Newkome and C. Shreiner, *Chem. Rev.*, 2010, **110**, 6338-6442.
117. R. M. Crooks, M. Zhao, L. Sun, V. Chechik and L. K. Yeung, *Acc. Chem. Res.*, 2000, **34**, 181-190.
118. R. W. J. Scott, O. M. Wilson and R. M. Crooks, *The Journal of Physical Chemistry B*, 2004, **109**, 692-704.
119. K. Esumi, K. Miyamoto and T. Yoshimura, *J. Colloid Interface Sci.*, 2002, **254**, 402-405.
120. Y. Shan, T. Luo, C. Peng, R. Sheng, A. Cao, X. Cao, M. Shen, R. Guo, H. Tomás and X. Shi, *Biomaterials*, 2012, **33**, 3025-3035.

121. L. W. Hoffman, G. G. Andersson, A. Sharma, S. R. Clarke and N. H. Voelcker, *Langmuir*, 2011, **27**, 6759-6767.
122. M. D. Sonntag, J. M. Klingsporn, A. B. Zrimsek, B. Sharma, L. K. Ruvuna and R. P. Van Duyne, *Chem. Soc. Rev.*, 2014.
123. M. Juliusa, S. Robertsa and J. Q. Fletchera, *Gold Bulletin*, 2010, **43**, 298-306.
124. S. E. Davis, M. S. Ide and R. J. Davis, *Green Chemistry*, 2013, **15**, 17-45.
125. M. S. Ide, B. Hao, M. Neurock and R. J. Davis, *ACS Catalysis*, 2012, **2**, 671-683.
126. G. C. Bond and D. T. Thompson, *Catalysis Reviews*, 1999, **41**, 319-388.
127. L. Prati and A. Villa, *Catalysts*, 2011, **2**, 24-37.
128. L. Delannoy, N. El Hassan, A. Musi, N. N. Le To, J.-M. Krafft and C. Louis, *The Journal of Physical Chemistry B*, 2006, **110**, 22471-22478.
129. Q. Xu, K. C. Kharas and A. K. Datye, *Catal. Lett.*, 2003, **85**, 229-235.
130. L. K. Ono and B. Roldan Cuenya, *The Journal of Physical Chemistry C*, 2008, **112**, 4676-4686.
131. H. Tsai, E. Hu, K. Perng, M. Chen, J.-C. Wu and Y.-S. Chang, *Surf. Sci.*, 2003, **537**, L447-L450.
132. S. Ivanova, C. Petit and V. Pitchon, *Applied Catalysis A: General*, 2004, **267**, 191-201.
133. G. A. Parks, *Chem. Rev.*, 1965, **65**, 177-198.
134. M. Haruta, N. Yamada, T. Kobayashi and S. Iijima, *J. Catal.*, 1989, **115**, 301-309.
135. M. Haruta, S. Tsubota, T. Kobayashi, H. Kageyama, M. J. Genet and B. Delmon, *J. Catal.*, 1993, **144**, 175-192.
136. E. D. Park and J. S. Lee, *J. Catal.*, 1999, **186**, 1-11.
137. R. Zanella, S. Giorgio, C.-H. Shin, C. R. Henry and C. Louis, *J. Catal.*, 2004, **222**, 357-367.
138. M. G. Aylmore, *Minerals & metallurgical processing*, 2001, **18**, 221-227.
139. R. Zanella, S. Giorgio, C. R. Henry and C. Louis, *The Journal of Physical Chemistry B*, 2002, **106**, 7634-7642.
140. M. Haruta, *Catalysis Surveys from Asia*, 1997, **1**, 61-73.
141. R. Mason and A. I. M. Rae, *Journal of the Chemical Society A: Inorganic, Physical, Theoretical*, 1968, 778-779.
142. C. O. Quicksall and T. G. Spiro, *Inorg. Chem.*, 1968, **7**, 2365-2369.
143. M. Faure, C. Saccavini and G. Lavigne, *Chem. Commun.*, 2003, 1578-1579.
144. F. Wen, U. Englert, B. Gutrath and U. Simon, *Eur. J. Inorg. Chem.*, 2008, **2008**, 106-111.
145. B. S. Gutrath, U. Englert, Y. Wang and U. Simon, *Eur. J. Inorg. Chem.*, 2013, **2013**, 2002-2006.
146. G. Brauer, Ed., *Academic Press, NY*, 1963, **1**.
147. B. K. N. M. I. Bruce, O. Bin Shawkataly, *Inorg. Synth.*, 2009, **26**, 326.
148. L. N. L. Malatesta, G. Simonetta, F. Cariati, *Coord. Chem. Rev.*, 1966, **1**, 255.

149. J. K. K. A. Tamaki, *J. Organomet. Chem.*, 1973, **61**, 441.
150. F. Piacenti, M. Bianchi, P. Frediani and E. Benedetti, *Inorg. Chem.*, 1971, **10**, 2759-2763.
151. G. Lavigne, F. Papageorgiou and J. J. Bonnet, *Inorg. Chem.*, 1984, **23**, 609-613.
152. M. G. Hernández–Cruz, G. Sánchez–Cabrera, M. Hernández–Sandoval, M. A. Leyva, M. J. Rosales–Hoz, B. A. Ordoñez–Flores, V. Salazar, A. G. Lara and F. J. Zuno-Cruz, *J. Organomet. Chem.*, 2011, **696**, 2177-2185.
153. D. P. Anderson, R. H. Adnan, J. F. Alvino, O. Shipper, B. Donoeva, J.-Y. Ruzicka, H. Al Qahtani, H. H. Harris, B. Cowie, J. B. Aitken, V. B. Golovko, G. F. Metha and G. G. Andersson, *PCCP*, 2013, **15**, 14806-14813.
154. D. P. Anderson, J. F. Alvino, A. Gentleman, H. A. Qahtani, L. Thomsen, M. I. J. Polson, G. F. Metha, V. B. Golovko and G. G. Andersson, *PCCP*, 2013, **15**, 3917-3929.
155. M. Z. Ahmad, *PhD Thesis*, 2013.
156. Z. Niu and Y. Li, *Chem. Mater.*, 2013, **26**, 72-83.
157. S. A. R. Knox, J. W. Koepke, M. A. Andrews and H. D. Kaesz, *J. Am. Chem. Soc.*, 1975, **97**, 3942-3947.
158. M. Walter, J. Akola, O. Lopez-Acevedo, P. D. Jadzinsky, G. Calero, C. J. Ackerson, R. L. Whetten, H. Grönbeck and H. Häkkinen, *Proceedings of the National Academy of Sciences*, 2008, **105**, 9157-9162.
159. Y. Lu and W. Chen, *Chem. Soc. Rev.*, 2012, **41**, 3594-3623.
160. S. Link and M. A. El-Sayed, *Annu. Rev. Phys. Chem.*, 2003, **54**, 331-366.
161. S. Link, Z. L. Wang and M. A. El-Sayed, *The Journal of Physical Chemistry B*, 1999, **103**, 3529-3533.
162. L. Zhao, D. Jiang, Y. Cai, X. Ji, R. Xie and W. Yang, *Nanoscale*, 2012, **4**, 5071-5076.
163. E. Della Gaspera, M. Bersani, G. Mattei, T.-L. Nguyen, P. Mulvaney and A. Martucci, *Nanoscale*, 2012, **4**, 5972-5979.
164. Y. Liu, H. Tsunoyama, T. Akita and T. Tsukuda, *Chem. Lett.*, 2010, **39**, 159-161.
165. A. A. Herzing, C. J. Kiely, A. F. Carley, P. Landon and G. J. Hutchings, *Science*, 2008, **321**, 1331-1335.
166. A. K. Datye, *J. Catal.*, 2003, **216**, 144-154.
167. S. E. Wanke, *J. Catal.*, 1977, **46**, 234-237.
168. A. I. Kirkland, S. Haigh and L. Y. Chang, *Journal of Physics: Conference Series*, 2008, **126**, 012034.
169. O. Scherzer, *Optik*, 1947, **2**, 114.
170. A. L. A. Bleloch, *Mater. Today*, 2004, **7**, 42.

171. C. Hetherington, *Mater. Today*, 2004, **7**, 50-55.
172. R. Erni, M. D. Rossell, C. Kisielowski and U. Dahmen, *Phys. Rev. Lett.*, 2009, **102**, 096101.
173. A. Leifert, Y. Pan-Bartnek, U. Simon and W. Jahnen-Dechent, *Nanoscale*, 2013, **5**, 6224-6242.
174. T. Akita, M. Kohyama and M. Haruta, *Acc. Chem. Res.*, 2013, **46**, 1773-1782.
175. Z. Y. Li, N. P. Young, M. Di Vece, S. Palomba, R. E. Palmer, A. L. Bleloch, B. C. Curley, R. L. Johnston, J. Jiang and J. Yuan, *Nature*, 2008, **451**, 46-48.
176. A. I. Frenkel, M. W. Cason, A. Elsen, U. Jung, M. W. Small, R. G. Nuzzo, F. D. Vila, J. J. Rehr, E. A. Stach and J. C. Yang, *Journal of Vacuum Science & Technology A*, 2014, **32**, -.
177. C. J. Powell and A. Jablonski, *Nuclear Instruments and Methods in Physics Research Section A: Accelerators, Spectrometers, Detectors and Associated Equipment*, 2009, **601**, 54-65.
178. C. J. Powell, A. Jablonski, I. S. Tilinin, S. Tanuma and D. R. Penn, *J. Electron. Spectrosc. Relat. Phenom.*, 1999, **98–99**, 1-15.
179. K. Kishi and S. Ikeda, *The Journal of Physical Chemistry*, 1974, **78**, 107-112.
180. A. M. Visco, F. Neri, G. Neri, A. Donato, C. Milone and S. Galvagno, *PCCP*, 1999, **1**, 2869-2873.
181. J. P. Y. Lykhach, I. Spirovova, Z. Bastl, *Collect. Czech. Chem. Commun.*, 2003, **68**, 14.
182. S. B. DiCenzo, S. D. Berry and E. H. Hartford, *Physical Review B*, 1988, **38**, 8465-8468.
183. D. M. Cox, W. Eberhardt, P. Fayet, Z. Fu, B. Kessler, R. D. Sherwood, D. Sondericker and A. Kaldor, *Zeitschrift für Physik D Atoms, Molecules and Clusters*, 1991, **20**, 385-386.
184. H. G. Boyen, A. Ethirajan, G. Kästle, F. Weigl, P. Ziemann, G. Schmid, M. G. Garnier, M. Büttner and P. Oelhafen, *Phys. Rev. Lett.*, 2005, **94**, 016804.
185. V. D. Borman, M. A. Pushkin, V. N. Tronin and V. I. Troyan, *Journal of Experimental and Theoretical Physics*, 2010, **110**, 1005-1025.
186. Y. Kitsudo, A. Iwamoto, H. Matsumoto, K. Mitsuhara, T. Nishimura, M. Takizawa, T. Akita, Y. Maeda and Y. Kido, *Surf. Sci.*, 2009, **603**, 2108-2114.
187. G. A. Battiston, G. Sbrignadello and G. Bor, *Inorg. Chem.*, 1980, **19**, 1973-1977.
188. G. A. Battiston, G. Bor, U. K. Dietler, S. F. A. Kettle, R. Rossetti, G. Sbrignadello and P. L. Stanghellini, *Inorg. Chem.*, 1980, **19**, 1961-1973.
189. J. d. P. Peter Atkins, *Oxford*, 2009, **5**.
190. M. Aslam, L. Fu, M. Su, K. Vijayamohanan and V. P. Dravid, *J. Mater. Chem.*, 2004, **14**, 1795-1797.
191. P. Biji, N. K. Sarangi and A. Patnaik, *Langmuir*, 2010, **26**, 14047-14057.
192. A. Kulkarni, R. J. Lobo-Lapidus and B. C. Gates, *Chem. Commun.*, 2010, **46**, 5997-6015.

193. J. F. Alvino, T. Bennett, D. Anderson, B. Donoeva, D. Ovoshchnikov, R. H. Adnan, D. Appadoo, V. Golovko, G. Andersson and G. F. Metha, *RSC Advances*, 2013, **3**, 22140-22149.
194. T. Bennett, R. H. Adnan, J. F. Alvino, V. Golovko, G. G. Andersson and G. F. Metha, *Inorg. Chem.*, 2014, **53**, 4340-4349.
195. I. Dolamic, B. Varnholt and T. Burgi, *PCCP*, 2013, **15**, 19561-19565.
196. T. R. Gilson and J. Evans, *J. Chem. Soc., Dalton Trans.*, 1984, 155-159.
197. G. Mestl, N. D. Triantafillou, H. Knoezinger and B. C. Gates, *The Journal of Physical Chemistry*, 1993, **97**, 666-672.
198. B. Yoon, H. Häkkinen, U. Landman, A. S. Wörz, J.-M. Antonietti, S. Abbet, K. Judai and U. Heiz, *Science*, 2005, **307**, 403-407.
199. M. W. Heaven, A. Dass, P. S. White, K. M. Holt and R. W. Murray, *J. Am. Chem. Soc.*, 2008, **130**, 3754-3755.
200. S. Malola, L. Lehtovaara, S. Knoppe, K.-J. Hu, R. E. Palmer, T. Bürgi and H. Häkkinen, *J. Am. Chem. Soc.*, 2012, **134**, 19560-19563.
201. O. Lopez-Acevedo, J. Akola, R. L. Whetten, H. Grönbeck and H. Häkkinen, *The Journal of Physical Chemistry C*, 2009, **113**, 5035-5038.
202. Y. Zhu, H. Qian and R. Jin, *J. Mater. Chem.*, 2011, **21**, 6793-6799.
203. Y. Liu, H. Tsunoyama, T. Akita, S. Xie and T. Tsukuda, *ACS Catalysis*, 2010, **1**, 2-6.
204. Y. Zhu, H. Qian, B. A. Drake and R. Jin, *Angew. Chem. Int. Ed.*, 2010, **49**, 1295-1298.
205. R. M. Laine, R. G. Rinker and P. C. Ford, *J. Am. Chem. Soc.*, 1977, **99**, 252-253.
206. A. B. Hungria, R. Raja, R. D. Adams, B. Captain, J. M. Thomas, P. A. Midgley, V. Golovko and B. F. G. Johnson, *Angew. Chem. Int. Ed.*, 2006, **45**, 4782-4785.
207. P. Gruene, D. M. Rayner, B. Redlich, A. F. G. van der Meer, J. T. Lyon, G. Meijer and A. Fielicke, *Science*, 2008, **321**, 674-676.
208. D. M. Adams and I. D. Taylor, *Journal of the Chemical Society, Faraday Transactions 2: Molecular and Chemical Physics*, 1982, **78**, 1561-1571.
209. S. F. A. Kettle and P. L. Stanghellini, *Inorg. Chem.*, 1979, **18**, 2749-2754.
210. S. Kishner, P. J. Fitzatrick, K. R. Plowman and I. S. Butler, *J. Mol. Struct.*, 1981, **74**, 29-37.
211. I. S. Butler, Z. H. Xu, D. J. Darensbourg and M. Pala, *Journal of Raman Spectroscopy*, 1987, **18**, 357-363.
212. T. R. Gilson, *J. Chem. Soc., Dalton Trans.*, 1984, 149-153.
213. E. Hulkko, O. Lopez-Acevedo, J. Koivisto, Y. Levi-Kalisman, R. D. Kornberg, M. Pettersson and H. Häkkinen, *J. Am. Chem. Soc.*, 2011, **133**, 3752-3755.
214. J. Petroski, M. Chou and C. Creutz, *J. Organomet. Chem.*, 2009, **694**, 1138-1143.

215. J. J. Bour, R. P. F. Kanters, P. P. J. Schlebos and J. J. Steggerda, *Recl. Trav. Chim. Pays-Bas*, 1988, **107**, 211-215.
216. L. Lin, P. Claes, P. Gruene, G. Meijer, A. Fielicke, M. T. Nguyen and P. Lievens, *ChemPhysChem*, 2010, **11**, 1932-1943.
217. L. Lin, T. Höltzl, P. Gruene, P. Claes, G. Meijer, A. Fielicke, P. Lievens and M. T. Nguyen, *ChemPhysChem*, 2008, **9**, 2471-2474.
218. M. R. Churchill, F. J. Hollander and J. P. Hutchinson, *Inorg. Chem.*, 1977, **16**, 2655-2659.
219. D. H. Farrar, P. F. Jackson, B. F. G. Johnson, J. Lewis, J. N. Nicholls and M. McPartlin, *J. Chem. Soc., Chem. Commun.*, 1981, 415-416.
220. P. J. Bailey, G. Conole, B. F. G. Johnson, J. Lewis, M. McPartlin, A. Moule, H. R. Powell and D. A. Wilkinson, *J. Chem. Soc., Dalton Trans.*, 1995, 741-751.
221. P. J. Bailey, M. A. Beswick, B. F. G. Johnson, J. Lewis, M. McPartlin, P. R. Raithby and M. C. R. de Arellano, *J. Chem. Soc., Dalton Trans.*, 1996, 3515-3520.
222. C. Willocq, D. Vidick, B. Tinant, A. Delcorte, P. Bertrand, M. Devillers and S. Hermans, *Eur. J. Inorg. Chem.*, 2011, **2011**, 4721-4729.
223. D. Braga, F. Grepioni, E. Tedesco, P. Dyson, C. Martin and B. G. Johnson, *Transition Met. Chem.*, 1995, **20**, 615-624.
224. B. Delley, M. C. Manning, D. E. Ellis, J. Berkowitz and W. C. Trogler, *Inorg. Chem.*, 1982, **21**, 2247-2253.
225. G. Gervasio, R. Bianchi and D. Marabello, *Chem. Phys. Lett.*, 2005, **407**, 18-22.
226. J. W. Lauher, *J. Am. Chem. Soc.*, 1986, **108**, 1521-1531.
227. B. Peng, Q.-S. Li, Y. Xie, R. B. King and H. F. Schaefer Iii, *Dalton Transactions*, 2008, 6977-6986.
228. G. Gervasio, D. Marabello, R. Bianchi and A. Forni, *The Journal of Physical Chemistry A*, 2010, **114**, 9368-9373.
229. B. F. G. Johnson, R. D. Johnston, J. Lewis, B. H. Robinson and G. Wilkinson, *Journal of the Chemical Society A: Inorganic, Physical, Theoretical*, 1968, 2856-2859.
230. B. F. G. Johnson, J. Lewis and I. G. Williams, *Journal of the Chemical Society A: Inorganic, Physical, Theoretical*, 1970, 901-903.
231. L. Fang, X. Shen, X. Chen and J. R. Lombardi, *Chem. Phys. Lett.*, 2000, **332**, 299-302.
232. R. Schlögl, *Angew. Chem. Int. Ed.*, 2003, **42**, 2004-2008.
233. K. C. Taylor, *Catalysis: Science and Technology*, 1984, **5**, 119-170.
234. S. E. Voltz, *Industrial & engineering chemistry product research and development*, 1973, **12**, 294-301.

235. K. Ziegler, E. Holzkamp, H. Breil and H. Martin, *Angew. Chem.*, 1955, **67**, 541-547.
236. G. Natta, P. Pino, P. Corradini, F. Danusso, E. Mantica, G. Mazzanti and G. Moraglio, *J. Am. Chem. Soc.*, 1955, **77**, 1708-1710.
237. H. C. Lee and R. J. Farrauto, *Industrial & Engineering Chemistry Research*, 1989, **28**, 1-5.
238. L. Prati and G. Martra, *Gold Bulletin*, 1999, **32**, 96-101.
239. M. Sankar, Q. He, M. Morad, J. Pritchard, S. J. Freakley, J. K. Edwards, S. H. Taylor, D. J. Morgan, A. F. Carley, D. W. Knight, C. J. Kiely and G. J. Hutchings, *ACS Nano*, 2012, **6**, 6600-6613.
240. C. Baatz, N. Decker and U. Prüße, *J. Catal.*, 2008, **258**, 165-169.
241. V. V. Smirnov, S. A. Nikolaev, L. A. Tyurina and A. Y. Vasil'kov, *Petroleum Chemistry*, 2006, **46**, 289-290.
242. N. Zheng and G. D. Stucky, *J. Am. Chem. Soc.*, 2006, **128**, 14278-14280.
243. N. Toshima, in *Fine Particles Science and Technology*, ed. E. Pelizzetti, Springer Netherlands, 1996, vol. 12, pp. 371-383.
244. Y.-G. Kim, S.-K. Oh and R. M. Crooks, *Chem. Mater.*, 2003, **16**, 167-172.
245. D. An, A. Ye, W. Deng, Q. Zhang and Y. Wang, *Chemistry – A European Journal*, 2012, **18**, 2938-2947.
246. N. Dupré, C. Brazel, L. Fensterbank, M. Malacria, S. Thorimbert, B. Hasenknopf and E. Lacôte, *Chemistry – A European Journal*, 2012, **18**, 12962-12965.
247. H.-L. Jiang, B. Liu, T. Akita, M. Haruta, H. Sakurai and Q. Xu, *J. Am. Chem. Soc.*, 2009, **131**, 11302-11303.
248. R. Wu, X. Qian, K. Zhou, H. Liu, B. Yadian, J. Wei, H. Zhu and Y. Huang, *Journal of Materials Chemistry A*, 2013, **1**, 14294-14299.
249. B. Ingham, T. H. Lim, C. J. Dotzler, A. Henning, M. F. Toney and R. D. Tilley, *Chem. Mater.*, 2011, **23**, 3312-3317.
250. C. Della Pina, E. Falletta, M. Rossi and A. Sacco, *J. Catal.*, 2009, **263**, 92-97.
251. R. Meyer, C. Lemire, S. K. Shaikhutdinov and H. J. Freund, *Gold Bulletin*, 2004, **37**, 72-124.
252. A. Villa, D. Wang, D. S. Su and L. Prati, *ChemCatChem*, 2009, **1**, 510-514.
253. C. Milone, M. L. Tropeano, G. Gulino, G. Neri, R. Ingoglia and S. Galvagno, *Chem. Commun.*, 2002, 868-869.
254. U. Hartfelder, C. Kartusch, M. Makosch, M. Rovezzi, J. Sa and J. A. van Bokhoven, *Catalysis Science & Technology*, 2013, **3**, 454-461.
255. D. Horváth, L. Toth and L. Guczi, *Catal. Lett.*, 2000, **67**, 117-128.

256. K. Juodkazis, J. Juodkazyt≒, V. Jasulaitien≒, A. Lukinskas and B. Šebeka, *Electrochem. Commun.*, 2000, **2**, 503-507.
257. B. Koslowski, H. G. Boyen, C. Wilderotter, G. Kästle, P. Ziemann, R. Wahrenberg and P. Oelhafen, *Surf. Sci.*, 2001, **475**, 1-10.
258. W. F. Egelhoff, *Surf. Sci. Rep.*, 1987, **6**, 253-415.
259. C. Kuhrt, *Surf. Sci.*, 1991, **245**, 173-179.
260. C. R. Henry, *Surf. Sci. Rep.*, 1998, **31**, 231-325.
261. S. Zafeiratos and S. Kennou, *Surf. Sci.*, 1999, **443**, 238-244.
262. M. Büttner and P. Oelhafen, *Surf. Sci.*, 2006, **600**, 1170-1177.
263. D.-C. Lim, C.-C. Hwang, G. Gantefor and Y. D. Kim, *PCCP*, 2010, **12**, 15172-15180.
264. C. C. Chusuei, X. Lai, K. A. Davis, E. K. Bowers, J. P. Fackler and D. W. Goodman, *Langmuir*, 2001, **17**, 4113-4117.
265. M. Grzelczak and L. M. Liz-Marzan, *Chem. Soc. Rev.*, 2014.
266. P. Mulvaney, *Langmuir*, 1996, **12**, 788-800.
267. R. Fenger, E. Fertitta, H. Kirmse, A. F. Thunemann and K. Rademann, *PCCP*, 2012, **14**, 9343-9349.
268. N. R. Jana, L. Gearheart and C. J. Murphy, *Langmuir*, 2001, **17**, 6782-6786.
269. P. M. T. M. Van Attekum, J. W. A. Van der Velden and J. M. Trooster, *Inorg. Chem.*, 1980, **19**, 701-704.
270. C. Battistoni, G. Mattogno, F. Cariati, L. Naldini and A. Sgamellotti, *Inorg. Chim. Acta*, 1977, **24**, 207-210.
271. J.-D. Grunwaldt and A. Baiker, *The Journal of Physical Chemistry B*, 1999, **103**, 1002-1012.
272. D. Reyes-Coronado, G. Rodríguez-Gattorno, M. E. Espinosa-Pesqueira, C. Cab, R. d. Coss and G. Oskam, *Nanotechnology*, 2008, **19**, 145605.
273. G. Pacchioni, *PCCP*, 2013, **15**, 1737-1757.
274. Y. Negishi, T. Nakazaki, S. Malola, S. Takano, Y. Niihori, W. Kurashige, S. Yamazoe, T. Tsukuda and H. Häkkinen, *J. Am. Chem. Soc.*, 2015, **137**, 1206-1212.
275. G. K. Wertheim, S. B. DiCenzo and S. E. Youngquist, *Phys. Rev. Lett.*, 1983, **51**, 2310-2313.
276. J.-D. Grunwaldt, C. Kiener, C. Wögerbauer and A. Baiker, *J. Catal.*, 1999, **181**, 223-232.
277. Y. Yuan, K. Asakura, A. P. Kozlova, H. Wan, K. Tsai and Y. Iwasawa, *Catal. Today*, 1998, **44**, 333-342.
278. N. Hammer, K. Mathisen and M. Rønning, *Top. Catal.*, 2013, **56**, 637-649.
279. K. Qian, Z. Jiang and W. Huang, *J. Mol. Catal. A: Chem.*, 2007, **264**, 26-32.
280. R. Zanella and C. Louis, *Catal. Today*, 2005, **107–108**, 768-777.

281. Y. Yuan, K. Asakura, H. Wan, K. Tsai and Y. Iwasawa, *Chem. Lett.*, 1996, **25**, 755-756.
282. H. Yin, Z. Ma, M. Chi and S. Dai, *Catal. Lett.*, 2010, **136**, 209-221.
283. M. J. Coutts, M. B. Cortie, M. J. Ford and A. M. McDonagh, *The Journal of Physical Chemistry C*, 2009, **113**, 1325-1328.
284. T. Dickinson, A. F. Povey and P. M. A. Sherwood, *Journal of the Chemical Society, Faraday Transactions 1: Physical Chemistry in Condensed Phases*, 1975, **71**, 298-311.
285. C. C. Chusuei, X. Lai, K. Luo and D. W. Goodman, *Top. Catal.*, 2000, **14**, 71-83.
286. J. J. Pireaux, M. Liehr, P. A. Thiry, J. P. Delrue and R. Caudano, *Surf. Sci.*, 1984, **141**, 221-232.
287. L.-Q. Zheng, X.-D. Yu, J.-J. Xu and H.-Y. Chen, *Analytical Methods*, 2014, **6**, 2031-2033.
288. N. Bogdanchikova, A. Pestryakov, M. H. Farias, J. A. Diaz, M. Avalos and J. Navarrete, *Solid State Sciences*, 2008, **10**, 908-914.
289. B. Schumacher, V. Plzak, M. Kinne and R. J. Behm, *Catal. Lett.*, 2003, **89**, 109-114.
290. S. Tsubota, 1995, pp. 227-235.
291. M. Haruta, *CATTECH*, 2002, **6**, 102-115.
292. K. Okazaki, Y. Morikawa, S. Tanaka, K. Tanaka and M. Kohyama, *Physical Review B*, 2004, **69**, 235404.
293. N. Lopez, J. K. Nørskov, T. V. W. Janssens, A. Carlsson, A. Puig-Molina, B. S. Clausen and J. D. Grunwaldt, *J. Catal.*, 2004, **225**, 86-94.
294. V. Schwartz, D. R. Mullins, W. Yan, B. Chen, S. Dai and S. H. Overbury, *The Journal of Physical Chemistry B*, 2004, **108**, 15782-15790.
295. G. G. Andersson, V. B. Golovko, J. F. Alvino, T. Bennett, O. Wrede, S. M. Mejia, H. S. Al Qahtani, R. Adnan, N. Gunby, D. P. Anderson and G. F. Metha, *The Journal of Chemical Physics*, 2014, **141**, -.
296. H. Zhu, Z. Ma, J. C. Clark, Z. Pan, S. H. Overbury and S. Dai, *Applied Catalysis A: General*, 2007, **326**, 89-99.
297. S. H. Overbury, L. Ortiz-Soto, H. Zhu, B. Lee, M. Amiridis and S. Dai, *Catal. Lett.*, 2004, **95**, 99-106.
298. S. D. Lin, M. Bollinger and M. A. Vannice, *Catal. Lett.*, 1993, **17**, 245-262.
299. B. F. Mangelson, M. R. Jones, D. J. Park, C. M. Shade, G. C. Schatz and C. A. Mirkin, *Chem. Mater.*, 2014, **26**, 3818-3824.
300. F. Boccuzzi, G. Cerrato, F. Pinna and G. Strukul, *The Journal of Physical Chemistry B*, 1998, **102**, 5733-5736.
301. V. R. Choudhary, D. K. Dumbre and S. K. Bhargava, *Industrial & Engineering Chemistry Research*, 2009, **48**, 9471-9478.

302. M. Comotti, W.-C. Li, B. Spliethoff and F. Schüth, *J. Am. Chem. Soc.*, 2005, **128**, 917-924.
303. V. R. Choudhary, A. Dhar, P. Jana, R. Jha and B. S. Uphade, *Green Chemistry*, 2005, **7**, 768-770.
304. B. Nkosi, M. D. Adams, N. J. Coville and G. J. Hutchings, *J. Catal.*, 1991, **128**, 378-386.
305. T. Mallat and A. Baiker, *Annual Review of Chemical and Biomolecular Engineering*, 2012, **3**, 11-28.
306. N. Dimitratos, J. A. Lopez-Sanchez and G. J. Hutchings, *Chemical Science*, 2012, **3**, 20-44.
307. H. Miyamura, M. Morita, T. Inasaki and S. Kobayashi, *Bull. Chem. Soc. Jpn.*, 2011, **84**, 588-599.
308. J. Kilmartin, R. Sarip, R. Grau-Crespo, D. Di Tommaso, G. Hogarth, C. Prestipino and G. Sankar, *ACS Catalysis*, 2012, **2**, 957-963.
309. V. R. Choudhary, R. Jha and P. Jana, *Green Chemistry*, 2007, **9**, 267-272.
310. T. Mallat and A. Baiker, *Catal. Today*, 1994, **19**, 247-283.
311. P. Gallezot, *Catal. Today*, 1997, **37**, 405-418.
312. R. Garcia, M. Besson and P. Gallezot, *Applied Catalysis A: General*, 1995, **127**, 165-176.
313. J. H. J. Kluytmans, A. P. Markusse, B. F. M. Kuster, G. B. Marin and J. C. Schouten, *Catal. Today*, 2000, **57**, 143-155.
314. M. Besson and P. Gallezot, *Catal. Today*, 2000, **57**, 127-141.
315. H. Tsunoyama, H. Sakurai, Y. Negishi and T. Tsukuda, *J. Am. Chem. Soc.*, 2005, **127**, 9374-9375.
316. P. Haider, B. Kimmerle, F. Krumeich, W. Kleist, J.-D. Grunwaldt and A. Baiker, *Catal. Lett.*, 2008, **125**, 169-176.
317. Q. Zhang, W. Deng and Y. Wang, *Chem. Commun.*, 2011, **47**, 9275-9292.
318. K. Y. Lee, Y. W. Lee, J.-H. Lee and S. W. Han, *Colloids and Surfaces A: Physicochemical and Engineering Aspects*, 2010, **372**, 146-150.
319. W. Huang, Q. Hua and T. Cao, *Catal. Lett.*, 2014, **144**, 1355-1369.
320. N. J. S. Costa and L. M. Rossi, *Nanoscale*, 2012, **4**, 5826-5834.
321. R.-Y. Zhong, X.-H. Yan, Z.-K. Gao, R.-J. Zhang and B.-Q. Xu, *Catalysis Science & Technology*, 2013, **3**, 3013-3019.
322. K. Chen, H. Wu, Q. Hua, S. Chang and W. Huang, *PCCP*, 2013, **15**, 2273-2277.
323. T. Yoskamtorn, S. Yamazoe, R. Takahata, J.-i. Nishigaki, A. Thivasasith, J. Limtrakul and T. Tsukuda, *ACS Catalysis*, 2014, **4**, 3696-3700.
324. X. Nie, C. Zeng, X. Ma, H. Qian, Q. Ge, H. Xu and R. Jin, *Nanoscale*, 2013, **5**, 5912-5918.
325. G. Li, C. Liu, Y. Lei and R. Jin, *Chem. Commun.*, 2012, **48**, 12005-12007.
326. G. Li, H. Qian and R. Jin, *Nanoscale*, 2012, **4**, 6714-6717.
327. P. Huang, G. Chen, Z. Jiang, R. Jin, Y. Zhu and Y. Sun, *Nanoscale*, 2013, **5**, 3668-3672.

328. G. Li, C. Zeng and R. Jin, *J. Am. Chem. Soc.*, 2014, **136**, 3673-3679.
329. Y. Liu, H. Tsunoyama, T. Akita and T. Tsukuda, *Chem. Commun.*, 2010, **46**, 550-552.
330. D. S. Ovoshchnikov, B. G. Donoeva, B. E. Williamson and V. B. Golovko, *Catalysis Science & Technology*, 2014, **4**, 752-757.
331. B. G. Donoeva, D. S. Ovoshchnikov and V. B. Golovko, *ACS Catalysis*, 2013, **3**, 2986-2991.
332. V. Peneau, Q. He, G. Shaw, S. A. Kondrat, T. E. Davies, P. Miedziak, M. Forde, N. Dimitratos, C. J. Kiely and G. J. Hutchings, *PCCP*, 2013, **15**, 10636-10644.
333. A. Villa, D. Wang, G. M. Veith, F. Vindigni and L. Prati, *Catalysis Science & Technology*, 2013, **3**, 3036-3041.
334. R. Balasubramanian, R. Guo, A. J. Mills and R. W. Murray, *J. Am. Chem. Soc.*, 2005, **127**, 8126-8132.
335. P. V. Kamat, *The Journal of Physical Chemistry B*, 2002, **106**, 7729-7744.
336. C. Yang, Y. Zhou, G. An and X. Zhao, *Opt. Mater.*, 2013, **35**, 2551-2555.
337. T. Ishida, M. Nagaoka, T. Akita and M. Haruta, *Chemistry – A European Journal*, 2008, **14**, 8456-8460.
338. H. Yang, Y. Wang, J. Lei, L. Shi, X. Wu, V. Mäkinen, S. Lin, Z. Tang, J. He, H. Häkkinen, L. Zheng and N. Zheng, *J. Am. Chem. Soc.*, 2013, **135**, 9568-9571.
339. M. Cargnello, V. V. T. Doan-Nguyen, T. R. Gordon, R. E. Diaz, E. A. Stach, R. J. Gorte, P. Fornasiero and C. B. Murray, *Science*, 2013, **341**, 771-773.
340. X. Liu, M.-H. Liu, Y.-C. Luo, C.-Y. Mou, S. D. Lin, H. Cheng, J.-M. Chen, J.-F. Lee and T.-S. Lin, *J. Am. Chem. Soc.*, 2012, **134**, 10251-10258.
341. M. M. Schubert, S. Hackenberg, A. C. van Veen, M. Muhler, V. Plzak and R. J. Behm, *J. Catal.*, 2001, **197**, 113-122.
342. T. Bennett, R. H. Adnan, J. F. Alvino, R. Kler, V. B. Golovko, G. F. Metha and G. G. Andersson, *The Journal of Physical Chemistry C*, 2015.
343. M. Daté, M. Okumura, S. Tsubota and M. Haruta, *Angew. Chem. Int. Ed.*, 2004, **43**, 2129-2132.
344. S. Tsubota, T. Nakamura, K. Tanaka and M. Haruta, *Catal. Lett.*, 1998, **56**, 131-135.
345. P. Buffat and J. P. Borel, *Physical Review A*, 1976, **13**, 2287-2298.
346. Y. Wu, Y. Li, P. Liu, S. Gardner and B. S. Ong, *Chem. Mater.*, 2006, **18**, 4627-4632.
347. Y. Yuan, K. Asakura, H. Wan, K. Tsai and Y. Iwasawa, *Catal. Lett.*, 1996, **42**, 15-20.
348. R. H. Adnan, G. G. Andersson, M. I. J. Polson, G. F. Metha and V. B. Golovko, *Catalysis Science & Technology*, 2015, **5**, 1323-1333.
349. A. G. Garcia, P. P. Lopes, J. F. Gomes, C. Pires, E. B. Ferreira, R. G. M. Lucena, L. H. S. Gasparotto and G. Tremiliosi-Filho, *New J. Chem.*, 2014.

350. A. Wang, X. Y. Liu, C.-Y. Mou and T. Zhang, *J. Catal.*, 2013, **308**, 258-271.
351. H.-L. Jiang and Q. Xu, *J. Mater. Chem.*, 2011, **21**, 13705-13725.
352. A. G. Shastri and J. Schwank, *J. Catal.*, 1985, **95**, 271-283.
353. T. Sreethawong, D. Sukjit, P. Ouraipryvan, J. Schwank and S. Chavadej, *Catal. Lett.*, 2010, **138**, 160-170.
354. S. Ghadamgahi, *PhD thesis*, 2014.
355. C. Marsden, E. Taarning, D. Hansen, L. Johansen, S. K. Klitgaard, K. Egeblad and C. H. Christensen, *Green Chemistry*, 2008, **10**, 168-170.
356. A. B. Powell and S. S. Stahl, *Org. Lett.*, 2013, **15**, 5072-5075.
357. W. Cui, M. Jia, W. Ao and B. Zhaorigetu, *Reaction Kinetics, Mechanisms and Catalysis*, 2013, **110**, 437-448.
358. S. Dunn, *Int. J. Hydrogen Energy*, 2002, **27**, 235-264.
359. F. D. Gregory, *Office of Safety and Mission Assurance*, 1997.
360. T. Hübert, L. Boon-Brett, G. Black and U. Banach, *Sensors and Actuators B: Chemical*, 2011, **157**, 329-352.
361. H. Gu, Z. Wang and Y. Hu, *Sensors*, 2012, **12**, 5517-5550.
362. A. Züttel, A. Remhof, A. Borgschulte and O. Friedrichs, *Philosophical Transactions of the Royal Society A: Mathematical, Physical and Engineering Sciences*, 2010, **368**, 3329-3342.
363. I. Cano, A. M. Chapman, A. Urakawa and P. W. N. M. van Leeuwen, *J. Am. Chem. Soc.*, 2014, **136**, 2520-2528.
364. T. Wang, G. Mpourmpakis, W. W. Lonergan, D. G. Vlachos and J. G. Chen, *PCCP*, 2013, **15**, 12156-12164.
365. I. I. Moiseev and M. N. Vargaftik, *New J. Chem.*, 1998, **22**, 1217-1227.
366. C. C. Li, W. Zhang, H. Ang, H. Yu, B. Y. Xia, X. Wang, Y. H. Yang, Y. Zhao, H. H. Hng and Q. Yan, *Journal of Materials Chemistry A*, 2014, **2**, 10676-10681.
367. L. Jörissen, in *Fuel Cells in the Waste-to-Energy Chain*, Springer London, 2012, pp. 189-203.
368. R. K. Ahluwalia and J. K. Peng, *Int. J. Hydrogen Energy*, 2009, **34**, 5476-5487.
369. S. O. N. Tasaltin, N. Kilinc, Z. Ziya Ozturk, *Appl. Phys. A*, 2009, **97**.
370. S. K. Arya, S. Krishnan, H. Silva, S. Jean and S. Bhansali, *Analyst*, 2012, **137**, 2743-2756.
371. X. Bévenot, A. Trouillet, C. Veillas, H. Gagnaire and M. Clément, *Sensors and Actuators B: Chemical*, 2000, **67**, 57-67.
372. S.-y. Guo and S. Han, *J. Power Sources*, 2014, **267**, 9-13.
373. Y.-f. Su, M.-c. Lee, G.-b. Wang and Y.-h. Shih, *Chem. Eng. J.*, 2014, **253**, 274-280.

374. C. Gómez-Solís, M. A. Ruiz-Gómez, L. M. Torres-Martínez, I. Juárez-Ramírez and D. Sánchez-Martínez, *Fuel*, 2014, **130**, 221-227.
375. M. Balat, *Int. J. Hydrogen Energy*, 2008, **33**, 4013-4029.
376. C. Wang, M. Boucher, M. Yang, H. Saltsburg and M. Flytzani-Stephanopoulos, *Applied Catalysis B: Environmental*, 2014, **154–155**, 142-152.
377. M. Levent, *Int. J. Hydrogen Energy*, 2004, **29**, 1429-1430.
378. D. U. Eberle and D. R. von Helmolt, *Energy & Environmental Science*, 2010, **3**, 689-699.
379. H. W. Langmi, J. Ren, B. North, M. Mathe and D. Bessarabov, *Electrochim. Acta*, 2014, **128**, 368-392.
380. S. Chavan, J. G. Vitillo, D. Gianolio, O. Zavorotynska, B. Civalleri, S. Jakobsen, M. H. Nilsen, L. Valenzano, C. Lamberti, K. P. Lillerud and S. Bordiga, *PCCP*, 2012, **14**, 1614-1626.
381. L. Wang, T. Zhang, H. He and J. Zhang, *RSC Advances*, 2013, **3**, 21949-21958.
382. H. Yamamoto, H. Miyaoka, S. Hino, H. Nakanishi, T. Ichikawa and Y. Kojima, *Int. J. Hydrogen Energy*, 2009, **34**, 9760-9764.
383. U. Eberle, B. Muller and R. von Helmolt, *Energy & Environmental Science*, 2012, **5**, 8780-8798.
384. A. Gurlo, *Nanoscale*, 2011, **3**, 154-165.
385. J. R. Stetter, W. R. Penrose and S. Yao, *J. Electrochem. Soc.*, 2003, **150**, S11-S16.
386. W. J. Buttner, M. B. Post, R. Burgess and C. Rivkin, *Int. J. Hydrogen Energy*, 2011, **36**, 2462-2470.
387. L. Boon-Brett, J. Bousek, G. Black, P. Moretto, P. Castello, T. Hübert and U. Banach, *Int. J. Hydrogen Energy*, 2010, **35**, 373-384.
388. M. Zhao, J. Huang and C.-W. Ong, *Int. J. Hydrogen Energy*, 2013, **38**, 15559-15566.
389. M. Penza, G. Cassano and F. Tortorella, *Sensors and Actuators B: Chemical*, 2001, **81**, 115-121.
390. D. Barreca, E. Comini, A. P. Ferrucci, A. Gasparotto, C. Maccato, C. Maragno, G. Sberveglieri and E. Tondello, *Chem. Mater.*, 2007, **19**, 5642-5649.
391. M. E. Franke, T. J. Koplin and U. Simon, *Small*, 2006, **2**, 36-50.
392. X. Liu, J. Zhang, T. Yang, X. Guo, S. Wu and S. Wang, *Sensors and Actuators B: Chemical*, 2011, **156**, 918-923.
393. Y.-S. Shim, L. Zhang, D. H. Kim, Y. H. Kim, Y. R. Choi, S. H. Nahm, C.-Y. Kang, W. Lee and H. W. Jang, *Sensors and Actuators B: Chemical*, 2014, **198**, 294-301.
394. Q. Xiang, G. F. Meng, H. B. Zhao, Y. Zhang, H. Li, W. J. Ma and J. Q. Xu, *The Journal of Physical Chemistry C*, 2010, **114**, 2049-2055.
395. G. Korotcenkov, *Materials Science and Engineering: B*, 2007, **139**, 1-23.

396. S. Nagata, A. Inouye, S. Yamamoto, B. Tsuchiya, K. Takano, K. Toh and T. Shikama, *J. Alloys Compd.*, 2007, **446–447**, 558-561.
397. S. J. Ippolito, S. Kandasamy, K. Kalantar-zadeh and W. Wlodarski, *Sensors and Actuators B: Chemical*, 2005, **108**, 154-158.
398. A. Wisitsoorat, M. Z. Ahmad, M. H. Yaacob, M. Horpratum, D. Phakaratkul, T. Lomas, A. Tuantranont and W. Wlodarski, *Sensors and Actuators B: Chemical*, 2013, **182**, 795-801.
399. M. Z. Ahmad, A. Z. Sadek, M. H. Yaacob, D. P. Anderson, G. Matthews, V. B. Golovko and W. Wlodarski, *Sensors and Actuators B: Chemical*, 2013, **179**, 125-130.
400. L. D. Rampino and F. F. Nord, *J. Am. Chem. Soc.*, 1941, **63**, 2745-2749.
401. G. C. Bond, P. A. Sermon, G. Webb, D. A. Buchanan and P. B. Wells, *J. Chem. Soc., Chem. Commun.*, 1973, 444b-445.
402. G. C. Bond and P. A. Sermon, *Gold Bulletin*, 1973, **6**, 102-105.
403. E. Bus and J. A. van Bokhoven, *PCCP*, 2007, **9**, 2894-2902.
404. T. He, Y. Ma, Y.-a. Cao, W.-s. Yang and J.-n. Yao, *PCCP*, 2002, **4**, 1637-1639.
405. M. Penza, C. Martucci and G. Cassano, *Sensors and Actuators B: Chemical*, 1998, **50**, 52-59.
406. Q. Sun, B. K. Rao, P. Jena, D. Stolcic, Y. D. Kim, G. Gantefor and A. W. Castleman, *The Journal of Chemical Physics*, 2004, **121**, 9417-9422.
407. B. Frühberger, M. Grunze and D. J. Dwyer, *Sensors and Actuators B: Chemical*, 1996, **31**, 167-174.
408. G. Orsini and V. Tricoli, *J. Mater. Chem.*, 2010, **20**, 6299-6308.
409. A. Georg, W. Graf, R. Neumann and V. Wittwer, *Thin Solid Films*, 2001, **384**, 269-275.
410. J. Z. Ou, M. H. Yaacob, M. Breedon, H. D. Zheng, J. L. Campbell, K. Latham, J. d. Plessis, W. Wlodarski and K. Kalantar-zadeh, *PCCP*, 2011, **13**, 7330-7339.
411. W. B. Cross, I. P. Parkin, S. A. O'Neill, P. A. Williams, M. F. Mahon and K. C. Molloy, *Chem. Mater.*, 2003, **15**, 2786-2796.
412. L. Lozzi, M. Passacantando, S. Santucci, S. La Rosa and N. Y. Svechnikov, *Sensors Journal, IEEE*, 2003, **3**, 180-188.
413. D. J. Dwyer, *Sensors and actuators. B, Chemical*, 1991, **5**, 155-159.
414. T. G. G. Maffeis, D. Yung, L. LePennec, M. W. Penny, R. J. Cobley, E. Comini, G. Sberveglieri and S. P. Wilks, *Surf. Sci.*, 2007, **601**, 4953-4957.
415. M. Regragui, M. Addou, B. El Idrissi, J. C. Bernède, A. Outzourhit and E. Ec-chamikh, *Mater. Chem. Phys.*, 2001, **70**, 84-89.
416. A. P. Shpak, A. M. Korduban, M. M. Medvedskij and V. O. Kandyba, *J. Electron. Spectrosc. Relat. Phenom.*, 2007, **156–158**, 172-175.

417. C. J. Powell and A. Jablonski, *J. Phys. Chem. Ref. Data*, 1999, **28**, 19-62.
418. E. Brauns, E. Morsbach, S. Kunz, M. Bäumer and W. Lang, *Sensors and Actuators B: Chemical*, 2014, **193**, 895-903.
419. E. Brauns, E. Morsbach, G. Schnurpfeil, M. Bäumer and W. Lang, *Sensors and Actuators B: Chemical*, 2013, **187**, 420-425.
420. D. Barreca, G. Carraro, E. Comini, A. Gasparotto, C. Maccato, C. Sada, G. Sberveglieri and E. Tondello, *The Journal of Physical Chemistry C*, 2011, **115**, 10510-10517.
421. L. De Luca, A. Donato, S. Santangelo, G. Faggio, G. Messina, N. Donato and G. Neri, *Int. J. Hydrogen Energy*, 2012, **37**, 1842-1851.
422. M. Z. Ahmad, V. B. Golovko, R. H. Adnan, F. Abu Bakar, J.-Y. Ruzicka, D. P. Anderson, G. G. Andersson and W. Wlodarski, *Int. J. Hydrogen Energy*, 2013, **38**, 12865-12877.
423. T. Fujitani, I. Nakamura, T. Akita, M. Okumura and M. Haruta, *Angew. Chem. Int. Ed.*, 2009, **48**, 9515-9518.
424. X. Li, W. Feng, Y. Xiao, P. Sun, X. Hu, K. Shimanoe, G. Lu and N. Yamazoe, *RSC Advances*, 2014, **4**, 28005-28010.
425. R. Calavia, A. Mozalev, R. Vazquez, I. Gracia, C. Cané, R. Ionescu and E. Llobet, *Sensors and Actuators B: Chemical*, 2010, **149**, 352-361.
426. M. Ahsan, M. Z. Ahmad, T. Tesfamichael, J. Bell, W. Wlodarski and N. Motta, *Sensors and Actuators B: Chemical*, 2012, **173**, 789-796.
427. J. Kukkola, J. Mäklin, N. Halonen, T. Kyllönen, G. Tóth, M. Szabó, A. Shchukarev, J.-P. Mikkola, H. Jantunen and K. Kordás, *Sensors and Actuators B: Chemical*, 2011, **153**, 293-300.
428. T. Stoycheva, S. Vallejos, C. Blackman, S. J. A. Moniz, J. Calderer and X. Correig, *Sensors and Actuators B: Chemical*, 2012, **161**, 406-413.
429. S. Fardindoost, A. Iraji zad, F. Rahimi and R. Ghasempour, *Int. J. Hydrogen Energy*, 2010, **35**, 854-860.
430. L. F. Zhu, J. C. She, J. Y. Luo, S. Z. Deng, J. Chen, X. W. Ji and N. S. Xu, *Sensors and Actuators B: Chemical*, 2011, **153**, 354-360.
431. S. Nishimura, N. Ikeda and K. Ebitani, *Catal. Today*.
432. C. D. Pina, E. Falletta and M. Rossi, *Chem. Soc. Rev.*, 2012, **41**, 350-369.
433. J. N. Kuhn, C.-K. Tsung, W. Huang and G. A. Somorjai, *J. Catal.*, 2009, **265**, 209-215.